

PEOPLE'S DEMOCRATIC REPUBLIC OF ALGERIA
MINISTRY OF HIGHER EDUCATION
AND SCIENTIFIC RESEARCH
UNIVERSITY OF SAAD DAHLEB BLIDA 1
INSTITUTE OF AERONAUTICS AND SPACE STUDIES
Department of space studies

End of studies project

In view of obtaining the MASTER Diploma in Aeronautics

Option: Space propulsion

**AEROHEATING OPTIMISATION OF A HYPERSONIC
THERMOCHEMICAL NON-EQUILIBRIUM FLOW AROUND
LIFTING BODIES DURING ATMOSPHERIC REENTRY**

Application to: Blunt body, Delta wing, Cone-flare body

Made by:

ZMIT Oumaima

DJABIR Houda

Led by:

Advisor: RENANE Rachid

Co- Advisor: ALLOUCH Rachid

2020/2021

Abstract

The objective of this work is to numerically simulate a thermochemical non-equilibrium hypersonic flow around blunt bodies during atmospheric re-entry. The flow field around the hypersonic vehicle is governed by NS equations with chemical reaction source terms, accounting for the mass, momentum, and energy conservation laws. The Park chemical-kinetic model involves five neutral species, N₂, O₂, NO, N, O, of a kinetic mechanism of 17 reactions is applied. The chemically reacting gas flow was simulated first around the Lobb sphere blunted body to study the non-equilibrium effect of an intensive shock wave under re-entry conditions, we then investigated the trajectory design on a delta body representative shuttle orbiter configuration for the deferent angle of attack 0° to 40° at an altitude range of from 60.96 to 76.20 km for 4.88 to 7.32 km/sec velocities. Finally, we proposed a shape optimisation study between a delta lifting body and a cone-flare ballistic body. The results obtained present a good agreement with the scientific literature. Moreover, a lifting body re-entry provides a high L/D ratio than a ballistic body re-entry which allow a landed intact on a runway.

Key word: hypersonic reactive flows, Nonequilibrium, dissociation, lifting reentry, Delta wing.

Resume

L'objectif de ce travail est de simuler numériquement un écoulement hypersonique hors d'équilibre thermochimique autour de corps émoussée lors de la réentrée atmosphérique. Le champ d'écoulement autour du véhicule hypersonique est régi par des équations NS avec des termes sources de réaction chimique, tenant compte des lois de la masse, de la quantité de mouvement et de la conservation de l'énergie. Le modèle cinétique de Park implique cinq espèces neutres, N₂, O₂, NO, N, O, d'un mécanisme cinétique de 17 réactions est appliqué. Le flux de gaz réagissant chimiquement a d'abord été simulé autour du corps émoussé de sphère de Lobb pour étudier l'effet de non-équilibre d'une onde de choc dans des conditions de rentrée, nous avons ensuite étudié la conception de la trajectoire sur une configuration d'orbiteur navette représentative du corps delta pour deferent angle d'attaque 0°, 20°, 30°, 40° à une plage d'altitude de 60,96 à 76,20 km pour des vitesses de 4,88 à 7,32 km/sec .Enfin, nous avons proposé une étude d'optimisation de forme entre un corps planeur delta et un corps balistique cone-flar. Les résultats obtenus présentent un bon accord avec la littérature scientifique. De plus, une rentrée de corps de plane offre un rapport L/D plus élevé qu'une rentrée de corps balistique qui permet un atterrissage intact.

Mots clés : Ecoulement hypersonique réactif, hors équilibre, dissociation, rentré atmosphérique plane, aile delta.

ملخص

الهدف من هذا العمل هو محاكاة عددية لتدفق تفوق سرعته سرعة الصوت في حالة عدم التوازن الكيميائي حول الأجسام غير الحادة أثناء إعادة الدخول في الغلاف الجوي. يخضع مجال التدفق حول السيارة التي تفوق سرعتها سرعة الصوت إلى معادلات نافيه ستوكس مع شروط مصدر التفاعل الكيميائي، والمحاسبة على الكتلة، والزخم، وقوانين الحفظ على الطاقة. ، بألية حركية لـ 17 تفاعلاً. تمت O، N، NO، O₂، N₂يشتمل نموذج بارك الكيميائي الحركي على خمسة أنواع محايدة، محاكاة تدفق الغاز المتفاعل كيميائياً أولاً حول جسم كرة لوب لدراسة التأثير غير المتوازن لموجة الصدمة تحت ظروف إعادة الدخول، ثم قمنا بالتحقيق في تصميم المسار على تكوين مركبة مكوكية تمثيلية لجسم دلتا على زاوية هجوم بين 0°، 20°، 30°، 40 درجة على نطاق ارتفاع من 60.96 إلى 76.20 كم لسرعات 4.88 إلى 7.32 كم / ثانية. أخيراً، اقترحنا دراسة تحسين الشكل بين جسم رفع دلتا وجسم باليستي مخروطي الشكل. النتائج التي تم الحصول عليها تتوافق بشكل جيد مع المؤلفات العلمية. علاوة على ذلك، توفر إعادة الدخول لجسم الرفع نسبة رفع دفع عالية مقارنةً بإعادة دخول الجسم الباليستية مما يسمح بهبوطه سليماً على المدرج

الكلمات المفتاحية: التدفق التفاعلي الذي يفوق سرعة الصوت، خارج التوازن، التفكك، إعادة الدخول إلى الغلاف الجوي المستوي، جناح دلتا

Acknowledgments

We would like to thank God (Allah) the Almighty for having given us the favour of succeeding in our studies.

At first, we would like to thank our advisors Mr RENAN Rachid and Mr ALLOUCHE Rachid, who were more than generous with their expertise and precious time. We are grateful for their valuable guidance and help throughout the execution of this work, they gave us the strength and knowledge to handle and complete this useful work.

Our sincere thanks to Mr LAAZAB Sbaa for his technical support in simulation and the advice they gave us in the realization of this end of studies project.

We thank also all the teachers of the Institute of Aeronautics and Space Studies who contributed to our training and all our friends and of the promotion as well as all those who collaborated closely or remotely in the realization of this end of studies project.

Finally, we extend our heartfelt and sincere thanks to the members of the Jury who agreed to honour our work with their presence.

Dedications

I would like to acknowledge with gratitude, the support and love of my parents, which has sustained me throughout my life.

To my brothers, my sister

To my friends

I dedicate this work.

ZMIT Oumaima

To my dear parents who have always been there for me, and who have given me a magnificent model of hard work and perseverance.

To my brothers and sisters.

To my teachers

I dedicate this work

DJABIR Houda

Table of Contents

Abstract	
Acknowledgment	
Dedication	
Table of content	
Nomenclature	
Figures and tables list	
Introduction	19
Atmospheric reentry characteristics and state of the art	22
1. Atmospheric re-entry characteristics	23
1.1 Introduction	23
1.2 Atmospheric re-entry characterisation	23
1.2.1 The atmosphere	23
1.2.2 Flows characterization	25
1.2.2.1. Velocity regimes	25
1.2.2.2 Dynamic behaviour	26
1.2.2.3 Flow regimes	26
1.2.3 The dynamics of gases at high temperatures in continuous hypersonic regime	28
1.2.3.1 Oblique shock wave	29
1.2.3.2 Oblique geometry and analysis	29
1.2.3.3.3 Oblique shock wave for perfect gas	31
1.2.3.3.4 Oblique shock relations	31
1.2.3.3.5 Rankine-Hugoniot relation	33
1.2.3.3.6 Normal shock wave	34
1.2.3.3.5 Right shock wave for a perfect gas	35
1.2.3.3 Shock wave in hypersonic flow	38

1.2.4 Physicochemical phenomena in the shock layer	39
1.2.4.1 Chemical environment evaluation	41
1.3 Re-entry trajectory	42
1.3.1.1 Ballistic re-entry	42
1.3.1.2 Lifting re-entry	43
1.3.1.3 Forces Acting on Re-entry Vehicle	44
1.3.2 Modelling the heat flow to the wall	45
1.3.2.1 Convection heat flux	45
1.3.3 State of the art	47
2. Mathematical and physical modelling	52
2.1. Introduction	53
2.2 Governing equations	53
2.2.1 Species conservation	53
2.2.2 The Global Continuity Equation	53
2.2.3 Global momentum conservation	54
2.2.4 Vibration energy conservation	54
2.3 Thermochemical modelling	55
2.3.1 Thermodynamic relations	55
2.3.1.1 Different forms of energy	56
2.3.1.2 Mixture properties	59
2.3.2 Chemical kinetic model	60
2.3.3 Vibration-dissociation coupling	62
2.3.3.1 Park Model	62
2.5 Turbulence modelling	63
2.5.1 Introduction	63
2.5.2 Statistical modelling (RANS)	63
2.5.2.1 The zero-equation model	65
2.5.2.2 One equation model	66
2.5.2.3 Two-equation model	66

2.5.2.4 K-Epsilon model	66
2.5.2.4.1 The transport equations for the standard model $k - \epsilon$	67
2.5.4.6 k-omega $k - \omega$ model	67
2.5.4.6.1 The transport equations for the standard model $k - \omega$	68
2.5.4.6.2 The constants and auxiliary functions for the model $k - \omega$	68
2.5.4.7 $k - \omega$ SST model	68
2.5.2.7.1 The transport equations for the model $k - \omega$ SST	69
2.5.2.7.2 The constants of the model $k - \omega$ SST	69
2.5.2.7.3 Model to $N \geq 2$ equations	69
2.5.3 Wall function	69
3. Numerical modelling	71
3.1 Introduction	72
3.2 Computational Fluid Dynamics code	72
3.2.1 Pre-Processing	72
3.2.2 Solver	72
3.2.3 post-Processing	74
3.3 Mesh	74
3.3.1 Mesh components	74
3.3.2 Mesh types	74
3.3.2.1 Structured grid	74
3.3.2.1.1 Body-Fitted Structured Grids	74
3.3.2.2 Unstructured mesh	75
3.3.2.3 Hybrid mesh	75
3.3.4 General mesh generation techniques	76
3.3.4.1 Mesh generation	76
3.3.5.1 Quality of a mesh	76
3.3.5.1.1 The different quality criteria	76
3.3.5.1.1.1 Clustering	76
3.3.5.1.1.2 Smoothness	77

3.3.5.1.1.3 Aspect ratio	77
3.3.5.1.1.4 Skewness	77
3.3.5.1.1.5 non-orthogonality	78
3.4 Problem and resolution	79
3.4.1 Mesh and geometry	79
3.4.1.1 Part A. study of physicochemical processes in a shock layer around a blunt body	79
3.4.1.1.1 geometry creation	79
3.4.1.1.2 Identification of the boundary conditions	80
3.4.1.1.3 Mesh construction	81
3.4.1.2 Part B: Study of re-entry trajectory design over delta body profile	82
3.4.1.2.1 Delta profile	82
3.4.1.2.1.1 Geometry creation	83
3.4.1.2.1.2 Identification of the boundary conditions	83
3.4.1.2.1.3 Mesh construction	85
3.4.1.2.2 Profile spike	85
3.4.1.2.2.1 Geometry creation	85
3.4.1.2.2.2 Mesh construction	85
3.4.1.3 Part C: shape optimization study on delta wing body and con-flare	87
3.4.1.3.1 Delta body shape	87
3.4.1.3.1.1 Geometry creation	87
3.4.1.3.1.2 Mesh construction	88
3.4.1.3.3 Delta body 3D study	89
3.4.1.3.2 Conical Geometry	91
3.4.1.3.3.1 Geometry creation	91
3.4.1.3.3.2 Mesh construction	91
3.4.2 Setting in data and simulation	93
3.4.2.1 Choice of calculation mode	93
3.4.2.2 Choice of solver	93

3.4.2.3 Choice of model	94
3.4.2.3.1 Choice of turbulence model	94
3.4.2.3.2 Building a Model for Species Reactions	97
3.4.2.3.3 Boundary condition specifications	100
3.4.2.4 Solution	101
3.4.2.4.1.1 Choice of the formulation algorithm	101
3.4.2.4.1.2 The choice of the spatial discretization scheme	102
3.4.2.4.1.2.1 Choice of Gradient method	102
3.4.2.4.1.2.2 The choice of the precision of the diagrams used	102
3.4.2.4.2 Control of the solution	102
3.4.2.4.2.1 Solution limits	102
3.4.2.4.3 Solution initialization	102
3.4.2.4.4 Calculation control	105
3.4.3.2 Grid independence study	106
3.4.3.1.1 Lobb sphere grid independence study	106
3.4.3.2 Delta profile grid independency	107
3.4.3.2 Delta profile grid independency	108
3.4.3.3 Delta body gride dependency	108
3.4.3.4 Conical body grid independency	109
3.5 Conclusion	112
4. Results and Discussions	113
4.1 Introduction	114
4.2 Thermochemical nonequilibrium flow study	114
4.2.1 Change in Mach number of flows after shock	114
4.2.2 Change in flow temperature after shock	115
4.2.3 Pressure field variation	117
4.2.4 Mass fractions of species	118
4.2.5 Effect of the Mack number	120
4.2.6 Effect of chemical model	126
4.2.7 computational domain effect	127

4.3 Delta profile	128
4.3.1 Chemical model effect	130
4.3.2 The angle of attack effect	136
4.3.3 Altitude Effect	142
4.4 Results of Blunt spike	147
4.5 Result of Hypersonic Flow over a delta body	150
4.5.1 Oblique shock wave	151
4.5.2 Reaction effect	153
4.5.3 Velocity Effect	155
4.6 Result of Hypersonic Flow over a Circular Cone	158
4.6.1 Shock wave	159
4.6.2 Reaction effects	161
4.7 Vehicle shape	163
4.7.1 Effects of Vehicle Shape on Deceleration	163

List of Figures:

Figure 1.1	: Atmospheric structure	24
Figure 1.2	: Flow regime as a function of altitude and speed	26
Figure 1.3	: Different approach for the Knudsen number limits	27
Figure 1.4	: Effects of real gas on the temperature behind the shock wave	29
Figure 1.5	: shows the passage of an oblique shock wave	30
Figure 1.6	: Oblique shock flow	31
Figure 1.7	: A right shock configuration for the balance sheet	34
Figure 1.8	: depicts the dissociation and ionization	40
Figure 1.9	: Superimposed zones	41
Figure1.10	: Soyuz ballistic re-entry	43
Figure1.11	: Returning from Space: Re-entry shows	43
Figure1.12	: lifting body hypersonic shapes	44
Figure1.13	: Significant Forces on a Reentry Vehicle.	44
Figure1.14	: The Kosmos-1445 sub-scale demonstrator	48
Figure1.15	: Japanese experimental spaceplane project	48
Figure 2.1	: The different energy modes.	56
Figure 3.1	: Algorithm of numerical approach used by simulation software's	73
Figure 3.2	: Mesh component	74
Figure 3.3	: Boddy fitted structured grid	75
Figure 3.4	: Mesh types	75
Figure 3.5	: Smooth and Non-Smooth Transitions in Cell Size	77
Figure 3.6	: Skewness quality	77
Figure 3.7	: Skewness mesh metrics spectrum	78
Figure 3.8	: Orthogonality quality	78
Figure 3.9	: Orthogonal Quality mesh metrics spectrum	78
Figure 3.10	: Lobb sphere Geometry creation	80

Figure 3.11	: Lobb sphere identification of boundary conditions	81
Figure 3.12	: Lobb sphere Geometry mesh	82
Figure 3.13	: Delta profile geometry creation	83
Figure 3.14	: Identification of boundary conditions	84
Figure 3.15	: Geometry mesh	85
Figure 3.16	: Configuration of the spiked blunt body for simulation	86
Figure 3.17	: Spiked blunt body Geometry creation	86
Figure 3.18	: Blunt spike mesh geometry	87
Figure 3.19	: Geometry creation	87
Figure 3.20	: Delta body geometry mesh	88
Figure 3.21	: Cone-flare geometry creation	89
Figure 3.22	: Geometry mesh	90
Figure 3.23	: Cone-flare geometry mesh	91
Figure 3.24	: Choice of calculation mode and type of dimension	92
Figure 3.25	: Choice of solve	93
Figure 3.26	: Overview of the Density-Based Solution Method	94
Figure 3.27	: Choice of model	95
Figure 3.28	: Activation of the Energy Equation	96
Figure 3.29	: Choice of turbulence model	97
Figure 3.30	: Species reaction model	97
Figure 3.31	: Choice of mixture material	98
Figure 3.32	: Create and edit materiel	98
Figure 3.33	: Reactions	99
Figure 3.34	: The Solution dialog box	101
Figure 3.35	: Solution method	101
Figure 3.36	: Solution control	102
Figure 3.37	: Solution limits	103
Figure 3.38	: Solution initialization	104
Figure 3.39	: Run calculation	104

Figure 3.40	: The evolution of the residues for the initial mesh	105
Figure 3.41	: Lobb sphere grid independency	107
Figure 3.42	: Delta profile gride independency	108
Figure 3.43	: Delta body grid independency	109
Figure 3.44	: Cone-flare body grid independency	110
Figure 3.45	: Lobb sphere Y+ wall profile of $k \omega$ SST model	110
Figure 3.46	: Delta profile Y+ wall profile of $k \omega$ SST model	111
Figure 3.47	: Blunt spike Y+ wall profile of $k \omega$ SST model	111
Figure 3.48	: Delta body Y+ wall profile of $k \omega$ SST model	111
Figure 3.49	: Cone-flare Y+ wall profile of $k \omega$ SST model	112
Figure 4.1	: Variation in Mach number through the shock wave	115
Figure 4.2	: Temperature field variation across the shock wave	116
Figure 4.3	: Temperature along the stagnation ling	117
Figure 4.4	: Pressure fields around the sphere	117
Figure 4.5	: Pressure field along the "Tristan [20]" relaxation range	117
Figure 4.6	: The mass fractions of the species along stagnation line	118
Figure 4.7	: Major species masse fraction	119
Figure 4.8	: Mineur species masse fraction	119
Figure 4.9	: Temperature distribution along the stagnation line	120
Figure 4.10	: Temperature field around the sphere at deferent Mach numbers	121
Figure 4.11	: Pressure field around the sphere at deferent Mach numbers	122
Figure 4.12	: Mass fraction of N around the sphere	123
Figure 4.13	: Mass fraction of N ₂ around the sphere	124
Figure 4.14	: Mass fraction of NO around the sphere	124
Figure 4.15	: Mass fraction of O ₂ around the sphere	125
Figure 4.16	: Mass fraction of O around the sphere	126
Figure 4.17	: Temperature distribution	126
Figure 4.18	: computational domain effect	127
Figure 4.19	: Temperature filed along outer streamline $\alpha = 20^\circ$.	129

Figure 4.20	: Density gradient	129
Figure 4.21	: Wall temperature distribution along surface streamlines	130
Figure 4.22	: Temperature field along surface streamline	131
Figure 4.23	: Pressure field along surface streamlines	132
Figure 4.24	: Mach number field along surface streamlines	133
Figure 4.25	: static enthalpy distribution along surface streamlines	134
Figure 4.26	: wall shear distribution along surface streamlines	135
Figure 4.27	: Drag coefficient and deceleration in function of angle of attack	136
Figure 4.28	: Drag coefficient in function of angle of attack	137
Figure 4.29	: Lift coefficient in function of angle of attack	137
Figure 4.30	: Wall temperature distribution for deferent angle of attack	139
Figure 4.31	: Mach number field along surface stream line	140
Figure 4.32	: Wall temperature distribution for deferent altitude	142
Figure 4.33	: Drag and lift coefficient in function of altitude	142
Figure 4.34	: Temperature field along surface stream line at deferent altitude	143
Figure 4.35	: Pressure field along surface stream line at deferent altitude	144
Figure 4.36	: Mach Number field along surface stream line at deferent altitude	145
Figure 4.37	: Flow field wave structure of spiked blunt body	146
Figure 4.38	: Blunt spike temperature contours	147
Figure 4.39	: Blunt spike density contours	148
Figure 4.40	: Blunt spike Mach number contours	148
Figure 4.41	: Blunt spike pressure contours	149
Figure 4.42	: wall temperature distribution along body surface streamline	150
Figure 4.43	: Iso-Temperature distribution along delta bod	151
Figure 4.44	: static entropy distribution along delta body	151
Figure 4.45	: Total pressure distribution along delta body	151
Figure 4.46	: Temperature distribution along delta body	151
Figure 4.47	: Velocity streamlines along 3D geometry	152
Figure 4.48	: Temperature distribution along delta body	152

Figure 4.49	: Major species distribution along delta body	153
Figure 4.50	: Mineur species distribution along delta body	154
Figure 4.51	: Maximum wall temperature in function of Mach number	165
Figure 4.52	: wall temperature stream lines for different Mach number	165
Figure 4.53	: recirculation region in delta body	156
Figure 4.54	: Comparison of Experimental Result with analytical result	157
Figure 4.55	: Mach number contour along conical body	158
Figure 4.56	: Temperature countor along conical body	159
Figure 4.57:	Cone-flare body outer streamlines distribution	159
Figure 4.58	: Major species flied along conical body	161
Figure 4.59	: Mineur species filed along conical body	162
Figure 4.60	: Drag coefficient in function of deferent angle of attack	163
Figure 4.61	: Lift coefficient in function of deferent angle of attack	164
Figure 4.62	: Wall temperature in function of Mach number	165

List of tables :

Table 2.1	: the constants of the model k-values	68
Table 2.2	: The various closure coefficients of the $k - \epsilon$ model	69
Table 2.3	: The various closure coefficients of the $k - \omega SST$	70
Table 3.1	: Structured vs unstructured mesh	77
Table 3.2	: Lobb sphere free stream boundary condition	80
Table 3.3	: Delta profile study free stream boundary condition	83
Table 3.4	: Delta body free stream boundary conditions	88
Table 3.5	: con-flarebody free stream boundary condition	92
Table 3.6	: Lobb sphere grid independency	108
Table 3.7	: Delta profile grid independency	109
Table 3.8	: Delta body grid independency	109
Table 3.9	: Cone-flare body grid independency	110
Table 4.1	: Position of the shock of the Lobb sphere	117

Nomenclature:

α	: parameter of the Dirichlet distribution.
β :	: apex angle
c_0	: local sound velocity
C_{VD}	: Vibration-dissociation coupling..
C_{VDV}	: Vibration-dissociation-vibration coupling.
C_p	: Mass heat at constant pressure (J.kg-1.K-1).
C_v	: Mass heat at constant volume (J.kg-1.K-1).
C_{ps}	: Constant pressure mass heat of the species (J.kg-1.K-1).
C_{vs} :	: Mass heat at constant volume of the species s(J.kg-1.K-1).
$C_{v,s(rot)}$:	: Mass heat at constant volume of rotation of the species
$C_{v,s(tr)}$: Mass heat with constant volume of translation of (J.kg-1.K-1).
$C_{v,s(v)}$:	: Mass heat at constant volume of vibration of .(J.kg-1.K-1)
D_a	: characteristic non-dimensional number of Damkölher
K	: Number of events the pmf q
l_0	: chord
L	: is a characteristic length of the obstacle
M	: Mach number
$M\alpha$: the molar weight of the species α , respectively
θ^{vib}	: vibrational characteristic temperature
Re_L	: the Reynolds number
ρ	: is the density of the fluid
μ	: is its dynamic viscosity
Kn .	: the Knudsen number
τ_{vib}	: the relaxation time of the vibrational mode
τ_{ec}	: time required for a flow particle to move in the shock layer

τ_{ch}	: characteristic time for chemistry to occur
u_0	: the local flow velocity
γ :	: sweep angle
E	:total energy
e	: wing thickness.
$Q \sim Dir(\alpha)$ parameter α .	: random pmf Q coming from a Dirichlet distribution with
q_{net}	: The net heat flux
$q_{radiative\ transfers}$: The heat flux radiative net
$q_{convec-diffus}$: The sum of the convective heat fluxes
$q_{convection}$: The process of convection
$q_{diffusion}$: The process of diffusion
R_u	: the universal gas constant
T^{tr}	: the translation temperature
$T^{(vib)}$: the vibrational temperature
$\Gamma(s)$: the gamma function evaluated at s, for $s > 0$.
$\Gamma(k,\theta)$: Gamma distribution with parameters k and θ
v_i	: i th entry of the vector v .
v_{-i}	: the vector v with the i-th entry removed.
$X\alpha$: the mass

INTRODUCTION

Introduction

Atmospheric re-entry is one of the most intricate problems in the Aerospace field. It concerns the dynamics and kinematics of a body coming from space that encounters significant planet atmosphere along its trajectory, either descending from a planet orbit, as is the case of satellites or entry space vehicles, or originating from eccentric hyperbolic orbits, as is the case of meteoroids.

Re-entry vehicles pass through several layers of Earth's atmosphere during their descent. The high Mach number flow around the re-entry vehicle is dominated by high-temperature thermo-chemical physics associated with molecular dissociation and ionization, skin friction between molecules engenders an important amount of heat which excites molecules in the air and release their vibrational energy and so the internal energy of these molecules[1]. This high-temperature effect will influence the surface temperature and heat flux of the vehicle, which acts as a thermal load. Thus, the maximum temperature that a spacecraft experiences in its hypersonic flight exceed the limit temperature of any materiel due to the important drag and aerodynamic heating, so the reduction of heat transfer rate plays an important role. Accurate calculation of the heat load is therefore important when designing the flight trajectory. Although computational research in this field has expanded in recent times, further research on the combined effects of thermal non-equilibrium and chemical reactions using the latest computational techniques are needed to fully comprehend the flow physics in hypersonic non-equilibrium flows around re-entry vehicles and how to ensure better thermal protection of spacecraft with good flight quality.

In the other hand, the extent of the heat flux and heat load depends on the shape of the vehicle and its flight trajectory design (altitude, angle of attack). The need for a safer access to space dictates the review of operational capabilities and hence of design approach for manned reentry vehicles. Current systems such as the Space Shuttle, still fly at relatively low L/D (<1.5) but are reusable. Research has shown that reentry vehicle designs with high L/D could be designed to take advantage of aerodynamic lift during reentry [2]. Higher L/D is desirable because it uses its ability of generating a significant lift force to dissipate energy in a controlled fashion during re-entry, being also capable of changing its trajectory to reach the

landing site safely. This leads to an important difference between ballistic and lifting entry: in a ballistic setting the entry body becomes invariably wasted due to the excessive damage it takes from the huge heat fluxes/g-loads, while in a lifting entry it is possible to save the re-entry body and reuse in future missions. So, a vehicle with high aerodynamic efficiency would have enhanced down-range and cross-range capability (more than twice that of the Space Shuttle). This leads to increase significantly the operational flexibility of re-entry space launcher, for which the ability to reach demanding orbits and to return quickly for reuse will be critical to their operations and economics.

Earth's atmosphere presents a dense, fluid medium, which, at orbital velocities, is not all that different from a lake's surface. Re-entry vehicle must plan to hit the atmosphere at the precise angle and speed for a safe landing. If it hit too steeply or too fast, its risk making a big "splash," which would mean a fiery end. If its impact is too shallow, it may literally skip off the atmosphere and back into the cold of space. This subtle dance between fire and ice is the science of atmospheric re-entry. Thus, the goal of atmospheric re-entry is to put a space vehicle on the ground safely.

For this to happen several conditions must be met: the vehicle must sustain the intensive aero heating, the trajectory must ensure descent, aerodynamic load limits must not be exceeded, the vehicle must have minimal guidance capabilities to guarantee that the correct path is followed. Constraints are different depending on the type of vehicle, initial conditions, and if it is manned.

In this work, a study of the phenomena of thermochemical non-equilibrium in the shock layer and the reduction of aerodynamic heating was considered with a step forward toward the improvement of the crew comfort and operational flexibility for the return of manned missions by using high lift-to-drag (L/D) ratios during the entry.

First a description of the hypersonic re-entry flows and its characterization are presented briefly, followed by a relations presentation of RANKINE HUGONIOT allowing the parameters of the flow upstream to be linked to those downstream of a shock wave. Part of this chapter has been devoted to a bibliographical synthesis on heating reduction and aerodynamic drag techniques in hypersonic flows around lifting bodies with a brief prestatation of our apport to the domain.

Secondly it would be interesting to treat, a mathematical and physical flow modulization of the reactive gas mixture in thermochemical nonequilibrium in the general case.

In the third chapter, it was proposed to study a viscous two-dimensional hypersonic flow in thermochemical non-equilibrium around sphere blunt body. In the second part of this study, we explore the mission requirements: trajectory design and vehicle design of vehicles entering earth atmosphere with an application of a blunt-spike at the nose of delta shape to ward off the shock and reduce heating load rate. We consider what engineers must trade in designing missions that must plunge into dense atmospheres. In particular, this chapter focuses on the feasibility of using a numerical computational code for fluid dynamics to simulate such a flow under re-entry conditions.

The last chapter provides an overall presentation of the results of the various studies envisaged from the trajectory simulations of different kinds of re-entry vehicles and finally, a general conclusion will be drawn.

Chapter 1:

Atmospheric re-entry characteristics and state of the art

1. Atmospheric re-entry characteristics

1.1 Introduction

When a spacecraft enters the upper layers of the atmosphere, its speed is still very important (hypersonic speeds). The associated aerodynamic processes create extremely high temperatures, particularly on the nose, necessitating the use of a heat shield. Given the complexities of the phenomena that occur in hypersonic flows, they are currently the topic of extensive research. Given to the complexities of the phenomena that occur in hypersonic flows, they are currently the topic of extensive research. We present in what follows some peculiarities of the trajectories of these vehicles and the important characteristics linked to the new physicochemical characteristics of the flows envisaged around space vehicles.

1.2 Atmospheric re-entry characterisation:

1.2.1 The atmosphere:

The atmosphere is a mixture of several gases that surrounds earth, nitrogen and oxygen make up about 99% of the atmosphere in front of the total volume of the gas, up to altitudes approximately 90 km, the air mixed stay in nearly the same proportions due to fluctuating winds and General atmospheric turbulence in all direction. [1]

The earth's atmosphere has two major zones or shells that we can distinguish by their composition of air:

The homosphere: The region of homosphere is from the ground extends to 100 km consider as the lowest earth's atmosphere layer where the composition of air is uniform and the concentration of molecules are the same in this layer, it includes the troposphere, the stratosphere and the mesosphere.

The heterosphere: is the upper part of the atmosphere between 100 km and 400 km in altitude, where the molecules are dissociated under form of ions and atoms and contains a higher proportion of lighter gases such as helium and hydrogen, it includes the exosphere and the thermosphere.

The most common criterion used is the temperature distribution for divide the atmosphere regions to the troposphere, stratosphere, mesosphere, thermosphere, and exosphere. Figure 1.1 the layers of the atmosphere defined by the composition and temperature.

- The troposphere, from sea level up to about 10 km altitude;
- The stratosphere lying between 10 km and 50 km altitude;
- The mesosphere between 50 km and 80 km altitude;
- The thermosphere lying between 80 to 700 km
- Exosphere: between 700 to 10,000 km

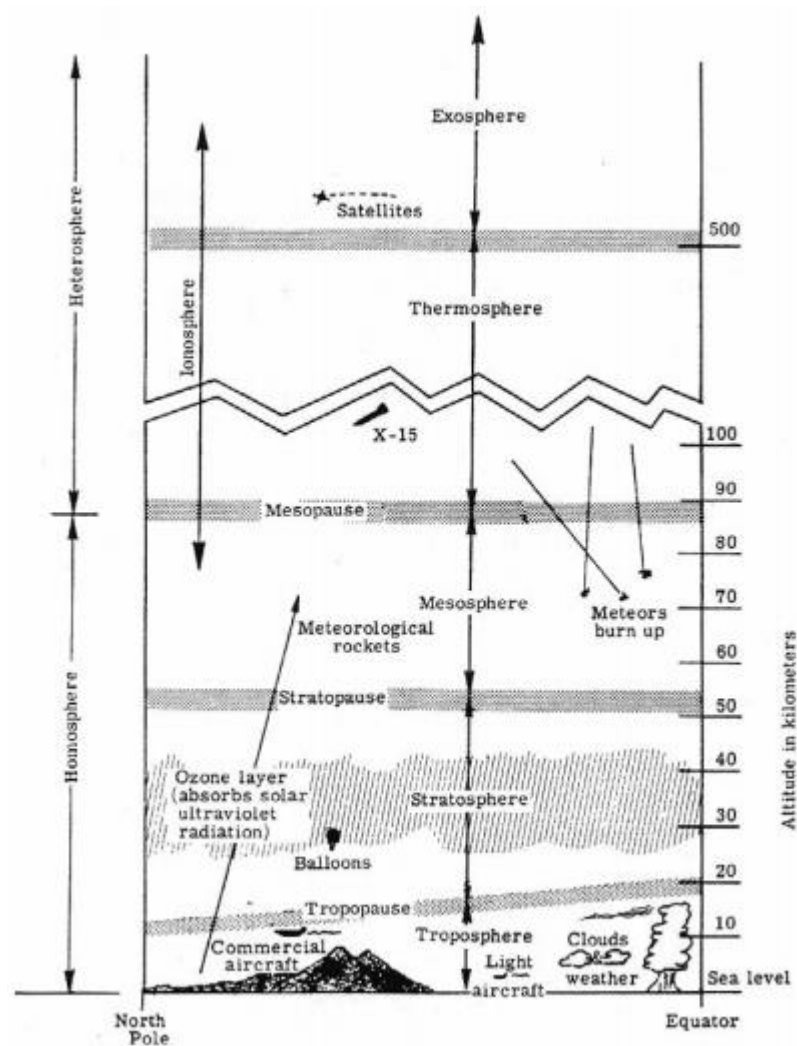


Figure 1.1- Atmospheric structure [1]

Troposphere: The most important layer of atmosphere where all weather conditions is appropriate also for aeronautics since the aircraft fly in this region, besides taken advantages of the ozone layer in the stratosphere protects live of earth by absorbing harmful ultraviolet radiation.

In this layer important climatic phenomena occur and give rise to fluctuations in atmospheric properties, this can induce a problem on the calculation of the end of the re-entry trajectory of a space shuttle, and the winds can influence its trajectory.

The stratosphere: The temperature of the atmosphere by 220 K to 230k.

The ionosphere: regions of earth's atmosphere begin in the mesosphere and extends outwards. The ionosphere is ionized by solar radiation in which the ionized regions of one or more of the atmospheric constituents is significant.

The thermosphere: temperature reached at this layer about 1500 °C (2700 °F), it is not very significant due to the remoteness of the molecules, The air is so rarefied.

The exosphere: The exosphere is the outermost layer of the atmosphere; the density of particles is too low that the effect between particles is neglected. The solar wind becomes a significant influence at this height of 500 km [1], resulting in an "atmosphere" that reaches all the way to the Sun.

1.2.2 Flows characterization:

Space shuttles experience several flow regimes during atmospheric re-entry, ranging from rarefied to continuous medium, [2] hypersonic to subsonic, laminar to turbulent. As a result, a flow depends on the flow regime, a speed regime, and a dynamic behaviour.

1.2.2.1 Velocity regimes:

The speed regime is defined by the Mach number M . It represents the ratio of the local flow velocity u_0 to the local sound velocity c_0 in the medium:

$$M = \frac{u_0}{c_0} \quad (1.1)$$

There are four types of velocity regimes as mentioned in figure 1.2:[2]

- The subsonic regime $M \leq 0.8$, in which the fluid is only moderately compressible.
- The transonic regime, with a value of $0.8 \leq M \leq 1.2$, which corresponds to a temporary state. The presence of both subsonic and supersonic zones characterizes the transition zone.
- In the supersonic regime $1.2 \leq M \leq 5$, A shock wave develops at the nose or upstream of the obstruction. The fluid's aero-thermochemical quantities change dramatically when it passes through this shock wave.
- The hypersonic regime $M \gg 5$, is more intense than the previous one, with physico-chemical phenomena such dissociation, ionization, and vibrational imbalance altering the flow.

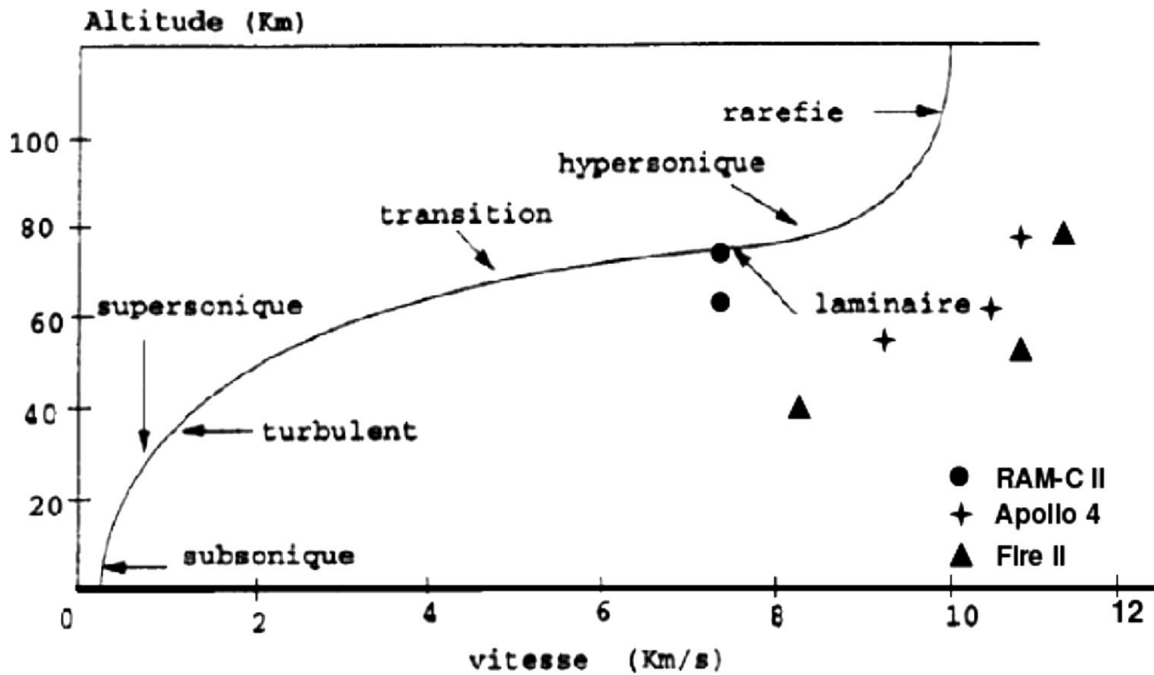


Figure 1.2: Flow regime as a function of altitude and speed for typical conditions of lunar re-entry [2]

1.2.2.2 Dynamic behaviour

The dynamic behaviour of the flow is defined by the Reynolds number Re , which defines the ratio of inertial forces to viscous forces.

$$Re_L = \frac{\rho u_0 L}{\mu} \quad (1.2)$$

Where μ is its dynamic viscosity and ρ is the density of the fluid, and L is a characteristic length of the obstacle.

- There are Three major regimes exist: [3]
- The laminar regime $Re_L < 10^5$, in which viscosity forces predominate. For external Flows, this limit value is valid.
- A transient flow regime in which the flow fluctuates between laminar and turbulent.
- The turbulent regime $Re_L > 10^5$, which appears at much larger Reynolds numbers, and is characterized by three-dimensional random occurrences that are irregular in space and time.[3]

1.2.2.3 Flow regimes:

Because the density of the earth's atmosphere varies with altitude, a hypersonic vehicle such as a planetary entry capsule or a reusable launch vehicle will experience widely diverse flow regimes along its flight trajectory (figure 1.3).[3]

The flow regime is described using the Knudsen number, K_n . It is defined by the report:

$$K_n = \frac{l}{L} \quad (1.3)$$

Where l indicates the average free path of the particles and L is the characteristic length of flow. There are three types of re-entry regimes in terrestrial atmospheric re-entry:

- Continuous regime, $K_n \leq 10^{-3}$, at altitudes below 80 km, the pressure and density of the fluid for this regime are high enough to completely define different macroscopic quantities that characterize the fluid.
- The intermediate regime, $10^{-3} \leq K_n \ll 1$, for altitudes lying between 80 to 100 kilometres. The flow is commonly described by the NS equations, but wall slip conditions are also required.
- The rarefied regime, $K_n \gg 1$, The density and pressure of which are extremely low. It is required to use a microscopic technique to characterize the fluid's evolution in this situation (Boltzmann equations). At very high altitudes, above 100 km, where air pressure is low, this type of flow is common.

The flow is described by solving the original Navier-Stokes's equations, which are predicated on the assumption that the medium is continuous. As a result, we concede that the volume, which we will call "fluid particle," is large enough to hold a huge number of molecules but tiny enough to define a "local" value and an infinitesimal volume element, permitting differential and integral calculus to be justified. [4]

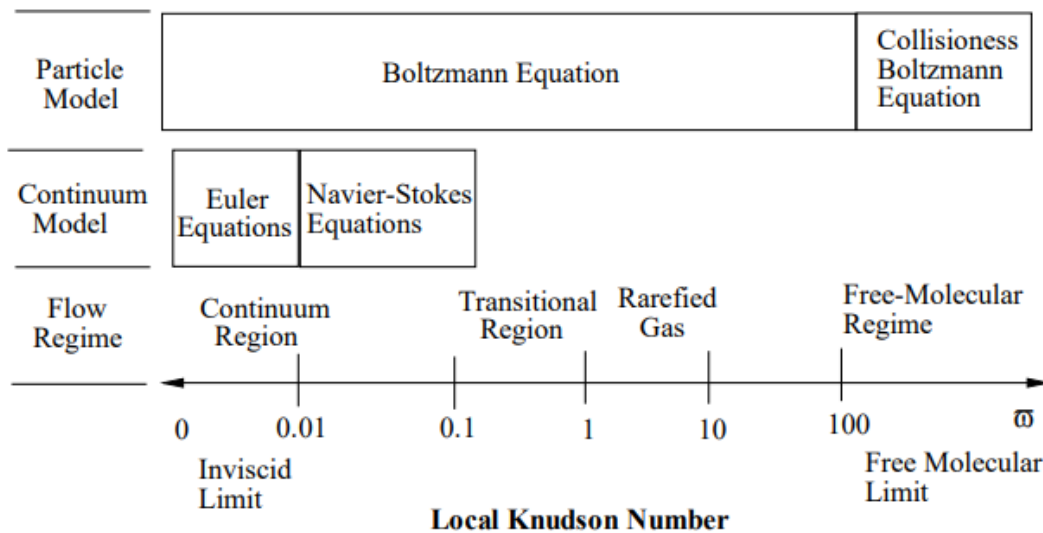


Figure (1.3): Different approach for the Knudsen number limits [3]

When the flow state undergoes a thermochemical non-equilibrium, thus, when a hypersonic vehicle crosses a shock wave that occurs upstream, the kinetic energy of the flow, which is very substantial, is transferred to the internal energy of the particles by collisions. Collision cause because of its power chemical reaction and/or excite the degrees of freedom of the particles, such as rotation, vibration, and electronics (the modes of rotation and vibration only concern molecules). In such situations, there are three sorts of collisions. [4]

- -Elastic collisions, in which only the energy associated with the modes of translation is implicated. Throughout a collision, particles transfer some of their kinetic energy (translation-translation exchanges). These collisions assist in bringing the environment closer to translational equilibrium. It's the Transnational relaxation phenomena.
- Inelastic collisions occur when particles exchange energy through translation as well as rotational, vibrational, and electronic degrees of freedom. As a result, various sorts of exchanges exist, including vibration translation (VT), vibration vibration (VV), rotation translation (RT), and so on. At temperature T, these exchanges will push the medium towards a state of local thermodynamic equilibrium.
- Chemical reactions like dissociation, ionization, and particle charge exchange are produced by reactive collisions.

1.2.3 The dynamics of gases at high temperatures in continuous hypersonic regime:

A strong shock arises upstream of a re-entry vehicle during a hypersonic flow surrounding it. Numerous practical applications require a study of the physicochemical processes which appear downstream of intense shocks where the Mach number is very high. These shocks produce high temperatures and, therefore, a deviation from the behaviour of an ideal gas is observed figure (1.4). [5]

The sudden increase in the internal energy of the gas through the shock manifests itself first as an increase in the translational and rotational thermal stirring energy of the molecules. Then, an evolution towards a state of equilibrium, characterized by the equipartition of energies, thanks to collisions between particles.

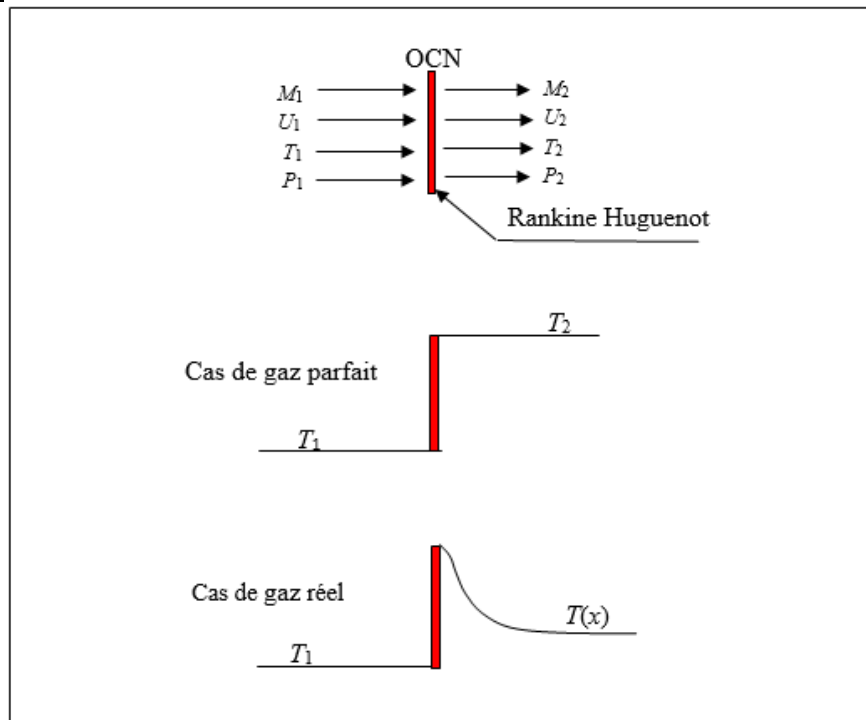


Figure 1.4: Effects of real gas on the temperature behind the shock wave [77]

1.2.3.1 Oblique shock wave:

A vast variety of high-speed compressible flows display highly fast fluctuations in flow characteristics for very small distances, often on the scale of the mean free path of molecules. It is obvious that the equations established to treat continuous media during their validity in this setup. It is consequently either essential to utilize a different model or to describe these phenomena, which we shall refer to as shocks, as discontinuities. [5] We shall be able to create a link between the parameters of the flow upstream and downstream of the shock wave by employing balance equations via these discontinuities., and so relate the values defining these two zones via a shock wave that alters the entropy of the fluid particles, and so relate the values defining these two zones via a shock wave that alters the entropy of the fluid particles.

1.2.3.2 Oblique geometry and analysis:

In the oblique shock flow the limits of the top and bottom are selected to lie along streamlines while only the boundaries parallel to the shock, we have in figure 1.5:

Area A; as a function of the upstream Mach number, M_1 , angle θ , behind an oblique shock T_0 provide it, we'll look at the velocity components normal to the oblique shock (denoted by u) and tangential to the shock (denoted by w).

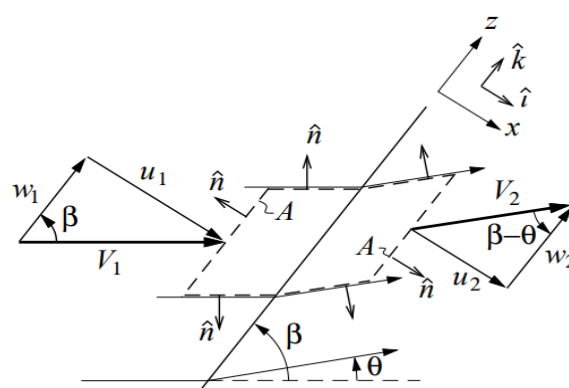


Figure 1.5 shows the passage of an oblique shock wave upstream (subscript 1) and downstream (subscript 2). [5]

The velocity components are calculated using the x-z coordinates normal and tangential to the shock. The wave angle skews the upstream flow velocity components away from the upstream flow direction, and the wave angle skews the tangential z axis, the upstream flow velocity components are:

$$w_1 = V_1 \cos \beta \quad (1.4)$$

$$u_1 = V_1 \sin \beta \quad (1.5)$$

We'll now develop the various conservation equations that will allow us to connect state (1) to state (2).

Mass continuity

$$-\rho_1 u_1 A + -\rho_2 u_2 A = 0 \quad (1.6)$$

$$\rho_1 u_1 = \rho_2 u_2 \quad (1.7)$$

The section does not change. Because the flow's shock is infinitely narrow, $A_1=A_2$.

x-Momentum

$$-\rho_1 u_1^2 A + -\rho_2 u_2^2 A - P_1 A + P_2 A = 0 \quad (1.8)$$

$$\rho_1 u_1^2 + P_1 = \rho_2 u_2^2 + P_2 \quad (1.9)$$

z-Momentum:

$$-\rho_1 u_1 A w_1 + \rho_2 u_2 A w_2 = 0 \quad (1.10)$$

$$w_1 = w_2 \quad (1.11)$$

Energy:

$$h_1 + \frac{1}{2}(u_1^2 + w_1^2) = h_2 + \frac{1}{2}(u_2^2 + w_2^2) \quad (1.12)$$

$$h_1 + \frac{1}{2}(u_1^2) = h_2 + \frac{1}{2}(u_2^2) \quad (1.13)$$

(1.7) is used to eliminate $\rho u A$ from both sides of equation (1.13), and then (1.11) is used to eliminate w from both sides.

1.2.3.3 Oblique shock wave for perfect gas

The state equation for a gas is represented quite simply, for example:

$$p = \rho r T \quad (1.14)$$

When we combine the state of the gas equation with the conservation equation, we get four equations that allow us to determine the four unknowns p_2 , ρ_2 , v_2 , and h_2 that characterize the state (1), for example (2).

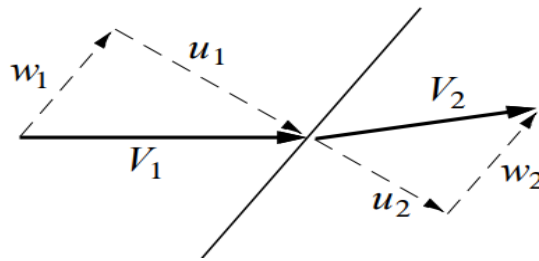


Figure 1.6 Oblique shock flow [6]

The velocity component normal to the shock undergoes the change in an oblique shock flow. As seen in Figure 1.6, the oblique shock jump relationships are: [5]

$$\rho_1 u_1 = \rho_2 u_2 \quad (1.15)$$

$$\rho_1 u_1^2 + P_1 = \rho_2 u_2^2 + P_2 \quad (1.16)$$

$$C_p T_1 + \frac{1}{2}(u_1^2) = C_p T_2 + \frac{1}{2}(u_2^2) \quad (1.17)$$

$$p = \rho r T \quad (1.18)$$

1.2.3.4 Oblique shock relations:

The upsetting thing about these connections is that if you know the upstream Mach number, you can use the normal shock relations to represent differences throughout the oblique shock. It's worth noting that the upstream Mach number must be rewritten in about the same way as the velocity into a Mach number normal to the shock in order to achieve this. [6]

$$M_{n1} \equiv \frac{u_1}{a_1} = \frac{V_1 \sin \beta}{a_1} = M_1 \sin \beta \quad (1.19)$$

$$M_{n2} \equiv \frac{u_2}{a_2} = \frac{V_2 \sin(\beta - \theta)}{a_2} = M_2 \sin(\beta - \theta) \quad (1.20)$$

This allows us to create the well-known equations that correspond to all of the changes that occur across a shock wave. These are the relations

$$\frac{\rho_2}{\rho_1} = \frac{(\gamma+1)M_{n1}^2}{2+(\gamma-1)M_{n1}^2} \quad (1.21)$$

$$\frac{P_2}{P_1} = 1 + \frac{2\gamma}{\gamma+1}(M_{n1}^2 - 1) \quad (1.22)$$

$$\frac{u_2}{u_1} = \frac{2+(\gamma-1)M_{n1}^2}{(\gamma+1)M_{n1}^2} \quad (1.23)$$

$$M_{n2}^2 = \frac{M_{n1}^2 + 2/(\gamma-1)}{[2\gamma/(\gamma-1)]M_{n1}^2 - 1} \quad (1.24)$$

$$\frac{T_2}{T_1} = \left(\frac{P_2}{P_1} \right) \quad (1.25)$$

If we replace the M_{n1} equation in the normal shock relation we get the flowing oblique shock equations

$$\frac{T_2}{T_1} = \left(\frac{2\gamma}{\gamma+1} M_1^2 \sin^2 \beta - \frac{\gamma-1}{\gamma+1} \right) \left(\frac{\gamma-1}{\gamma+1} + \frac{2}{(\gamma+1 \sin^2 \beta) M_1^2} \right) \quad (1.26)$$

$$\frac{P_2}{P_1} = \frac{2\gamma}{\gamma+1} M_1^2 \sin^2 \beta - \frac{\gamma-1}{\gamma+1} \quad (1.27)$$

$$\frac{\rho_2}{\rho_1} = \frac{(\gamma+1)M_1^2 \sin^2 \beta}{2+(\gamma-1)M_1^2 \sin^2 \beta} \quad (1.28)$$

As a result of these equations, we can deduce that the fluctuation of thermodynamic parameters caused by oblique shock is dependent on two variables: the Mach number upstream of the shock wave M_1 and the shock angle.

Figure 1.5 shows how to calculate the Mach number behind an oblique shock using the angles θ, β . As a result, the expression :

$$M_{n2}^2 = \frac{1 + \frac{\gamma-1}{2} M_{n1}^2}{\gamma M_{n1}^2 - \frac{\gamma-1}{2}} \quad (1.29)$$

$$M_2 = \frac{M_{n2}}{\sin(\beta - \theta)} \quad (1.30)$$

The $\theta - \beta - M$ relation:

The wave angle β is still required for these relations. The equation 1.30, is a function that is dependent on M_1 and as a result, in order to calculate M_2 , a relationship can be found from the geometry in figure 1.5. [6]

$$\tan \beta = \frac{u_1}{w_2} \quad (1.31)$$

$$\tan(\beta - \theta) = \frac{u_2}{w_2} \quad (1.32)$$

Equation (1.32) can be recast by adding the result from the momentum equation in terms of the tangential component.

$$\frac{\tan(\beta - \theta)}{\tan \beta} = \frac{u_2}{u_1} \quad (1.33)$$

We get equation (1.7), (1.19), and (1.21) by solving this for u_2/u_1 and entering it into the typical shock relations.

$$\frac{\tan(\beta - \theta)}{\tan \beta} = \frac{u_2}{u_1} = \frac{\rho_1}{\rho_2} = \frac{(\gamma + 1)M_1^2 \sin^2 \beta}{2 + (\gamma - 1)M_1^2 \sin^2 \beta} \quad (1.34)$$

Solving this for θ and with some trigonometric manipulations it can be expressed as

$$\tan \theta = \frac{2}{\tan \beta} \frac{M_1^2 \sin^2 \beta - 1}{M_1^2 (\gamma + \cos 2\beta) + 2} \quad (1.35)$$

Equation 1.35 is called the $\theta - \beta - M$ relation and specifies θ as a unique function of M_1 and β . In the analysis of oblique shock waves, this equation is crucial.

The last relation we'll employ is the one that calculates the entropy change across the shock wave. To accomplish this, we write :

$$\frac{s_2 - s_1}{c_v} = \ln \left(\frac{p_2}{p_1} \left(\frac{\rho_1}{\rho_2} \right)^\gamma \right) \quad (1.36)$$

We already know the pressure and density ratios as a function of the upstream Mach number. After that, we may simply obtain:

$$\frac{S_2 - S_1}{C_v} = \ln \left(\frac{1}{\gamma + 1} \right)^{\gamma + 1} (2\gamma M_1^2 \sin^2 \beta - \gamma + 1) \left(\frac{2}{M_1^2 \sin^2 \beta} + \gamma - 1 \right)^\gamma \quad (1.37)$$

For $M_1 = 1$, we can observe that the entropy variation disappears (infinitely weak shock wave). The entropy variation is positive for $M_1 > 1$, but negative for $M_1 < 1$. We can observe that a standing right shock wave can only occur in a flow supersonic because the last hypothesis is impossible and according to second principle of thermodynamics ΔS should be positive.

1.2.3.3.5 Rankine-Hugoniot relation:

The Rankine-Huguenot equation uses a shock wave to relate the pressure and density ratios. To get it, we use the previously created relations (1.27) and (1.28): [7]

$$\frac{P_2}{P_1} = \frac{2\gamma}{\gamma+1} M_1^2 \sin^2 \beta - \frac{\gamma-1}{\gamma+1} \quad (1.38)$$

$$\frac{\rho_2}{\rho_1} = \frac{(\gamma+1)M_1^2 \sin^2 \beta}{2 + (\gamma-1)M_1^2 \sin^2 \beta} \quad (1.39)$$

To begin, we'll use M1 from the first equation:

$$M_1^2 \sin^2 \beta = \frac{(\gamma+1)P_2 + (\gamma-1)P_1}{2\gamma P_1} \quad (1.40)$$

And we get by deferring in the second equality:

$$\frac{\rho_2}{\rho_1} = \frac{(\gamma+1) \frac{P_2}{P_1} + (\gamma-1)}{(\gamma+1) + (\gamma-1) \frac{P_2}{P_1}} \quad (1.41)$$

By reversing this relationship, we get the Rankine-Huguenot equation:

$$\frac{P_2}{P_1} = \frac{\frac{\gamma+1}{\gamma-1} \frac{p_2}{P_1} - 1}{\frac{\gamma+1}{\gamma-1} - \frac{p_2}{P_1}} \quad (1.42)$$

This relationship allows the thermodynamic state upstream of the shock wave, (p_1, ρ_1) , to be connected to the state downstream, (p_2, ρ_2) ,

1.2.3.3.6 Normal shock wave:

The shock wave is thought to represent a surface of discontinuity perpendicular to the flow as shown in figure 1.7, dividing an upstream region (index (1)) from a downstream region (index (2)) in the configuration we're looking at. This shock wave is stationary.

As a result, by applying balance equations to these discontinuities, we'll be able to relate the properties of the flow upstream and downstream of the shock wave, and hence the values that characterize these two zones.

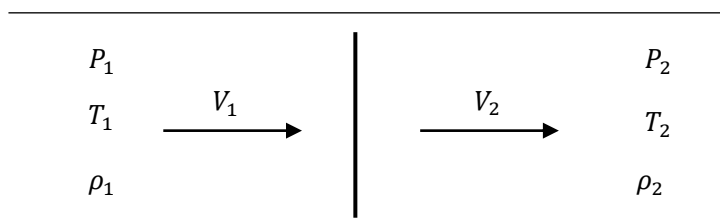


Figure 1.7 – A normal shock configuration for the balance sheet [8]

We'll now develop the various conservation equations that will allow us to relate state (1) to state (2). It's as simple as that to maintain mass conservation.

$$\rho_1 v_1 = \rho_2 v_2 \quad (1.43)$$

Because the shock is infinitely thin perpendicular to the flow, the section remains constant ($A_1=A_2$).

One acquires momentum as a result of this.

$$\dot{m}v_2 - \dot{m}v_1 = p_1 A_1 - p_2 A_2 \quad (1.44)$$

Assume that the flow rate remains constant and that the only source of variation in momentum is pressure forces. Because ($A_1 = A_2$) and (2. 5) are used, we can conclude:

$$p_1 + \rho_1 v_1^2 = p_2 + \rho_2 v_2^2 \quad (1.45)$$

The energy balance is simply written in the absence of effort and heat input:

$$h_1 + \frac{v_1^2}{2} = h_2 + \frac{v_2^2}{2} \quad (1.46)$$

By introducing the state equation to these equations, we obtain four equations, allowing, from the knowledge of the state (1), to calculate the four unknowns, p_2 , ρ_2 , v_2 , h_2 which characterize the state (2). Mass balance: [8]

$$\rho_1 v_1 = \rho_2 v_2 \quad (1.47)$$

Momentum balance:

$$p_1 + \rho_1 v_1^2 = p_2 + \rho_2 v_2^2 \quad (1.48)$$

Energy balance:

$$h_1 + \frac{v_1^2}{2} = h_2 + \frac{v_2^2}{2} \quad (1.49)$$

Equation of state (several possible shapes):

$$p = p(s, p) \quad (1.50)$$

1.2.3.3.5 Normal shock wave for a perfect gas:

We know that the equation of state of the gas is fairly simple in this situation, for example, in the form:

$$p = \rho r T \quad (1.51)$$

The equations for the balances are then simplified to obtain:

Mass balance:

$$\rho_1 v_1 = \rho_2 v_2 \quad (1.52)$$

Momentum balance sheet:

$$p_1 + \rho_1 v_1^2 = p_2 + \rho_2 v_2^2 \quad (1.53)$$

Energy balance:

$$C_p T_1 + \frac{v_1^2}{2} = C_p T_2 + \frac{v_2^2}{2} \quad (1.54)$$

Energy balance:

$$p = \rho r T \quad (1.55)$$

To achieve simple ratios, we will now try to display the upstream and downstream Mach numbers. As a result, we have for the energy equation:

$$C_p T_1 + \frac{v_1^2}{2} = C_p T_1 \left(1 + \frac{v_1^2}{2C_p T_1} \right) = C_p T_1 \left(1 + \frac{\gamma-1}{2} M_1^2 \right) \quad (1.56)$$

Since $c_1^2 = \gamma r T$ The energy balance equation is as follows: $C_p = \frac{\gamma r}{\gamma-1}$

$$\frac{T_2}{T_1} = \frac{1 + \frac{\gamma-1}{2} M_1^2}{1 + \frac{\gamma-1}{2} M_2^2} \quad (1.57)$$

The equation for momentum balance can now be transformed using:

$$p_1 + \rho_1 v_1^2 = p_1 \left(1 + \frac{\rho_1 v_1^2}{p_1} \right) = p_1 (1 + \gamma M_1^2) \quad (1.58)$$

Using $c_1^2 = \frac{\gamma p}{\rho}$ So here's the second relation we're looking for:

$$\frac{p_2}{p_1} = \frac{1 + \gamma M_1^2}{1 + \gamma M_2^2} \quad (1.59)$$

The evolution of the ratio can be quickly deduced using the equation of state of ideal gases:
 ρ_2/ρ_1

The upstream and downstream Mach numbers must now be connected. The mass balance is employed in this process:

$$\frac{\rho_2}{\rho_1} = \frac{v_1}{v_2} = \frac{M_1 c_1}{M_2 c_2} \quad (1.60)$$

The first and third members of this equality can be transformed by employing:

$$\rho = \frac{p}{rT} \quad c = (\gamma r T)^{\frac{1}{2}} \quad (1.61)$$

To get:

$$\frac{p_2}{p_1} = \frac{M_1}{M_2} \left(\frac{T_2}{T_1} \right)^{1/2} \quad (1.62)$$

Changes in Mach numbers have previously been linked to pressure and temperature ratios. We may establish the following relationship between the upstream and downstream Mach numbers by simple substitution:

$$\frac{1 + \gamma M_1^2}{1 + \gamma M_2^2} = \frac{M_1}{M_2} \left(\frac{1 + \frac{\gamma-1}{2} M_1^2}{1 + \frac{\gamma-1}{2} M_2^2} \right)^{\frac{1}{2}} \quad (1.63)$$

This second-degree equation can be easily solved by elevating everything to the square and treating, M_2^2 , for example, as an unknown function of, M_1^2 . $M_2^2 = M_1^2$ is a simple solution that has been discarded. We finally:

$$M_2^2 = \frac{2 + (\gamma-1)M_1^2}{2\gamma M_1^2 + 1 - \gamma} \quad (1.64)$$

The equation 1.25, when combined with the formulas previously discovered for the pressure, temperature, and density ratios, now gives the value of these ratios as a function of the number of upstream Mach numbers (for example). As a result, we have:

$$\frac{T_2}{T_1} = \left(\frac{2\gamma}{\gamma+1} M_1^2 - \frac{\gamma-1}{\gamma+1} \right) \left(\frac{\gamma-1}{\gamma+1} + \frac{2}{(\gamma+1)M_1^2} \right) \quad (1.65)$$

Similarly, we discover:

$$\frac{p_2}{p_1} = \frac{2\gamma}{\gamma+1} M_1^2 - \frac{\gamma-1}{\gamma+1} \quad (1.66)$$

Finally, using the state equation:

$$\frac{\rho_2}{\rho_1} = \frac{p_2}{p_1} \frac{T_1}{T_2} = \frac{2 + (\gamma-1)M_1^2}{1 + (\gamma-1)M_1^2} \quad (1.67)$$

Like $\rho_1 v_1 = \rho_2 v_2$ Finally, using the state equation:

$$\frac{v_1}{v_2} = \frac{2 + (\gamma-1)M_1^2}{1 + (\gamma-1)M_1^2} \quad (1.68)$$

Taking into account all of these connections, we can observe that $M_1 \rightarrow \infty$ also has $T_2 \rightarrow \infty$ et $p_2 \rightarrow \infty$. The ratios of densities and velocities, on the other hand, have a finite limit:

$$\lim_{M_1 \rightarrow \infty} \frac{\rho_2}{\rho_1} = \lim_{M_1 \rightarrow \infty} \frac{v_2}{v_1} = \frac{\gamma+1}{\gamma-1} \quad (1.69)$$

Obtaining the relationship between the total pressures on both sides of the shock may also be beneficial. To accomplish this, we write:

$$\frac{P_{i2}}{P_{i1}} = \frac{P_2}{P_1} \frac{P_2}{P_1} \frac{P_1}{P_{i1}} \quad (1.70)$$

The normal member's second ratio is (1.27), whereas the first and third simply correspond to the isentropic relation. So, in the end, we:

$$\frac{P_{i2}}{P_{i1}} = \left(\left(\frac{\gamma-1}{\gamma+1} + \frac{2}{(\gamma+1)M_1^2} \right)^\gamma \left(\frac{2\gamma}{\gamma+1} M_1^2 - \frac{\gamma-1}{\gamma+1} \right) \right)^{-\frac{1}{\gamma-1}} \quad (1.71)$$

The last relation we'll look at is the one that shows how entropy changes as a result of a shock wave. To accomplish this, we write:

$$\frac{s_2 - s_1}{c_v} = \ln \left(\frac{P_2}{P_1} \left(\frac{\rho_1}{\rho_2} \right)^\gamma \right) \quad (1.72)$$

The last relation we'll look at is the one that shows how entropy changes as a result of the shock wave. To do so, we use the following formula: [8]

$$\frac{s_2 - s_1}{c_v} = \ln \left(\left(\frac{1}{\gamma+1} \right)^{\gamma+1} 2\gamma M_1^2 - \gamma + 1 \right) \left(\frac{2}{M_1^2} + \gamma - 1^\gamma \right) \quad (1.73)$$

For $M_1 = 1$, we can see that the entropy variation balances out (infinitely weak shock wave). The fluctuation of entropy is positive for $M_1 > 1$, but negative for $M_1 < 1$. We can see that a standing normal shock wave can only exist in a supersonic flow because the last hypothesis is impossible according to the second law of thermodynamics.

1.2.3.3.6 Shock wave in hypersonic flow:

The formulae for pressure, density, and temperature following the shock wave reach a mathematical limit when the Mach number of the upstream flow grows progressively hypersonic. [9]

Oblique shock wave equations

$$\frac{T_2}{T_1} = \left(\frac{2\gamma}{\gamma+1} M_1^2 \sin^2 \beta - \frac{\gamma-1}{\gamma+1} \right) \left(\frac{\gamma-1}{\gamma+1} + \frac{2}{(\gamma+1)M_1^2 \sin^2 \beta} \right) \quad (1.74)$$

$$\frac{P_2}{P_1} = \frac{2\gamma}{\gamma+1} M_1^2 \sin^2 \beta - \frac{\gamma-1}{\gamma+1} \quad (1.75)$$

$$\frac{\rho_2}{\rho_1} = \frac{(\gamma+1)M_1^2 \sin^2 \beta}{2 + (\gamma-1)M_1^2 \sin^2 \beta} \quad (1.76)$$

$$\frac{P_2}{P_1} \approx \frac{2\gamma}{\gamma+1} M_1^2 \sin^2 \beta \quad (1.77)$$

$$\frac{\rho_2}{\rho_1} \approx \frac{\gamma+1}{\gamma-1} \quad (1.78)$$

The hypersonic limit for the density ratio is 6 for a perfect atmospheric gas approximation using $\gamma = 1.4$. Hypersonic post-shock dissociation of O₂ and N₂ into O and N, on the other hand, lowers, permitting larger density ratios in nature. The temperature ratio of hypersonic is :

$$\frac{T_2}{T_1} = \frac{2\gamma(\gamma-1)}{(\gamma+1)^2} M_1^2 \sin^2 \beta \quad (1.79)$$

Normal shock wave equations

$$\frac{T_2}{T_1} = \left(\frac{2\gamma}{\gamma+1} M_1^2 \right) \quad (1.80)$$

$$\frac{P_2}{P_1} = \left(\frac{2\gamma}{\gamma+1} M_1^2 \right) \quad (1.81)$$

$$\frac{v_2}{v_1} = \frac{\gamma+1}{\gamma-1} \quad (1.82)$$

However, the state equation $h = cpT$, which was proposed to complete this system, is insufficient to capture the effects of genuine gases arriving at high temperatures. This equation of state is a simplified version of the relations, which is derived from the assumption $cp = \text{constant}$: [9]

$$h(T) = h(T_0) + \int_{T_0}^T c_p(\tau) d\tau \quad (1.83)$$

It is impossible to view cp as a constant at high temperatures due to the gradual stimulation of interior levels of molecules. It is no longer possible to solve the Rankine-Huguenot equations analytically when a realistic equation of state is taken into consideration, which becomes a nonlinear function of temperature.

1.2.4 Physicochemical phenomena in the shock layer:

When the free stream Mach number is increased from a supersonic value, the temperature behind the shock wave rises, in the event of an external flow, the internal energy modes of the molecules are stimulated. Even at extremely high Mach levels, the temperature can rise to the point where the diatomic molecules dissociate. If the Mach number is raised much higher, some species may get ionized. Radiation may emit or absorbed by the gas. The gas cools as it expands across the flow field. This allows the constituents to recombine, causing the internal energy levels to relax. High-temperature effects refer to the thermochemical excitation of vibration, dissociation, ionization, and radiation. As a result, the flow properties diverge from the ideal gas values. To be vibrated excited, a molecule must endure a particular number of collisions (typically a few hundred). This quantity, although,

changes based on the chemical species under consideration, as well as the amount of kinetic energy involved in collisions, and hence the medium's temperature. For the oxygen molecule to dissociate, 200,000 collisions are required.

Because only the translational and rotational modes of internal energy are fully stimulated at low temperatures (800 K), a combination of gases can be described as a mixture of calorically perfected gases with constant specific heats. When the temperature of the air is raised over 800 K, the molecules may experience vibrational excitation, causing the specific heats to become a function of the temperature; the gas is then considered to be thermally perfect. Chemical reactions can occur when the temperature rises, and air becomes a chemically reactive mixture of thermally ideal gases.

O_2 dissociation ($O_2 \rightarrow 2O$) begins about 2000 K for air at 1 atm pressure, and the molecular oxygen is completely dissociated around 4000 K. As seen in Figure (1.8), N_2 dissociation ($N_2 \rightarrow 2N$) begins at this temperature and is essentially completely dissociated by 9000K. Ion's form ($N \rightarrow N^+ + e^-$, $O \rightarrow O^+ + e^-$), and the gas forms a partly ionized plasma, above a temperature of 9000 K. [10]

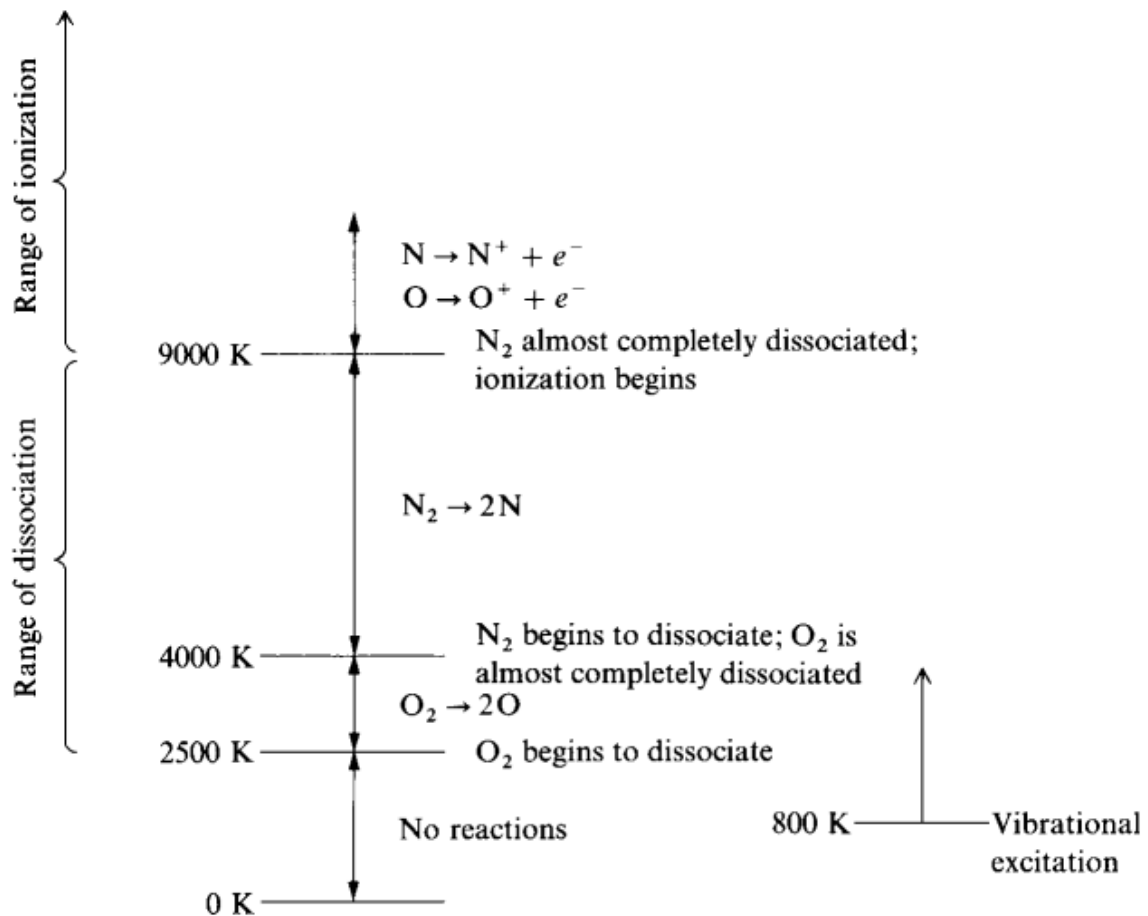


Figure 1.8 depicts the dissociation and ionization ranges in air at 1 atm pressure. [11]

Figure 1.8 provides a direct link to Figure 1.9. The flying zones linked with various chemical effects in air are depicted on this velocity-altitude map. The effective beginning and end of various sections where these effects are prominent are denoted by the 10 and 90% labels at the top of Figure 1.8. In the lower-left corner and mentally "ride up" the flight route in reverse, we will arrive at our destination. At about $V = 14.1$ km/s, vibrational excitation is initially observed in the flow field as the velocity increases. The vibrational mode is virtually fully activated at a higher velocity of roughly 2.5 km/s, and oxygen dissociation initiated. The shaded zone labeled "oxygen dissociation" is affected by this impact. At roughly 5 km/s, O₂ dissociation is virtually complete, and N₂ dissociation begins. The darkened zone labeled "nitrogen dissociation" is affected by this impact. The N₂ dissociation is finally complete above 10 km/s, and ionization begins. The fact that zones of diverse dissociations and ionization are so distinct on the velocity-altitude map, with little overlap, is fascinating.[11]

Finally, based on Figure 1.9, we can make the following general observation. The entry flight pathways slash through large regions of the velocity-altitude map that are critical for chemical reactions and vibrational stimulation.

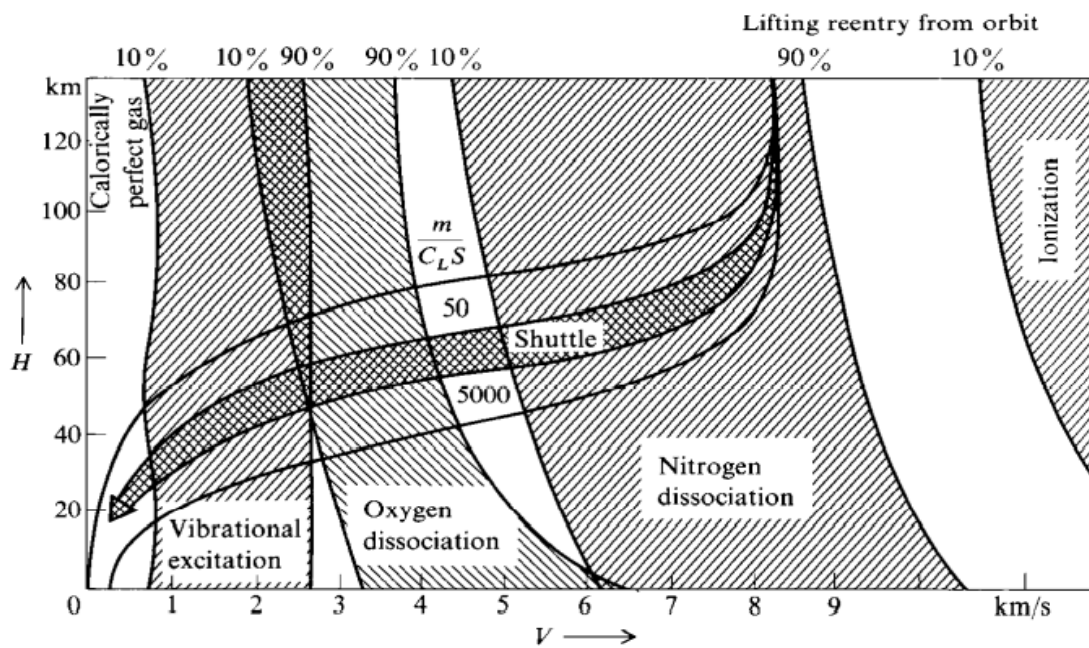


Figure 1.9 Superimposed zones of vibrational excitation, dissociation, and ionization on a velocity-altitude map.[10]

The above-mentioned high-temperature effects are triggered and propagated via molecular collisions. In general, these phenomena have predictable time scales for reaching equilibrium; in translational mode, only a few collisions are required to achieve equilibrium. In rotational mode, around 10 collisions are required, while in vibrational mode, about 200,000 collisions are required [10]. A molecule must collide with other molecules several times to obtain complete excitation of a vibrational energy mode, for example. A chemically reactive medium must do the same to reach its equilibrium composition at a given pressure and temperature. As a result, the vibrational mode's relaxation duration is clearly longer than the other modes.

When the relaxation time of the vibrational mode τ_{vib} is compared to the time required for a flow particle to move in the shock layer τ_{ec} , three flow states can be distinguished:

- $\tau_{vib} \ll \tau_{ec}$ The flow is considered to be in thermochemical equilibrium
- $\tau_{vib} \gg \tau_{ec}$ Vibrationally, the flow is frozen. After passing the shock wave, the thermodynamic condition remains unchanged.
- $\tau_{vib} \sim \tau_{ec}$ Because the vibration temperature of each vibrating molecule may differ from the translation-rotation temperature of the mixture, the flow is in vibrational equilibrium, also known as thermal equilibrium

1.2.4.1 Chemical environment evaluation:

Flow chemistry include a huge variety of processes and microscopic phenomena, which are normally contained in a series of chemical reactions, each with its own kinetics, and which yet include numerous forward and backward reactions. It's a difficult task to account for the chemical state of a mixture. The ultimate stable state is equilibrium.

Different perspectives on chemical non-equilibrium could be used. Damköhler proposed a characteristic non-dimensional number (D_a) to account for the chemical non-equilibrium of a gas mixture. In the same location, he proposed comparing a characteristic time for chemistry to occur (τ_{ch}) with a characteristic time for flow (τ_{ec})

$$D_a = \frac{\tau_{ec}}{\tau_{ch}} \quad (1.84)$$

$\tau_{ch} \gg \tau_{ec}$ Within a frozen flow $D_a \rightarrow 0$ chemical processes do not have time to develop. When traveling through a shock wave. Because the thickness of the shock reflects only a few mean free pathways of a particles, the flow behavior rapidly changes. For a few collisions, however, the rotating mode can relax and approach equilibrium. Everything happens as if the gas downstream of the shock has the same composition as the gas upstream. When a flow is exposed to a large amount of expansion, it might get frozen. [12]

$\tau_{ch} \ll \tau_{ec}$ For chemical equilibrium flow: $D_a \rightarrow \infty$ When compared to the flow's time scale, chemical reactions where the approach to equilibrium is incredibly fast. To put it another way, the gas's chemical composition changes to local temperature and pressure conditions in a very short amount of time, and hence over a very small distance. Chemical equilibrium is achieved at each point in the flow. As a result, the local composition of the gas is entirely determined by local pressure and temperature, or any other combination of variables.

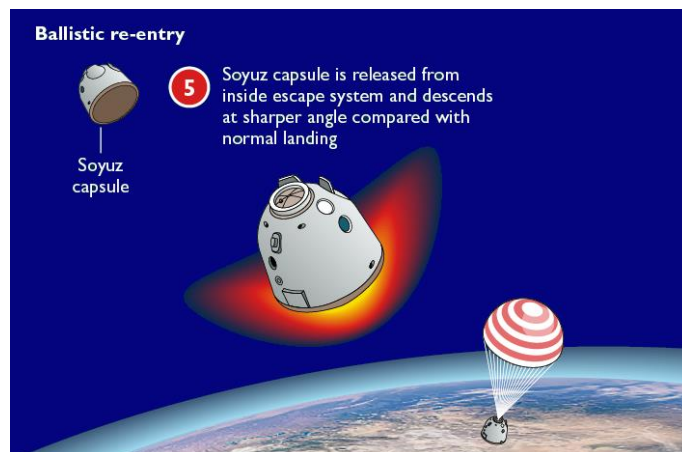
$\tau_{ch} \sim \tau_{ec}$ the flow is a Chemical non-equilibrium, The chemical composition of the gas varies depending on the flow parameters. It will require more time or space to reach equilibrium.

1.3 Re-entry trajectory

As the spacecraft travels through the planetary atmosphere, this energy is converted to heat, and the vehicle's velocity is considerably reduced due to atmospheric drag, the vehicle is subjected to extremely high thermal and mechanical loads during re-entry [13]. Analysis of re-entry trajectories present deferent of systematic classification of spacecraft types and re-entry methods. The distinction between ballistic, semi-ballistic, and lifting trajectories is due to the aspect of lift to drag ratio.

1.3.1 Ballistic re-entry

The vast majority of unmanned spacecraft returning to Earth take a ballistic entry trajectory, meaning they don't generate any aerodynamic lift. Under the influence of gravity and drag, the spacecraft enters the atmosphere and falls through it as described in figure 1.10. The vehicle is slowed by the drag force until parachutes may be deployed for a smooth landing. Conditions when the vehicle first enters the atmosphere define the landing point, and there is no control over the spacecraft once it begins the ballistic entry. The downrange distance, [12] or ground track, from the point when the spacecraft initially entered the atmosphere until landing is small compared to a vehicle following lifted re-entry since the



spacecraft enters at a sharp entry angle into the atmosphere.

Figure 1.10: Soyuz ballistic re-entry

1.3.2 Lifting re-entry

The lifting trajectory, in which the spacecraft flies through the atmosphere like an airplane, is another re-entry method. The spacecraft enters the atmosphere at a steep angle of attack,

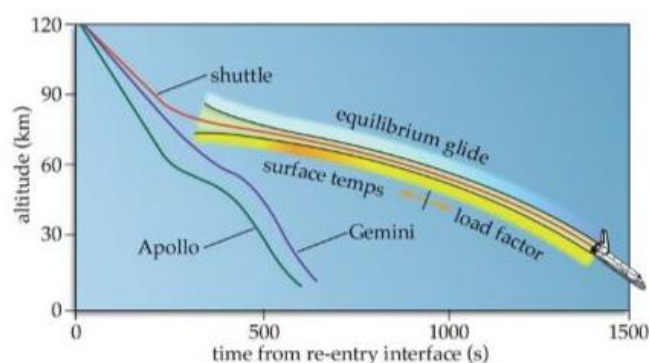


Figure1.11 : Returning from Space: Re-entry shows "Re-entry Profiles for the Shuttle Versus Gemini and Apollo"[14]

creating aerodynamic lift that allows it to fly farther downrange than a ballistic vehicle

The lifting trajectory as represented in figure 1.11, in which the spacecraft flies through the atmosphere like an airplane, is another re-entry method. The spacecraft enters the atmosphere at a steep angle of attack, creating aerodynamic lift that allows it to fly farther downrange than a ballistic vehicle. The primary benefit of this method is that the vehicle has more control over its trajectory and speed. Another benefit is that the vehicle is usually landed intact on a runway and can potentially be reused. This approach is used by the Space Shuttle which is currently the only vehicle that uses a lifting entry trajectory to return from an orbital mission. For interplanetary re-entry missions, Monti et al. and Wingrove investigated re-entry scenarios employing lift forces scenarios employing lift forces. interplanetary re-entry missions, Monti et al. [14] and Wingrove [15] investigated re-entry scenarios employing lift forces.

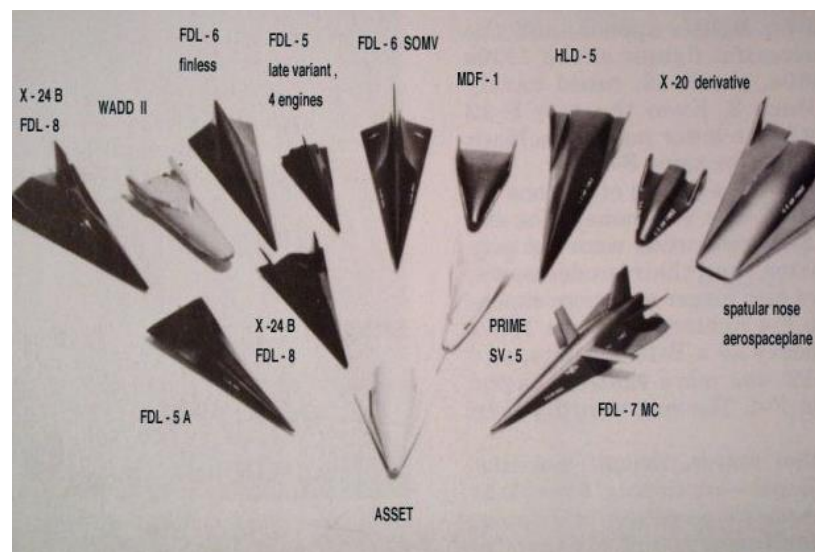


Figure 1.12: lifting body hypersonic shapes [15]

1.3.3 Forces Acting on Re-entry Vehicle

The distribution of the friction forces on the surface of the body, the decomposition of the aerodynamic resultant whose point of application is the centre of thrust (which moves as a function of the angle of incidence figure 1.13) gives a vertical component denoted "L" and called lift and a horizontal component denoted "D" and called drag these two components are always defined with respect to the direction of the relative flow.

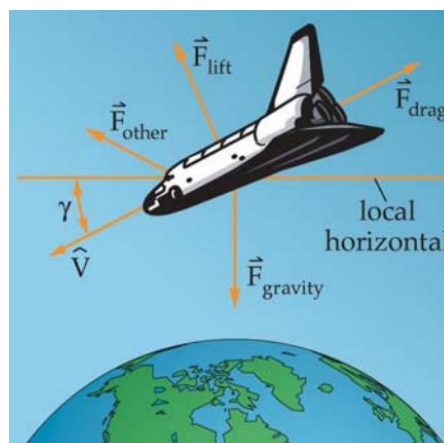


Figure 1.13: Significant Forces on a Re-entry Vehicle. A re-entry vehicle could potentially encounter lift, drag, and gravity forces. Of these, drag is by far the most important [14]

Lift force

It is the aerodynamic force that keeps an aircraft in the air and must be greater than or equal to the weight of the vehicle. The intensity of this force is calculated by the following formula:

$$L = \frac{1}{2} \rho S V^2 C_L \quad (1.85)$$

With: C_L : Lift Coefficient which depends on the shape of the profile, the surface condition, the angle of attack and the upstream infinite speed.

Drag force

It is the force which opposes the movement of the plane through the air it is applied in the opposite direction to the speed of the vehicle.

The intensity of this force is calculated by the following formula:

$$D = \frac{1}{2} \rho S V^2 C_D \quad (1.86)$$

C_D : drag coefficient which depends on the shape of the profile, the surface condition, the angle of attack and the upstream infinite speed.

Ballistic coefficient

The ballistic coefficient (BC) of a body is a measure of its ability to overcome air resistance in flight. It is inversely proportional to the negative acceleration. [15]

$$BC = \frac{\rho l}{C_d} \quad (1.87)$$

Where ρ is the density, l is the characteristic length of the body and C_d is the drag coefficient?

1.3.2 Modelling the heat flow to the wall:

Heat flow is an important parameter to consider while studying an atmospheric re-entry vehicle. During an aerothermodynamic study, the goal is to make sure that the vehicle and its cargo can survive the heat load.[8] Convection is the primary means of heat transfer to a vehicle entering Earth's atmosphere at speeds under about 15,000 m/s. [16] Above this speed, the air molecules get so hot and begin to transfer more of their energy to the vehicle.

1.3.2.1 Convection heat flux:

The heat transport from the gas to the wall owing to convection $q_{\text{convection}}$ is characterized as follows:

$$q_{\text{convection}} = h(T_{\text{wall}} - T_{\text{gas}}) \quad (1.88)$$

T_{wall} is the temperature of the wall, T_{gas} is the temperature of the gas just upstream of the wall.

Our ability to accurately calculate this heating is limited by uncertainties in the heat transfer coefficient for the atmospheric re-entry phase. The familiar form which is dependent on the free-stream Reynolds number scaled by the nose radius to calculate the convection is given as follow (equation 5.1) [75]. we are led to follow the 1958 approach and the derivations of Lees and Allen [51], and Eggers [52], who produced an approximation that allows us to quantify the Stanton number at the stagnation point for typical re-entry conditions at high Mach numbers. [16]

$$St_{High\ speed} \approx 1.57 \sqrt{\frac{M_{\infty}}{Re(r_{nose})}} \quad (1.89)$$

Were,

$$Re(r_{nose}) = \frac{\rho_{\infty} v_{\infty} r_{nose}}{\mu_{\infty}} \quad (1.90)$$

And therefore

$$C_h = St \rho v_{\infty} C_p \quad (1.91)$$

The Equation 5.1 is an acceptable expression for estimating peak blunt-nose heat flux. Based on low densities on re-entry problems, The well-known studies by Lees, Allen [51] and Eggers [52] and their colleagues have also shown that for high velocity stagnant flows, the heat flow is inversely proportional to the square root of the radius of the nose. Lees' interpretation of this dependence on the blunt nose radius is that "at hypersonic speeds all re-entry bodies need to be blunt to some extent in order to reduce the rate of re-entry heat transfer at high speeds. manageable proportions".

Using a similar set of underlying boundary layer assumptions, Sutton and Graves calculated the constant A for the equivalent heat transfer at the stagnation point, this calculation being made on the basis of the assumption that the air downstream of the shock wave is completely dissociated. They also included in their calculations the Newtonian model for the stagnation point velocity gradient, the value of A can be approximated to:

$$A = 1.74 \times 10^{-4} \sqrt{\text{Kg}/\text{m}}$$

On the other hand, the Stanton number can be calculated as follows: [16]

$$ST_{high\ speed} = \frac{h}{\rho_{\infty} c_p V_{\infty}} \quad (1.92)$$

H : convection coefficient $w/(m^2k)$

c_p : specific heat at constant pressure in $j/(Kg.k)$

V_{∞} : speed of the upstream infinite flow in meters

1.3.3 State of the art

Theoretical study on lifting bodies started in the 1950s at the National Advisory Committee for Aeronautics (NACA) laboratories in the United States. Horizontal half-cones with rounded noses and flat summits were the first lifting bodies.

In January 1964 Clarence Cohen, Julius Schetzer, and John Sellars, engineers with the aerospace firm TRW, [17] filed a patent application for a piloted lifting-body spacecraft design that could carry out what they called a "staged reentry".

Cohen, Schetzer, and Sellars innovate an offset centre of gravity around which they would roll at high speeds to gain lift and to gain lift and cross range capabilities while limiting deceleration loads. NASA Gemini and Apollo capsules would become unsteerable and lose lift as they dropped speed, [18] and their parachutes would not be able to guide them to a specified landing site. Both have been considered with steerable triangular para-Wings, but such systems would be difficult.

The flat-bottomed DynaSoar had been designed for both steerable, low-deceleration Earth atmosphere re-entry and stability and steerability at low speeds; however, the Department of Defense space plane's flat belly and narrow-edged wings and fins made it difficult to cover with heat shield materials. [17] Protecting the triangular glider adequately from re-entry heating threatened to boost its weight so much that its ability to manoeuvre in the lower atmosphere might be compromised.

On 10 May 1967, on its 16th flight, these problems caught up with the M2-F2. With Bruce Peterson at its controls, the M2-F2 crashed onto the Edwards AFB dry lake bed. Miraculously, [17] Petersen survived, as did NASA's lifting body research program.

Past experience of winged and lifting body re-entry demonstration has been focused on some particular vehicles such as the USA X-15, X-38 (and others), the Russian BORs and the Japanese HYFLEX. The Space Shuttle program took advantage of numerous experimental lifting vehicles, [19] such as ASSET, X-15, X-23A, X-24. The X-38 permitted to gain experience in the frame of nose and body flap technology in Europe as well as in the field of aerodynamic characterization at high speeds, shape design, GNC, TPS architecture. A space flight has never been performed.

Russian experimental flight vehicle. under the BURAN program was to split the re-entry demonstration in order to avoid the management of the compromise between aerothermodynamic problems and aerodynamic ones, due to the scale effect of the

demonstrator. As a result of that logic, BOR-4 (flown between 1982-1984 up to Mach 25) was dedicated to orbital re-entry with a shape representative at scale 1 of the BURA

N nose/windward curvature. [19] The BOR-5 (flown between 1983-1988, up to Mach 18) was a subscale of BURAN dedicated to aerodynamic efficiency, flight worthiness and GNC.



Figure 1.14: The Kosmos-1445 sub-scale demonstrator being retrieved at sea after some flight test

In Japan, an important fleet of experimental vehicles has been developed to support the development of the HOPE-X programmed. The HYFLEX and HSFD have



Figure 1.15 : Japanese experimental spaceplane project designed by a partnership between NASDA and NAL (both now part of JAXA)

been developed in this frame, [19] but the high hypersonic domain has never been explored with a controlled glider.

Cole and Brainerd [59], Kennet [60] and later **Antonov and Hayes [61]** applied to flows of relevance to hypersonic wings and then in 1962 effectively dealt with low aspect ratio wings at high angles of attack.

Messiter in 1963 recast in a particularly concise set of the equation of thin shock layer theory, the solution was complex and was also restricted [62] to the detached shock condition.

Experiments started in 1970 have confirmed that if at least a portion of the under-surface heatshield has anhedral, a body of basically delta planform will produce significant increases in maximum lift coefficient and CL per unit LD at re-entry Mach numbers (6 M 22) and re-entry angles of attack (25° 70° , say). [18]

By mean 1970 Squire [63,64] developed numerical solutions for conical wings with flat, diamond, and caret cross-sections, and then Hillier [74] added yaw effects.

In 1970, Roe [67] and Squire [73] began investigating the hypothesis that concave under surfaces on a delta wing would allow it to support a larger shock at a given angle of attack, resulting in a higher C L per unit L/D.

Hillier [68] has since extended thin shock layer theory to explore a variety of nonconical shapes; this, as well as additional work on conical wings [69,70], was presented by Hillier et al. at Euromech [74] in 1976., By finding simple correlations to link the heating rates on the centre line of a conical body with the shock wave standoff angle, Roe has extended thin shock layer theory to include the treatment of heat transfer. Roe's correlations [70] are obtained as now described.

Richards and Houwink [71] have evaluated a free flight test in an airflow of Mach 15 and at Reynolds number $2 \cdot 10^6$ to compare flat and caret delta models (the latter having $\alpha = 8.7^\circ$). For the flat and caret delta, the angles of attack ranged from under 40° to just under 50° and 60° , respectively.

Squire [72] and Shanbhag [69] innovate the principal theoretical contributions for the design of lifting re-entry vehicles with nonuniform anhedral especially for high Mach numbers, and Roe for moderate Mach numbers), hillier has considered the performance of wings with complex anhedral and wing-body combination.

Squire [72] investigated delta wing performance as aspect ratio and anhedral distribution varied between Mach 3.5 and 8, and at angles of attack up to 60 degrees. They confirm that aerodynamic advantages are significant at both Mach numbers, and the results reveal that raising the aspect ratio from $2/3$ to $4/3$ diminishes their advantage over identical flat deltas just partially.

Haibo Niu, Shihe Yi, Xiaolin Liu, Xiaoge Lu, Dundian Gang 2019 conduct an experimental study on the boundary layer transition over a delta wing at Mach number 6 in a quiet wind tunnel. The Nano-tracer-based Planar Laser Scattering (NPLS) and Temperature-Sensitive Paints (TSP) techniques were used. The following results were obtained. The cross-flow instability controls the boundary layer transition between the leading edge and the centre line. When the crossflow broke up to the turbulence the Stanton number gets its maximum value. [18] The spanwise pressure gradient on the windward side of the delta wing grew when the angle of attack was raised, creating crossflow instability and advancing the boundary layer transition front. The increased angle of attack, on the other hand, caused the transition front to move backwards on the leeward side. The sensitivity of the boundary layer transition to the Reynolds number also varied depending on the angle of attack and the region.

G. N. Dudin presents an experimental study of hypersonic viscous gas flow past three-dimensional bodies over a finite-length flat delta wing with wake flow in the intermediate interaction. Data for flow over a delta wing with a given pressure at the trailing edge, pressure distributions along the x coordinate in the plane of symmetry, and the distribution of the displacement thickness are compared. [20] Computers were beginning to emerge as practical design tools in the early stages of entry-level vehicle design here is some digital experiment that has been done to optimize lifting re-entry understanding.

Izv. Akad. Nauk SSSR, Mekh. Zhidk. Gaza, No. 3, 164 (1982) study conduct a Zahid numerical flow model for a viscous reacting gas in the shock layer near the windward side of blunt elongated bodies was used to investigate heat transfer on the surface of a Delta Wing[21] with blunt edges and various catalytic surface properties in a hypersonic air flow at 40° and 60° angles of attack and to describe the flow in the shock layer.

S. A. Gorokhov, V. V. Eremin, and A. M. Polyakov analyses in hypersonic flow over blunt delta wings to do the difference between the behaviour of the entropy layers [22] in two limiting cases of flow over blunt delta wings with a sweep angle X: i) blunt plate ($X = 0$), and 2) blunt cylinder ($X = 90$).

L. Gonor and N. A. Ostepenکو studies a hypersonic flow through a slender delta wing with supersonic leading edges by considering the solution of the boundary problem and Calculation of flow past a wing with rhombic cross section which conclude that the reduction of the standoff [23] as a result of increase of the intensity of the gas spreading flow from the plane of symmetry with increase of the angle of attack.

G.Z. Genhuni, E. M. Zhukhovitskii and III. s. Iurkov they examine the flow over a triangular plate at an angle of attack, and shaped cross section for several angel of

attack releasing the solution of the hypersonic flow past a slender conical wing assuming that the disturbed flow region is a heavily compressed thin layer and the solutions surface of the wing is the stream surface, according to an analytical theory for the mode of flow over the windward side of a supersonic leading edge wing., [24] they conclude that wings have a region of homogeneous flow near the edges,

M. Cevdet Celenligil and James N. Moss The study of hypersonic rarefied flow over a highly swept delta wing, a design that will be used in future space planes. For a transitional flow of a direct simulation, results are obtained for all aerodynamic coefficients, and they examine the Flow field translational temperature and quantity along the stagnation streamline, [25]as well as the pressure distribution.

A. V. Vaganov, D. V. Grachikov, V. M. Kashin, V. D. Nemykin, A. Yu. Noev, V. N. Radchenko, A. S. Skuratov, and V. I. Shalaev They investigated the influence of delta wing nose tip geometry, Reynolds number, angle of sweep, [26]and attack on laminar-turbulent transition in the vicinity of attachment lines on leading edges of wing in hypersonic flow. And the results showed that in region lying far downstream from nose tip transition onset and end location in the vicinity of edge does not practically depend on nose tip shape with increasing angle of attack.

Golubkin and Negodam 1995 distinguished two problems for more complex optimization hypersonic lifting bodies, is the wave rider vehicles and the optimization of general shapes using local-pressure methods, and used in this optimization framework. the design variables were the locations of all nodes in the unstructured grid, leading to 20,325 design variables, optimized using a conjugate-gradient method. The results indicate that there are sharp transitions that will have severe aerothermal consequences. [18] The optimization technique produced excellent results, with a maximum L / D of nearly double that of the original design at a fixed angle of attack of 20. However, including limitations will most likely lower this score, indicating that considerable changes are required.

Kinney (2006) describes the results [18] of shape optimization of the HL-20 utilizing only inviscid methods, where optimization of L / D at a single design point is evaluated.

The present work computationally investigated the combined effects of thermochemical non-equilibrium and chemical reactions on hypersonic air flows around blunted bodies during its re-entry. The chemically reacting gas flow around the orbital vehicle was simulated for different re-entry shapes vehicle, with a computational solver based on the Navier–Stokes’s equations.

We then investigated the distribution of heat flux and the drag on the surface of a representative shuttle orbiter configuration and the coupled effects of thermochemical non-equilibrium and chemical reactions on the hypersonic air flows for deferent angle of attack

0°,20° ,30°,40° at altitude range of from 60.96 to 76.20 km at velocities of 4.88 to 7.32 km/sec. Finally, we propose a comparison of a delta wing body vehicle with a cone-flare body in order to optimize the lifting re-entry vehicle. The result will be presented in the next chapters.

Chapter2

Mathematical and physical modeling

2.1 Introduction:

The governing equations for a multi-species gas that is both thermally excited and chemically reactive are discussed in this chapter. The Navier-Stokes's equations, which are statements of global continuity, provide the basis for these equations: total mass conservation, total momentum conservation, and total energy conservation. The Navier-Stokes's equations are based on the continuum postulate, which asserts that there are a large number of molecules within a computational volume, and that the average statistical properties of the molecules accurately represent the properties of the fluid in this elementary region.

The sum of a molecule's translational, rotational, vibrational, and zero-point energies is its total energy. Only translational and electronic energies exist for a single atom. Each of the species in the combination is considered to act like a perfect gas.

Separate and independent temperatures are presented to characterize the thermal state of the gas.

Ionization is ignored in this study, and only chemical and vibrational nonequilibrium phenomena are considered. According to these theories, the air mixture consists of five species (O_2, N_2, O, N, NO), with O_2, N_2 and NO vibrating in non-equilibrium.

2.2 Governing equations

2.2.1 Species conservation:

For species in a mixture, the mass conservation equation is dictated by:

$$\underbrace{\frac{\partial \rho_\alpha}{\partial t}}_1 + \underbrace{\frac{\partial}{\partial x}(\rho_\alpha u - (-q_{\alpha x}^D))}_2 + \underbrace{\frac{\partial}{\partial y}(\rho_\alpha v - (-q_{\alpha y}^D))}_3 = \underbrace{\dot{w}_\alpha}_4 \quad (2.1)$$

In the above equation, [27]

- The term (1) represents the rate of change of mass of species α per unit volume in a cell centered at point (x, y)
- In term (2),
 - $\rho_\alpha u$ represents the x- component of flux of mass of species α , convected across cell walls
 - $q_{\alpha x}^D$ is the component of species diffusion flux across cell walls.
- Term (3) has the same meaning as term (2) but in the y- direction
- Term (4) represents the mass production rate of species α due to chemical reactions.

Clearly $\sum_{\alpha=1}^{N_s} \dot{w}_\alpha$ is zero, since mass is conserved in chemical changes.

2.2.2 Global continuity:

Summing the N_s individual species mass conservation equations yield the total mass conservation for the mixture as a whole. The global continuity equation looks like this:[27]

$$\underbrace{\frac{\partial \rho}{\partial t}}_1 + \underbrace{\frac{\partial}{\partial x}(\rho u)}_2 + \underbrace{\frac{\partial}{\partial y}(\rho v)}_3 = 0 \quad (2.2)$$

In the above equation,

- Term (1) is the rate of change of mass of the mixture per unit volume in a cell centered at (x, y).
- Terms (2) and (3) are x and y components of the mass flux.

2.2.3 Global momentum conservation:

The mixture's momentum balance is given by [27]

$$\underbrace{\frac{\partial \rho u}{\partial t}}_1 + \underbrace{\frac{\partial}{\partial x}(\rho u^2 + p - \tau_{xx})}_2 + \underbrace{\frac{\partial}{\partial y}(\rho uv - \tau_{xy})}_3 = 0 \quad (2.3)$$

$$\underbrace{\frac{\partial \rho v}{\partial t}}_1 + \underbrace{\frac{\partial}{\partial x}(\rho uv - \tau_{xy})}_2 + \underbrace{\frac{\partial}{\partial y}(\rho v^2 + p - \tau_{yy})}_3 = 0 \quad (2.4)$$

In the above equation

- Term (1) is the rate of change of x- component of momentum per unit volume in a cell centered at point (x, y)
- In term (2),
 - ρu^2 is the flux of component of momentum convected across cell walls,
 - p is the pressure forces acting on the cell walls in the direction.
 - τ_{xx} is the viscous forces acting on cell walls in the x direction.
- Term (3) has the same meaning as term (2) but in the y direction.

The terms in Eq. (2.4) have the same meaning as those in Eq (2.3).

2.2.4 Vibrational energy conservation:

Vibrational energy conservation is a phenomenological characterization of the average energy in each molecular species' vibrational mode. The conservation of vibrational energy is regulated by:

$$\underbrace{\frac{\partial}{\partial t}(\rho_m e_m^{vib})}_1 + \underbrace{\frac{\partial}{\partial x}(\rho_m e_m^{vib} u - q_{mx}^{vib})}_2 + \underbrace{\frac{\partial}{\partial y}(\rho_m e_m^{vib} v - q_{my}^{vib})}_3 = \underbrace{\Omega_m}_4 \quad (2.5)$$

In the above equation

- The term (1) denotes the rate of change of vibrational energy of the molecule m. per unit volume in a cell centered at (x, y)
- In term (2),
 - $\rho_m e_m^{vib} u$ is the x component of the vibrational energy flux that passes through cell walls
 - q_{mx}^{vib} consists of two parts:
 - ✓ The conduction of vibrational energy across cell walls caused by vibrational temperature gradients in the x direction is the first part.
 - ✓ The diffusion of vibrational energy across cell walls due to molecule concentration gradients in the x direction is the second term.
- Term (3) is the same as term (2), but in the y direction

- Term (4) represents the source term resulting of various energy exchange processes and is expressed as

$$\Omega_m = \Omega_{VD} + \Omega_{VT} + \Omega_{VV} \quad (2.6)$$

Where Ω_{VD} is the vibrational energy lost or gained due to molecular depletion (dissociation) or production (recombination) in the cell

- Ω_{VT} is the energy exchange between vibrational and translational modes due to collisions within the cell.
- Ω_{VV} is the energy exchange between vibrational modes of molecule with different m molecules

Total energy conservation:

- Total energy conservation (internal + kinetic) is regulated by

$$\underbrace{\frac{\partial(\rho E)}{\partial t}}_1 + \underbrace{\frac{\partial}{\partial x}(\rho E + p)u - (u\tau_{xx} + v\tau_{yx} + qt_x)}_2 + \underbrace{\frac{\partial}{\partial y}((\rho E + p)v - (u\tau_{xx} + v\tau_{yx} + q_y t))}_3 \quad (2.7)$$

- In the above equation: [27]
- The term (1) in a cell centered is the rate of change in total energy per unit of volume (x, y).
- In the term (2):
 - $(\rho E + p)$ is the component of the total enthalpy flow convected through the cell walls
 - $u\tau_{xx} + v\tau_{yx}$ is the work carried out by shear forces
 - qt consists of two parts:
 - ✓ The first is the conduction of thermic energy through the walls of cells due to temperature gradients in the x direction.
 - ✓ The diffusion of enthalpy through cell walls is the second term
- Term (3) has the same meaning as term (2), but in the other direction.

2.3 Thermochemical modelling:

2.3.1 Thermodynamic relations:

The ability to understand the thermodynamic properties of the gas is a critical component of any high-temperature flow-field investigation. The energy stored in a molecule, as well as related quantities like specific heat, are used to precisely construct aerothermodynamic flow fields. [27]

For the suitable temperature range, enthalpy and entropy must be known. Statistical mechanics methods can be used to calculate the equilibrium thermodynamic parameters of high-temperature gases quickly and accurately.

2.3.1.1 Different forms of energy:

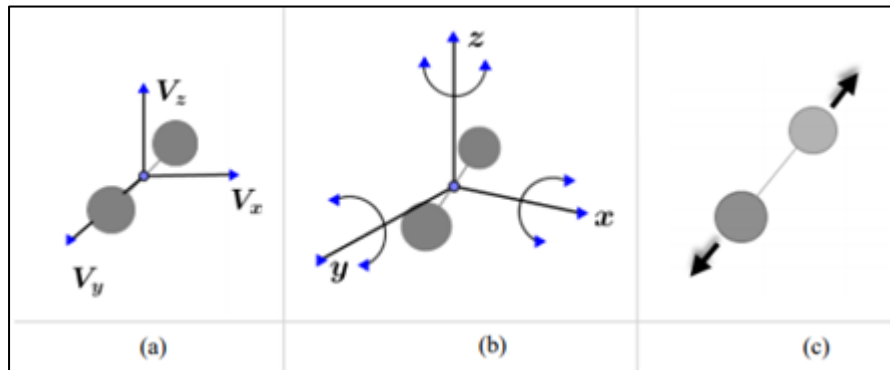
A molecular component's internal specific energy is given by

$$e_m = e_m^{(Tr)} / e_m^{(int)} \quad (2.8)$$

The separation of a translational energy $e_m^{(Tr)}$ and an interior energy $e_m^{(int)}$ is perfectly adequate for gases with weakly interacting particles. $e_m^{(int)}$ can be written as follows for most engineering purposes:

$$e_m^{(int)} = e_m^{(Tr)} - e_m^{(rot)} + e_m^{(vib)} + e_m^{(0)} \quad (2.9)$$

For atomic components, the last two terms are identically zero. The dissociation energy of the



molecule at ground state is assumed to be the molecular component's zero-point energy. [27]

figure 2.1: The different energy modes: (a): translational energy, (b): rotational energy, (c): vibrational energy [27]

The energy of the molecules is distributed over so many energy levels in gas dynamic problems as shown in figure 2.1 that a Boltzmann distribution of the molecules over the energy levels can be assumed. For a system of molecules in thermodynamic equilibrium, a Boltzmann distribution has the form.

$$N_j = Ng_j \frac{\frac{\partial_j}{e^{KT}}}{Q} \quad (2.10)$$

Were

- N_j is the number of molecules present at a particular energy level.
- ϵ_j, g_j is the Boltzmann constant, and is the degeneracy of the level j .
- The partition function Q is defined as

$$Q = \sum g_j e^{\frac{-\epsilon_j}{KT}} \quad (2.11)$$

The average energy per unit mass of species α in energy mod i can be represented as

$$e_i = R_\alpha T^2 \left(\frac{\partial \log(Q_\alpha)}{\partial T} \right) \quad (2.12)$$

At constant volume, the corresponding specific heat capacity is given. $c_{v,\alpha}^{(i)}$ as

$$C_{v,\alpha} = \left(\frac{\partial e_\alpha(i)}{\partial T} \right) \quad (2.13)$$

Translation: For weakly interacting particles, the translational mode yields the following relations:

$$Q_\alpha^{(tr)} = \left(\frac{2\pi M \alpha k T (i)}{N_a h^2} \right) V \quad (2.14)$$

$$e_\alpha^{(tr)} = \frac{3}{2} R_\alpha T \quad (2.15)$$

$$C_{v,\alpha}^{(tr)} = \frac{3}{2} R_\alpha \quad (2.16)$$

Rotation: For the rotational mode of energy, the following relations are found at sufficiently high temperatures:

$$Q_\alpha^{(rot)} = \frac{1}{\Lambda} \frac{T}{\theta_\alpha (rot)} \quad (2.17)$$

$$e_\alpha^{(rot)} = R_\alpha T \quad (2.18)$$

$$C_{v,\alpha}^{(rot)} = R_\alpha \quad (2.19)$$

Were

- Λ is a symmetry factor that is 2 for homo nuclear and 1 for heteronuclear molecules.

The characteristic temperature for rotation is written as follows in terms of the molecule's moment of inertia i :

$$\theta = \frac{h^2}{8\pi^2 k I} \quad (2.20)$$

Vibration: The following relations are found for a frequency harmonic oscillator: [27]

$$Q_\alpha^{(vib)} = \frac{1}{1 - e^{-\frac{\theta}{T}}} \quad (2.21)$$

$$e_\alpha^{(vib)} = \frac{R_\alpha \theta_\alpha}{e^{\frac{\theta_\alpha}{T}} - 1} \quad (2.21)$$

$$C_{v,\alpha}^{(vib)} = \frac{R_\alpha \left(\frac{\theta_\alpha^{vib}}{T} \right)^2 e^{-\frac{\theta_\alpha^{vib}}{T}}}{\left[e^{\frac{\theta_\alpha^{vib}}{T}} - 1 \right]^2} \quad (2.22)$$

The above relationships were calculated using an infinite number of vibrational energy states. The number of vibrational states is assumed to be finite at sufficiently high temperatures that dissociation occurs, and the upper vibrational level is assumed to correspond to dissociation energy. The following are the results in this case:

$$\theta_\alpha^{vib} = \frac{h\nu}{k} \quad (2.23)$$

Zero-point energy:

Since the zero-point energy is constant, the following relations are obtained for it:

$$Q_\alpha^0 = e^{-\frac{\theta_\alpha^0}{T}} \quad (2.24)$$

$$e_\alpha^0 = -R_\alpha \theta_\alpha^0 \quad (2.25)$$

$$C_{v,\alpha}^0 = 0 \quad (2.26)$$

The specific heat capacity of a component at constant volume is calculated as follows:

$$C_{v,\alpha} = C_{v,\alpha}^{(tr)} + C_{v,\alpha}^{(rot)} + C_{v,\alpha}^{(vib)} \quad (2.37)$$

A component's specific heat capacity at constant pressure is defined as:

$$C_{p,\alpha} = \left(\frac{\partial h_\alpha}{\partial T} \right) \quad (2.28)$$

Where the enthalpy per unit is the species α mass and is expressed as

$$h_\alpha = e_\alpha + \frac{p_\alpha}{P_\alpha} \quad (2.29)$$

The partial pressure of each species is derived by assuming that it acts like a thermally perfect gas and obeys the perfect gas equation.

$$P_\alpha = \rho_\alpha R_\alpha T \quad (2.30)$$

Using the above equation $C_{p,\alpha}$ can be expressed as [27]

$$C_{p,\alpha} = C_{v,\alpha} + R_\alpha = C_{v,\alpha} + \frac{R_u}{M} \quad (2.31)$$

2.3.1.2 Mixture properties:

Summing all of the partial densities and partial pressures of all species yields the mixture density and mixture pressure:

$$\rho = \sum \rho_{\alpha} \quad (2.32)$$

$$P = \rho R_u T^{(Tr)} \sum X_{\alpha} / M_{\alpha} \quad (2.33)$$

were

- $X_{\alpha} = \rho_{\alpha} / \rho$ is the mass fraction
- M_{α} is the molar weight of the species α
- R_u is the universal gas constant
- T^{tr} is the translation temperature.

Translational and rotational modes are given the same temperature.

$T_{N_2}^{vib}$, $T_{O_2}^{vib}$, T_{NO}^{vib} For the vibrational modes of the molecular components, separate temperatures is introduced. When considering flows in thermal equilibrium, numerical simulations assign a same temperature to all modes. The translational pressure is the only factor that affects the pressure.

The sum of kinetic and interior energies is defined as the total energy E per unit mass:

$$E = \frac{1}{2} (u^2 + v^2) + \sum X_{\alpha} e_{\alpha} \quad (2.34)$$

Were

- e_{α} is the total specific energy per unit mass of the species α ,
- u and v are the velocity components x, y indirections, respectively.

The mixture's specific heat capacities are provided by

$$C_v = \sum X_{\alpha} C_{v,\alpha} \quad (2.35)$$

$$C_p = \sum X_{\alpha} C_{p,\alpha} = C_v + R_u \sum X_{\alpha} / M_{\alpha} \quad (2.36)$$

The ratio of specific temperatures is calculated as follows:

$$\gamma = \frac{C_p}{C_v} = 1 + \frac{R_u}{C_v} \sum \frac{X_{\alpha}}{M_{\alpha}} \quad (2.37)$$

The total enthalpy per unit mass is calculated as follows:[27]

$$H = E + \frac{P}{\rho} \quad (2.38)$$

2.3.2 Chemical kinetic model:

The chemical source names are formed from reactions that take place between the gas's constituents. A mass transfer mechanism occurs between species as reactions occur. The term w_α on the right-hand side of the species conservation equation represents this. Eq. 2.1.

The formulas for these mass transfer rates are determined in this section. Several separate elementary chemical reactions between species in the gas can take place at the same time.

Consider the r^{th} chemical reaction of N_r elementary reactions between N_s chemically reacting species:

$$\sum v'_{\alpha,r} X_\alpha = \sum v''_{\alpha,r} X_\alpha \quad (2.39)$$

Were

- $v'_{\alpha,r}$ and $v''_{\alpha,r}$ represent the stoichiometric mole numbers of reactants and products of reaction r , respectively.
- X_α is the molar concentration of the species α .

There is a forward and backward portion to the chemical reaction equation, eq. 2.39. The forward and backward reaction rates are calculated as follows:

Forward:

$$\frac{d[X_\alpha]_r^f}{dt} = (v''_{\alpha,r} - v'_{\alpha,r}) \left[k_{f,r} \prod_{\alpha=1}^{N_s} [X_\alpha]^{v'_{\alpha,r}} \right] \quad (2.40)$$

Backward:

$$\frac{d[X_\alpha]_r^b}{dt} = (v''_{\alpha,r} - v'_{\alpha,r}) \left[k_{b,r} \prod_{\alpha=1}^{N_s} [X_\alpha]^{v''_{\alpha,r}} \right] \quad (2.41)$$

Were

- $K_{f,r}$ and $K_{b,r}$ are the forward and backward reaction rate coefficients of reaction r , which are both affected by the temperature of the reaction.
- The net rate for the above general reaction r can be written as

$$\frac{d[X_\alpha]}{dt} = \frac{d[X_\alpha]_r^f}{dt} - \frac{d[X_\alpha]_r^b}{dt} = (v''_{\alpha,r} - v'_{\alpha,r}) \left[k_{f,r} \prod_{\alpha=1}^{N_s} [X_\alpha]^{v'_{\alpha,r}} - k_{b,r} \prod_{\alpha=1}^{N_s} [X_\alpha]^{v''_{\alpha,r}} \right] \quad (2.42)$$

The equation above is a general form of the law of mass action, which assures that total mass is preserved during a chemical reaction.

The mass rate of species production per unit volume is calculated as follows:

$$w_\alpha = \frac{d}{dt}(\rho_\alpha) = M_\alpha \sum_{r=1}^{N_r} \frac{d}{dt} [X_\alpha]_r \quad (2.43)$$

When the necessary equations for the forward and backward rate coefficients are provided for a collection of N_r reactions, a chemical kinetic model is defined. Experimentally measured forward reaction rates are common. Many reactions have empirical relationships that can be connected in the form of :

$$K_{f,r} = C_{f,r} T_{f,r}^{n_{f,r}} e^{\frac{-E_{f,r}}{kT_{f,r}}} \quad (2.44)$$

Where

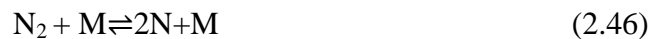
- $E_{f,r}$ is the activation energy
- $C_{f,r}$ is a constant.

The Arrhenius equation is known as equation 2.44. Experimental data is used to determine the parameters $C_{f,r}$, $n_{f,r}$, and the activation energy $E_{f,r}$ for various reactions. The backward reaction rate coefficients are presented under the normal assumptions.

$$k_{b,r} = \frac{k_{f,r}(T_{b,r})}{k_{eq,r}(T_{b,r})} \quad (2.45)$$

Where

- $k_{eq,r}$ is the equilibrium constant for the r^{th} reaction. The activation energy of the forward reaction and the partition functions of the reactants and products can be used to calculate the equilibrium constant. The activation energy of the forward reaction and the partition functions of the reactants and products can be used to calculate the equilibrium constant.
- In the present work, a five component air model consisting of species N_2, O_2, NO, N and O is considered. The most important chemical reactions between these species are:



- M is the catalyst particle that acts as a collision partner in the reaction. [27]

The first three reactions are dissociation events, whereas the last two are bimolecular exchange reactions.

The two most essential events for the generation of nitric oxide NO in air are the exchange reactions. It should be noticed that the sum of the mass transfer rates is identically zero and that elemental conservation holds, as necessary, when determining the chemical source term. The use of elemental conservation yields the following two equations:

$$\rho_N + \rho_{N_2} + \frac{M_N}{M_{NO}} \rho_{NO} = const \quad (2.51)$$

$$\rho_O + \rho_{O_2} + \frac{M_O}{M_{NO}} \rho_{NO} = const \quad (2.52)$$

The set of equations used to calculate the chemical source term becomes overdetermined with these two equations. Numerical approaches, in general, are extremely sensitive to any changes in elemental conservation. To ensure elemental conservation, the mass production rates of molecular components are calculated using equation 2.43, while the mass production rates of atomic components are calculated using equations 2.51-2.52.

2.3.3 Vibration-dissociation coupling:

Chemical changes of molecules (such as dissociation and recombination) are affected by their internal chemical states of motion. Only individuals with a total energy level above a certain threshold can initiate a chemical transformation. The typical durations for chemical and vibrational relaxation are comparable at high temperatures, resulting in reciprocal interaction.

The vibrational temperature of a shock wave will be less than the translational-rotational temperature. The non-equilibrium molecular dissociation rate will be lower than the equilibrium dissociation rate because the molecules have less vibrational energy than at equilibrium. As a result, the dissociation rate must be changed if there is vibrational non-equilibrium. [27]

Simultaneously, because vibrationally excited molecules are more likely to dissociate, there is a drain on vibrational energy, slowing vibrational relaxation. To forecast the accurate nonequilibrium dissociation rates, it is crucial to first understand and quantify this interaction.

Macroscopic flow properties such as heating rates and shock forms are heavily influenced by these rates. Small changes in shock shape, as well as ensuing pressure field differences, can result in considerable differences in anticipated aerodynamic moments.

2.3.3.1 Park model:

Park developed a model based on the examination of shock tube reaction rate data. Park assumes that certain types of reactions can be characterized by a single rate-controlling temperature that is an adequate average of local translational and vibrational temperatures in this model. He recommends calculating the dissociation rate coefficient k_d at room temperature

$$T_{av} = T_{tr}^n T_{vib}^{n-1} \text{ where } n \text{ is proposed to be between } 0.5 \text{ and } 0.7. [27]$$

A molecule's vibrational energy is lost as it dissociates, but some energy is placed into molecular vibrational modes during atomic recombination events. These two effects, dissociation-induced depletion and recombination-induced augmentation, must be accounted for as a source term. According to Park, molecular dissociation and recombination occur at

the vibration temperature T_v . Therefore, the amount of energy lost or gained due to molecular depletion or production of species is given by m .

$$\Omega_{VD} = w_m e_{vm} \quad (2.53)$$

2.5 Turbulence modelling :

2.5.1 Introduction:

In the literature, three main methods to modelling turbulent flows are provided. Statistical Navier Stokes equations modelling, direct simulation, and large-scale simulation are examples of these. [28] The modelling and simulation of turbulence are fundamentally different.

2.5.2 Direct Simulation (DNS):

The direct numerical simulation of turbulence (DNS) involves numerically solving the Navier-Stokes's equations in space and time with physically consistent accuracy, in order to resolve all of the important turbulent scales whose size is dictated by the fluid's viscosity. If the mesh is fine enough, the time step is short enough, and the numerical scheme is designed to minimize dissipation errors [28]. Because it necessitates considerable computing power, this technology is difficult to apply to moderately complex industrial applications.

2.5.3 Large Eddy simulation (LES):

This technology is intermediate between statistical approach (RANS) and simulation (DNS). Indeed, large structures that depend on the geometry of the flow are directly simulated (DNS) while smaller,[28] much more scales are modelled (RANS). This means that large scales that transmit mass, quantity of movement, and energy must be clearly represented without the use of a model, whereas small vortex-nary structures, are modelling.

2.5.4 Statistical modelling (RANS):

RANS (Reynolds Averaged Navier Stokes), is used to describe the mean movement of turbulent flow [28]. The mixing-length model, two-level models, the Algebraic Stress Model (ASM), and the second-order Reynolds Stress Model are among the models that have been created (RSM). It's a model that produces good results while requiring minimal IT resources.

Averaged equations:

Direct simulation of the instantaneous Navier-Stokes's equations is still limited to low Reynolds number flows and simple geometric designs. When we're looking for realistic flows, an alternative is to be just interested in average quantities and hence to acquire the system of equations that these quantities verify. To do so, practice the Reynolds decomposition on the problem's unknowns and apply the set average operator to the instantaneous equations. Averaged equations are the new equations obtained.[29]

The solution of the general equations of viscous fluid motion, which include the continuity and Navier-Stokes's equations, is required for many flows of technical significance. As a result, continuity equation can be written as:

$$\frac{\partial u_i}{\partial x_i} = 0 \quad (2.54)$$

and the momentum equation:

$$\frac{\partial u_i}{\partial t} + u_j \frac{\partial u_i}{\partial x_j} = -\frac{1}{\rho} \frac{\partial p}{\partial x_i} + \nu \frac{\partial^2 u_i}{\partial x_j \partial x_j} \quad (2.55)$$

❖ The equations of mean motion

In the case where the flow is turbulent, decomposing the instantaneous variables (such as velocity components and pressure) into a mean value and a fluctuating value is desirable.

$$u_{i(\bar{x},t)} = U_{(\bar{x},t)} + u'_{(\bar{x},t)} \quad (2.56)$$

$$p_{i(\bar{x},t)} = p_{i(\bar{x},t)} + P'_{i(\bar{x},t)} \quad (2.57)$$

When measuring flow quantities, we are more interested in mean values than fluctuating values. Instead of that, solving numerically the Navier-Stokes's equation would necessitate an extremely fine grid to resolve all turbulent scales, as well as a fine time resolution.

We get the following result for the mean field by introducing the Reynolds decomposition into the continuity equation and obtaining the ensemble mean:

$$\frac{\partial U_i}{\partial x_i} = 0 \quad (2.58)$$

We get the velocity fluctuations by subtracting this equation from the equation of instantaneous motion continuity:

$$\frac{\partial u_i}{\partial x_i} = 0 \quad (2.59)$$

As a result, we can see that both the mean and fluctuation quantities confirm the continuity equation.

The following are the three components of the average velocity:

$$\frac{\partial U_i}{\partial t} + U_j \frac{\partial U_i}{\partial x_j} + \overline{u_j \frac{\partial u_i}{\partial x_j}} = -\frac{1}{\rho} \frac{\partial P}{\partial x_i} + \nu \frac{\partial^2 U_i}{\partial x_j \partial x_j} \quad (2.60)$$

The incompressibility criterion for fluctuations implies that:

$$\overline{u_j \frac{\partial u_i}{\partial x_j}} = \overline{\frac{\partial u_i}{\partial x_j}} \quad (2.61)$$

The Reynolds tensor is therefore defined as follows:

$$R_{ij} = -\rho \overline{u_i u_j} \quad (2.62)$$

Finally, the averaged equations are written as:

$$\frac{\partial U_i}{\partial t} + U_j \frac{\partial U_i}{\partial x_j} = -\frac{1}{\rho} \frac{\partial P}{\partial x_i} + \frac{1}{\rho} \frac{\partial}{\partial x_j} (\overline{\tau_{ij}} + R_{ij}) \quad (2.63)$$

Where,

$$\overline{\tau_{ij}} = \mu \left(\frac{\partial U_i}{\partial x_j} + \frac{\partial U_j}{\partial x_i} \right) \quad (2.64)$$

As a result, the equations of the mean field of velocity differ from the equations of continuity and momentum in this form, because a new term related to the effect of the fluctuating field shows in these equations. This term is known as the Reynolds stress and it expressed as:[29]

$$R_{ij} = -\rho \begin{bmatrix} \overline{u'u'} & \overline{u'v'} & \overline{u'\omega'} \\ \overline{u'v'} & \overline{v'v'} & \overline{v'\omega'} \\ \overline{u'\omega'} & \overline{v'\omega'} & \overline{\omega'\omega'} \end{bmatrix} \quad (2.65)$$

As a result, this tensor generates six more unknowns. Thus, close the RANS equations by modelling the Reynolds stress term R_{ij} as a function of the mean flow, removing any reference to the fluctuating part of the velocity. This is the issue of closure.

The problem of closure:

We have four unknown functions U_1, U_2, U_3 , and P , as well as four equations, the continuity equation and the three NAVIER-STOKES equations, with the Reynolds equations substituting the NAVIER-STOKES equations, for a turbulent issue, we have the 6 unknown functions of the Reynolds tensor $u_i u_j$, therefore we have 10 unknown functions but only 4 equations in the general case. The system, is not closed. To solve this problem, you'll need to find a sufficient number of additional equations.

This is the central problem of turbulence, problem of closure. For this, many researchers have invested in the field and several contributions of resolution models have been proposed. Among these models we can cite:

Classification of turbulence models:

There are two types of models in general:

- First-order models (turbulent viscosity models), which involve modelling Reynolds stresses directly using a turbulent viscosity.
- Second-order models: The Reynolds stresses are directly estimated.[30]

There are numerous types of turbulence models for first-order models dependent on the number of equations of fluctuating motion added to the conservation equations:

2.5.4.1 The zero-equation model:

This is a model that uses only the average field equations to find an expression for the Reynolds $u_i u_j$ constraint based on the average values [30]. Because of their limited uses, zero-equation models are being employed less and less in comparison to other models (they completely ignore the locality characteristics of turbulence).

2.5.4.2 One equation model:

In these models, a transport equation is solved for a turbulent variable (typically the turbulent kinetic energy) and an algebraic expression is used to generate a second turbulent quantity (usually the turbulent length scale) [30].

2.5.4.3 Two-equation model:

The turbulent kinetic energy k and its dissipation ε are described by two transport equations [30]. The Reynolds stress tensor is calculated using an assumption that links the Reynolds stress tensor to velocity gradients and eddy viscosity.

2.5.4.4 K-epsilon (k- ε) model

The most frequent model used in Computational Fluid Dynamics (CFD) to simulate mean flow characteristics for turbulent flow conditions is the K-epsilon (k- ε) turbulence model. It's a two-equation model that uses two transport equations to give a general explanation of turbulence (PDEs) [31]. The K-epsilon model was created with the goal of improving the mixing-length model. The turbulent length scale is calculated as follows

$$l = \frac{k^{3/2}}{\varepsilon} \quad (2.66)$$

- The k- ε focus on the mechanisms that influence the turbulent kinetic energy (per unit mass) k .
- If we know k and ε , we may present turbulent viscosity as follows:

$$v_t \propto \vartheta l \propto C_\mu k^{1/2} \frac{k^{3/2}}{\varepsilon} = C_\mu \frac{k^2}{\varepsilon} \quad (2.67)$$

In turbulence theory, we consider the $k - \varepsilon$ model:

$$k_t = \alpha \left(\frac{k^2}{\varepsilon} k_x \right)_x - \varepsilon \quad (2.68)$$

$$\varepsilon_t = \beta \left(\frac{k^2}{\varepsilon} \varepsilon_x \right)_x - \gamma \frac{\varepsilon^2}{k} \quad (2.69)$$

Where

- k is the turbulence kinetic energy.
- ε is the dissipation rate of turbulent energy.
- α, β and γ are positive constants.

Advantages :

- Calculations are more stable and converge more quickly.
- Reasonable forecasts for a variety of flows.

• **Disadvantages:** [31]

- Unfavourable predictions for:
 - swirling and rotating flows,
 - flows with strong separation,
 - axisymmetric jets,
 - certain unconfined flows

– Valid only for fully turbulent flows.

2.5.4.5.1 The transport equations for the standard model $k - \varepsilon$:

The kinetic energy of turbulence, k , and its dissipation rate, are computed using the corresponding transport equations: [30]

$$\frac{\partial k}{\partial t} + U_j \frac{\partial k}{\partial x_j} = \nu_t \left[\frac{\partial U_i}{\partial x_j} + \frac{\partial U_j}{\partial x_i} \right] \frac{\partial U_i}{\partial x_j} + \frac{\partial}{\partial x_j} \left[\frac{\nu_t}{\sigma_k} \frac{\partial k}{\partial x_j} \right] + \nu \frac{\partial^2 k}{\partial x_i \partial x_j} - \varepsilon \quad (2.70)$$

$$\frac{\partial \varepsilon}{\partial t} + U_j \frac{\partial \varepsilon}{\partial x_j} = \left[\frac{\nu_t}{\sigma_\varepsilon} \frac{\partial \varepsilon}{\partial x_j} \right] + C_{\varepsilon 1} \nu_t \left[\frac{\partial U_i}{\partial x_j} \frac{\partial U_j}{\partial x_i} \right] \frac{\partial U_i}{\partial x_j} \frac{\partial}{\partial x_j} - C_{\varepsilon 2} \frac{\partial^2}{\partial x_j^2} \varepsilon \quad (2.71)$$

The various closure coefficients of the $k - \omega$ model is given as

- $C_{\varepsilon 1}, C_{\varepsilon 2}$ are constants,
- $\sigma_k, \sigma_\varepsilon$ are the turbulent Prandtl numbers for k and ε respective.

The various closure coefficients of the $k - \varepsilon$ model is given as

Table 2-1: the constants of the model k -values [31]

C_μ	$C_{\varepsilon 1}$	$C_{\varepsilon 2}$	$\sigma_k,$	σ_ε
0.09	1.44	1.92	1	1.3

2.5.4.6 k-omega k- ω model

The K-omega ($k - \omega$) model is a two-equation model, meaning it adds two additional transport equations to explain the flow's turbulent features. This model also solves two more PDEs: [31]

The conventional k equation is solved, but it is employed as a length determining equation. From its definition $\omega \propto \frac{\varepsilon}{k}$, this quantity is commonly referred to as specific dissipation.

2.5.4.6.1 The transport equations for the standard model k – ω :

The following transport equations yield the turbulent kinetic energy (k) and the specific rate of dissipation (ω).

$$\frac{\partial(\rho k)}{\partial t} + \frac{\partial(\rho k U_j)}{\partial x_j} = P - \beta^* \rho \omega k + \frac{\partial}{\partial x_j} \left[\left(\mu + \sigma_k \frac{\rho k}{\omega} \right) \frac{\partial K}{\partial x_j} \right] \quad (2.72)$$

$$\frac{\partial(\rho \omega)}{\partial t} + \frac{\partial(\rho \omega U_j)}{\partial x_j} = P - \beta^* \rho \omega k + \frac{\partial}{\partial x_j} \left[\left(\mu + \sigma_k \frac{\rho k}{\omega} \right) \frac{\partial K}{\partial x_j} \right] \quad (2.73)$$

Following that, the turbulent viscosity is determined as follows:[31]

$$\mu_t = \rho \frac{k}{\omega} \quad (2.74)$$

2.5.4.6.2 The constants and auxiliary functions for the model k – ω

The various closure coefficients of the k – ω model is given as

Table 2.2 The various closure coefficients of the k – ε model [31]

σ_k	σ_ω	β^*	γ	C_{lim}	β_0
0.6	0.5	0.09	13/25	7/8	0.0708

2.5.4.7 k – ω SST model:

The $k-\omega$ SST model predicts flow separation better than most RANS models and a high performance under adverse pressure gradients.

- It can account for the transfer of the primary shear stress in boundary layers with a negative pressure gradient.
- In places with high normal stress, such as standstill and severe acceleration, the SST model creates some substantial turbulence levels. [31]

The turbulent viscosity is then calculated in the following manner:

$$v_T = \frac{a_1 k}{\max(a_1 \omega, SF_2)} \quad (2.75)$$

2.5.4.7.1 The transport equations for the model $k - \omega$ SST [31]

$$\frac{\partial k}{\partial t} + U_j \frac{\partial k}{\partial x_j} = P_k - \beta^* k \omega + \frac{\partial}{\partial x_j} \left[(v + \sigma_k v_T) \frac{\partial k}{\partial x_j} \right] \quad (2.76)$$

$$\frac{\partial \omega}{\partial t} + U_j \frac{\partial \omega}{\partial x_j} = \alpha S^2 - \beta \omega^2 + \frac{\partial}{\partial x_j} \left[(v + \sigma_k v_T) \frac{\partial \omega}{\partial x_j} \right] + 2(1 - F_1) \sigma_{\omega 2} \frac{1}{\omega} \frac{\partial k}{\partial x_i} \frac{\partial \omega}{\partial x_i} \quad (2.77)$$

2.5.4.7.2 The constants of the model $k - \omega$ SST

The various closure coefficients of the $k - \omega$ SST model is given as:

Table 2.3: The various closure coefficients of the $k - \omega$ SST [31]

a_1	a_2	β_1	β_2	β^*	σ_{k1}	σ_{k2}	$\sigma_{\omega 1}$	$\sigma_{\omega 2}$
5/9	0.44	3/40	0.0828	9/100	0.85	1	0.5	0.856

2.5.4.7.3 Model to $N \geq 2$ equations:

Despite the fact that two-equation models produce good results in a variety of applications, this is not the case for some complex flows, such as gradient versus fed flows.[31]

2.5.5 Wall function:

Some mature turbulence models, are only valid in fully formed turbulence and do not function well in the vicinity of the wall. The employment of so-called wall functions, which can model the near wall region. The first cell centre must be positioned in the log-law zone to assure the accuracy of the outcome. Wall functions are empirical equations used to fulfil the physics of the flow in the near wall region.

Rather than specifying boundary conditions at the wall, wall functions are utilized to bridge the inner region between the wall and the turbulence fully formed region in order to provide near-wall boundary conditions for the momentum and turbulence transfer equations.[32]

It should be noted that when employing the wall functions approach, the boundary layer does not need to be resolved, resulting in a significant reduction in mesh size and computing domain.

Approximations of "log - layer," are wall functions. The "law of the wall" describes the velocity profile.

$$u(y) = u\tau\kappa(\ln y + C) \quad (2.78)$$

Where

- κ is von Karman constant
- The constant C is affected by the roughness of the wall as well as the friction velocity.

Wall law:

The wall y^+ is a non-dimensional number that determines whether the influences in the wall-adjacent cells are laminar or turbulent, and hence indicates which part of the turbulent boundary layer they resolve.

In a turbulent boundary layer, the subdivisions of the near-wall area can be summarized as follows [37]:

- a) $y^+ < 5$: viscous sublayer region (velocity profiles are considered to be laminar, and viscous stress dominates wall shear): [32]
- b) $5 < y^+ < 30$: buffer region (both viscous and turbulent shear dominates)
- c) $30 < y^+ < 300$: Fully turbulent portion or log-law region (corresponds to the region where turbulent shear predominates).

Chapter 3

Numerical

modelling

3.1 Introduction

Simulation is defined as the use or resolution of models corresponding to a given system to study its behaviour in a specific context. It is the logical continuation of the modelling that is the first approach of a simulation, which are executed using a CFD Computational Fluid Dynamics code.

3.2 Computational Fluid Dynamics code

CFD codes are structured around numerical algorithms that can be tackle fluid problems. All codes contain three main elements:

3.2.1 Pre-Processing:

The pre-processor transforms the input of a flow problem into a suitable form for the use by the solver. The Pre-processing stage involves:

- The computational domain: Definition of the geometry
- Grid generation: the subdivision of the domain into a number of small, subdomains (or control volumes).
- Fluid properties definition.
- Define the solution of a flow problem (velocity, pressure, Temperature) in every signal cell, by the specification of appropriate boundary conditions at cells.

The accuracy of CFD solutions is governed by number of cells in the grid. In general, the larger numbers of cells better the solution accuracy. Both the accuracy of the solution & it's cost in terms of necessary computer hardware & calculation time are dependent on the fineness of the grid.

3.2.2 Solver

The FLUENT CFD code has extensive interactivity, so we can make changes to the analysis at any time during the process. This saves time and enables to refine designs more efficiently.

The numerical solution of Navier–Stokes's equations in CFD codes usually implies a discretization method: it means that derivatives in partial differential equations are approximated by algebraic expressions which can be alternatively obtained by means of the finite-difference or the finite-element method. Otherwise, in a way that is completely different from the previous one, the discretization equations can be derived from the integral form of the conservation equations: this approach, known as the finite volume method, is implemented in FLUENT [78], because of its adaptability to a wide variety of grid structures. The result is a set of algebraic equations through which mass, momentum, and energy transport are predicted at discrete points in the domain.

Because the governing equations are non-linear and coupled, several iterations of the solution loop must be performed before a converged solution is obtained and each of the iteration is carried out as follows (figure3.1):

1. Fluid properties are updated in relation to the current solution; if the calculation is at the first iteration, the fluid properties are updated consistent with the initialized solution.
2. The three momentum equations are solved consecutively using the current value for pressure so as to update the velocity field.

3. Since the velocities obtained in the previous step may not satisfy the continuity equation, one more equation for the pressure correction is derived from the continuity equation and the linearized momentum equations: once solved, it gives the correct pressure so that continuity is satisfied. The pressure–velocity coupling is made by the SIMPLE algorithm, as in FLUENT default options.
4. Other equations for scalar quantities such as turbulence, chemical species and radiation are solved using the previously updated value of the other variables.
5. Finally, the convergence of the equations set is checked and all the procedure is repeated until convergence criteria are met.

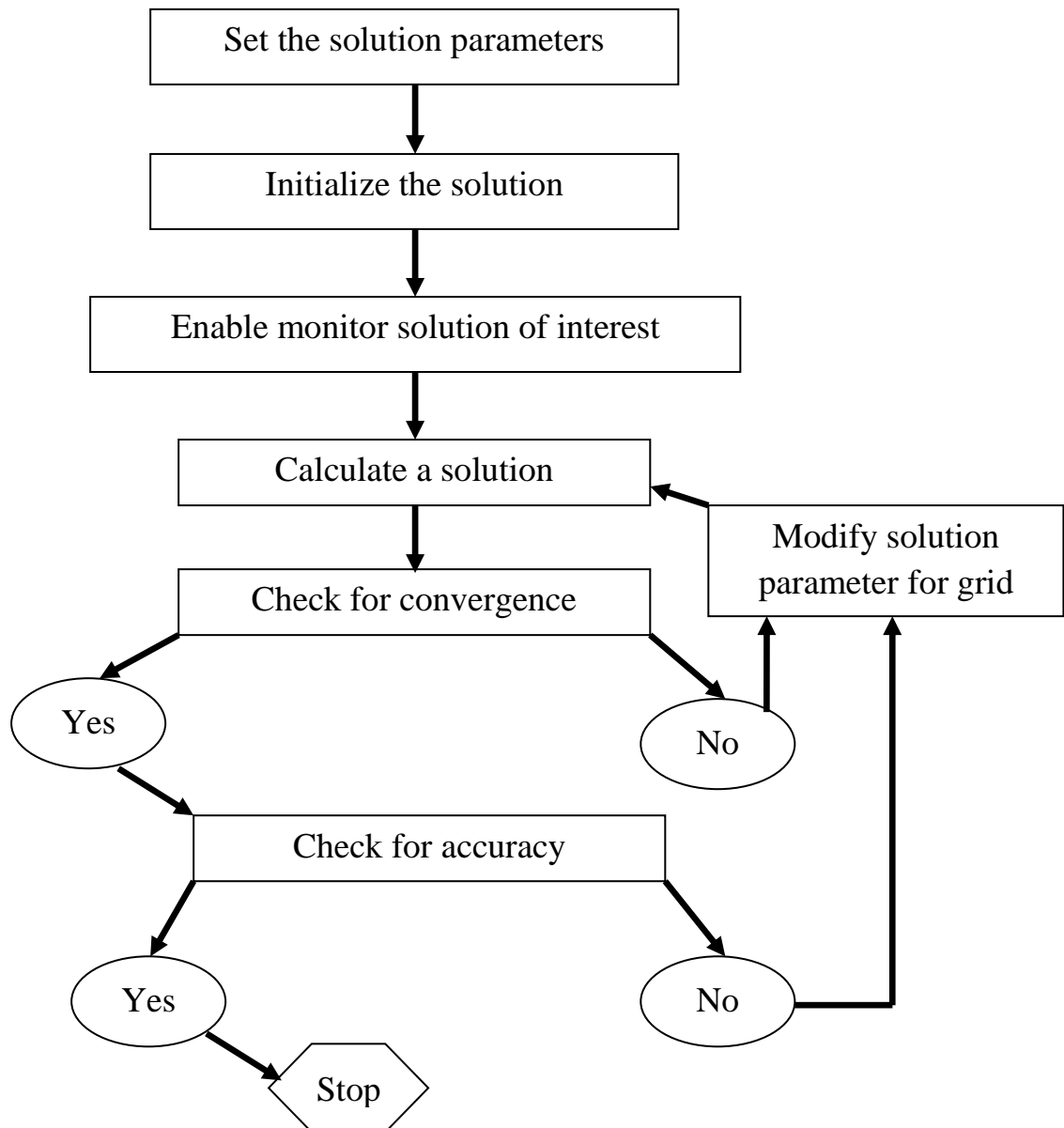


Figure 3.1 Algorithm of numerical approach used by simulation software's [78]

3.2.3 post-Processing:

This is the final step in CFD analysis, [34] and it involves the organization and interpretation of the predicted flow data and the production of CFD images and animations.

3.3 Mesh

A mesh is a partition of space or a domain in cells called mesh. Usually convex, it is used to solve an EDP; the mesh must be made in such a way as to minimize the diffusion of the digital error. As well as topological forms of mesh are often two-dimensional triangles or quadrangles, and tetrahedrons, cubes or three-dimensional hexahedrons.

3.3.1 Mesh components:

The mesh consists of the following elements (figure 3.2):

- Cell: control volume dividing geometry.
- Face: border of a cell.
- Edge: border of a face.
- Node: mesh point.

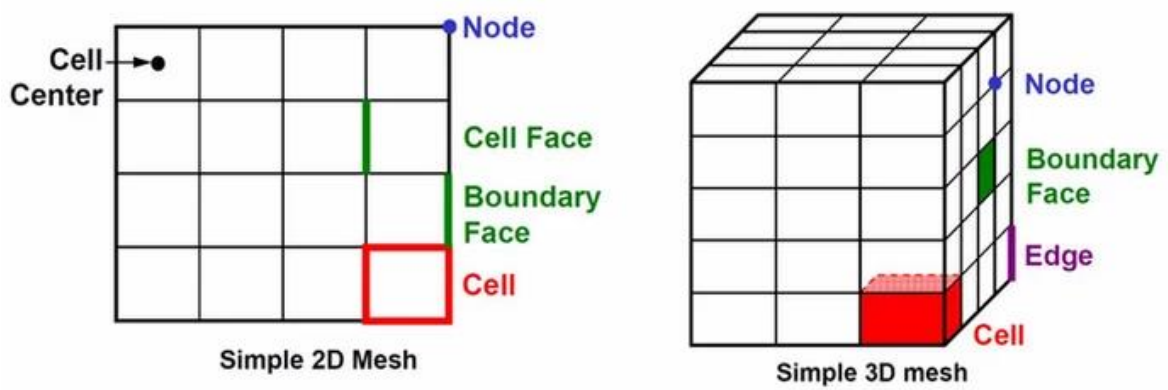


Figure 3.2: Mesh component [34]

3.3.2 Mesh types:

3.3.2.1 Structured grid

Refers to that the number of grid cells subordinate to any internal node is the same for all grids within a given computational domain or geometry, and the connection relationship between adjacent cell nodes is apparent boundary without having to store all the information of grids.

3.3.2.1.1 Body-Fitted Structured Grids

Various configurations can be used depending on the orientation of the grid lines in order to get the requirements for smoothness and continuity of cell sizes, as indicated by the letter to which they are most similar: Grids of the H-type, C-type, O-type, I-type as represented in figure 3.3.

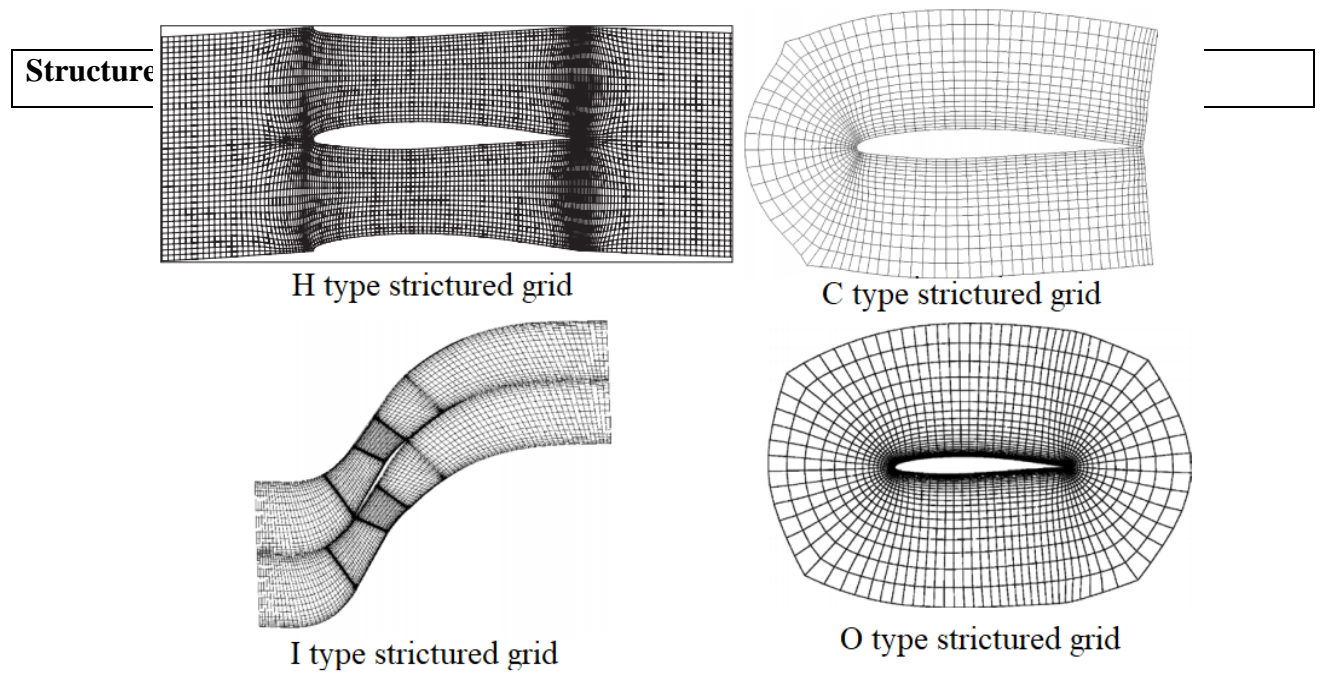


Figure 3.3: Body fitted structured grid [34]

3.3.2.2 Unstructured mesh:

The elements of this type of mesh are generated arbitrarily without any constraint as to their disposition.[34] [35]

- ✓ In a two-dimensional mesh (2D), the elements that make it up are triangle-type or quadrilateral.
- ✓ In three dimensions (3D), we have elements such as tetrahedrons, prisms, hexahedrons and pyramids.

3.3.2.3 Hybrid mesh:

Hybrid meshes contain a variety of elements, such as a mix of triangular and quadrangular elements. This mesh is mostly used to discretize difficult fluid mechanics issues. The four-node elements discretize the rest of the domain of analysis, while the triangles cover the regions around the contact surfaces. [35]

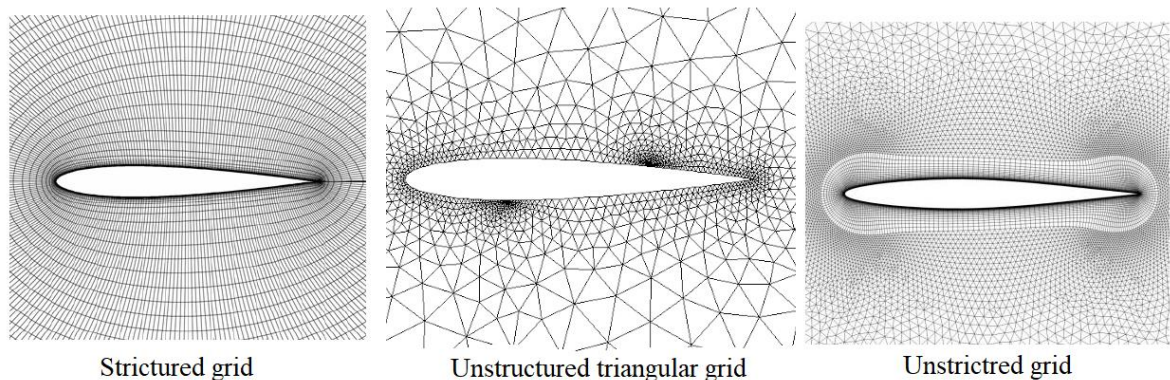


Figure 3.4 Mesh types [34]

Domain must verify some constraints	Valid for arbitrary domains
More restrictive for dealing with non-constant element size	More flexible for dealing with non-constant element size
Preferable for aligning elements with boundaries / material properties	Can be used for aligning elements with boundaries / material properties
Easier to developed	More complex to develop

Table 1: Structured vs unstructured mesh [35]

3.3.4 General mesh generation techniques:

To have a good quality of mesh there are some techniques that allow to achieve a good result, depends on:[35]

- ✓ A faithful representation of surfaces
- ✓ A good accuracy of the solution
- ✓ Minimization of calculation times
- ✓ Reduced disk space usage
- ✓ Good Resolution in high-gradient regions.

3.3.4.1 Mesh generation:

The generation of the mesh is an important step which will help us to have a good result on our CFD analysis using the necessary parameters that we must follow by using a fine mesh in the vicinity of the object where the phenomena are more dominated, on the other hand, a coarse mesh far from the object to reduce the calculation time and avoid numerical errors between refined and unrefined areas by a transition.

3.3.5.1 Quality of a mesh:

Mesh Quality refers to the properties of a mesh that allow a numerical PDE simulation to be run effectively [35]. With fidelity to the underlying physics, and with the precision required for the problem.

3.3.5.1.1 The different quality criteria:

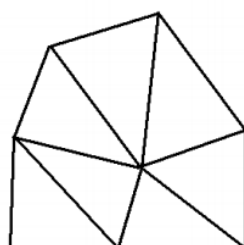
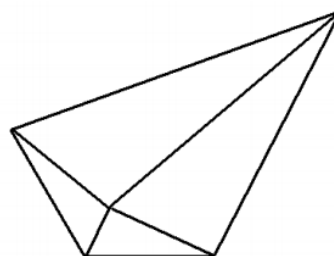
Mesh quality is determined by a number of factors, [35] which are briefly discussed in this section.

3.3.5.1.1.1 Clustering

Ensure that the mesh must be refined enough to resolve the primary features for the analyzed flow [34]. The resolution depends on the parameters that control the interior and the initial boundary mesh.

3.3.5.1.1.2 Smoothness

The transition from one face or cell to the next in a high-quality mesh should be

smooth change
in cell sizeLarg jump
in cell size

smooth. large changes in size between consecutive faces or cells will result in a poor computational grid figure 3.5. [35]

Figure 3.5: Smooth and Non-Smooth Transitions in Cell Size [35]

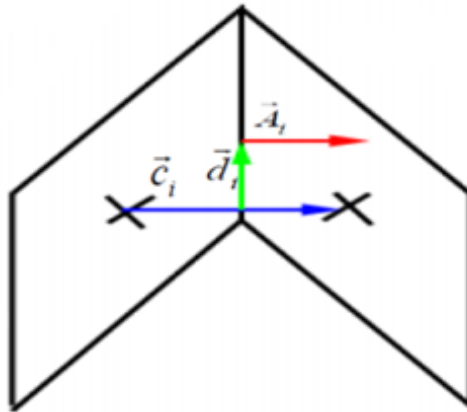
3.3.5.1.1.3 Aspect ratio

The ratio of the longest edge length to the smallest edge length is the aspect ratio of a face or cell. The aspect ratio is defined differently for each element type and applies to triangular, tetrahedral, quadrilateral, and hexahedral elements. [35]

- For an equilateral face or cell, the aspect ratio will be 1.
- For less regularly-shaped faces or cells, the aspect ratio will be greater than 1, since the edges differ in length.
- For triangular and tetrahedral faces and cells, as well as pyramids, we should usually focus on improving the skewness, which will improve the smoothness and aspect ratio as well.

3.3.5.1.1.4 Skewness

One of the most important quality indicators for a mesh which refers to how close a face or cell is to being ideal (i.e., equilateral or equiangular) as represented in figure 3.6. A number of 0 represents an equilateral cell (optimal) and a value of 1 suggests a fully



degenerate cell (worst). [35]

Figure 3.6: Skewness: the distance between the common face centre (black dot) and intersection of the common face and line connecting the cell centres [35]

Two methods for determining skewness:

1. Equilateral Volume deviation: Applies only for triangles and tetrahedrons

$$skewness = \frac{optimal\ cell\ size - cell\ size}{optimal\ cell\ size} \quad (3.1)$$

2. Normalized Angle deviation:

$$Skewness = \max \left[\frac{\theta_{max} - \theta_e}{180 - \theta_e}, \frac{\theta_{min} - \theta_e}{\theta_e} \right] \quad (3.2)$$

were

θ_{max} = largest angle in the face or cell

θ_{min} = smallest angle in the face or cell

θ_e = angle for an equiangular face/cell (60 for tets and tris, and 90 for quads and hexes), Applies to all cell and face shapes [38]

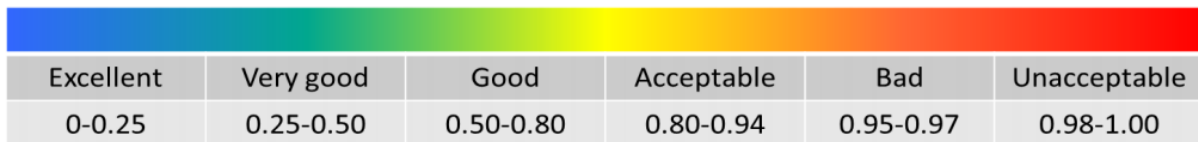


Figure 3.7 Skewness mesh metrics spectrum [78]

3.3.5.1.1.5 non-orthogonality:

This is a very important parameter of which we measure the angle between the line connecting two cell centers and the normal of their common face (figure 3.8,9). [38]

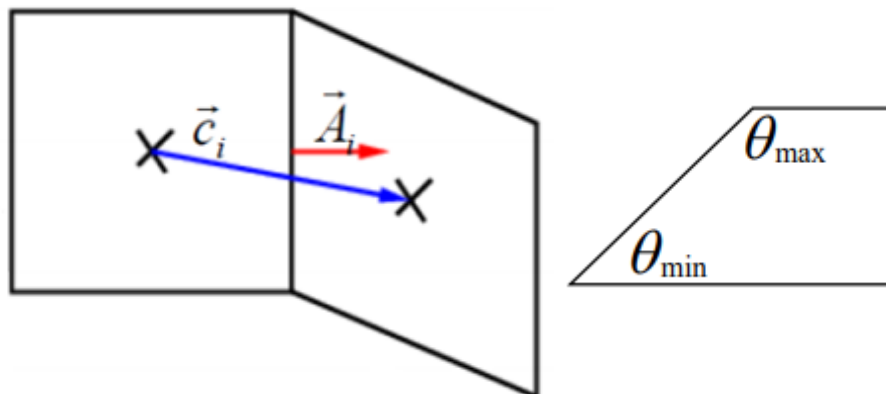


Figure 3.8 Orthogonality: the vector

connecting two cell centers and the surface normal vector of their common face [38]

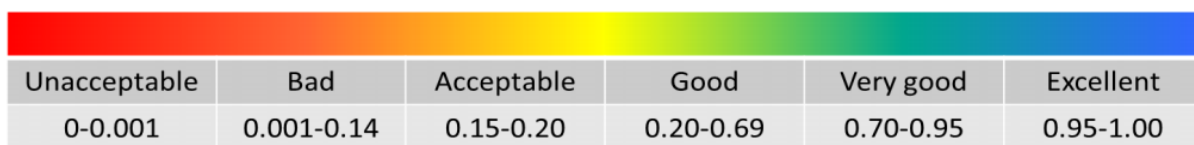


Figure 3.9 Orthogonal Quality mesh metrics spectrum [78]

3.4 Problem and resolution

We aim in this work to perform a simulation of two-dimensional, viscous and chemically unbalanced hypersonic flows around re-entry atmospheric blunt bodies. We have made the hypothesis of a chemical flow at vibrational equilibrium, the ionization phenomena have been neglected: for upstream speeds up to 6000 ms-1 [25], the radiation only becomes significant from 8000 ms-1 [25], and cannot be studied here. Air is therefore considered to be a mixture of five ideal gases (O2, N2, NO, O, N) in chemical nonequilibrium.

First, the problem was treated around a simple rounded body "half sphere" The rounded body chosen for the simulation was the sphere of "Lobb", to better understand the phenomenon and master the calculation code, then, an attempt was made to carry out a study

around a delta profile of a representative shuttle orbiter configuration with the same Lobb sphere radius to determine the re-entry trajectory design.

Finally, we investigated the conceptual design of a re-entry vehicle, by varying the shape and geometry of the vehicle in order to evaluate its impact on performance. we studied the two classes of shape optimization in vehicles, delta wing body and con-flare shape.

3.4.1 Mesh and geometry

3.4.1.1 Part A. study of physicochemical processes in a shock layer around a blunt body

The rounded body chosen for the simulation was the "Lobb" sphere experiment performed on a sphere-cone body with:[39] [40]

- ✓ The radius of the sphere is $R = 6.35\text{mm}$
- ✓ the length of the cylinder is 1.3m

Th study was simulated under the flowing free stream conditions (table 3.2):

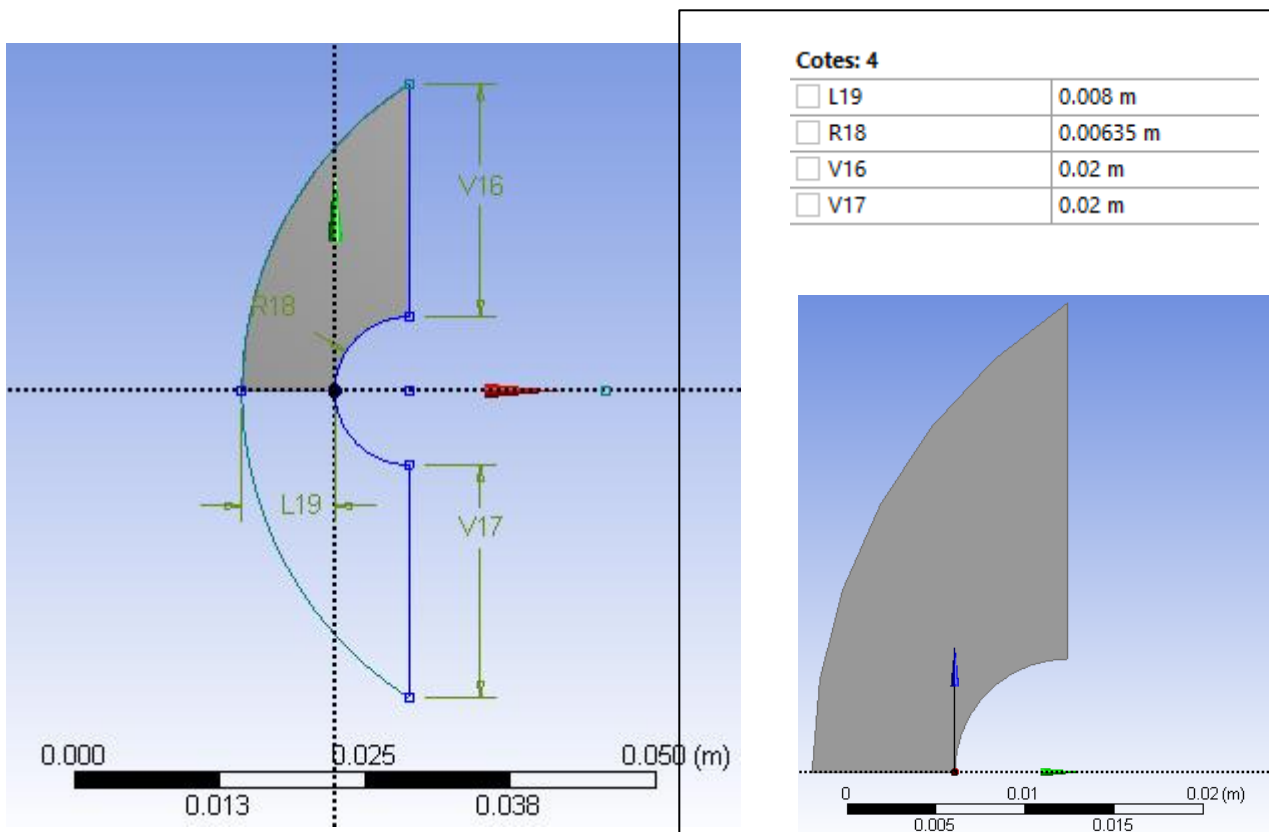
Table 3.2 Lobb sphere free stream boundary condition [39]

α	M_∞	Reaction. N	T_∞ [k]	ρ_∞ (kg/m^3)	P_∞ [Pa]	K	ω
0°	15.35	5	293	$7.896 \cdot 10^{-3}$	664	3245.962	64.607

3.4.1.1.1 geometry creation

Is the first step in simulation which consists in drawing the geometry of the problem: the body and the surrounding fluid domain, with the ANSYS DesignModeler software.

The geometry in figure 3.10 was created in a way that the simulation will be run using the axisymmetric Navier-Stock's equations, therefore, a two-dimensional symmetric geometry is created, with an axis defined at the radial centre of the studied body. This technique makes it possible to reduce the computational domain used and consequently reduce the calculation time.



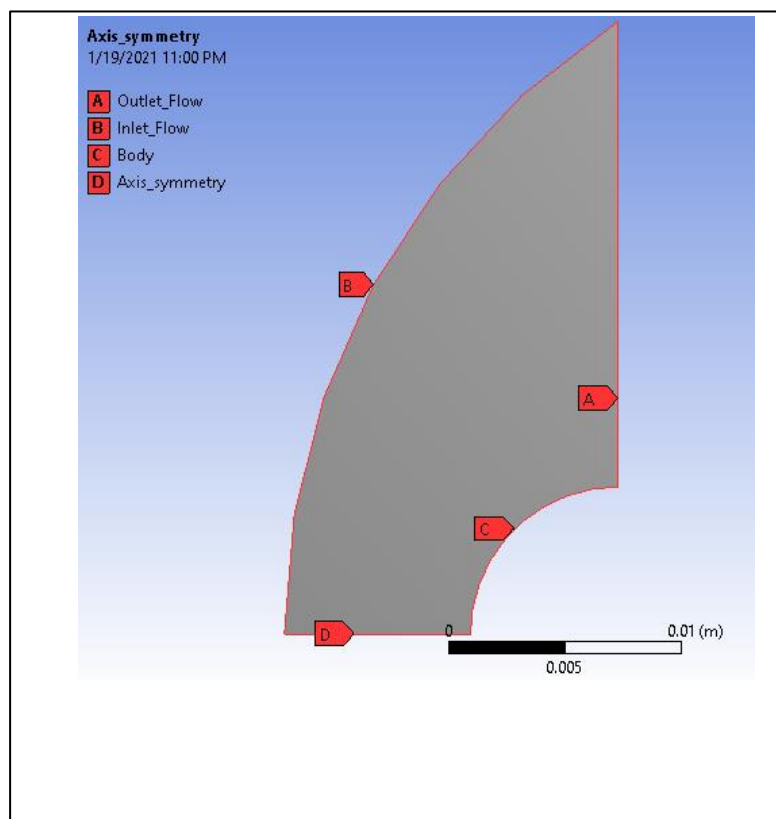
3.4.1.1.2 Identification of the boundary conditions

In order to simplify our work later on ANSYS Fluent, we should label each boundary in the geometry by creating named selections (inlets, the outlet, body and the symmetry surface) as described in figure 3.11 so we can

- ✓ Define the boundary conditions of the problem
- ✓ Define the conditions on the mesh at the level of the different selections

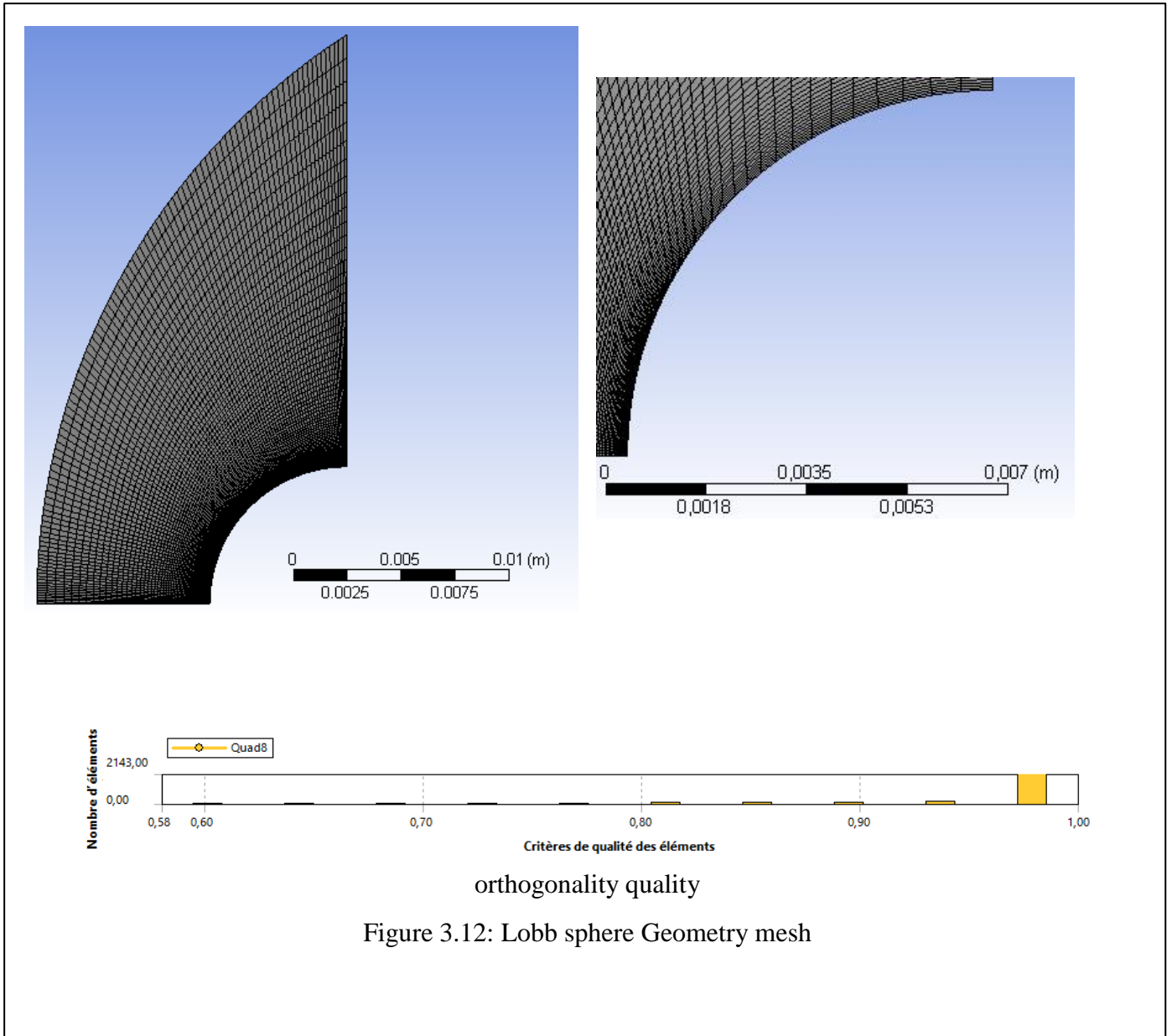
In 2D, to express the outputs, inputs, etc., the different edges of the geometry must be

selected.



3.4.1.1.3 Mesh construction

Our geometry is quite simple where the flow is practically the shape of geometry. So, using a quadrilateral cell mesh, we will have flow alignment with our mesh, whereas with triangular cells never will. This last point will guarantee a minimum of digital diffusion, Consequently, an initial 2D structured mesh with quadrilateral cells represented in figure 3.12 was carried out.



3.4.1.2 Part B: Study of re-entry trajectory design over delta body profile

Assuming the same flow hypothesis, we simulate a blunted delta profile body with the same nose radius of the previous blunted Lobb sphere.

- ✓ $R=0.00635\text{m}$
- ✓ Length of 0.23m
- ✓ Sweep angle 15°

3.4.1.2.1 Delta profile

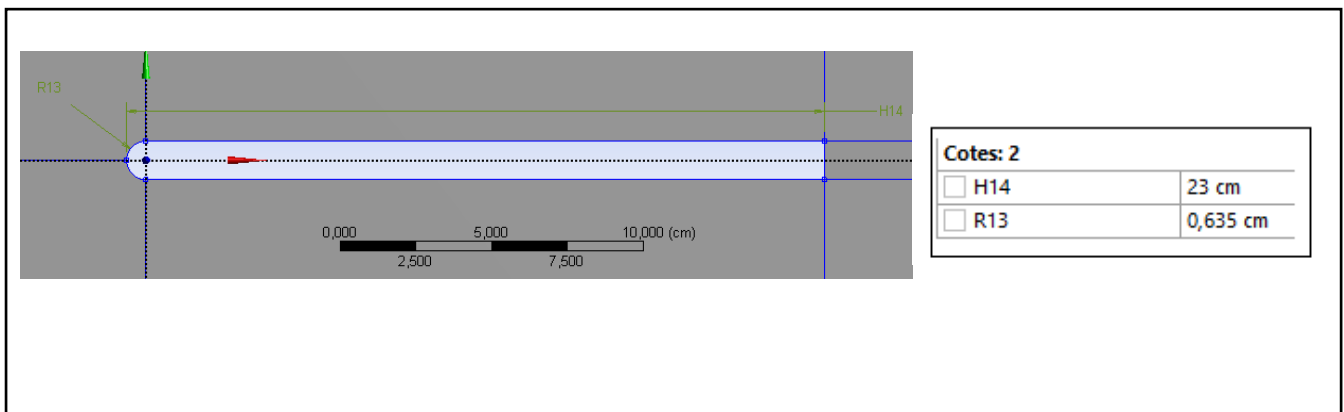
In order to study the flow along body surface streamline, we simulate a flow over a delta body profile so that we can study the trajectory design: the maximum deceleration, maximum heating rate and wall temperature with respect to angle of attack, altitude, re-entry velocity variations. The free flow condition is obtained based on the flight condition for three typical shuttle trajectory points in the altitude range of 60.96 to 76.20 km (200 000 to 250 000 ft) at velocities of 4.88 to 7.32 km/sec (16 000 to 24 000 ft/sec), respectively.[41]

Table 3.3 Delta profile study free stream boundary condition [41]

Altitude [Km]	M	P_{∞} [Pa]	ρ_{∞} [Kg/m^3]	T_{∞} [K]
60.96	15.562	19.259	$2.745 \cdot 10^{-4}$	244.4
67.06	20.154	8.102	$1.239 \cdot 10^{-4}$	227.6
76.20	25.420	1.968	$3.327 \cdot 10^{-5}$	206.1

3.4.1.2.1 Geometry creation

By the same way, we sketch the delta profile geometry but this time we can't split the computational domain where the flow will not be axisymmetric when we change the angle of attack as shown in figure 3.13.



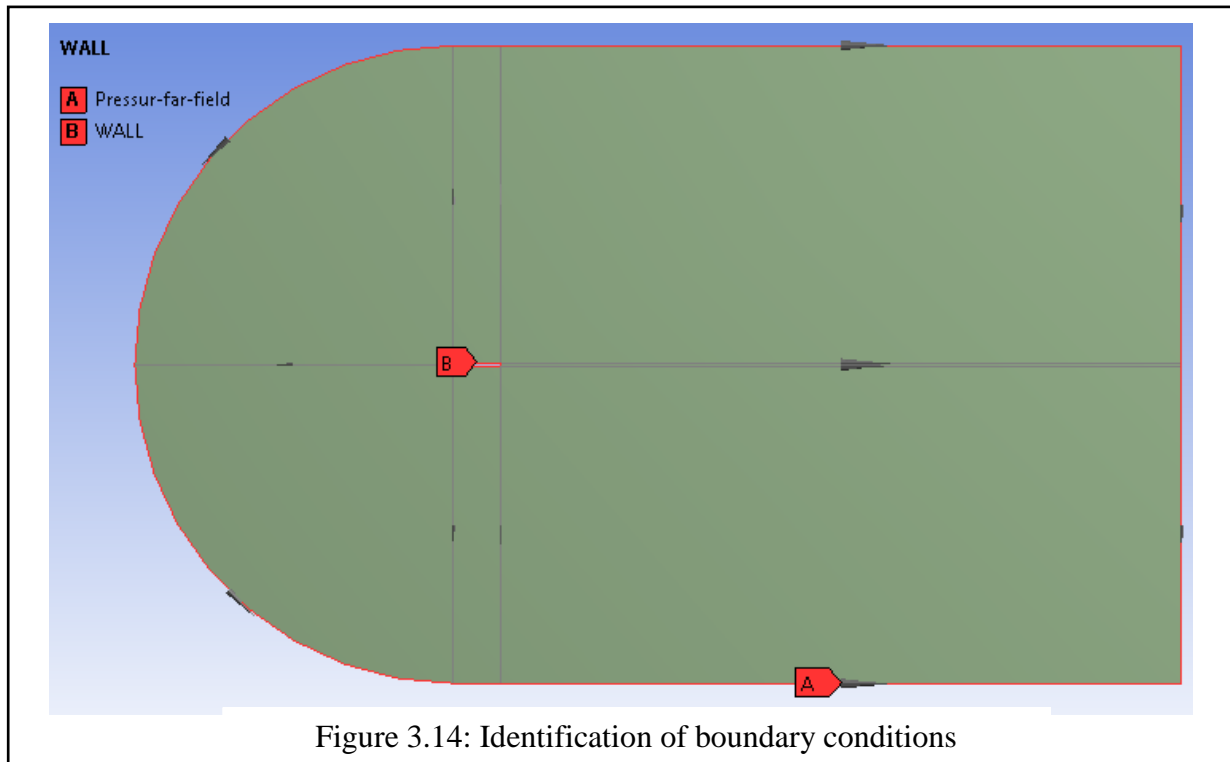
3.4.1.2.1.2 Identification of the boundary conditions

The surrounding of the model was cut off by the computational domain and represented as a boundary condition as shown in Figure (3.14). The top boundary was extended 5L vertically from the ground of the model and 5L from the side walls. Where L is the length of the wall and set to be 0.23m.

On the other hand, the inlet and outlet boundary were extended 5H and 15H from the wall, respectively. The size of the domain was built based on recommendation by Franke et al. [42] and Tominaga et al. [43].

To simplify our work after in Ansys Fluent we labelled the boundary conditions of the geometry as follow:

- ✓ Wall
- ✓ Computational Domain which is the surrounding space as the pressure far field



❖ This boundary condition identification has been applied in all subsequent

3.4.1.2.1.3 Mesh construction

The flow is completely the shape of geometry; so structured grid with quadratically cells was developed for the computational domain (figure 3.15).

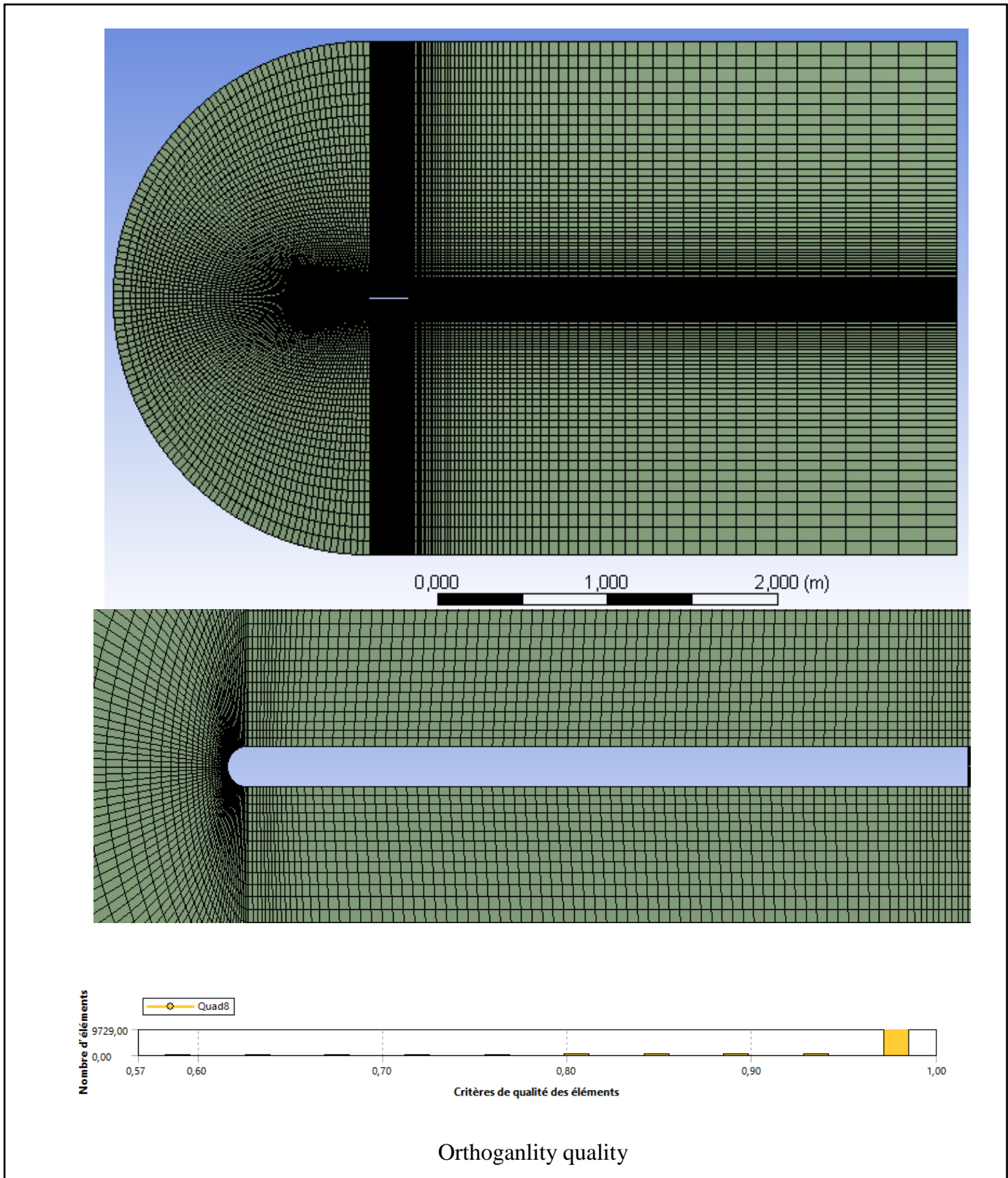


Figure 3.15 Delta profile mesh

3.4.1.2.2 Profile spike

In this simulation we set up Spikes in the front of the same delta body profile to reconfigure the flow field and reduce the overheating in hypersonic flight.

3.4.1.2.2.1 Geometry creation

The configuration and dimension of the spiked are shown in Figure (3.16).[44]

- The diameter D of the spherical head profile was chosen as the characteristic length, and the diameter of the spike was set to $d/D=0.1$.
- The L/D denotes spike length and was set as 0.9.
- R_t stands for transition part radius at the spike root and was set as $R_t/D=0.2$.

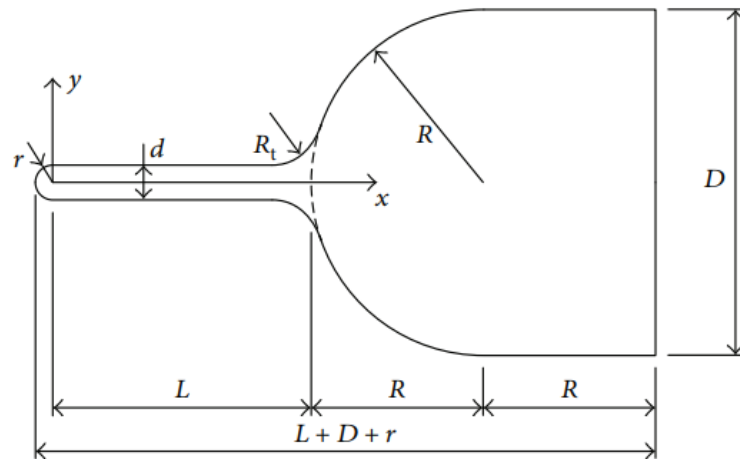


Figure 3.16: Configuration of the spiked blunt body for simulation

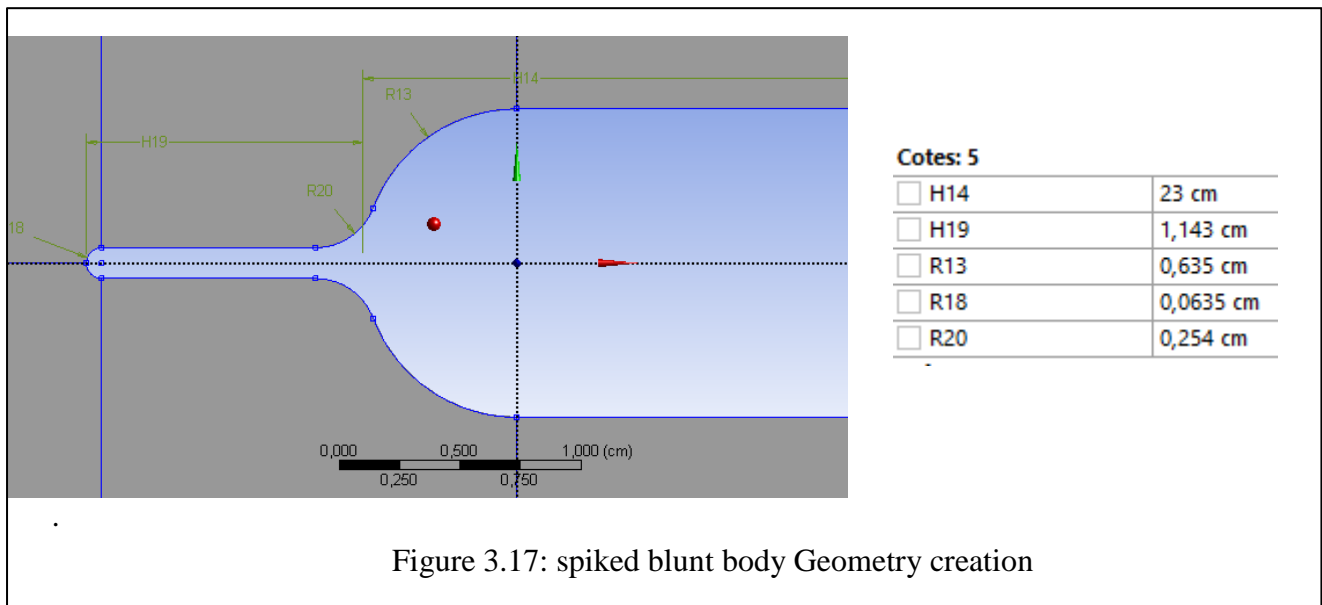


Figure 3.17: spiked blunt body Geometry creation

3.4.1.2.2.2 Mesh construction

The spiked blunt body model and the corresponding grid system are shown in Figure (3.18) in which orthogonality is satisfied in each grid system and refined by algebraic method near the wall boundary.

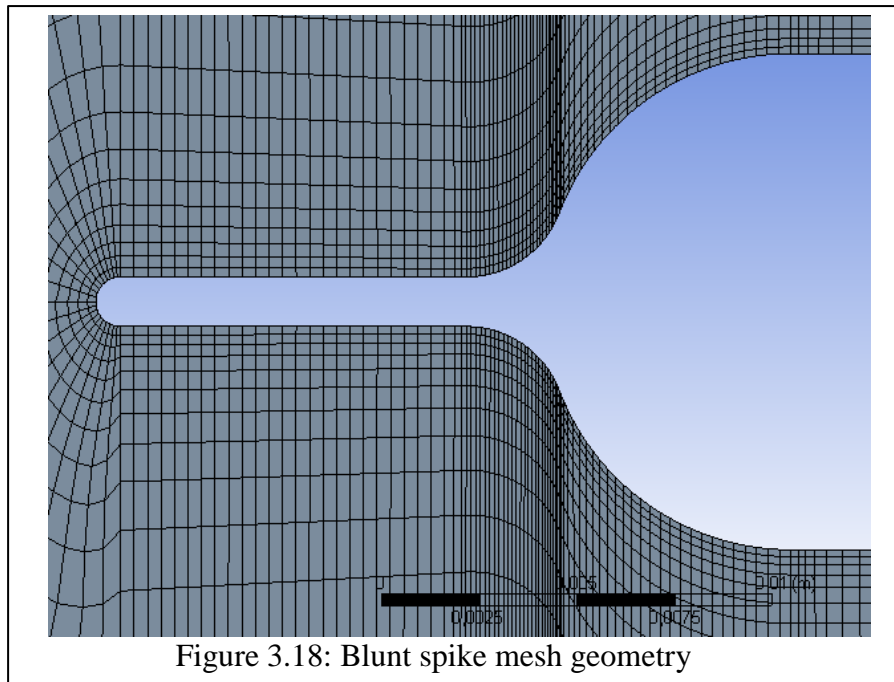


Figure 3.18: Blunt spike mesh geometry

3.4.1.3 Part C: shape optimization study on delta wing body and cone-flare shape

3.4.1.3.1 Delta body shape

In this part we will simulate a chemical non-equilibrium flow over a representative space shuttle configuration delta body [41] in order to modulate the drag force and the heating rate at the atmospheric re-entry phase.

The study was simulated under the flowing free stream conditions:

Table 3.4: Delta body free stream boundary conditions [41]

α	M_∞	<i>Reaction.N</i>	T_∞ [k]	ρ_∞ (kg/m ³)	P_∞ [Pa]	K	ω
0°	15.35	17	293	$7.896 \cdot 10^{-3}$	664	3245.962	64.607

3.4.1.3.1.1 Geometry creation

The geometry was sketched based on a representative space shuttle configuration delta body

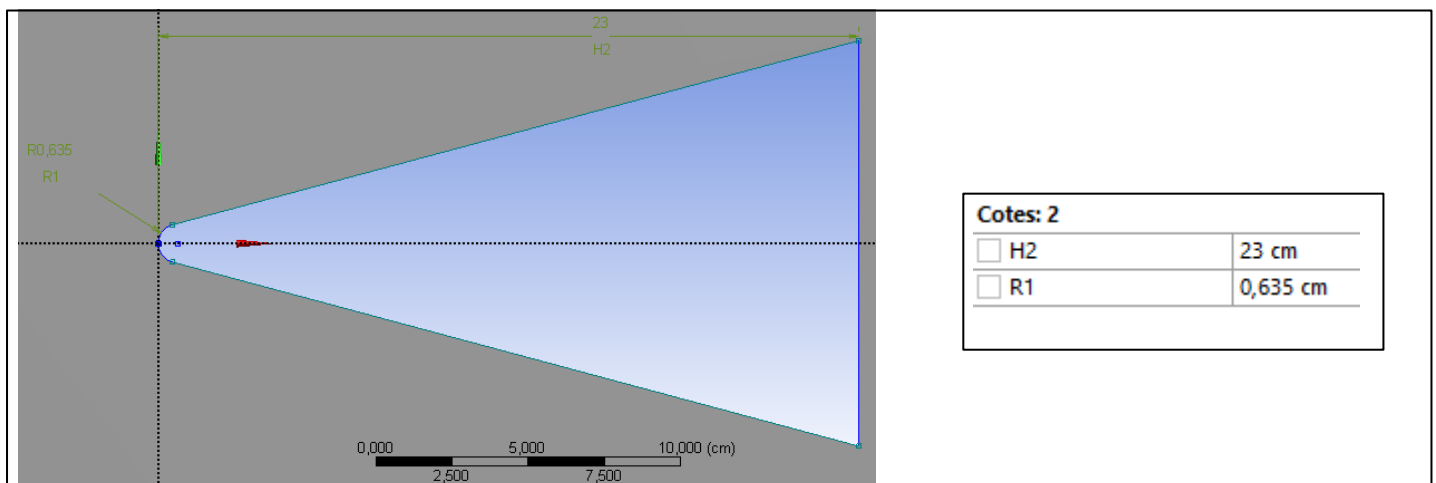


Figure 3.19: Geometry creation

as follow figure (3.19).

3.4.1.3.1.2 Mesh construction

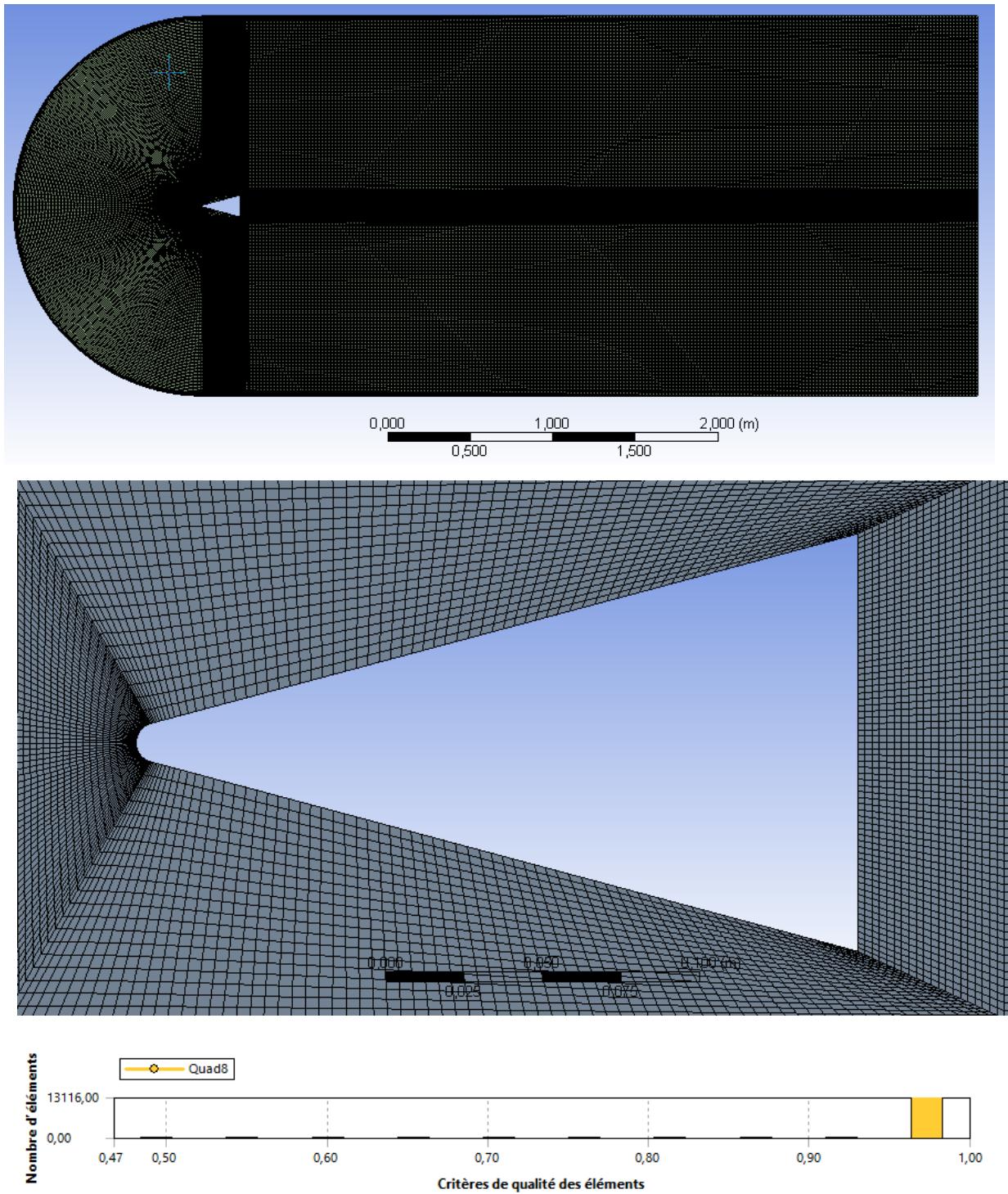


Figure 3.20: Delta Geometry mesh

3.4.1.3.3 Delta body 3D study

To fully enhance our result, we accompany our 2d study by a 3d delta-shaped study of a configuration of an orbiter of a space shuttle.

First, we created a 3d geometry by sketch as illustrated in figure (3.21) with a thickness of 0.635cm, we then used the option Englobler that allows us to create our control volume in 3d of the same dimension as in the 2d case.

We then use the boolean option that allows to select different solids to subtract or add through using the suppress solid option.

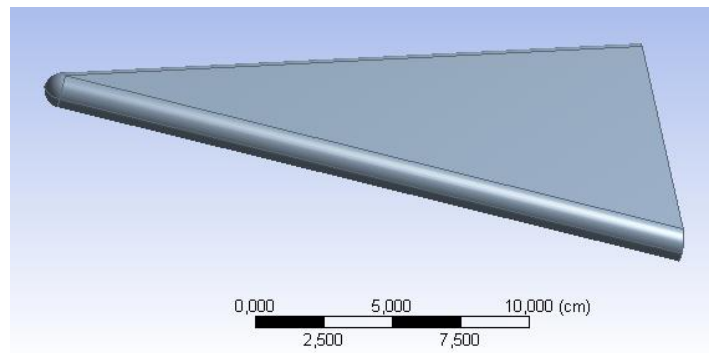
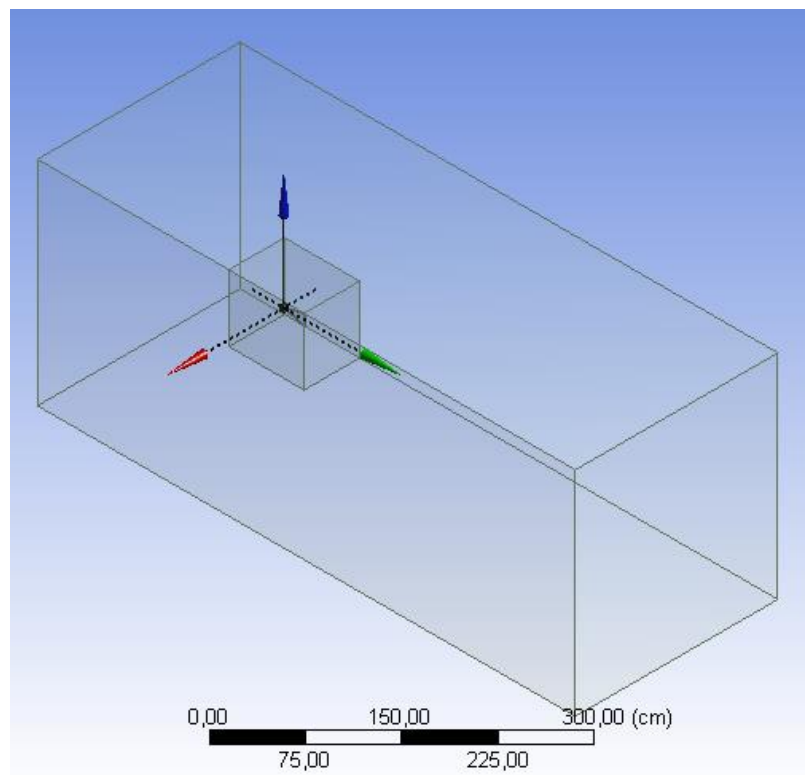


Figure 3.21 3D Delta body geometry



Mesh construction

In order to minimize the numerical resources, we used a multigrade mesh so that we can refine our mesh only in the vicinity of the body like illustrated in figure (3.22).

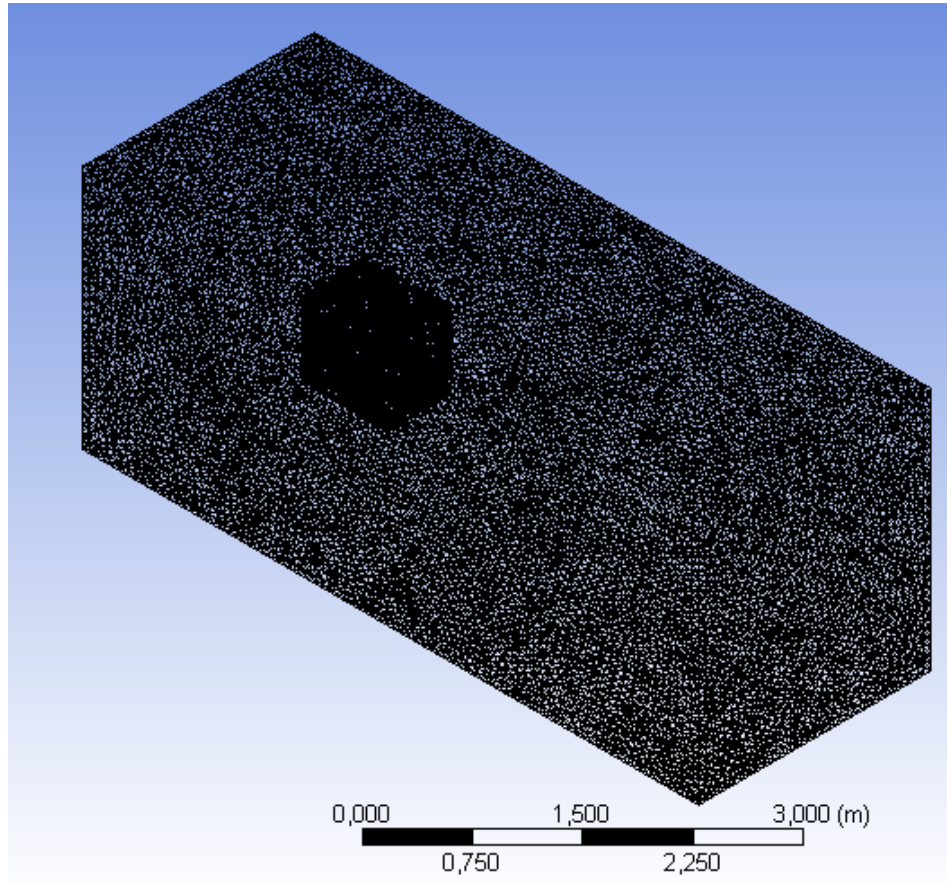


Figure 3.22 3D Delta body geometry mesh

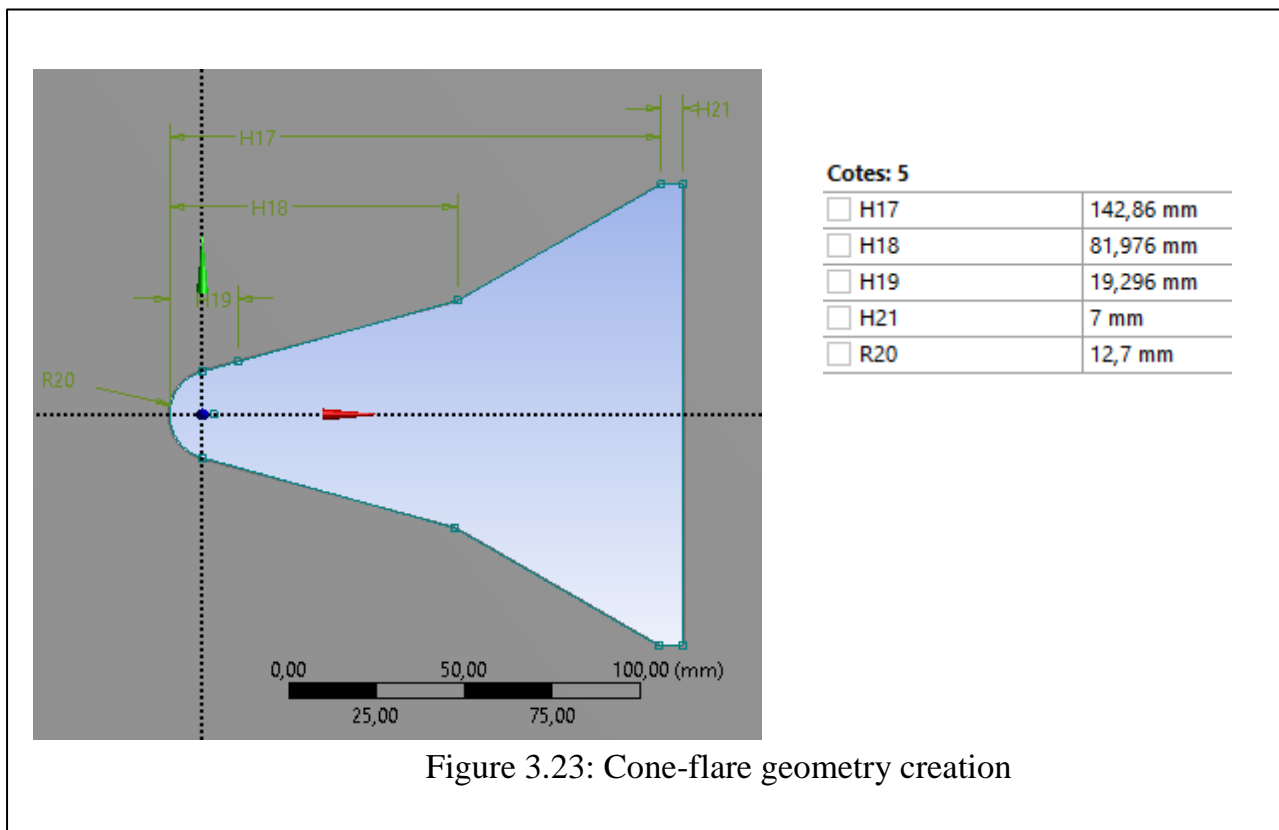
3.4.1.3.3 Conical Geometry

The second geometry is A 2D DART (Delft Aerospace re-entry test vehicle) model, re-entry vehicle has been used to simulate a chemical non-equilibrium flow to investigated the conceptual design of a re-entry vehicle compared with the previous delta body shape.[45]

Table 3.5 con-flare body free stream boundary condition [45]

α	M_∞	Reaction. N	T_∞ [k]	ρ_∞ (kg/m ³)	P_∞ [Pa]	K	ω
0°	15.35	17	293	$7.896 \cdot 10^{-3}$	664	3245.962	64.607

3.4.1.3.3.1 Geometry creation:



3.4.1.3.3.2 Mesh construction

In this model, hybrid meshing is used. The majority of the domain's space is made up of an unstructured grid. All triangles method is inserted in meshing. To establish a structured grid around the (re-entry) vehicle's boundary, edge sizing and inflation are used. The structured grid is made up of 7 layers, each with a thickness of 1 millimetre, and it is used to investigate fluctuations in variables such as temperature, pressure, and Mach number near the boundary. Curvature guides the mesh size function which result in a fine mesh as shown in figure 3.24.

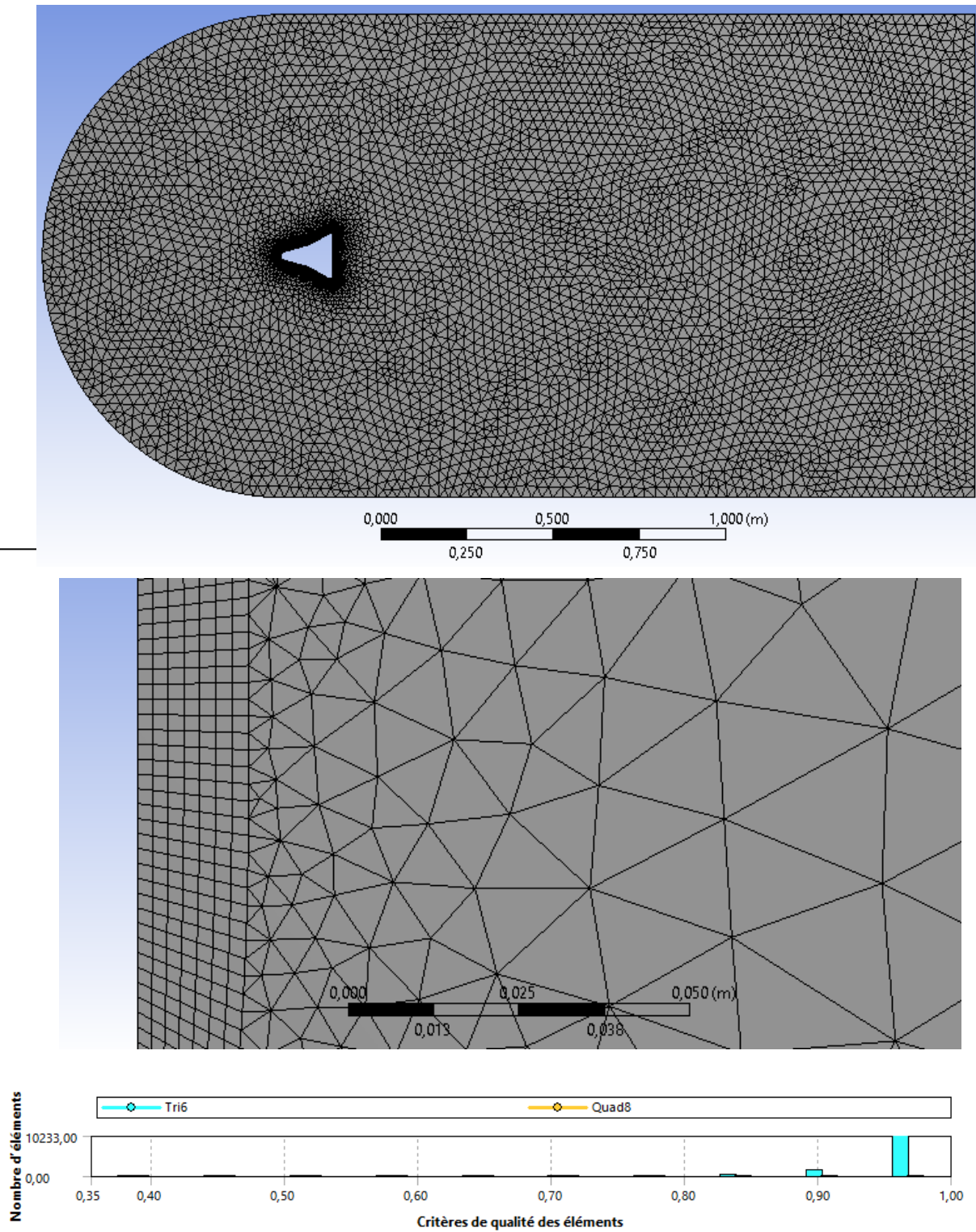


Figure 3.24 cone-flare geometry mesh

3.4.2 Setting in data and simulation

3.4.2.1 Choice of calculation mode:

FLUENT Launcher appear, where we can specify the dimensionality of the problem (2D or 3D), as well as other options in figure 3.26:

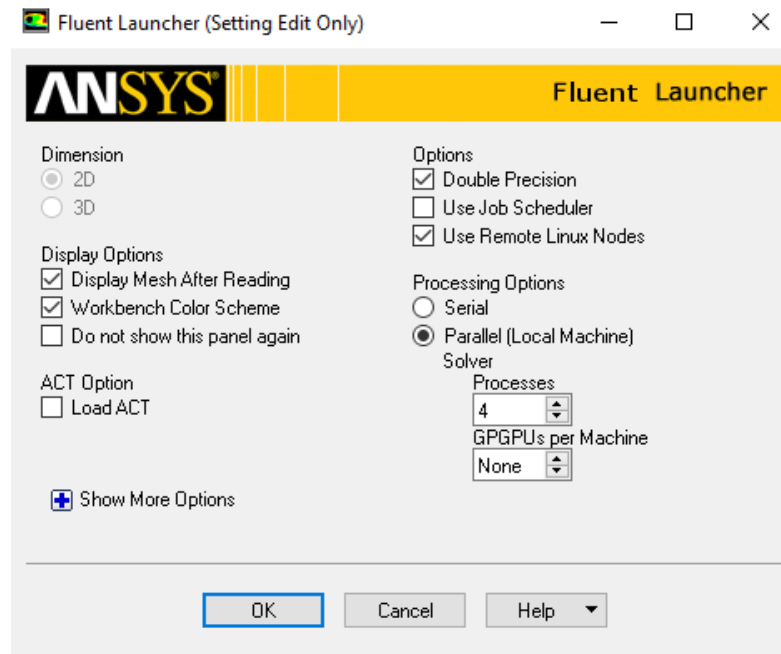


Figure 3.26 choice of calculation mode and type of dimension

Under Processing Options select Parallel Settings tab allows to specify settings for running Ansys FLUENT in parallel. Parallel processing takes away the computation from single core to multiple cores.

For most cases, the single-precision solver will be sufficiently accurate, but certain types of problems may benefit from the use of a double-precision version. If the geometry has features of very disparate length scales single-precision calculations may not be adequate to represent the node coordinates. Double-precision calculations may therefore be necessary to resolve the problem. Therefore, the double precision mode is the mode that we will use.

3.4.2.2 Choice of solver:

In the steps that follow, we will select a solver and specify physical models, material properties, and zone conditions for our simulation using the Setting Up Physics ribbon tab (figure 3.27)

ANSYS Fluent allows us to choose one of the two numerical methods:

- ✓ The pressure-based approach was traditionally developed for low-speed incompressible flows.
- ✓ The density-based approach was traditionally used for high-speed compressible flows.

The velocity field is obtained from the momentum equations in both methods:

- ✓ In the density-based approach, the density field is obtained from the continuity equation while the pressure field is determined from the equation of state.

- ✓ In the pressure-based approach, the pressure field is extracted by solving a pressure or pressure correction equation which is obtained by manipulating continuity and momentum equations.

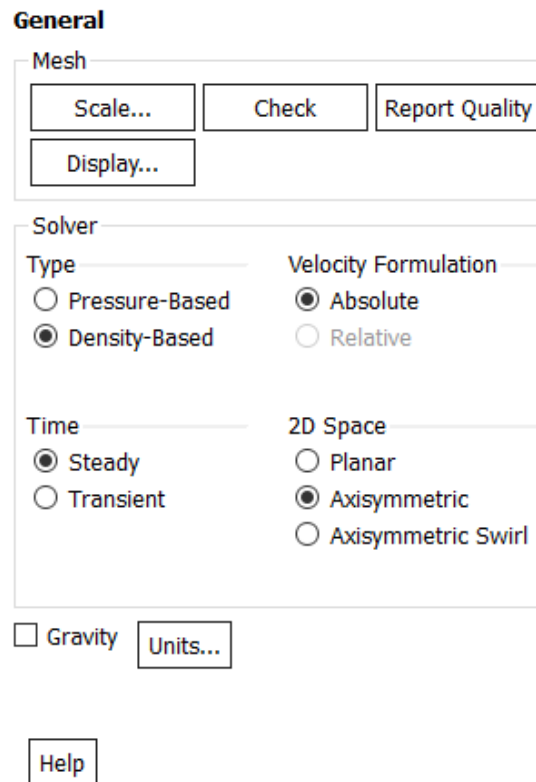


Figure 3.27 choice of solve

The two numerical methods employ the same finite-volume discretization process, but the approach used to linearize and solve the discretized equations is different. Using either method, the governing integral equations for the conservation of mass, momentum, and for energy and other scalars such (turbulence and chemical species) will be solved by Ansys Fluent as follow:

- a) The density-based solver (figure 3.28)
 - Solves the governing equations of continuity, momentum, energy and species transport simultaneously.
 - Governing equations for additional scalars will be solved afterward and sequentially.
 - Because the governing equations are non-linear (and coupled), several iterations of the solution loop must be performed before a converged solution is obtained.
 - Each iteration consists of the steps illustrated in Figure (3.26): These steps are continued until the convergence criteria are met.

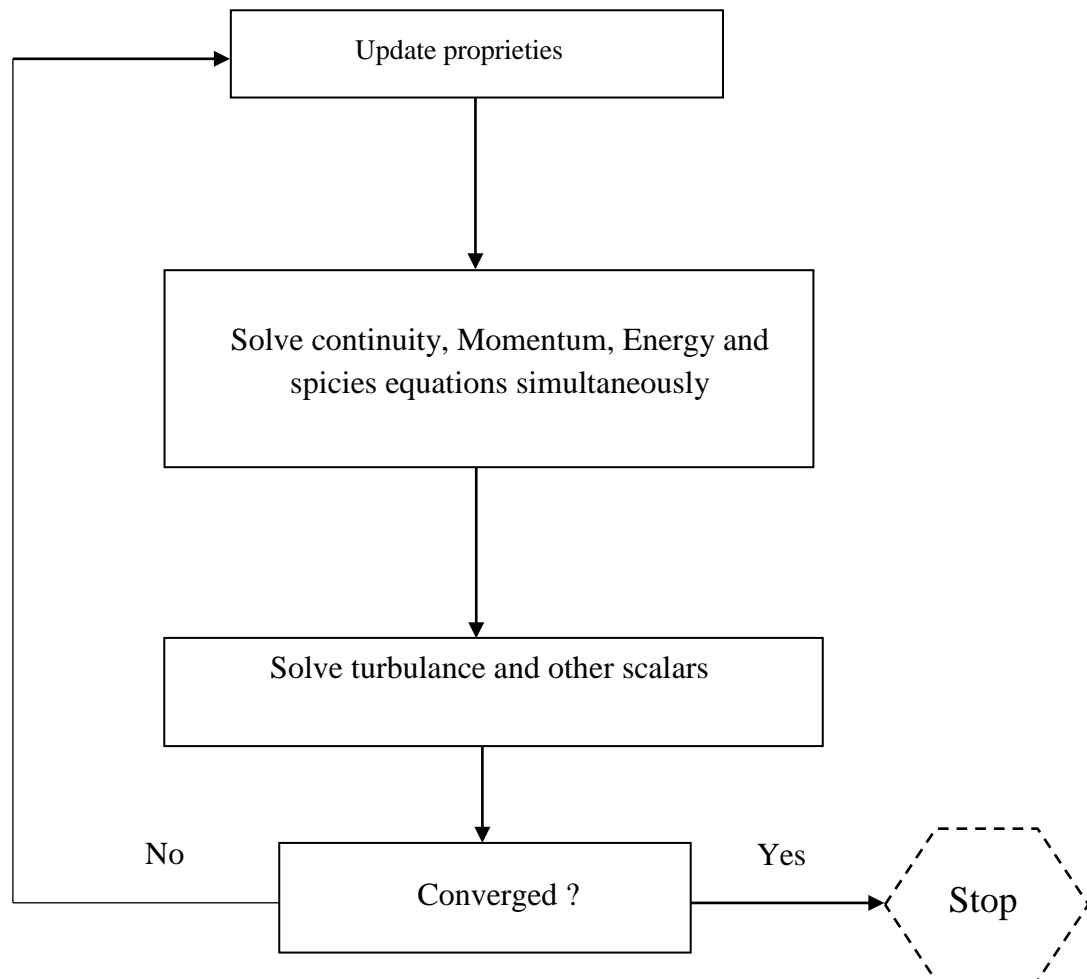


Figure 3.28: Overview of the Density-Based Solution Method [46]

- b) In the pressure-based model, since the governing equations are nonlinear and coupled to one another, the solution process involves the following iterations:
- The solver employs an algorithm which belongs to a general class of methods called the projection method, where, the constraint of mass conservation (continuity) of the velocity field is achieved by solving a pressure equation.
 - The pressure equation is derived from the continuity and the momentum equations in such a way that the velocity field, corrected by the pressure, satisfies the continuity.
 - The solution process involves iterations wherein the entire set of governing equations is solved repeatedly until the solution converges

We are studying a hypersonic flow, therefore, the stationary density-based solver with an axisymmetric space was chosen.

- ❖ The geometry was created with the fact that the simulation will be run using the axisymmetric Navier-Stock's equations, this technique has an advantage of:
 - ✓ Reduce the number of meshes used
 - ✓ Consequently, reduce the calculation time.

3.4.2.3 Choice of model

ANSYS fluent represent the different models available as shown in figure 3.29. We first activate the energy equation (figure 3.30).

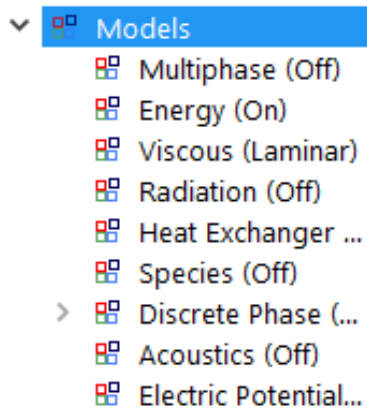


Figure 3.29: Choice of model

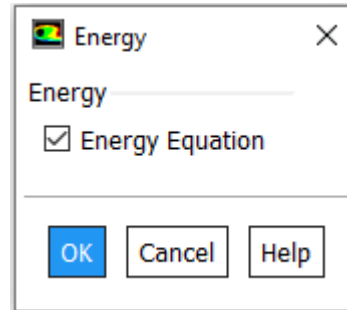


Figure 3.30: Activation of the Energy Equation

3.4.2.3.1 Choice of turbulence model

The successful choice of turbulence model depends on:

- Flow physics
- Computer resources available
- Project requirements
 - Accuracy
 - Turnaround time
- Near-Wall treatments

The turbulence model must be selected carefully and upon the following procedures to decide the appropriate model that fine with physical flow:

- Determine whether the flow is turbulent by calculating Re .
- Estimate y^+ before generating the mesh.
- Begin with standard k- ϵ and change to kw standard, SST.
- Use wall functions for wall boundary conditions.

The kw sst is the model that have been chosen for our simulation as shown in figure 3.31 since it is a hybride model combining the near wall and the free stream treatment and provides more accurate prediction of flow separation. This ensures that the appropriate model is utilized throughout the flow field while we are simulating a flow over a thin viscous boundary layer where turbulence is strongly damped and phenomena due to molecular viscosity are predominant.

By another method ANSYS fluent allows to uses a function called "Wall Function" which connects the wall to the outer layer.

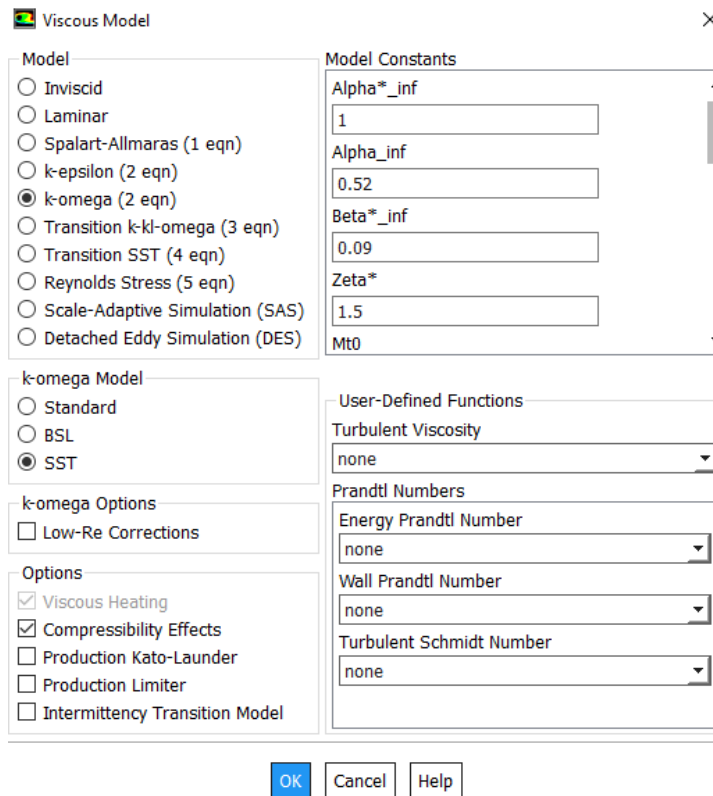


Figure 3.31: Choice of turbulence model

3.4.2.3.2 Building a Model for Species Reactions and Transport

The mixing and transport of chemical species can be modelled by solving conservation equations describing convection, diffusion and reacting sources for each component species. Fluent offers the possibility of defining the reaction process simulation in figure 3.32 as follow:

First, we select species transport and volumetric reactions under reaction type to introduce reactions. The laminar finite-rate model computes the chemical source terms using Arrhenius expressions, and ignores the effects of turbulent fluctuations. It's the model that was chosen in

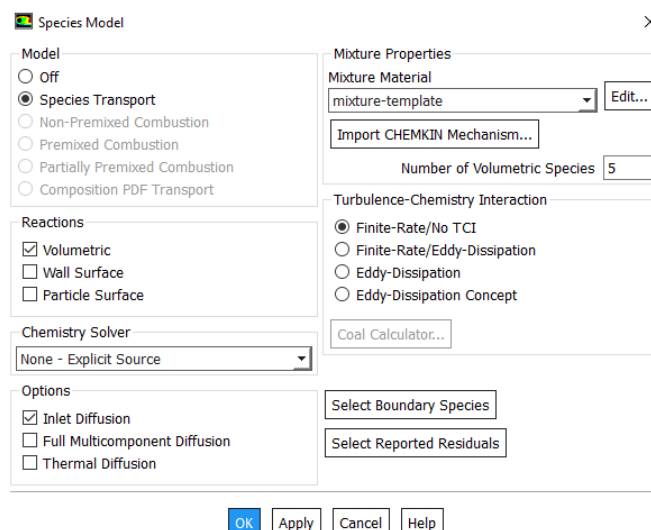


Figure 3.32: Species reaction model

our study.

Because the air is considered as a reactive mixture, Fluent offers the possibility of specifying the different species of the mixture, from its database of we have created a reactive mixture of the species (O_2 , N_2 , NO, O, N).

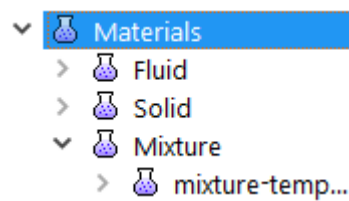


Figure 3.33: Choice of mixture material

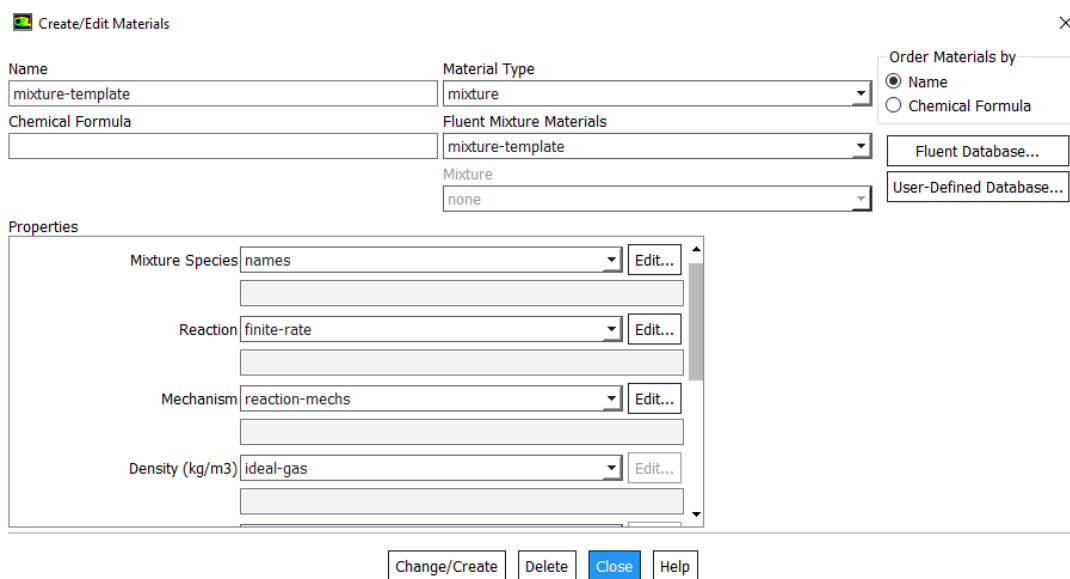
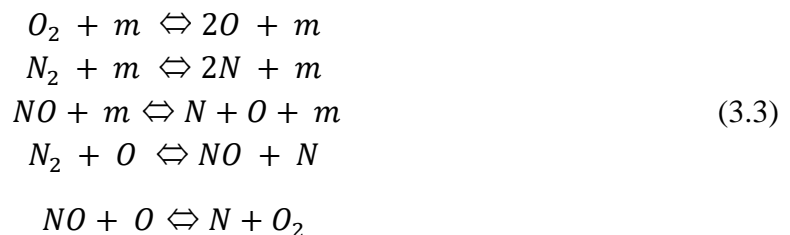


Figure 3.34: Create and edit material

The appropriate Reaction model will be displayed in the Reaction drop-down list in the Edit Material dialog box in figure 3.34. The reactions are modeled in the following form :



Where M is the catalyst which can be any of the five species (O_2 , N_2 , NO, O, N).

Our reactions are reversible so we activate the Include Backward Reaction option and therefore the velocity exponent for each species is equivalent to the stoichiometric coefficient of that species which is the constant $v'_{i,r}$ and $v''_{i,r}$ in Equation 3.4. (Stoic. Coefficient = Rate Exponent),

$$\sum_{i=1}^N v'_{i,r} \mathcal{M}_i \xrightleftharpoons[k_{b,r}]{k_{f,r}} \sum_{i=1}^N v''_{i,r} \mathcal{M}_i
 \tag{3.4}$$

In Fluent ,and for reversible reactions the molar production rate of species s from reaction r is given by:

$$\hat{R}_{i,r} = \Gamma(v''_{i,r} - v'_{i,r}) \left(k_{f,r} \prod_{j=1}^N [C_{j,r}]^{n'_{j,r}} - k_{b,r} \prod_{j=1}^N [C_{j,r}]^{v'_{j,r}} \right) \quad (3.5)$$

Where

$v'_{i,r}$ stoichiometric coefficient for reactant i in reaction r

$v''_{i,r}$ stoichiometric coefficient for product i in reaction r

$v'_{j,r}$ rate exponent for reactant species j in reaction r

$v''_{j,r}$ rate exponent for product species j in reaction r

Because we are using the laminar finite-rate we have to enter the following parameters for the Arrhenius rate as shown in figure 3.35:

Pre-Exponential Factor

$$k_{f,r} = A_r T^{\beta_r} e^{-E_r/RT} \quad (3.6)$$

Activation Energy the constant $E_{r,f}$ in the precedent equation

Temperature Exponent the value for the constant β_r in the Arrhenius equation

Third-Body Efficiencies the values for $\gamma_{j,r}$ in following Equation

Reactions

Mixture: mixture-template Total Number of Reactions: 5

Reaction Name: reaction-1 ID: 1 Reaction Type: Volumetric Wall Surface Particle Surface Electrochemical

Number of Reactants: 1 Number of Products: 1

Species	Stoich. Coefficient	Rate Exponent
o2	1	1

Species	Stoich. Coefficient	Rate Exponent
o	2	1

Arrhenius Rate

Pre-Exponential Factor: 1e+19

Activation Energy (j/kgmol): 4.947e+08

Temperature Exponent: -1.5

Include Backward Reaction Specify...

Third-Body Efficiencies Specify...

Pressure-Dependent Reaction Specify...

Coverage-Dependent Reaction Specify...

Mixing Rate

A: 0 B: 0

OK Cancel Help

$$\Gamma = \sum_j^N \gamma_{j,r} C_j \quad (3.7)$$

Figure 3.35: Reaction

3.4.2.3.3 Boundary condition specifications

ANSYS Fluent provides different types of boundary zone types for the specification of flow inlets and exits. In Our study we have chosen the following types:

Pressure far field for *(Inlet_flow)*

Pressure far-field boundary condition model the free-stream compressible flow at infinity, with static conditions specified and free-stream Mach number, this boundary condition is applicable only when the density is calculated using the ideal-gas law. And since the number of Mach, the pressure, temperature and mass composition of the mixture (76.7% of N₂ and 23.3% of O) at the inlet are givens so "Pressure far field" is the appropriate entry condition for our problem.

Pressure outlet for *(Outlet_Flow)*

In our case the condition does not require any specification because the flow is supersonic at the outlet, all the flow quantities are extrapolated from the interior.[46]

The Average Pressure Specification option at the pressure outlet boundary allows the pressure along the outlet boundary to vary, but maintain an average equivalent to the specified value in the Gauge Pressure input field. The pressure variation allowed in this boundary implementation slightly diminishes the reflectivity of the boundary as compared with the default uniform pressure specification.

In the density-based solver in our study, the face pressure at the boundary equals the value specified in the Pressure Outlet where the computed average pressure value does not match the specified pressure value at the boundary then the weak average pressure enforcement can be used.

Wall boundary condition for Body

Wall boundary conditions are used to link fluid and solid regions. in our study we used these two wall boundary conditions,

The Dirichlet boundary condition allows to select the fixed temperature condition. we will need to specify the temperature at the wall surface. And the Neumann boundary condition by specifying the Heat flux option under thermal condition for a set heat flux condition. A zero-heat flux condition can be used to define an adiabatic wall.

Axis boundary condition for symmetry axis

The axis boundary type is used as the centreline of a cylindrical-polar quadrilateral, hexahedral mesh or an axisymmetric geometry like the case in our study. We do not need to define any boundary conditions at axis boundaries.

3.4.2.4 Solution:

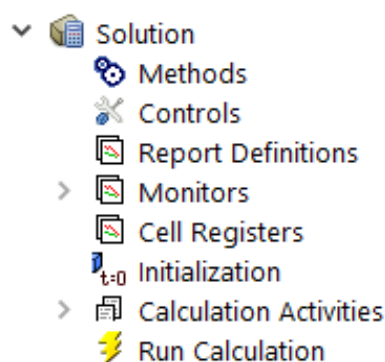


Figure 3.36 - The Solution dialog box

3.4.2.4.1 Choice of the formulation algorithm:

The Solution Methods in figure 3.37 task page allows specify different parameters to

Solution Methods

Formulation

Flux Type

Spatial Discretization

Gradient

Flow

Turbulent Kinetic Energy

Specific Dissipation Rate

be used in the calculation.

Figure 3.37 Solution method

3.4.2.4.1.1 Choice of the formulation algorithm:

Formulation provides an available types of solver formulations: Implicit and Explicit:

Implicit: The unknown value for a given variable in each cell is computed using a relation that includes both unknown and existing values from adjacent cells. Therefore, each unknown value will appear in several equations in the system, and these equations must be solved simultaneously to give the unknown quantities.

Explicit: The unknown value for a given variable in each cell is computed using a relation that includes just the existing values. Therefore, each unknown value will appear in only one equation in the system and to determine the unknown value we can solve one at a time the equation for the unknown values in each cell.

If we choose the implicit option of the density-based solver, we get a system of linear equations with N equations for each cell in the domain, where N is the number of coupled equations in the set because each equation in the coupled set of governing equations is linearized implicitly with respect to all dependent variables in the set

If we choose the explicit option of the density-based solver, as in the implicit option, this too will result in a system of equations with N equations for each cell in the domain and likewise, all dependent variables in the set will be updated at once because each equation in the coupled set of governing equations is linearized explicitly.

Flux Type provides a list of the convective flux types Roe-FDS and AUSM:

3.4.2.4.1.2 The choice of the spatial discretization scheme

3.4.2.4.1.2.1 Choice of Gradient method

Gradients of solution variables are needed for constructing values of a scalar at the cell faces, and so for computing secondary diffusion terms and velocity derivative. The gradients are computed in our study according to Least-Squares Cell-Based which has more accurate results, minimizes false diffusion and is less computationally intensive.

3.4.2.4.1.2.2 The choice of the precision of the diagrams used

When first-order accuracy is desired, quantities at cell faces are determined by assuming that the cell centre values of any field variable represent a cell-average value and hold throughout the entire cell; the face quantities are identical to the cell quantities. While, when second-order accuracy is desired, quantities at cell faces are computed using a multidimensional linear reconstruction approach. In this approach, higher-order accuracy is achieved at cell faces through a Taylor series expansion of the cell-centered solution about the cell centroid.[46]

When the flow is aligned with the grid the first-order discretization may be acceptable, when the flow is never aligned with the grid, The second order discretization will generally give more accurate results. For complex flow, even with grid aligned flows, it's required to use the second order discretization to minimize the numerical diffusion

For most cases, it is possible to use the second-order scheme from the start of the calculation. In some cases, we may need to start with the first-order scheme and then switch to the second-order scheme after a few iterations.

In summary, while the first-order discretization generally yields better convergence than the second-order scheme, it generally will yield less accurate results, especially on tri/tet grids.

3.4.2.4.2 Control of the solution

The **Solution Controls** task page allows you to set common solution parameters (figure 3.38).

Courant Number sets the fine-grid Courant number (time step factor) when the density-based solver is used

Setting Under-Relaxation Factors

The default under-relaxation parameters for all variables are set suitable for many problems. but for some particularly nonlinear problems it is prudent to reduce the under-relaxation factors initially (e.g., some turbulent).

The screenshot shows the 'Solution Controls' task page with the following settings:

- Courant Number:** 5
- Under-Relaxation Factors:**
 - Turbulent Kinetic Energy: 0.8
 - Specific Dissipation Rate: 0.8
 - Turbulent Viscosity: 1
- Solid:** 0.7

A 'Default' button is visible at the bottom left of the form.

Figure 3.38: Solution control

We should alter the default under relaxation factor only if the residuals continue to increase after the first 4 to 5 iteration, in this case we need to reduce the under-relaxation factor from their default value to about 0.2, 0.5, 0.5 and 0.5.

3.4.2.4.2.1 Solution limits

The Solution Limits dialog box in figure 3.39 allows to improve the stability of the solution

Parameter	Value
Minimum Absolute Pressure (pascal)	1
Maximum Absolute Pressure (pascal)	5e+10
Minimum Static Temperature (k)	1
Maximum Static Temperature (k)	5000000
Minimum Turb. Kinetic Energy (m2/s2)	1e-14
Minimum Spec. Dissipation Rate (1/s)	1e-20
Maximum Turb. Viscosity Ratio	100000
Positivity Rate Limit	0.2

Figure 3.39: Solution limits

ANSYS FLUENT applies limiting values for pressure, static temperature, and turbulence quantities. The purpose of these limits is to keep the absolute pressure or the static temperature from becoming 0, negative, or excessively large during the calculation, and to keep the turbulence quantities from becoming excessive.

Typically, we will not need to change the default solution limits. If pressure, temperature, or turbulence quantities are being reset to the limiting value repeatedly (as indicated by the appropriate warning messages in the console), we should check the dimensions, boundary conditions, and properties to be sure that the problem is set up correctly and try to determine why the variable in question is getting so close to zero or so large. In very rare cases, we may need to change the solution limits, for example in our case we know that the temperature will accede the minimum set temperature so only in this case that we have to change the solution limits.[46]

Positivity Rate Limit control the reduction of temperature by a default value of 0.2 means that the temperature should not decrease from one iteration to the next by more than 20% of its previous value. If the temperature change exceeds this limit, the time step in that cell is reduced to bring the change back into range and a "time step reduced" warning is printed. Rapid reduction of temperature is an indication that the temperature may become negative.

3.4.2.4.3 Solution initialization

Before starting our CFD simulation, we must provide ANSYS Fluent with an initial boundary condition of the solution flow.

```

iter      scalar-0
1         1.000000e+00
2         5.600216e-04
3         2.325211e-04
4         8.715283e-05
5         3.594547e-05
6         1.484151e-05
7         5.677905e-06
8         2.087339e-06
9         7.785277e-07
10        2.944086e-07

Hybrid initialization is done.

```

Figure 3.40: solution initialization

To obtain the most exact solution possible, the Fluent solver proceeds by successive iterations to solve the matrix system obtained by discretization of the equations by a finite volume method as shown in figure 3.40.

The iteration procedure requires that all the variables are initialized before the start of the calculation. An initialization improves the stability and the speed of convergence. In some cases, a correct initial solution is necessary [47]. For our calculation We set a velocity field equal to the entry velocity in the whole domain as the starting point of the iterations.

The solver starts from the initial solution and due to an iterative algorithm of resolution of the matrix system obtained by discretization, will perform iterations. If all goes well, each iteration must modify the current solution to replace it with a solution closer to the exact solution sought. With each iteration and for each equations an error, called residue, is calculated compared to an exact solution of the system. A calculation diverges if the residuals increase during iterations.

3.4.2.4.4 Calculation control

The Run Calculation task page in figure 3.41 allow us to start the solver iterations

Number of iterations

- For steady flow calculations: sets the number of iterations to be performed.
- For unsteady calculations: using the explicit unsteady formulation, this will specify the number of time steps, since each iteration will be a time step.

Select solution steering option so that we can choose the flow type (hypersonic in our study).

The Courant number defines the time step size. In our case for density-based implicit solver:

- ✓ The Courant number is not limited by stability constraints.
- ✓ Default value is 5.

Convergence and stability

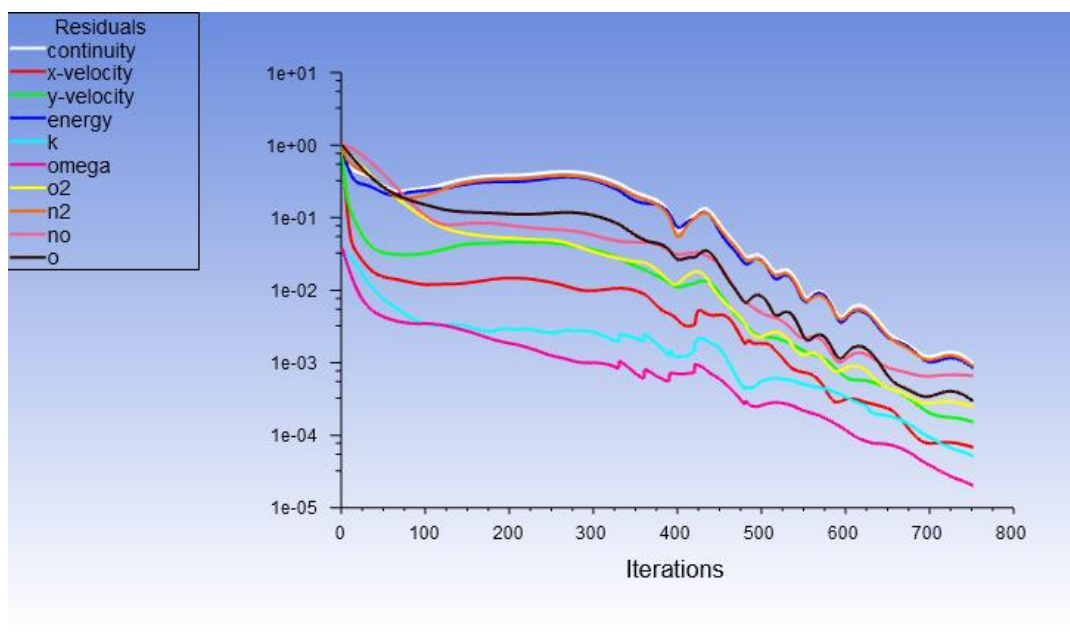
At convergence, the following should be satisfied:

Figure 3.41: Run calculation

- ✓ Overall mass, momentum, energy, and scalar balances are achieved.
- ✓ Monitoring convergence using residual history:
- ✓ Generally, a decrease in residuals by three orders of magnitude indicates at least qualitative convergence. At this point, the major flow features should be established.
- ✓ Scaled energy residual should decrease to 10^{-6} (for the pressure-based solver).
- ✓ Scaled species residual may need to decrease to 10^{-5} to achieve species balance.
- ✓ Monitoring quantitative convergence :
- ✓ Monitor other relevant key variables/physical quantities for a confirmation.
- ✓ Ensure that overall mass/heat/species conservation is satisfied.

Convergence can be accelerated by:

- ✓ Supplying better initial conditions
- ✓ Starting from a previous solution (using file/interpolation when necessary)
- ✓ Gradually increasing under-relaxation factors or Courant number
- ✓ Excessively high values can lead to solution instability convergence problems
- ✓ You should always save case and data files before continuing iterations
- ✓ Default settings provide a robust Multigrid setup and typically do not need to be changed.



✓ Figure 3.42: The evolution of the residues for the initial mesh

3.4.3 Grid independence study:

Prior to performing the CFD simulations, a grid independence study was conducted over several grid resolutions. Because the heat transfer occurring between the surrounding air

and the vehicle wall played a key role in this study, particular effort was made to ensure the near-wall mesh quality.

In this study, to strike a balance between accuracy on the one hand side and computational time and memory consumption on the other hand side the mesh should be constructed with reasonable mesh densities. This means that not every region of a spatial simulation domain is of particular importance for the solution of the numerical problem. So, the idea is to use a finer mesh in simulation domains where a high resolution is necessary and simultaneously reduce the memory consumption by applying a gradient mesh in regions of high importance.

To overcome this issue, the region located near from the wall was meshed with a gradient structured mesh. which allows to mark or refine cells inside or outside a specified range of a selected field variable function.

We will observe the effect of refining the mesh on the flow results. And we will stop the process until the number of cells changes will be equal to 0 which means that the result of the study is independent of the mesh and so the temperature will remain the same for more cells number. And because we are interested in the temperature evaluation in our study, we chose to refine the mesh where the gradient of temperature is important. The first is the default defined by Automatic Mesh Sizing. Each Adaptation contains mesh refinements based on the previous results field.

3.4.3.1.1 Lob sphere grid independence study

The table below compares the different maximum values of the temperature of the fluid for the five different densities of meshes.

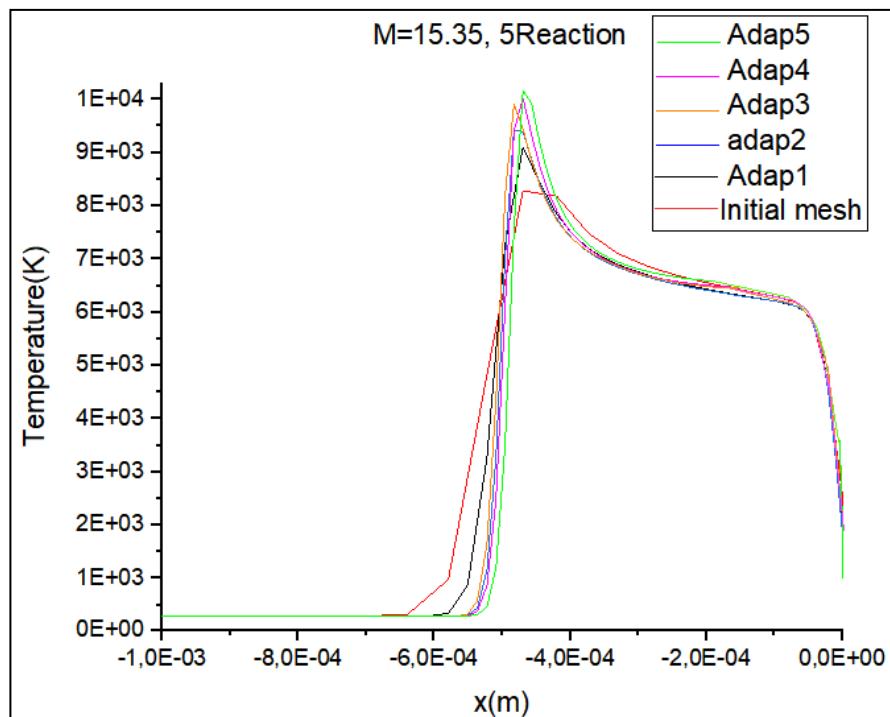
Table 3.6: Lobb sphere grid independency

Adaption	Initial	Adption1	Adaption2	Adaption3	Adaption4	Adaption5
Cells	2500	4858	10570	25146	80974	129963
Noeuds	5601	7054	15990	11575	37546	89125
T(K)	8743.415	9193.686	9691.146	9808.36	10130	1028

We notice on table 3.6, that, the less dense mesh (2500), the maximum value of the temperature of the flow is weak compared to the two denser meshes (41753 and 141500). we have adapted the mesh until the number of cells changed became 0.

The sensitivity test with respect to the mesh was performed for five different mesh densities, by comparing the flow temperature profiles under the same boundary-Axis_symm line- so that we can notice the maximum value of the temperature just behind the shock and the distance of the relaxation zone. The figure 3.43 shows that for the initial mesh the temperature varies from a minimum value of the free stream temperature to a maximum value of 8000k in a distance of 0.05m. The Temperature profiles shows that every time we adapt the mesh, the maximum temperature increases while the relaxation distance decreases from adapt 1 until it became invariable in adapt 5 to a temperature of 10130 in a distance less of 0.02.

The result become independent of mesh from adapt 4 cause the variation of temperature is no longer observed during the refinement, so we can consider that the “adapted 4 mesh” is the optimum mesh where the temperature result is stable even if we refine the mesh more and



more.

Figure 3.43: Lobb sphere grid independency

3.4.3.2 Delta profile grid independency

Always by the same reffinement methode, the sensitivity test with respect to the mesh was performed for five different mesh densities (table 3.7). we notice that the result become independent of mesh from adapt 4 because the variation of temperature is no longer observed during the refinement in figure 3.44, from adapt 4 with a temperature of 7684.52k to adapt 5 with temperature 7983.87k so we can consider that the “adapted 4 mesh” is the optimum mesh.

Adaption	Initial	Adption1	Adaption2	Adaption3	Adaption4	Adaption5
Cells	11200	26869	51690	74685	81526	129963
Noeuds	11480	27461	53471	75584	82679	13010
T(K)	4547.27	5147.56	6045.12	7145.61	7684.52	7983.87

Table 3.7 : delta profile grid independency

3.4.3.3 Delta body gride dependency

By the same manner, we adapt the delta body by refining the temperature gradient as shown if table 3.8. In this case, the result become independent from the mesh from adapt 3 where the variation of temperature is no longer observed in figure 3.45 during the refinement, so we can carry out our result on “adapted 3 mesh” as the optimum mesh where the temperature result is stable even if we refine the mesh more and more.

Table 3.8: Delta body grid independency

Adaption	Initial	Adption1	Adaption2	Adaption3	Adaption4
Cells	14708	42400	141326	487133	575384
Noeuds	30222	23094	75608	26081	30069
T(K)	6863.415	7143.666	8091.16	8296.87	8443.74

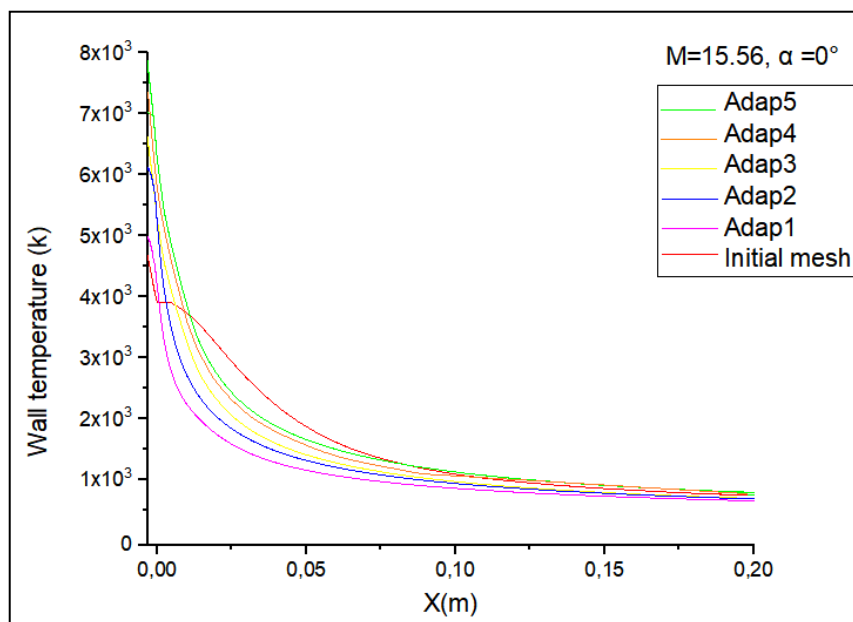


Figure 3.44: Delta profile gride independency

The sensitivity test with respect to the mesh was performed for four different mesh densities, by comparing the flow temperature profiles under the same boundary-Axis_symm line- so that we can notice that the results start be independent from the grid from adapt 3 while the temperature changed insignificantly from 8293.87k to 8443.74k for adapt 3 to adapt 4 respectively.

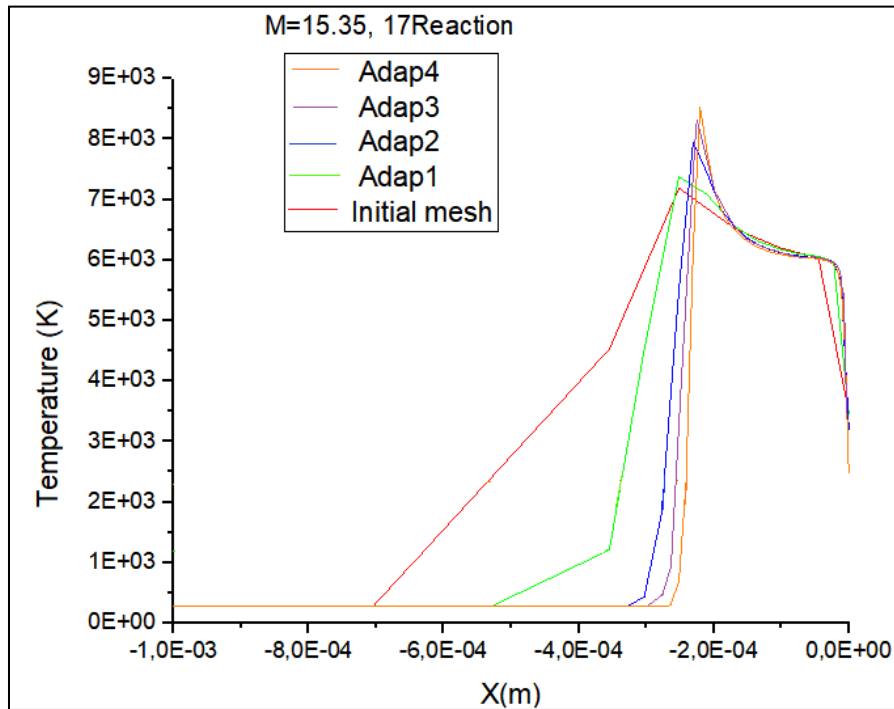


Figure 3.45 : delta body grid independency

3.4.3.4 Conical body grid independency

The sensitivity test with respect to the mesh was performed for four different mesh densities, so we can notice from figure 3.46 that the results start be independent from the grid from adapt 3 while the temperature changed insignificantly from 814789k to 14959k for adapt 3 to adapt 4 respectively.

Table 3.9 : cone-flare body grid independency

Adaption	Initial	Adption1	Adaption2	Adaption3	Adaption4
Cells	15302	40703	151635	151172	572744
Noeuds	9323	35498	29854	110535	378518
T(K)	6863.415	7143.666	8091.16	14789	14959

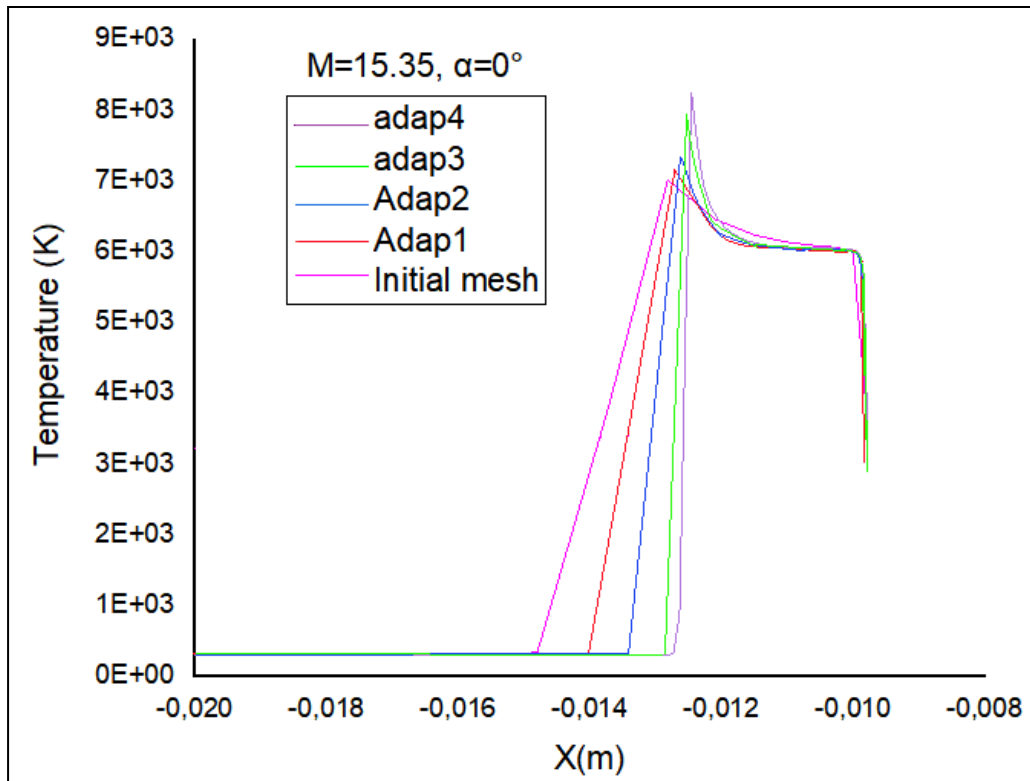


Figure 3.46: Cone-flare body grid independency

Turbulence model independency:

We used the $k-\omega$ SST turbulence model which is the appropriate model to deal with the small viscous distance between the wall and the shock wave. So, to ensure the good precision in the determination of the proprieties of the boundary layer which is a small viscous area we have ensured that y^+ is less than 5 far from the wall and less than 1 in the zone close to the wall for our deferent geometries as shown in figures (3.47-51).

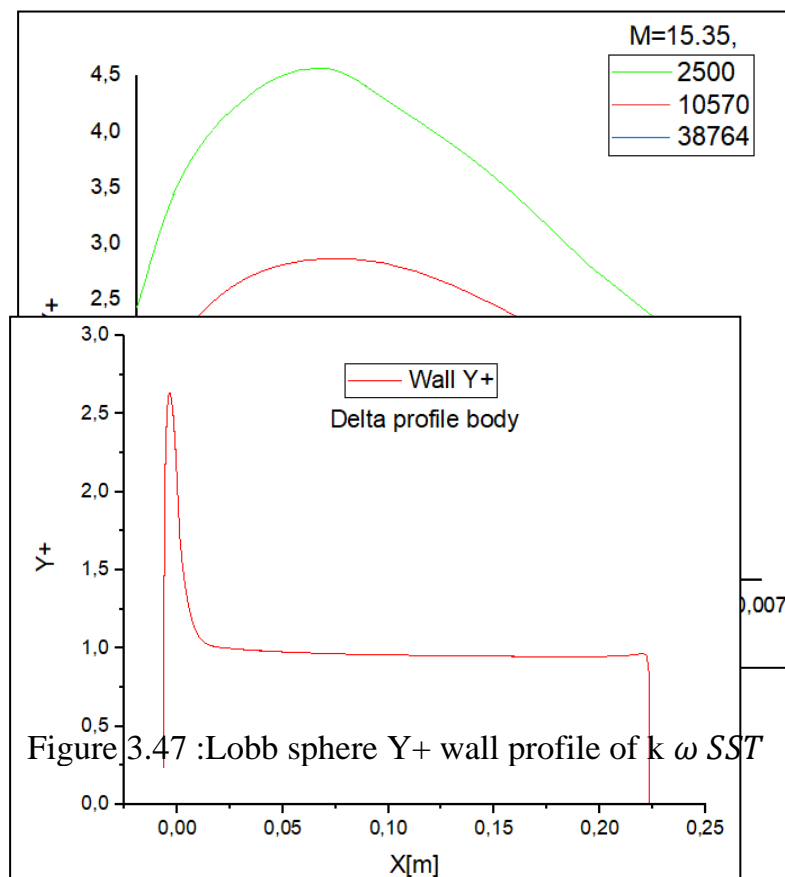


Figure 3.47 :Lobb sphere Y^+ wall profile of $k-\omega$ SST

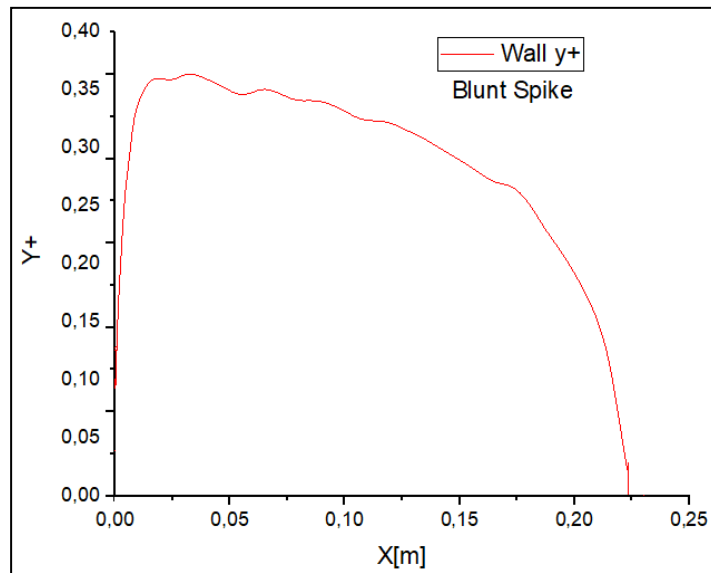


Figure 3.48: Delta profile Y^+ wall profile of $k-\omega$ SST model

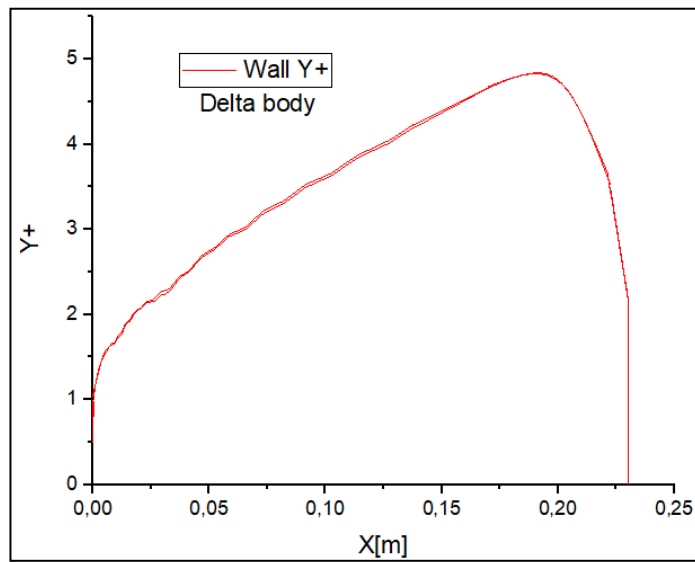


Figure 3.49: Blunt spike Y^+ wall profile of $k-\omega$ SST model

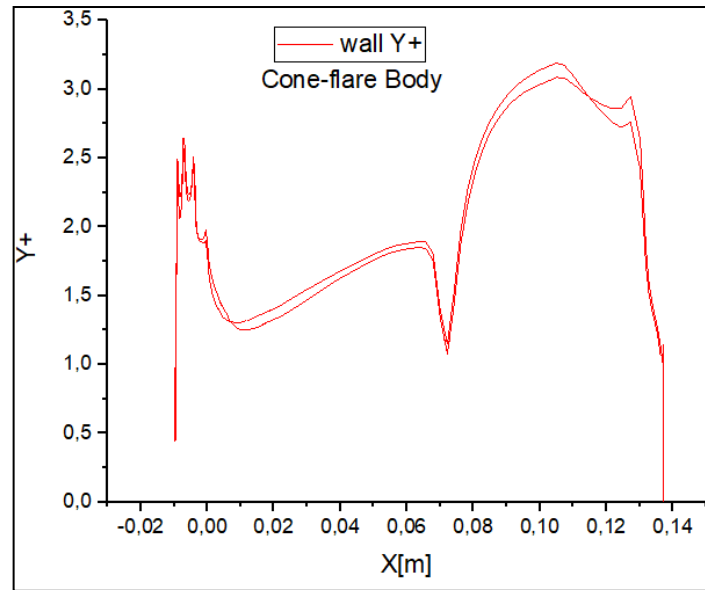


Figure 3.51 :Cone-flare Y+ wall profile of k ω SST model

3.5 Conclusion

Our main object in this chapter was to perform a simulation of a hypersonic chemical non-equilibrium flow under the ANSYS environment. First, we presented the simulation software used (ANSYS software), geometry and mesh were studied for every signal body, specifying the main steps followed under the Fluent calculation code. It should be noted that the methods of the numerical solution cited previously for example the stability, the convergence are all controlled and checked during our simulations made. Finally, we presented the last step of our CFD process, i.e., the grid dependency and turbulence model verification. In the next chapter, we will present the results obtained during the simulation around various geometries studied and validating them by comparison with the scientific literature.

Chapter 4

Results and Discussion

4.1 Introduction

Re-entry mission requirement affects the vehicle design. Deceleration, heating and accuracy are the major parameters that affect the trajectory which are driven by the design. So as an aerospace engineer our work is to trade-off between the trajectory and the vehicle design until we reach some compromise vehicle that satisfies mission requirements.

We used Ansys fluent simulations to balance all the competing mission requirements by approaching them on two broad fronts

- Thermochemical non equilibrium effect around blunt body
- Trajectory design, which includes changes to
 - Re-entry flight-path angle, γ
 - Re-entry altitude
 - Re-entry Velocity, $V_{re-entry}$
- Vehicle design, which includes changes to
 - Vehicle shape

Trajectory design involves the vehicle's velocity as it enters the effective atmosphere which defines the re-entry initial conditions. The vehicle design improves the vehicle's shape to modulate the drag force

In this chapter, we present:

- ✓ Lobb sphere blunted nose to study the thermochemical nonequilibrium effect in re-entry hypersonic flow
- ✓ The delta profile to study the trajectory design
- ✓ The delta body to study the vehicle design of a reusable re-entry vehicle (lifting body) compared with a conical body which represents a ballistic vehicle.

4.2 Thermochemical nonequilibrium flow study

4.2.1 Change in Mach number of flows after shock

Figure (4.1) represents the iso-Mach contours shows a drop in Mach number just after the shock wave which reaches a value less than unity because the flow is perpendicular to the wall so in this area the shock is considered to be a normal shock wave where the flow becomes subsonic downstream.

While there is a creation of an oblique shock wave in the other parts around the sphere, the downstream Mach number is not necessarily less than unity.

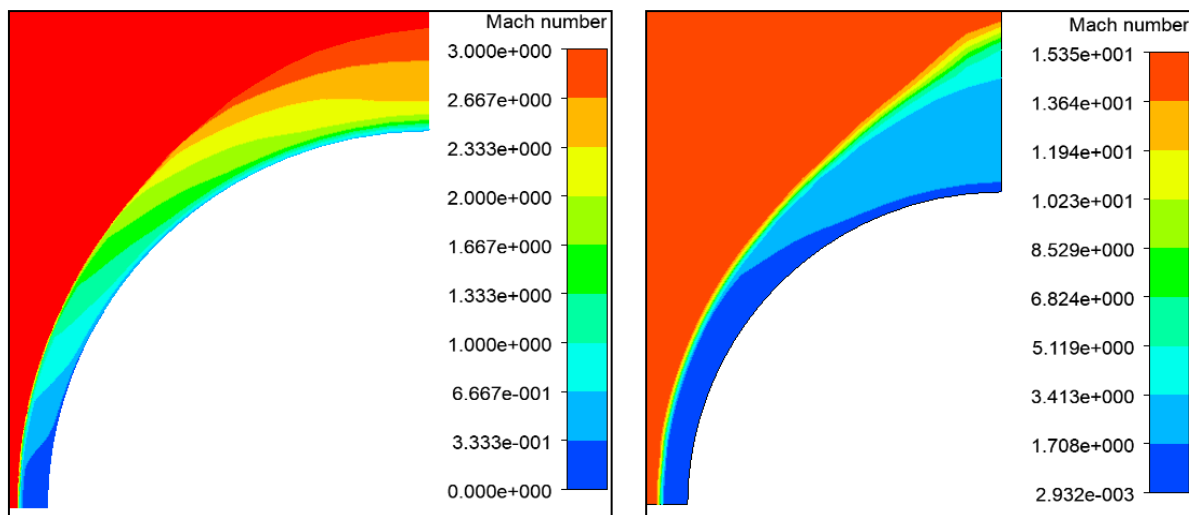


Figure 4.1 - Variation in Mach number through the shock wave

4.2.2 Change in flow temperature after shock

The high kinetic energy in the flow interacts with the surface of the vehicle and the kinetic energy transforms to thermal energy, forming a strong bow-shaped shock wave in the fore body of the vehicle. Figure (4.2) shows the normal shock wave formation in front of the body. The shock wave formation compresses and slowdown the hypersonic upstream flow suddenly to a subsonic regime, there the molecules kinetic stored energy transforms to thermal energy by colliding intensively among themselves causing the abrupt temperature rise from 293k free stream temperature to 10130k.

The maximum temperature behind the shock decreases until it reaches the equilibrium temperature of approximately 6000K in a distance of 0.50 mm. the appearance of the reactions of dissociation and exchange in the shock wave (chemical phenomena) which are endothermic phenomena, molecules absorb energy to recombinant or to break the links between them which cause a decrease in temperature to the wall by approximately 40% it's maximum value.

During this process, because the number of collisions required to reach equilibrium in the translational and rotational relaxation is fer less than that required for the vibrational equilibrium, the translational and rotational relaxation time is much shorter than the vibrational relaxation time. [48]

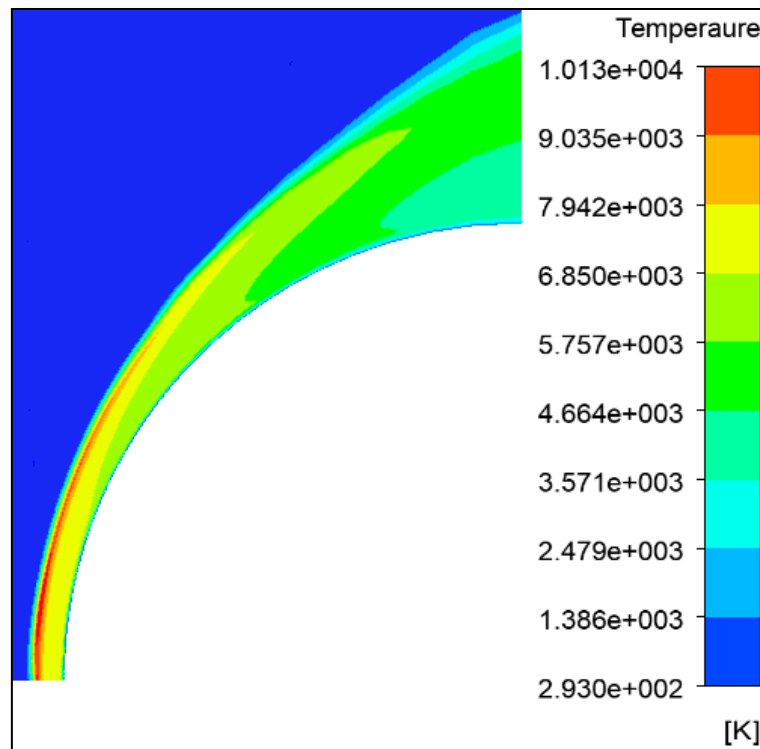


Figure 4.2 - Temperature field variation across the shock wave in the non-equilibrium flow

❖ Validation:

By comparing our result of figure (4.3) with that of Tristan [49] which shows the variation of the temperature along the relaxation range, one notices a good agreement between the two results in terms of pace and in quantitative term.[40]

The slight difference is due to the fact that Tristan [49] considered a flow out of vibrational equilibrium. As vibrational relaxation is no longer instantaneous, its energy contribution is weaker. This lost energy is found in the form of temperature and in the form of kinetic energy; this is why the temperature of the mixture is higher and the shock moves away from the obstacle compared to the case of vibrational equilibrium.[19]

Table 4.1 illustrates that this result agrees well with the experimentally determined value with an error of 2.89% [50] and the numerical values obtained in the literature [51, 52, 53].

Tab. 4.1: Position of the shock of the Lobb sphere

Source	Shock position [mm]
Present results	0.536
Tristan	0.535
Tchuen	0.531
Joly et al	0.598
S'error	0.557
Lobb	0.552±0.032

of the shock of [49]

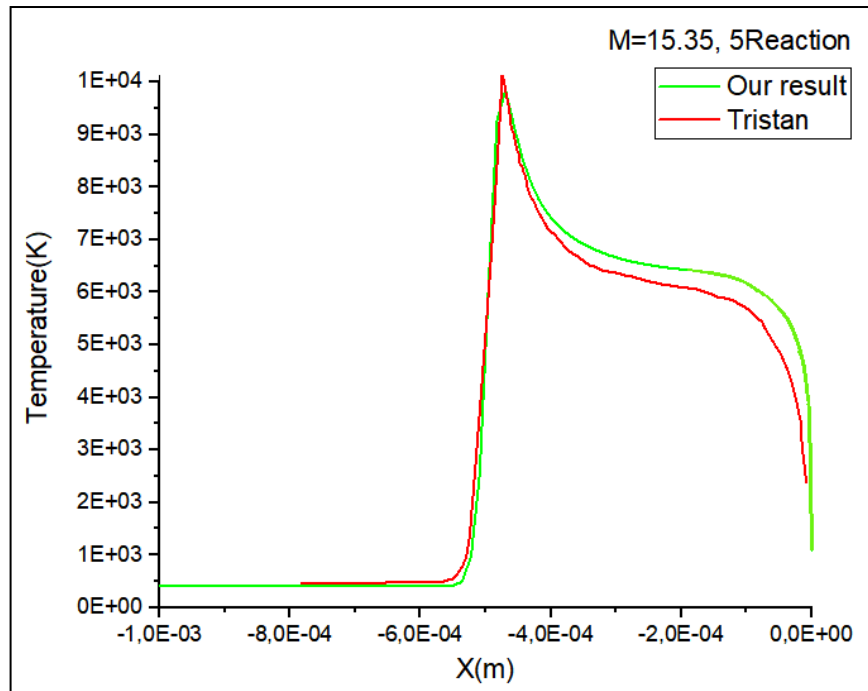
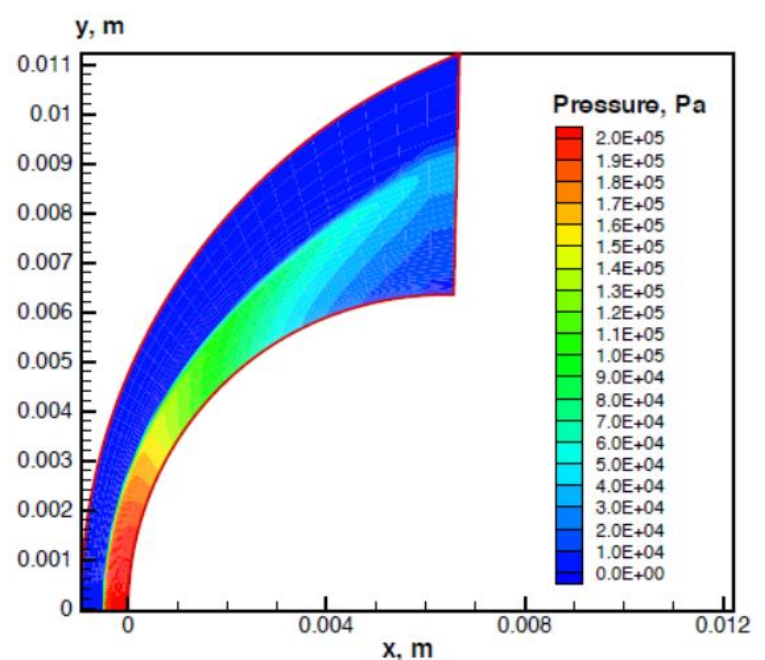
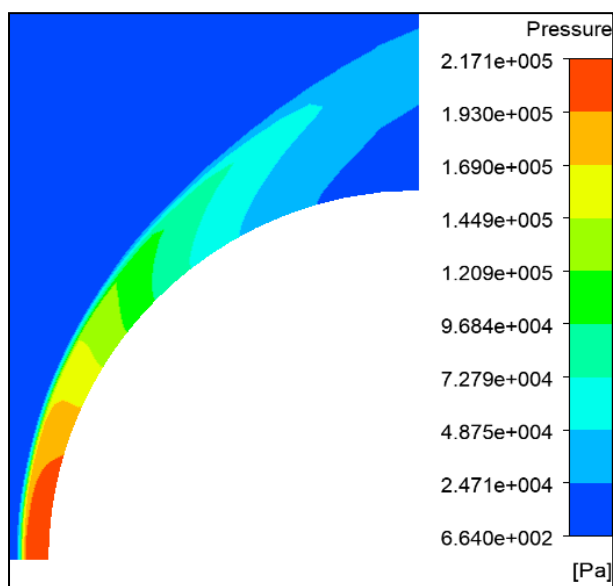


Figure 4.3: Temperature along the stagnation ling

4.2.3 Pressure field variation

The detachment shock is clearly obvious on the pressure field, the temperature increases gradually before it reaches its maximum value 20000Pa due to the compression waves created because of the abrupt deceleration from hypersonic to subsonic regime by the normal shock as describe earlier. The pressure decreases in the relaxation zone in parallel with the temperature due to endothermic phenomena.

Again, comparing our results in figure (4.4) with that of Tristan in figure (4.5), one can notice an excellent similarity with a slight error of 8.55%. between the two results for the different isobar zones in the relaxation zone.



4.2.4 Mass fractions of species

As mentioned before, the nitrogen molecule starts to dissociate at around 4000 K and the oxygen molecular at 2000K. It is apparent that with increasing temperature, the degree of dissociation increases. Crossing the shock in the post-shock region these two endothermic components start to dissociate and therefore non-existent species appears, which are nitrogen and oxygen atoms as well as nitrogen monoxide.

The characteristic temperature of the O₂ molecules is twice lower than of N₂ molecules what explain the dissociation of oxygen molecules at more than 95% while nitrogen molecules dissociate at less than 10% of their respective values at infinity upstream.

The disappearance of the O₂ and N₂ molecules makes the O and N molecules appear parallel and this is well represented and noticed by the curves figure (4.6), that the formation rates of O and N are almost equal to the disappearance rates of O₂ and N₂ respectively but opposite in signs. In addition, the dissociated nitrogen atoms recombine to produce molecular nitrogen, atomic nitrogen interacts with oxygen molecules and the "Tristan [20]" relaxation range, recombination reactions releasing energy appear as can be shown in figure (4.8).

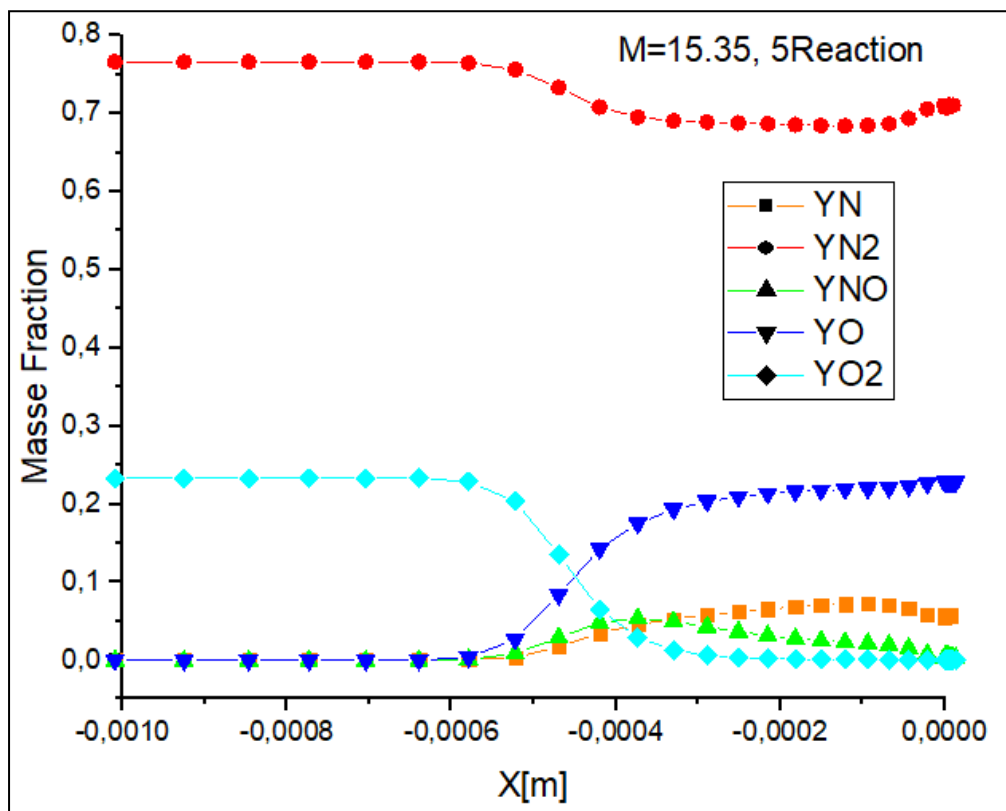
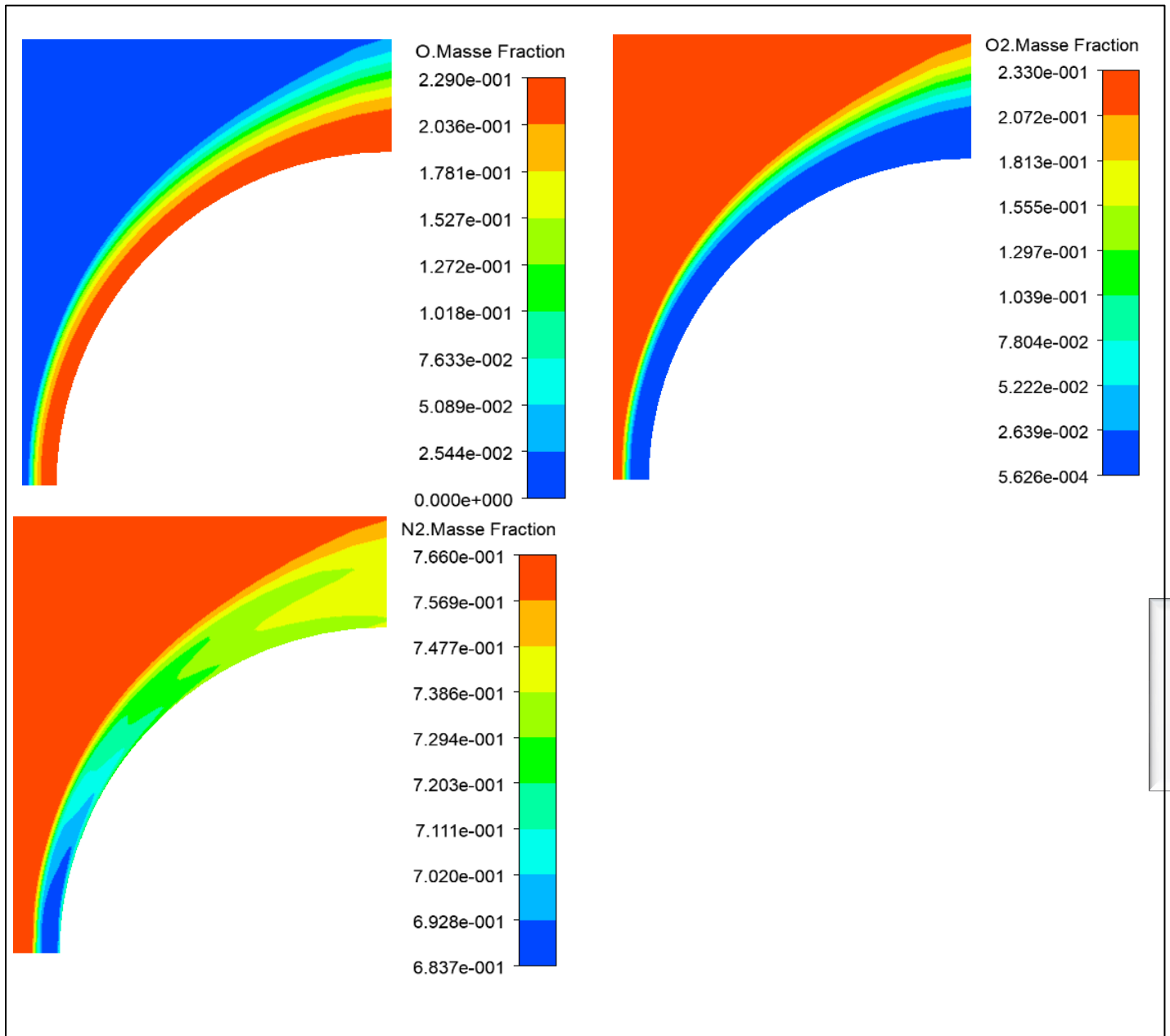


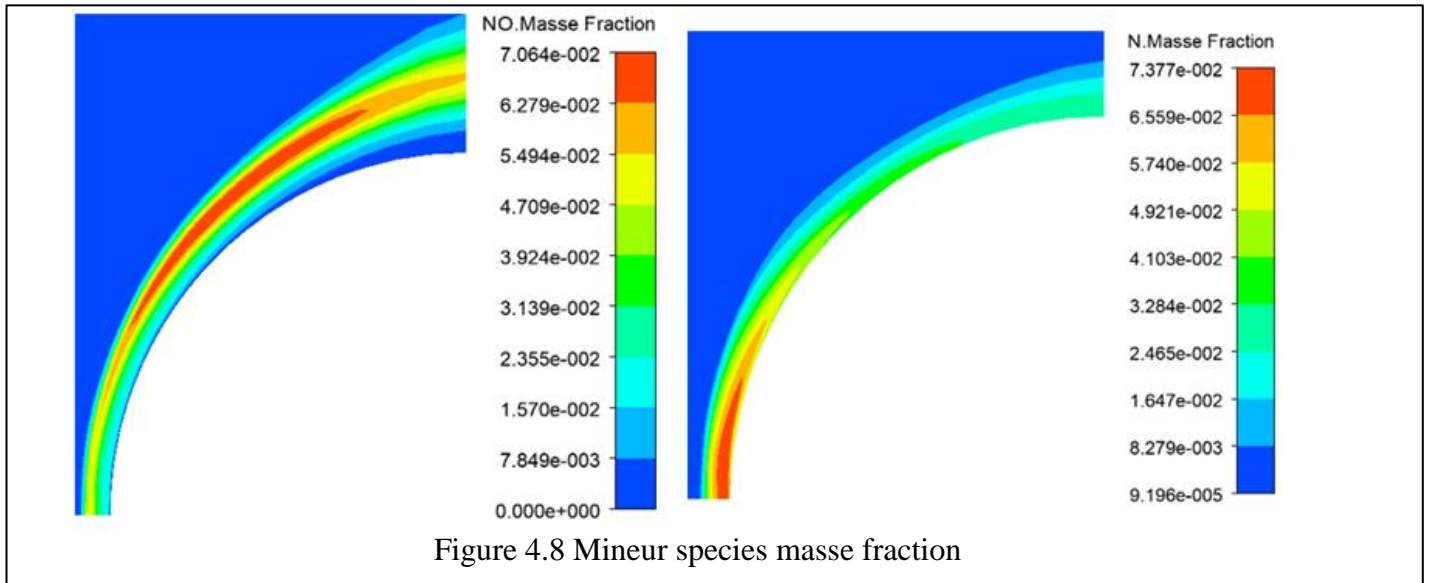
Figure 4.6: The mass fractions of the species along stagnation line

Nonetheless, it can be seen that nitrogen does not dissociate completely, although the temperature was as high as 10130 K, it was not sufficient to dissociate all the molecules. This

is primarily due to the high degree of thermal non-equilibrium, yielding an insufficient number of collisions for full dissociation.[28]



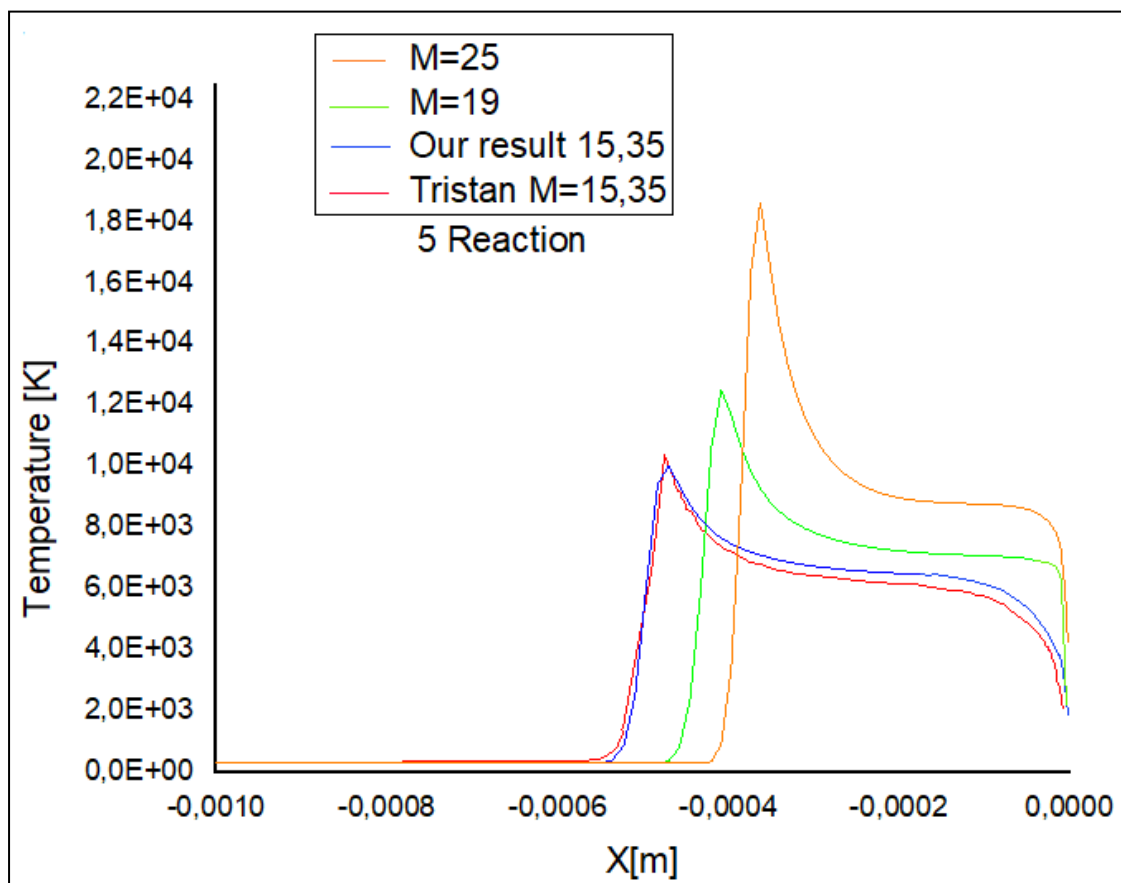
Fig



4.2.5 Mack number effect:

At 25 Mach number, it was observed that the maximum temperature in the flow field reaches 17 000 K. However, the shock standoff distance is the shortest as shown in figure (4.9), because the wave compression is done more quickly compared to 15 and 19 Mach numbers (figure 4.11) and therefore the temperature just after the shock is the highest (figure 4.10).

Because the characteristic time of dissociation is less than the recombination time and from figure (4.9), we notice that the relaxation zone decreases for high Mach numbers this allows the appearance of N and O masse fractions only (figure 4.12,16) due to the short reaction time which explain the important dissociation process (figure 4.13,15) counter to the recombination process which increases for low Mach numbers as shown in figure (4.14) for



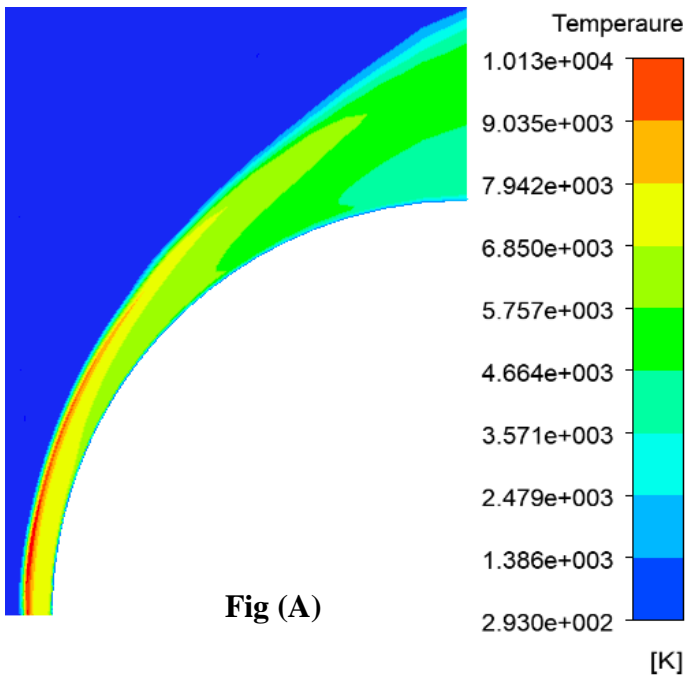


Fig (A)

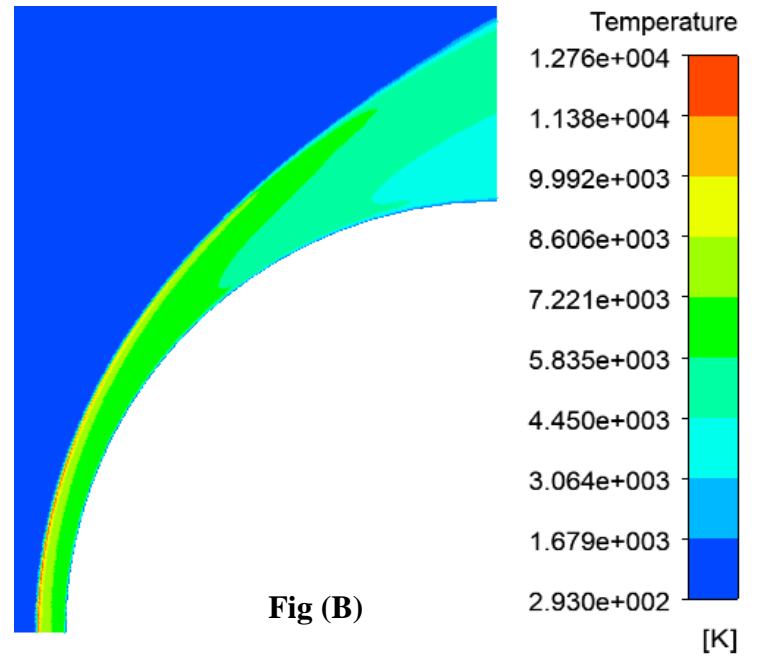


Fig (B)

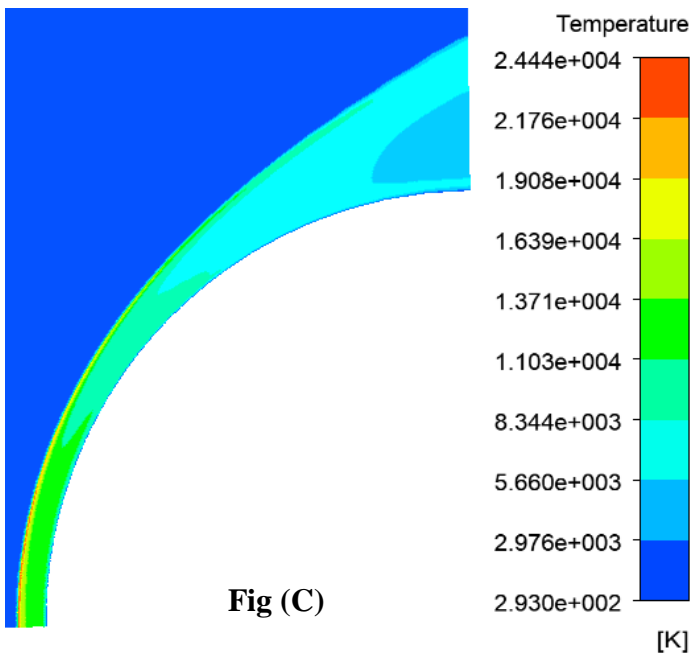


Fig (C)

they have the available time to recombined.

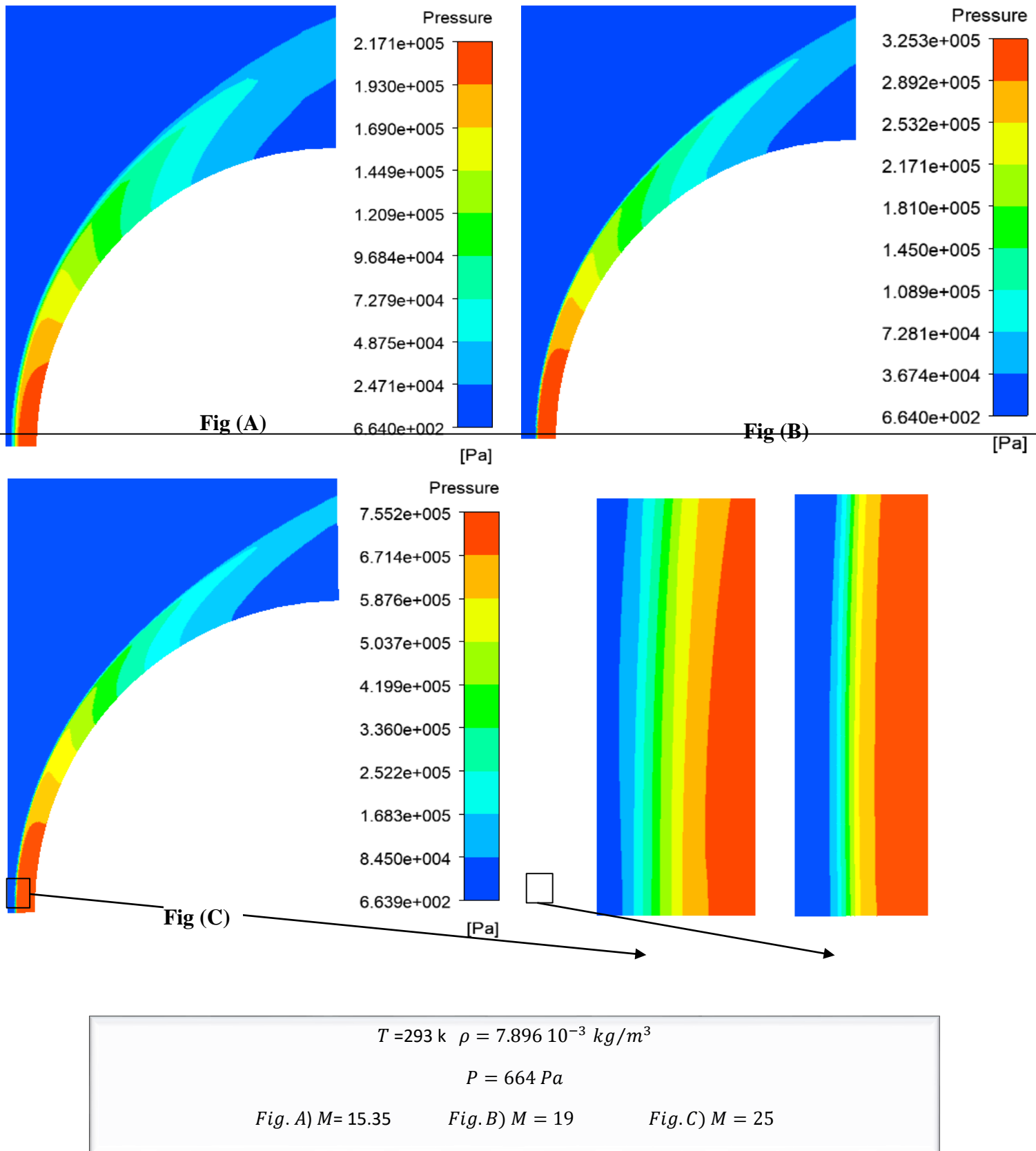


Figure 4.11: Pressure field around the sphere at deferent Mach numbers

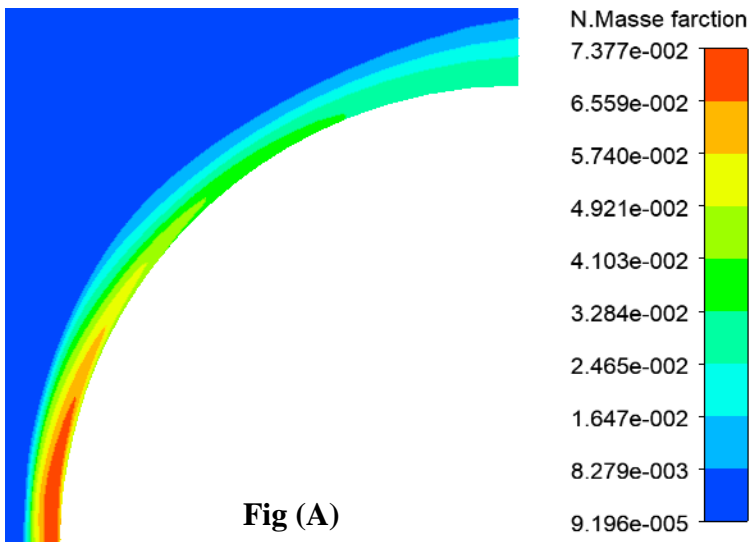


Fig (A)

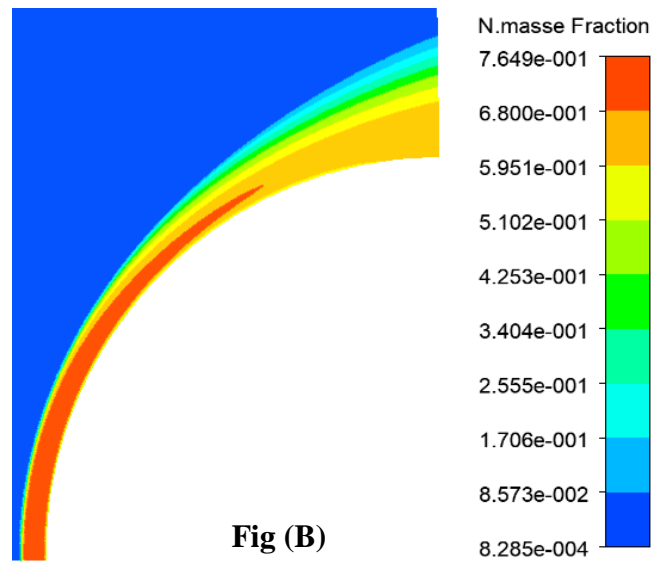


Fig (B)

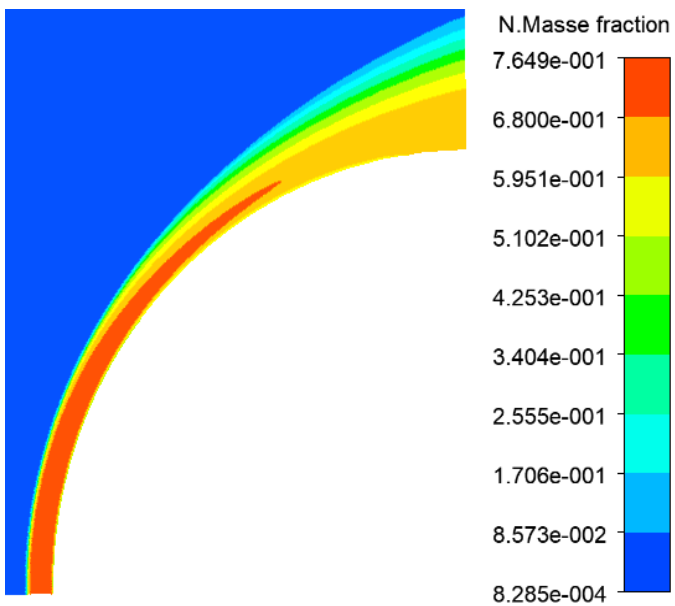


Fig (C)

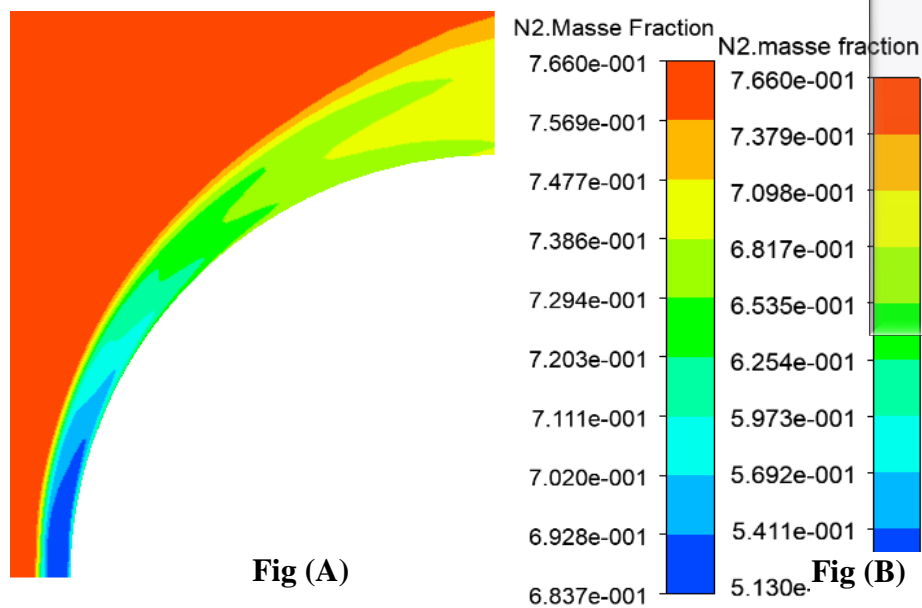


Fig (A)

Fig (B)

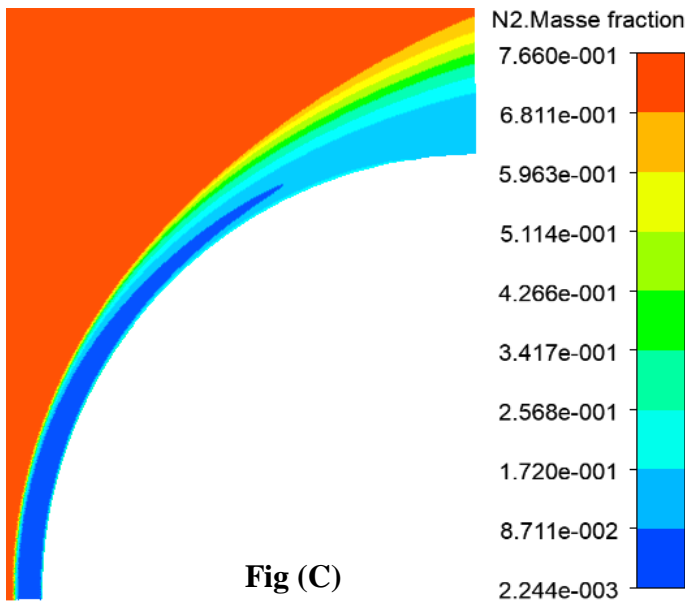


Fig (C)

$T = 293 \text{ k}$ $\rho = 7.896 \cdot 10^{-3} \text{ kg/m}^3$

$P = 664 \text{ Pa}$

Fig. A) $M = 15.35$

Fig. B) $M = 19$

Fig. C) $M = 25$

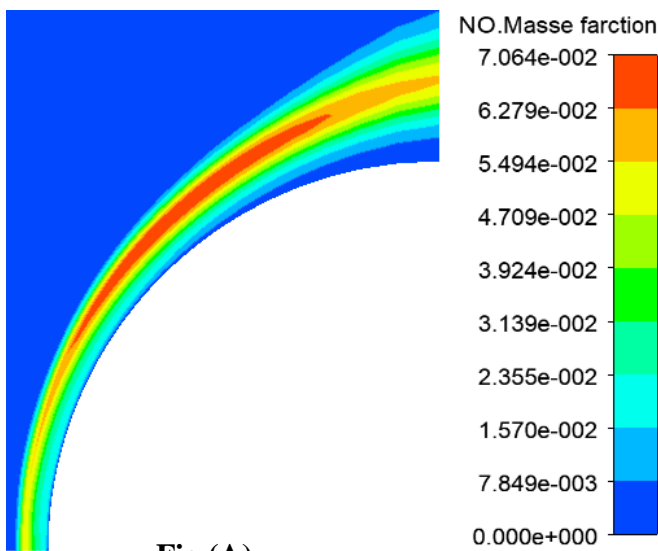


Fig (A)

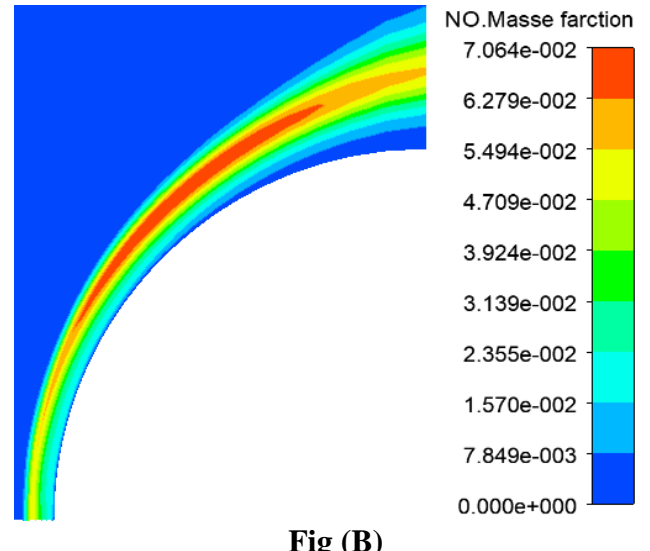


Fig (B)

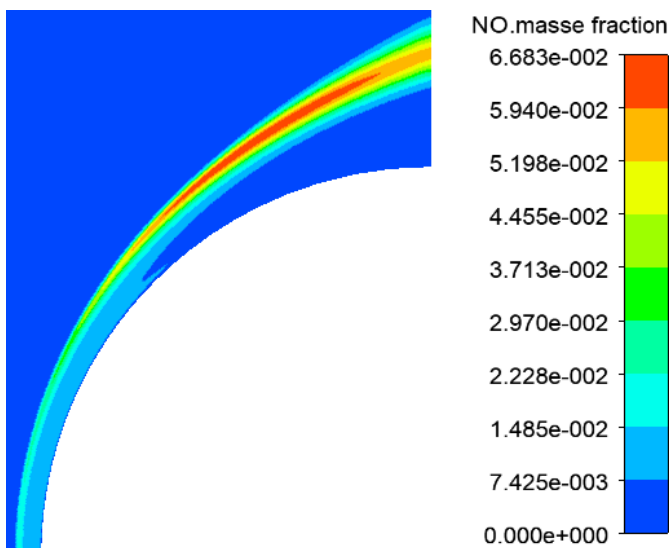


Fig (C)

$T = 293 \text{ k}$ $\rho = 7.896 \cdot 10^{-3} \text{ kg/m}^3$

$P = 664 \text{ Pa}$

Fig. A) $M = 15.35$

Fig. B) $M = 19$

Fig. C) $M = 25$

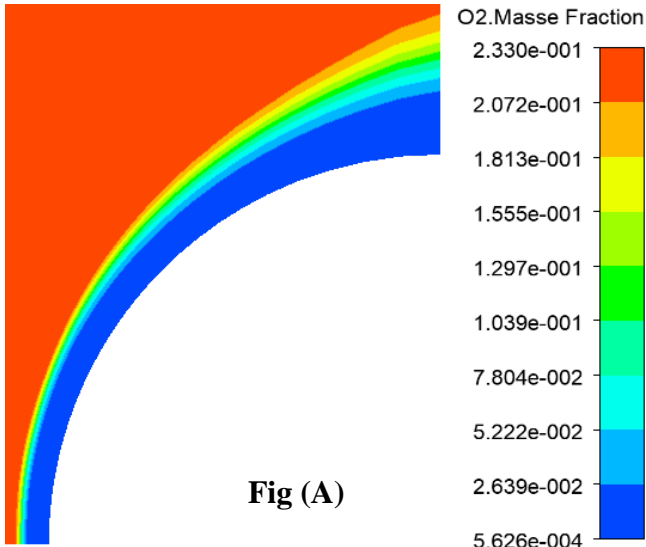


Fig (A)

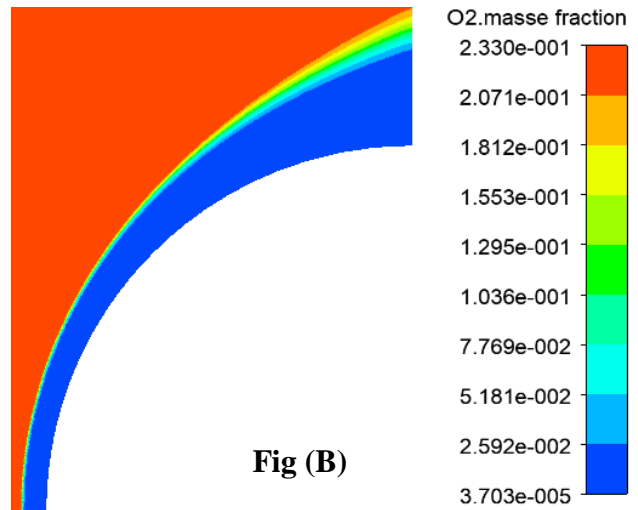


Fig (B)

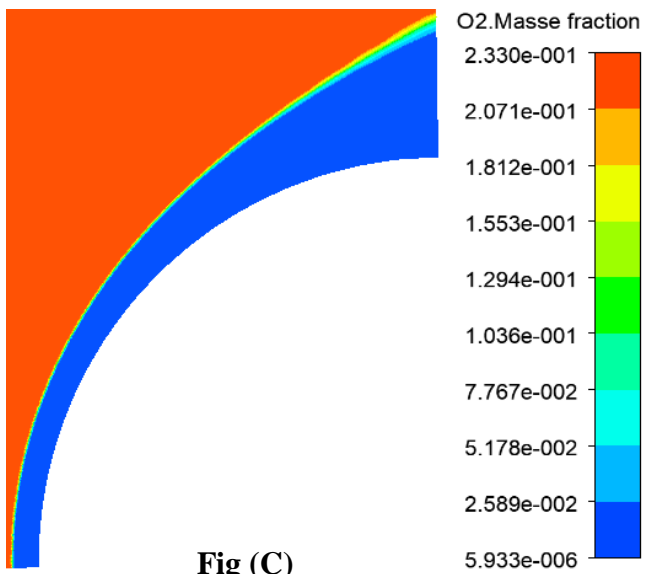


Fig (C)

$T = 293 \text{ k}$ $\rho = 7.896 \cdot 10^{-3} \text{ kg/m}^3$

$P = 664 \text{ Pa}$

Fig. A) $M = 15.35$

Fig. B) $M = 19$

Fig. C) $M = 25$

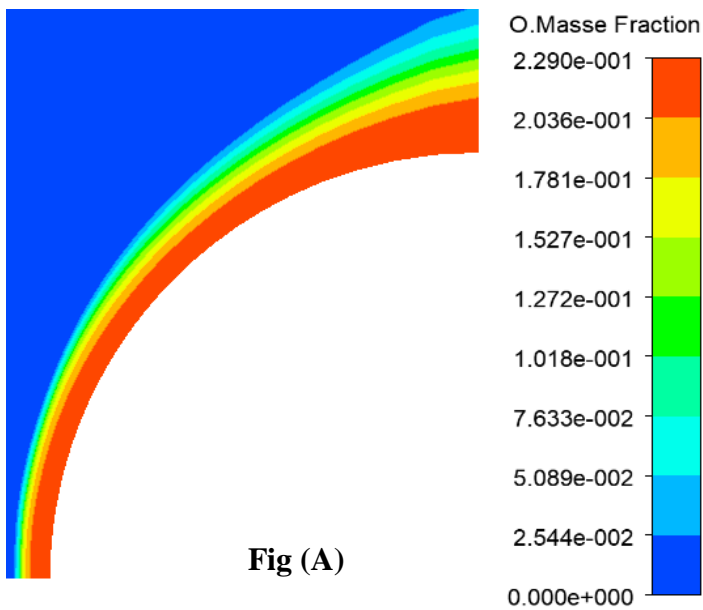


Fig (A)

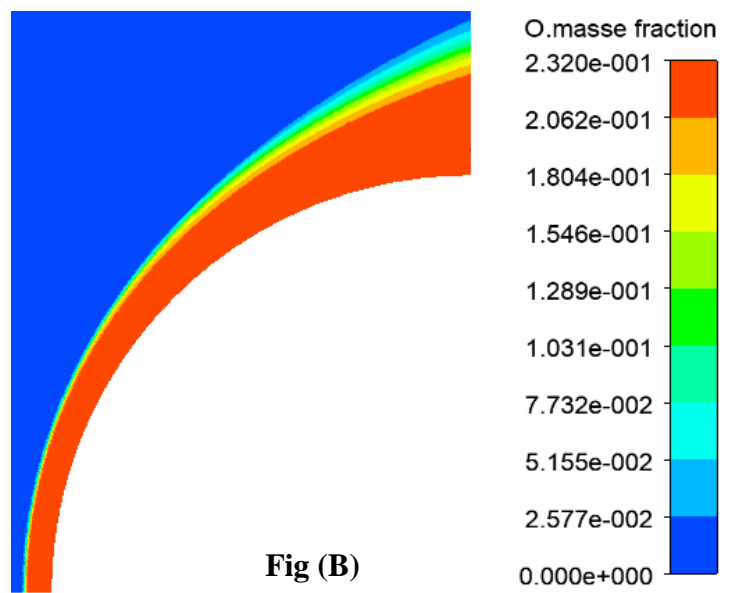


Fig (B)

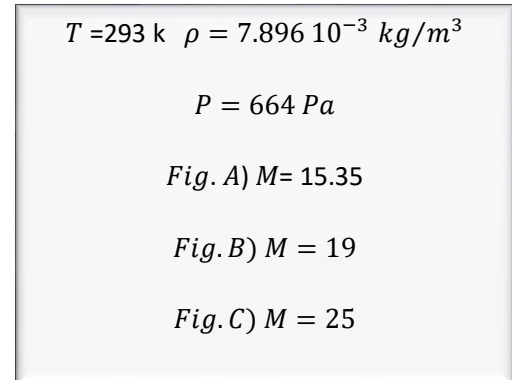
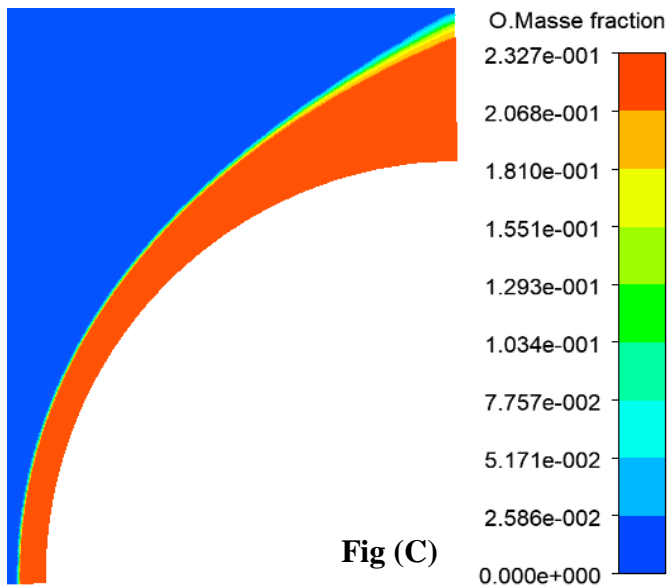
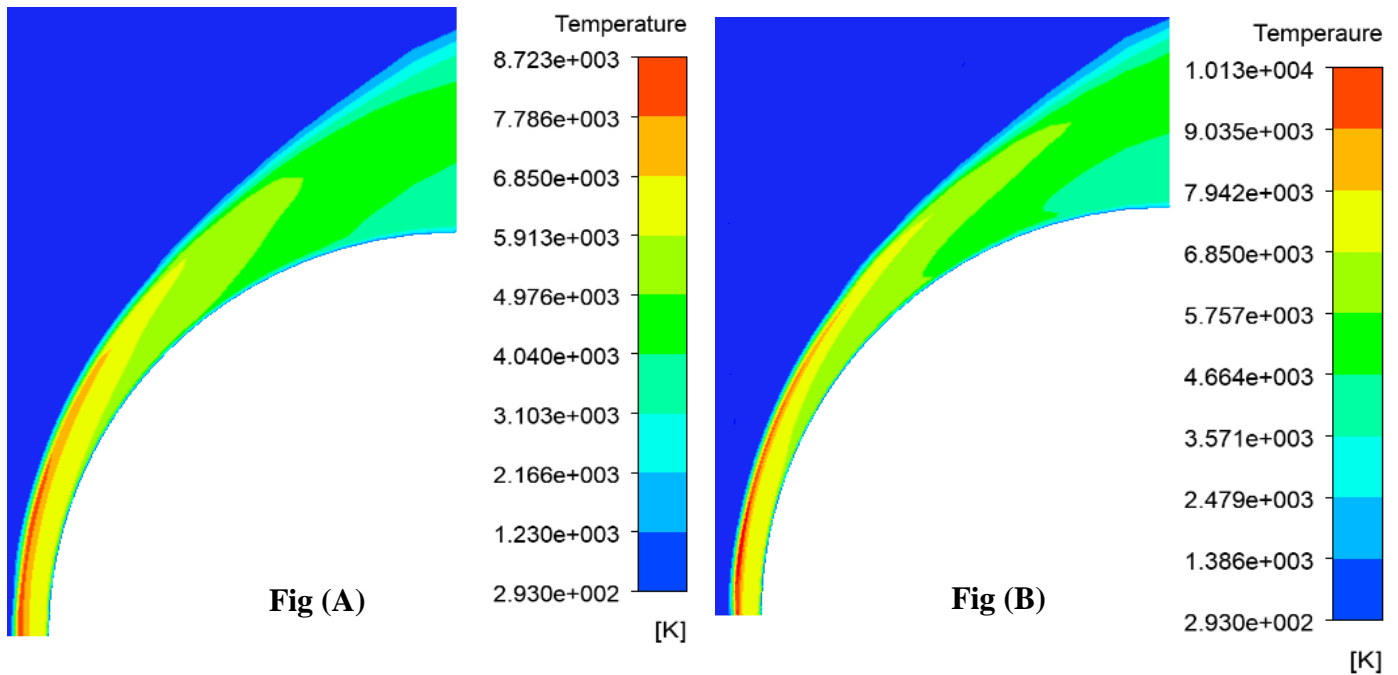


Figure 4.16: Mass fraction of O around the sphere

4.2.6 Effect of chemical model

The 17 reactions kinetic model decreases the maximum temperature by 12.5% compared to the 5 reactions kinetic model, this is due to the presence of a catalyst in the 17 reactions model, there are a greater number of effective collisions than in the absence of a catalyst (5 reaction kinetic model) at the same temperature because a catalyst accelerates the reaction by providing a new path way involving lower amount of activation energy, that what explain the decrease in temperature in the 17-reactions model more as shown in figure (4.17).[54]



4.2.7 Computational domain effect

While doing our simulations we noticed something interesting upon the control volume, the formation of the shock wave in front of the blunt shape depends on the control volume, we notice from figure (4.18) that the shock wave compressed just in the normal part of the nose whereas when the geometry is not limited by the control volume the shock propagates and curved along with the nose.

We supposed that this is right only if our study is limited in the relaxation region and at a high Mach number where the reflected flow will not be affected by the high flow velocity.

Figure 4.17: Temperature distribution:

Fig(A): 5 reactions model, Fig(B) :17 reactions model

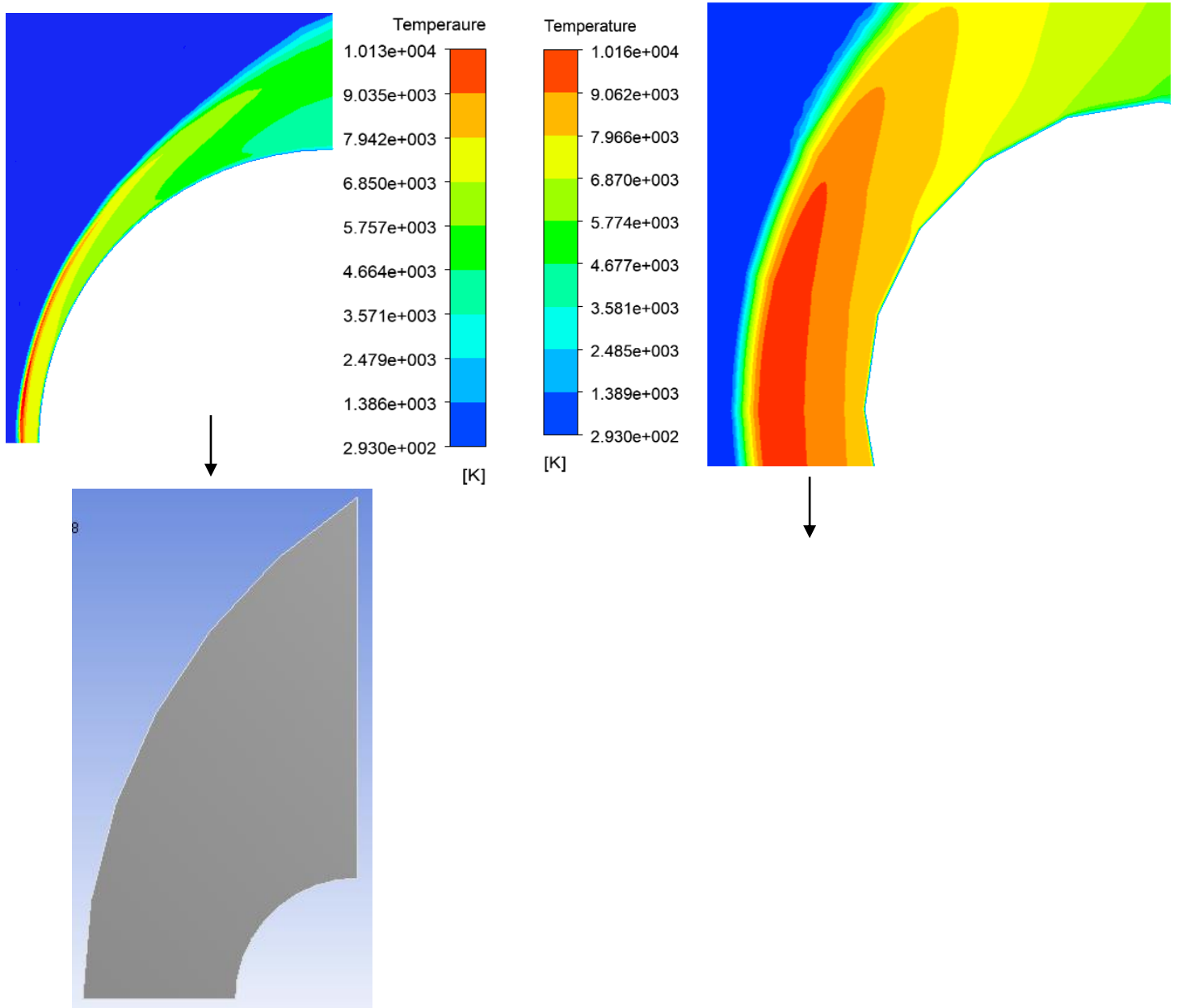


Figure 4.18: computationnel Domain effect

4.3 Delta profile

From our re-entry vehicle simulation, we can plot wall temperature, along the vehicle wall for various chemical model, re-entry velocities, flight path angle and altitude in order to study the trajectory design of lifting body.



Our ability to accurately calculate this heating is limited by uncertainties in the heat transfer coefficient for the atmospheric re-entry phase. The familiar form which is dependent on the free-stream Reynolds number scaled by the nose radius to calculate the convection which is given as follow (equation 4.1).[75][51][52] The equivalent expression for St is:

$$St_{High\ speed} \approx 1.57 \sqrt{M_\infty / Re_{(r_{nose})}} \quad (4.1)$$

Were,

$$Re_{(r_{nose})} = \frac{\rho_\infty v_\infty r_{nose}}{\mu_\infty} \quad (4.2)$$

$$C_h = St \rho v_\infty C_p \quad (4..3)$$

The Equation 4.1 is an acceptable expression for estimating peak blunt-nose heat flux. Based on low densities on re-entry problems so radiant heating can be neglected

❖ Validation

By comparing our result of figure (4.19) with that of the article [41] which shows the variation of the temperature along body surface streamline, one notices a good agreement between the two results. The difference is due to the fact that John.Lourdi considered the ionization process which absorbed more heat in the post shock region than the dissociation considered in our case.

Due to the significant mass difference between electron and usual species, the magnitude of electron speed would be 4 to 5 orders higher than that of other species which will ionize important number of molecules in small time compared with the dissociation process and therefore absorb more energy in the post-shock region.

Density gradient in the y direction was used to describe a Schlieren photograph and reconfigured flow field as shown in figure 4.20

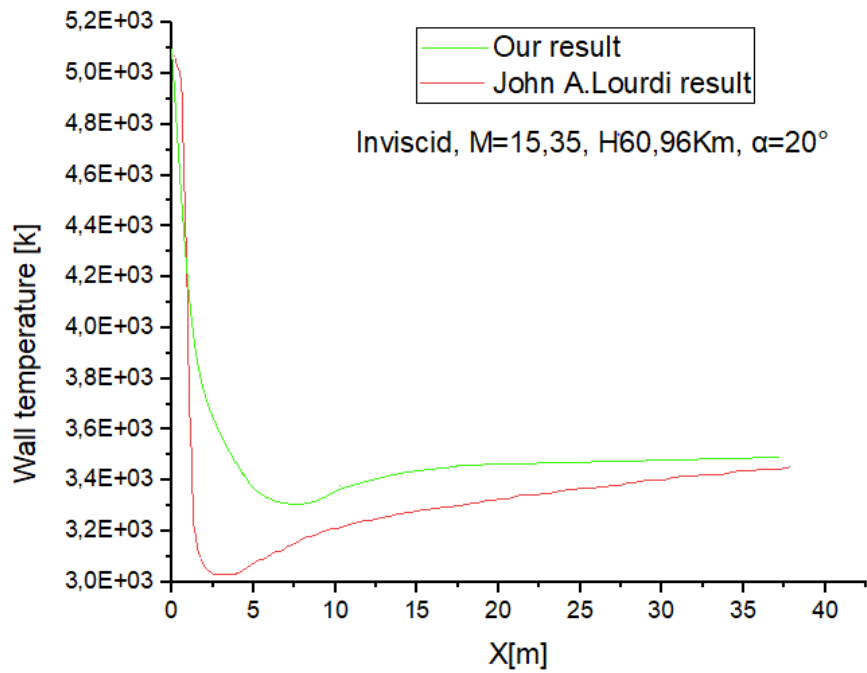


Fig. (a) $\alpha = 0^\circ$

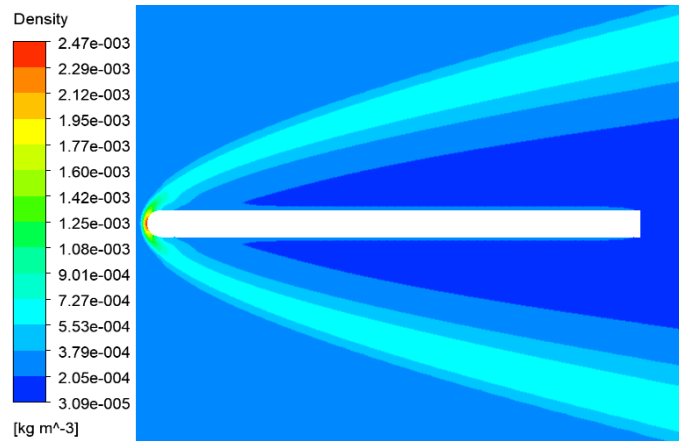


Fig. (b) $\alpha = 0^\circ$

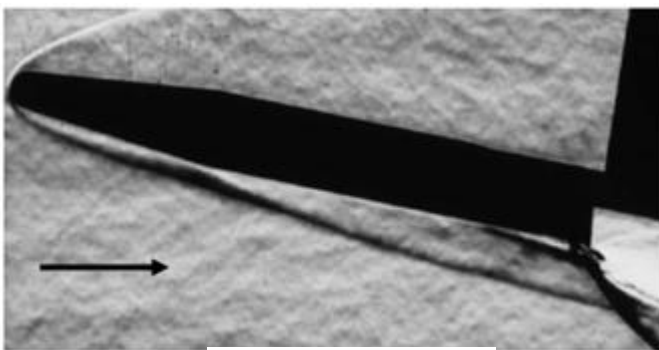


Fig. (a) $\alpha = 20^\circ$

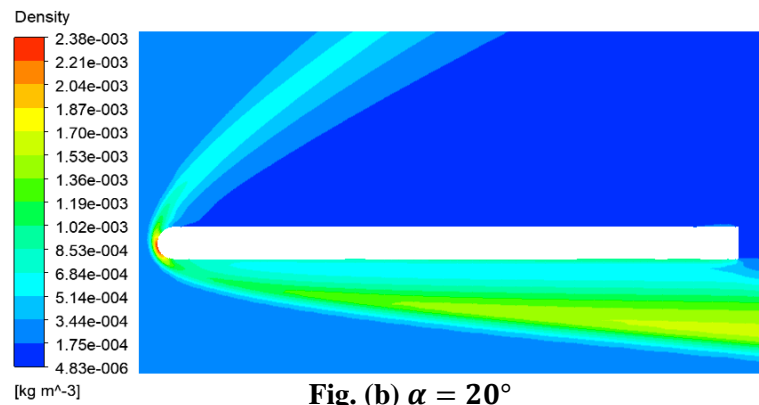


Fig. (b) $\alpha = 20^\circ$

Figure 4.19 – Temperature filed along outer streamline $\alpha = 20^\circ$.

Figure 4.20: Density gradient Fig (a) Schlieren experimental photograph, Fig(b) CFD simulation [58]

4.3.1 Chemical model effect

This time we studied the effect of the chemical reaction model in terms of wall temperature. As we have seen before, the chemical reactions decrease the maximum temperature by 28% from 12000K for the perfect gas assumption to 8600K for 17 reactions chemical model (figure 4.22), So the more molecules dissociate in the post-shock region, they will need more energy to break the links between them and so absorb more energy and heat, the endothermic process as mentioned in (§.4.2.2).

The convective heat load from the dissociation, as well as the energy released by atom recombination at the surface, are all thermal loads on a material sample. The low surface temperature, however, causes an increase in convective heat transfer to the vehicle as can be seen in Figure (4.21). The reason for this is that the low surface temperature increases the temperature gradient at the wall, which according to Fourier's law increases the convective heat transfer to the vehicle. The increase in the heat transfer is localized to a small region near the stagnation point where it's exposed directly to the intense shock wave. The 17-reactions case decrease the stagnation temperature by approximately 2000K compared to 5 reactions and perfect gas cases as shown in figure (4.21). The pressure decreases in their turn from a perfect gas to 17 reactions dissociated gas (Figure 4.23).

This shows that the choice of gas-phase reactions and the consideration of boundary recession have an effect on the flow field heat flow and wall temperature.[55] [56]

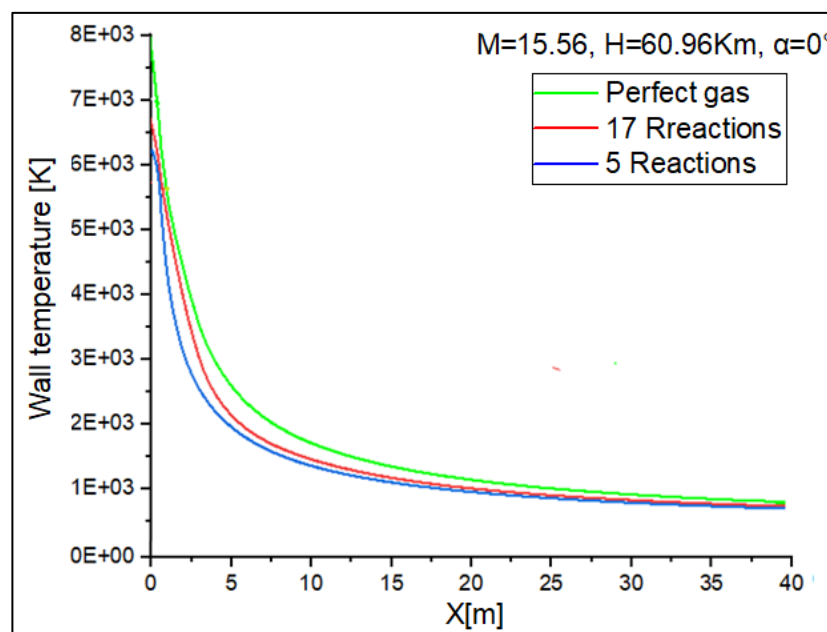


Figure 4.21: Wall temperature distribution along surface streamlines

The 17-reactions kinetic model is the model that decrease the wall temperature most. So, the next studies are all carried out in the 17-reactions kinetic model

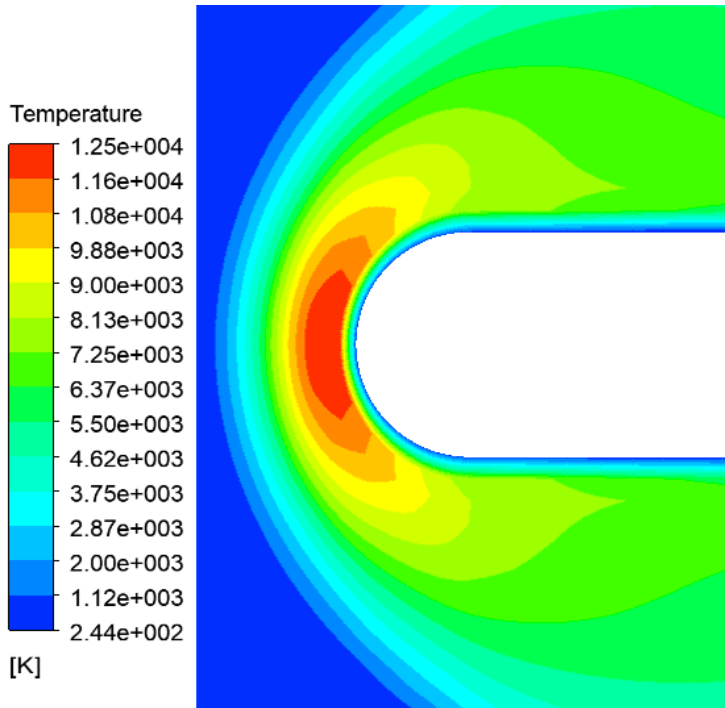


Fig (A)

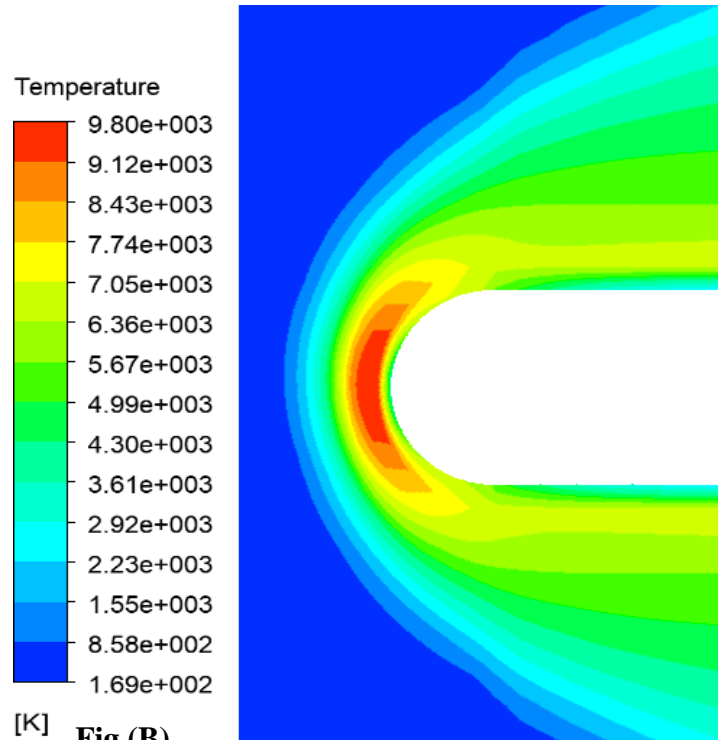


Fig (B)

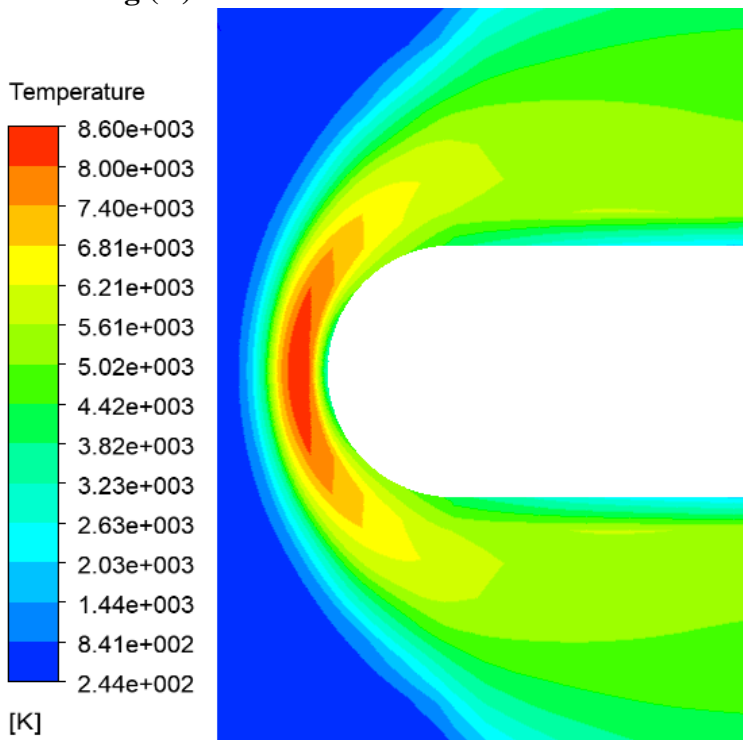
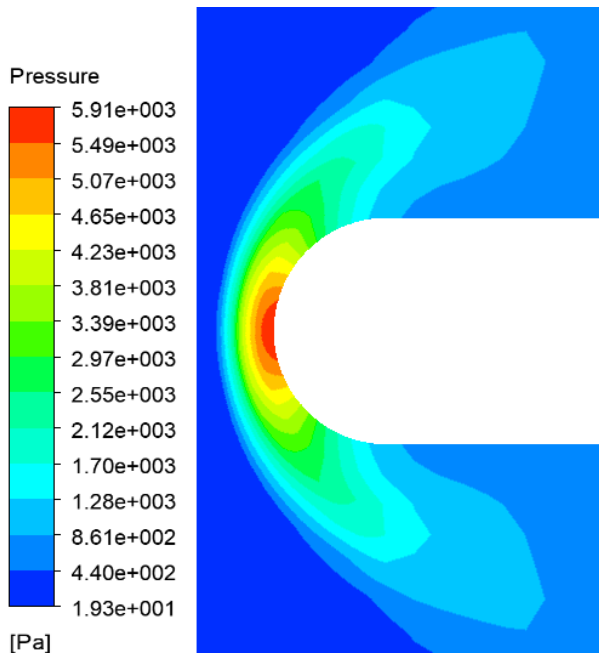
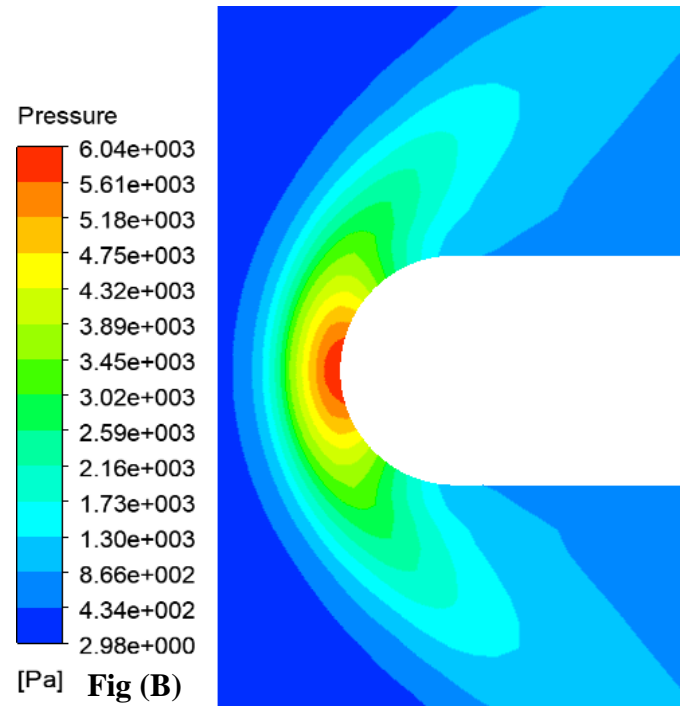
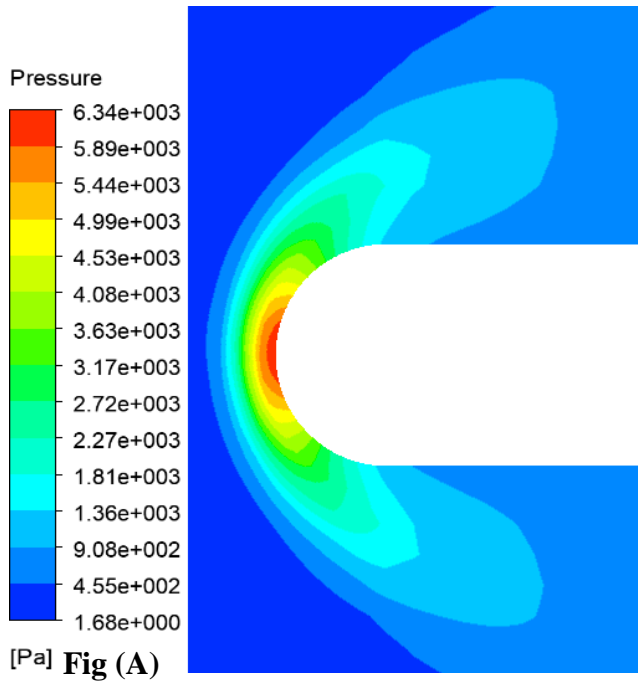


Fig (C)

$M=15.65, H = 60.96 \text{ Km},$
 $T = 244.4 \text{ k}, \rho = 2.745 \cdot 10^{-4} \text{ kg/m}^3$
 $P = 19.26 \text{ Pa}, \alpha = 0^\circ$
 Fig. A) Perfect gas
 Fig. B) 5 Reactions
 Fig. C) 17 Reactions



$$M=15.65, H = 60.96 \text{ Km},$$

$$T = 244.4 \text{ k}, \rho = 2.745 \cdot 10^{-4} \text{ kg/m}^3$$

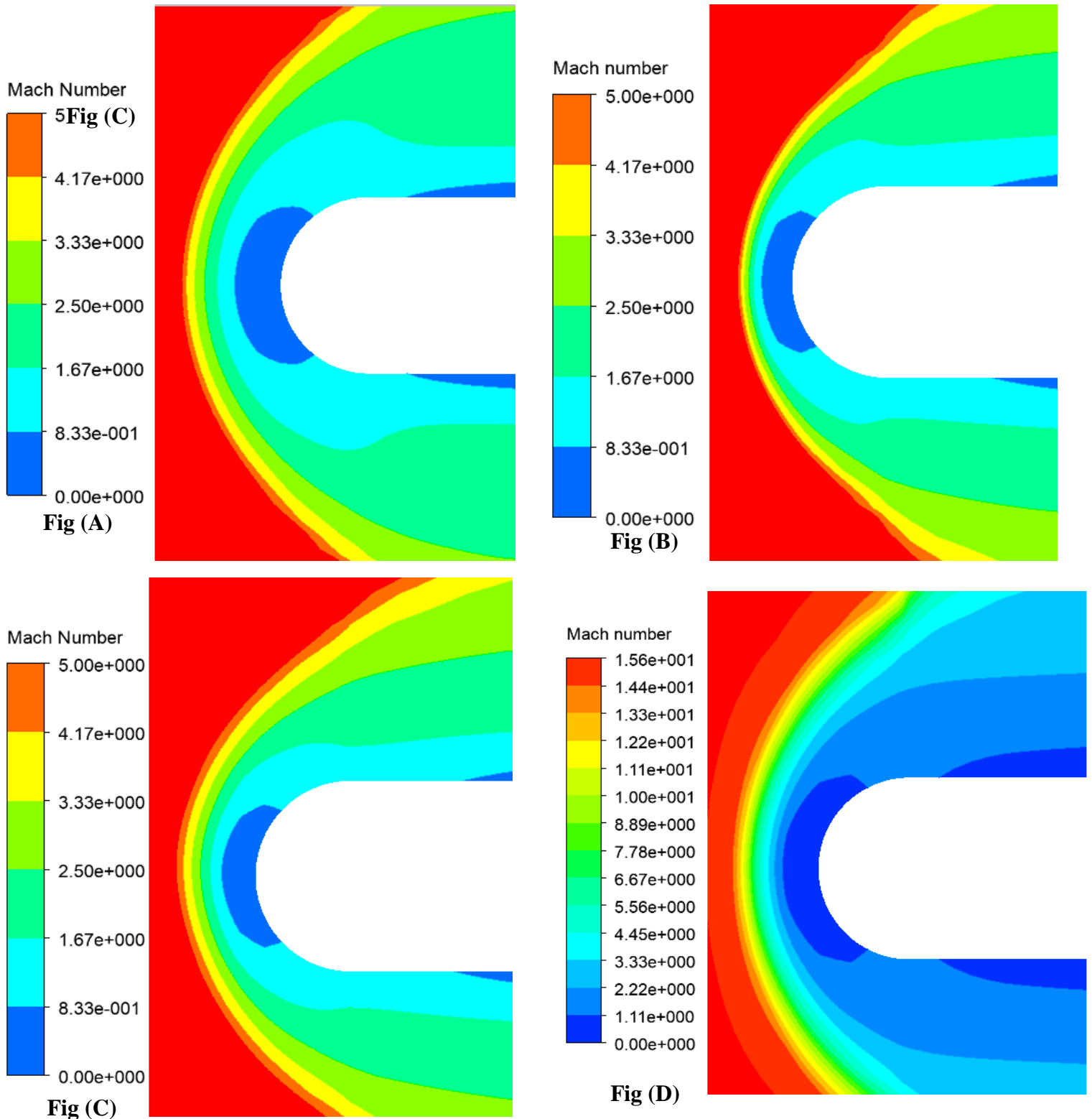
$$P = 19.26 \text{ Pa}, \alpha = 0^\circ$$

Fig. A) Perfect gas

Fig. B) 5 Reactions

Fig. C) 17 Reactions

Figure 4.23: Pressure field along surface streamlines



M=15.65, $H = 60.96 \text{ Km}$, $T = 244.4 \text{ k}$, $\rho = 2.745 \cdot 10^{-4} \text{ kg/m}^3$, $P = 19.26 \text{ Pa}$, $\alpha = 0^\circ$ Fig. A)
 Perfect gas Fig. B) 5 Reactions Fig. C) 17 Reactions Fig. D) Global Mach contour

High enthalpy flow:

Re-entry vehicles which are high speed vehicles operate in a high enthalpy range. In this range, real gas effects occur, it originates from the necessity of taking into account the interior structure of colliding gaseous particles, which can include molecular rotation, molecular vibration, chemical dissociation and exchange.

To explain more the decrease in temperature while introducing the real gas effect we introduce the enthalpy propriety that measures the heat content of a chemical system, the change in enthalpy is equal to the heat released by the reaction so when the temperature increases to the dissociation temperature, the number of molecular interactions also increases. When the number of interactions increase, the internal energy of molecules raises, then the temperature decreases therefore due to the endothermic effect of the colliding molecules that absorbs the heat. In our case, 12.4 MJ is the static enthalpy as shown in figure 4.25 where the total energy of the product will be higher than the total energy of the reactant. [57]

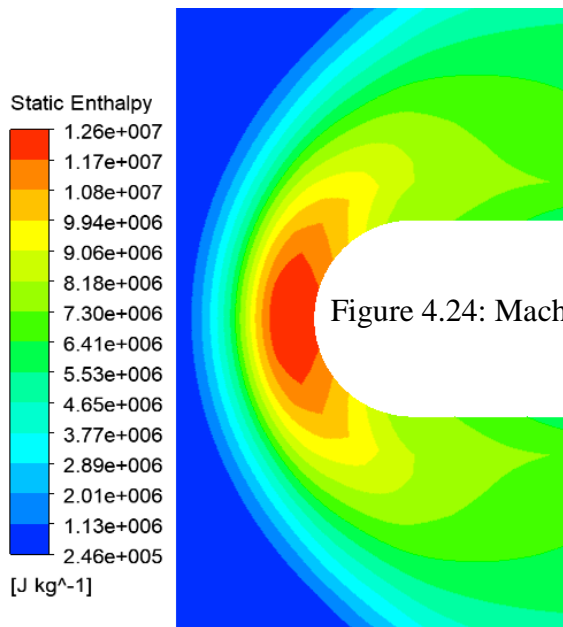


Fig (A)

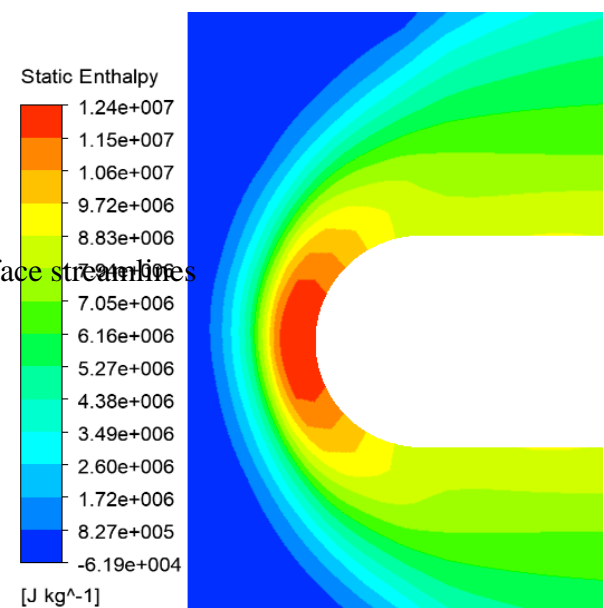
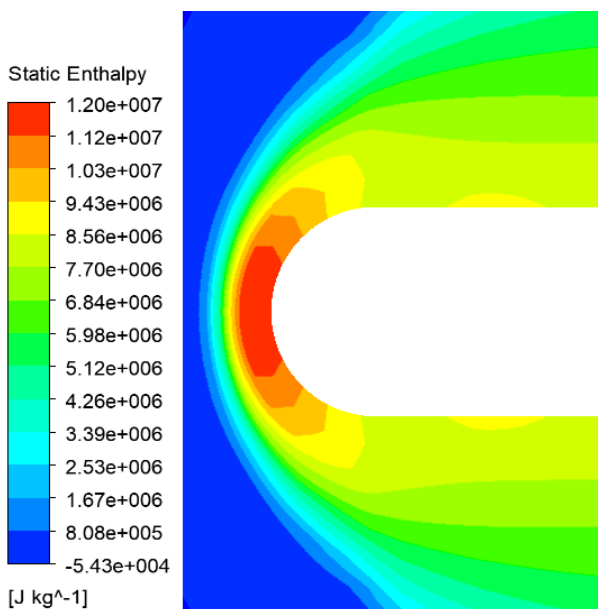


Fig (B)

Figure 4.24: Mach number field along surface streamlines



$$M=15.65, H = 60.96 \text{ Km},$$

$$T = 244.4 \text{ k}, \rho = 2.745 \cdot 10^{-4} \text{ kg/m}^3$$

$$P = 19.26 \text{ Pa}, \alpha = 0^\circ$$

Fig. A) Perfect gas

Fig. B) 5 Reactions

Fig. C) 17 Reactions

Figure 4.25: static enthalpy distribution along surface streamlines

Fig (C)

Wall shear

Fluid flow is fastest at the centre and slowest close to the wall as shown in figure 4.26. The fluid velocities assume a parabolic profile referred to as the "laminar flow" profile. This pattern of flow is the result of friction within the fluid and between the fluid and the vehicle wall which is related to the fluid viscosity.

This friction creates a tangential force exerted by the flowing fluid and is referred to as the "wall shear stress". The magnitude of wall shear stress depends on how fast the fluid velocity increases when moving from the vehicle wall toward the long side of the vehicle.

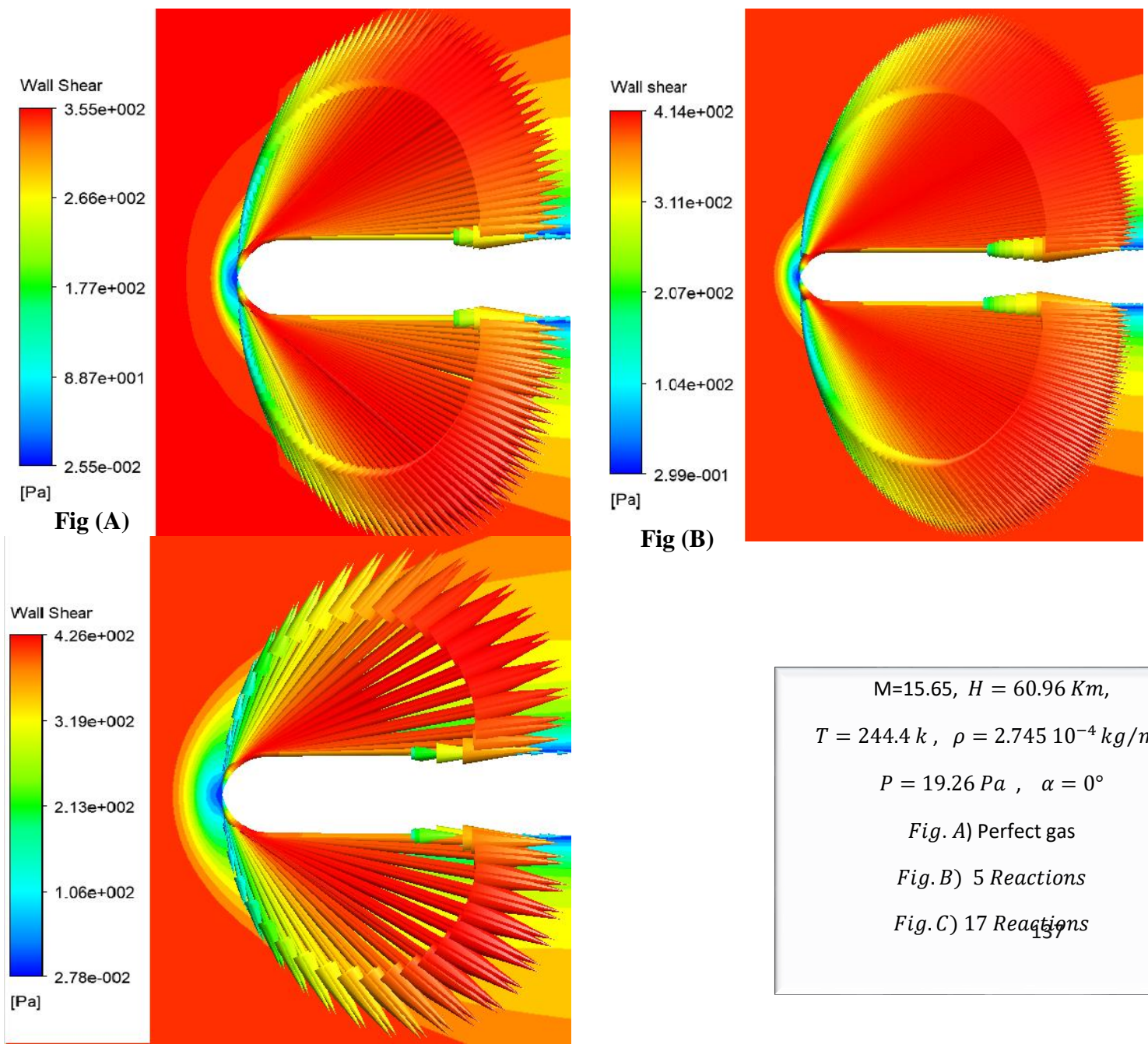


Fig (C)

Figure 4.26: wall shear distribution along surface streamlines

4.3.2 The angle of attack effect

The ability to change the forces operating on the vehicle during the re-entry manoeuvre can be quite useful, whether to optimize the re-entry or to withstand any potential emergencies. Thus, it may be desirable to fly a re-entry vehicle from different angles of attack.

The results show from figure (4.28) that the steeper the re-entry angles the more severe the peak deceleration, if we consider the Mach number 6, we can notice that the drag coefficient increase from 0.2 to 1.4 for 0° to 40° angle of attack respectively so the drag coefficient increases by a rate of approximately 83% going from a 0° AOA to an AOA of 40° . In the other hand, a decrease in this coefficient is recorded as a function of the Mach number evaluated at 89% from Mach 6 to Mach 20 as shown in figure (4.27)[39]. This means that:

- Steep re-entry angles cause low wall heating rates but for a short time
- Shallow re-entry causes high wall heating rates but for a long time

A steep (small re-entry angle) re-entry causes a lower surface heating rate but for a brief time, so the overall effect on the vehicle may be small. On the other hand, shallow re-entries lead to much higher surface heating rates figure (4.30). However, because heating continues longer, the vehicle is more likely to “soak up” heat and be damaged.

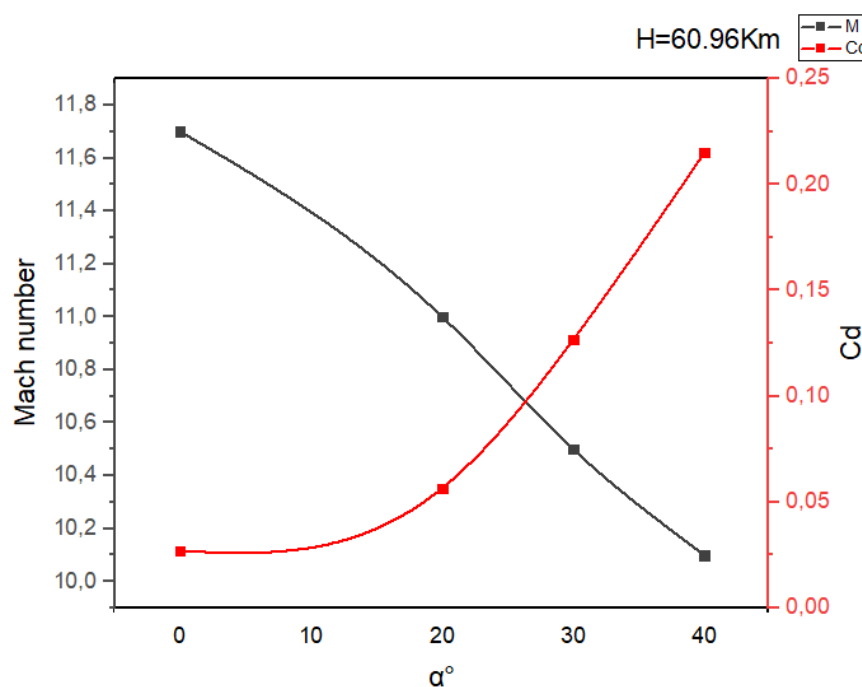


Figure 4.27: Drag coefficient and deceleration in function of angle of attack

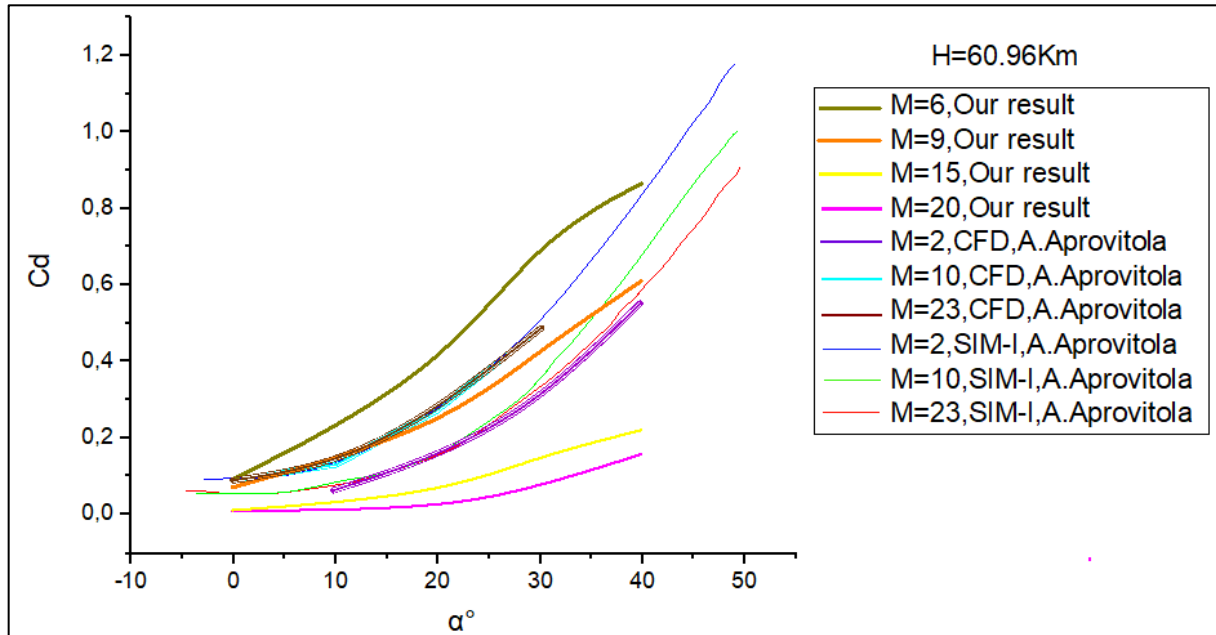
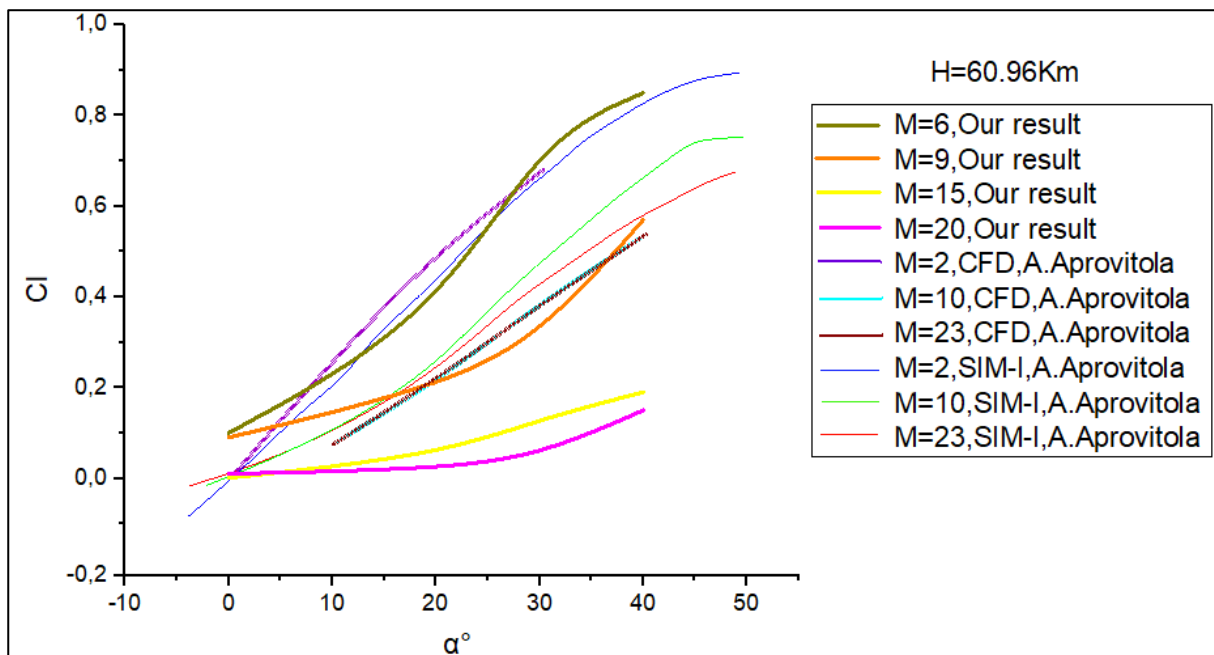


Figure 4.28: Drag coefficient in function of angle of attack for different Mach numbers by



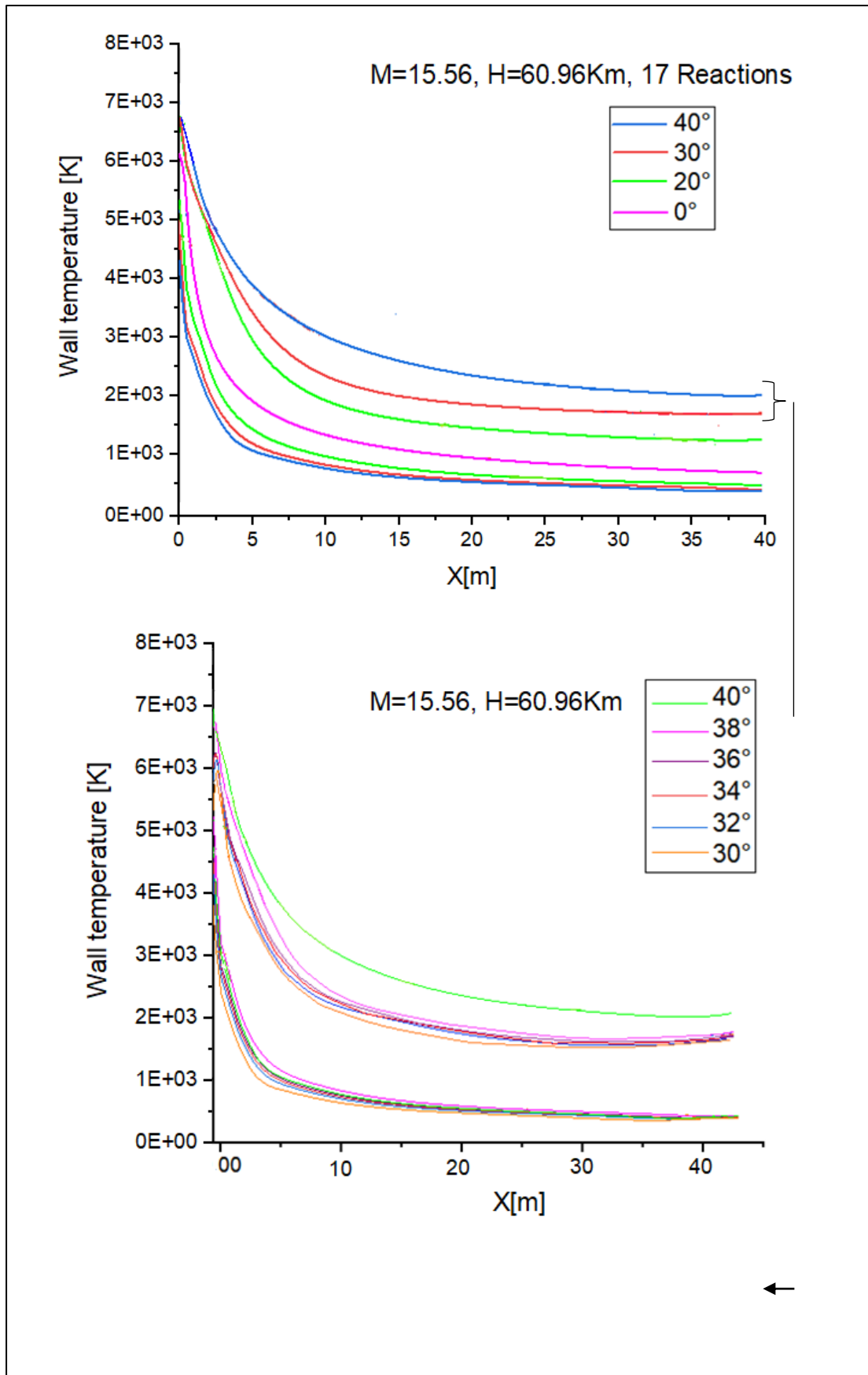
Comparing our result between A. APROVITOLA Aerodynamic computations performed using SIM-I and Eulerian CFD computations results. [79]

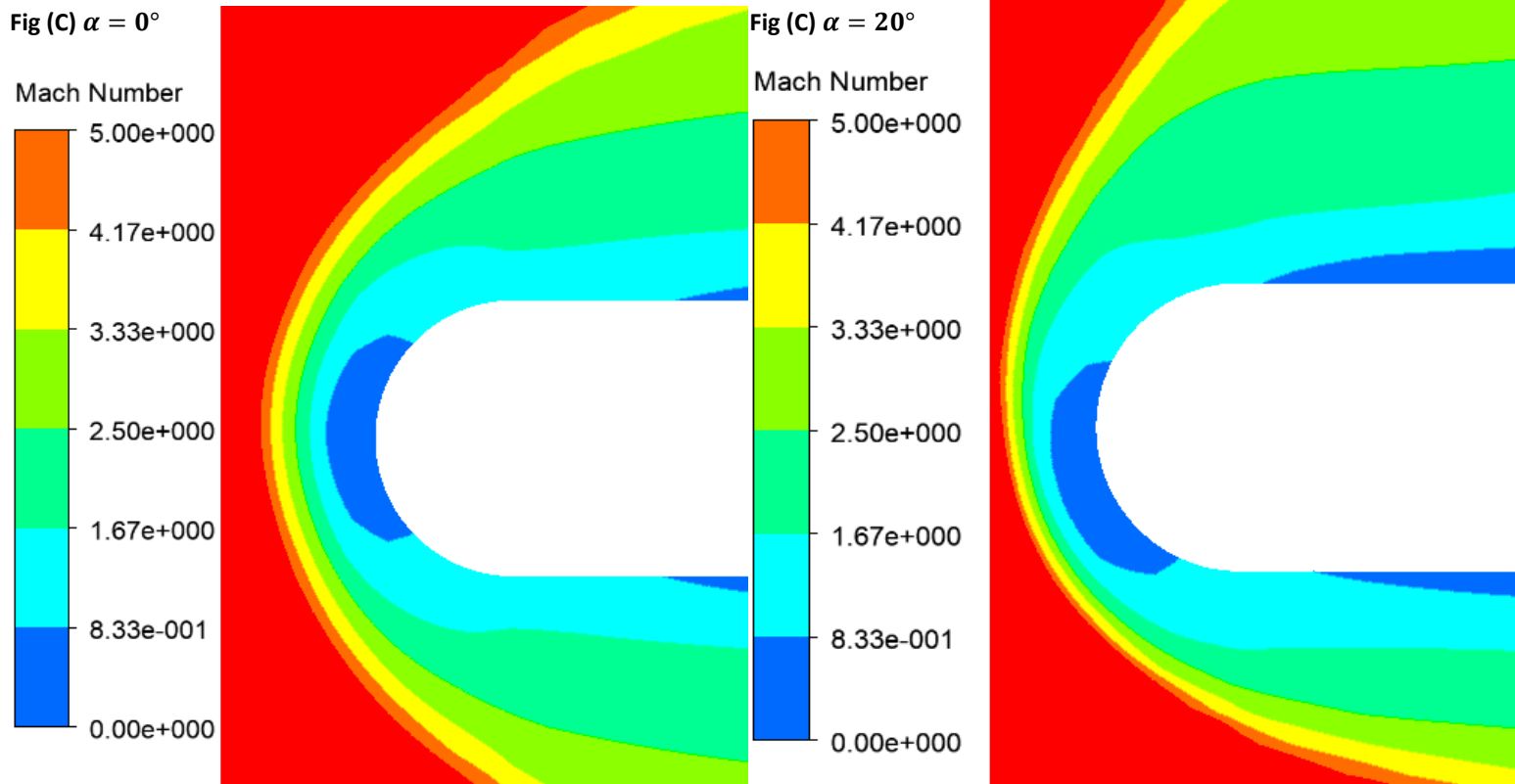
Figure 4.29: Lift coefficient in function of angle of attack for different Mach numbers [79]

In comparison to a completely ballistic re-entry, controlling lift enhances accuracy. We can improve lift by changing the vehicle's angle of attack figure (4.29) by an 85 % from 0° to 40° , making it fly more like an airplane than a rock. This allows our delta planner vehicle to manoeuvre the forces operating on it to the intended landing area.

Figure (4.30) depicts the temperature distributions on the structure's surface. As the angle of attack increases, the maximum temperature stays approximately the same while the shock moves toward the windward side, while the temperature differential grew between the windward and leeward side. If we consider the 40° angle of attack, we notice that the temperature deferential increase between the windward and the leeward side by approximately 2500k due to the high gradient temperature between the flow and the windward side which leads to the increase of the convective heat transfer to the vehicle. [55]

We notice from (4.28) that the drag increases sharply from 30° to 40° . So, in order to equilibrate our chance between the compromise of a minimum heating (for the dissociation case only) and the maximum drag (deceleration), we investigate the drag force between 30° AOA and 40° AOA to conclude the optimum angle of attack which has the minimum heating and the maximum drag. From Figure (4.30), we notice that the wall temperature evaluation keeps going in the same linear manner while we have an abrupt increase in aerodynamic forces, so we conclude from our results that the angle of attack rang that optimize the aerodynamic forces for a manoeuvrable landing and minimize the aero heating load of the vehicle confined between 30° and 40° .





4.3.3 Altitude Effect

The returning spacecraft needs to be in a specific Earth orbit before it can initiate its

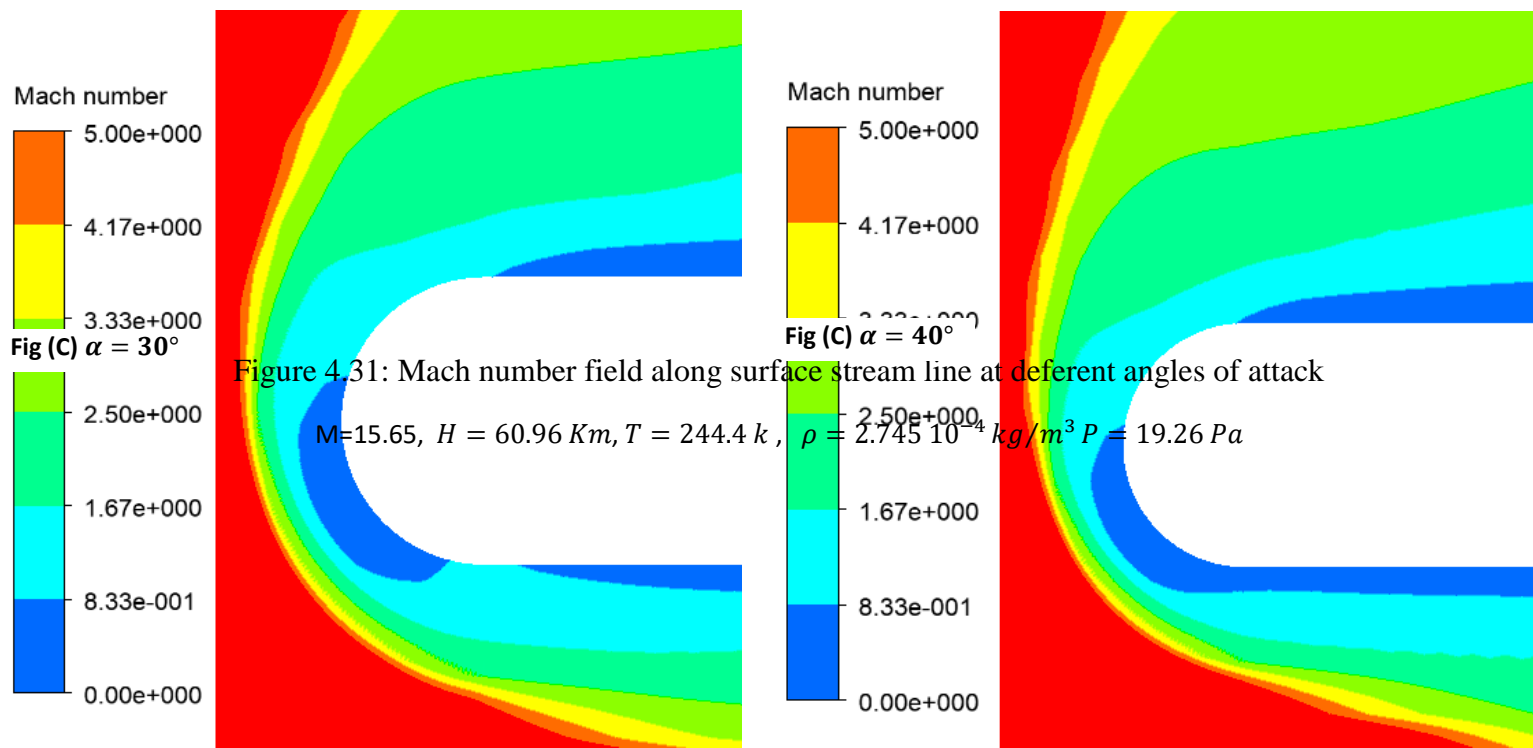


Figure 4.31: Mach number field along surface stream line at deferent angles of attack

$M=15.65, H = 60.96 \text{ Km}, T = 244.4 \text{ k}, \rho = 2.745 \cdot 10^{-4} \text{ kg/m}^3 P = 19.26 \text{ Pa}$

return journey. This return flight must occur in a narrow passage in space called the “re-entry corridor”. It is within this passage that the atmospheric drag on the spacecraft is large enough to let it fall to Earth instead of letting it veer off into space but not so large that the resistance it receives from the surrounding air destroys it.

Now that we know how the angle of attack effect the maximum heating and deceleration, let’s study the effect of altitude, to do so we covered an altitude range of 60.96 to 76.20 km (200 000 to 250 000 ft) at velocities of 4.88 to 7.32 km/sec (16 000 to 24 000 ft/sec), respectively and fixing the angle of attack at 30° . We get from the resulting figure (4.32,33) a high drag coefficient of 82% in the lower altitudes (60km) more than the upper altitude(76km) accompanied by a high surface heating rate while the maximum temperature becomes significant with 16754k value, as illustrated in figure (4.34). This is due to the increase in dynamic pressure as shown in figure (4.35), density and the low Mach number related to the low altitude.

From the definition of re-entry altitude, we can think of the overshoot or upper boundary as the “skip out” boundary., from figure (4.33) we can notice that the drag force is insignificant at high altitude, a vehicle entering the atmosphere above this boundary risks the vehicle degradation, the important Mach number play an important role at high altitudes, thus, the change in density is dominant and makes it easier for the vehicle to squeeze through.

As we’ve just shown, maximum deceleration and maximum heating rate, the two parameters that set the undershoot boundary, increase directly with increased re-entry velocity, $V_{re-entry}$, or re-entry flight-path angle, γ , (steeper re-entry). But in the same time, we can investigate methods of thermal protection in order to reduce the aero heating by introducing a spike at frontal region of the nose which was studied in the next section.

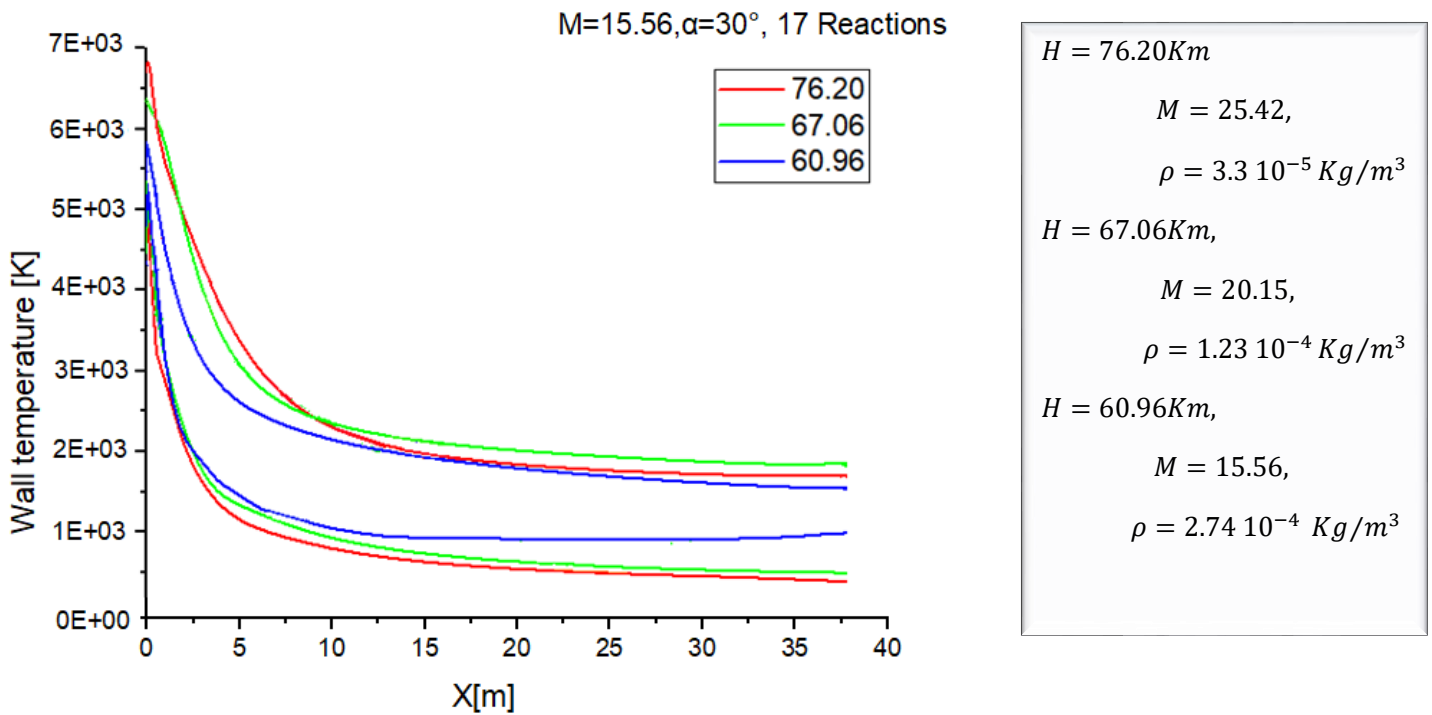


Figure 4.32: Wall temperature distribution along surface streamlines for different altitude

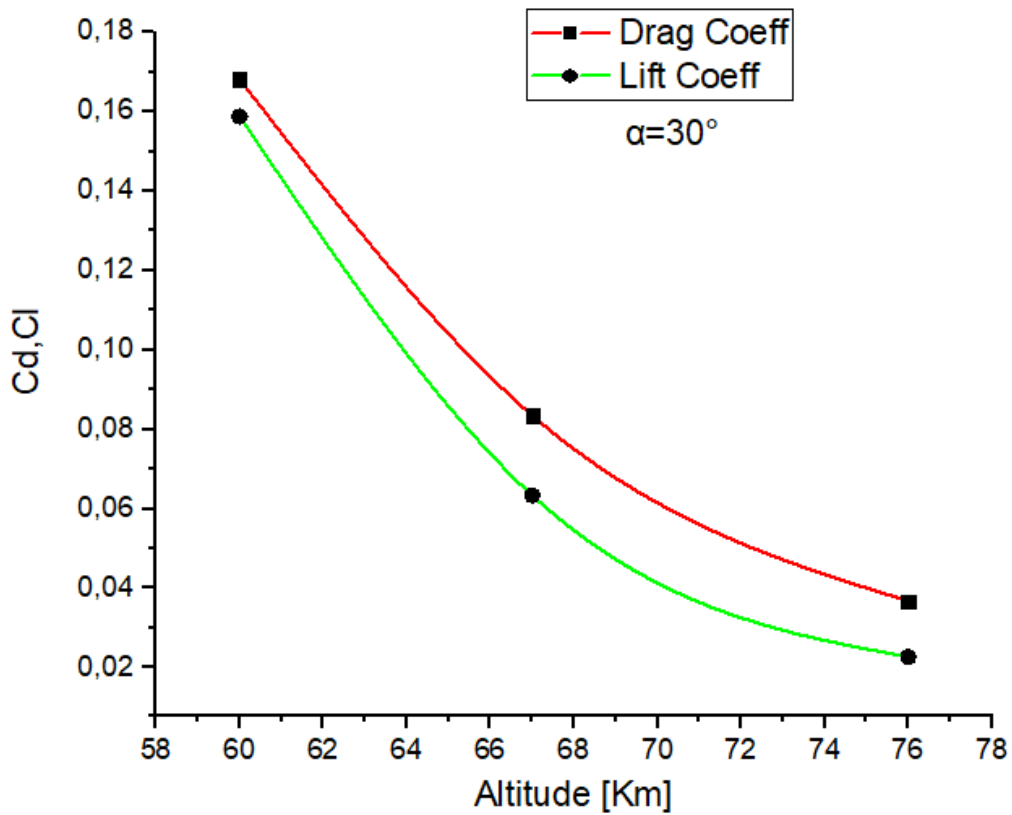


Figure 4.33: Drag and lift coefficient in function of altitude

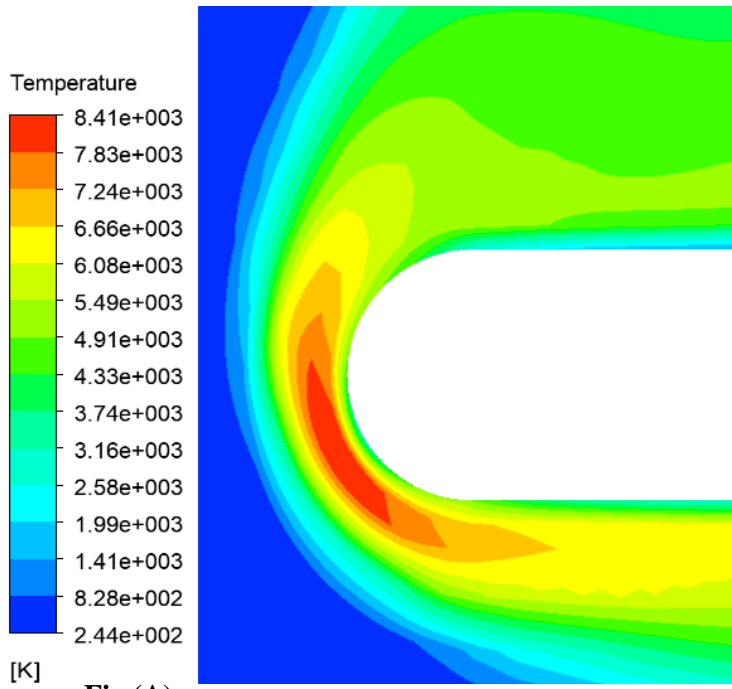


Fig (A)

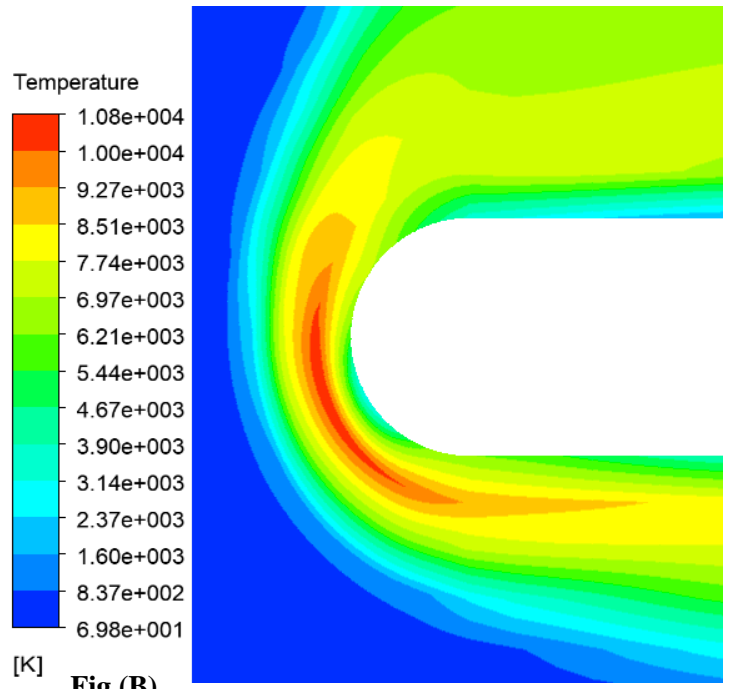


Fig (B)

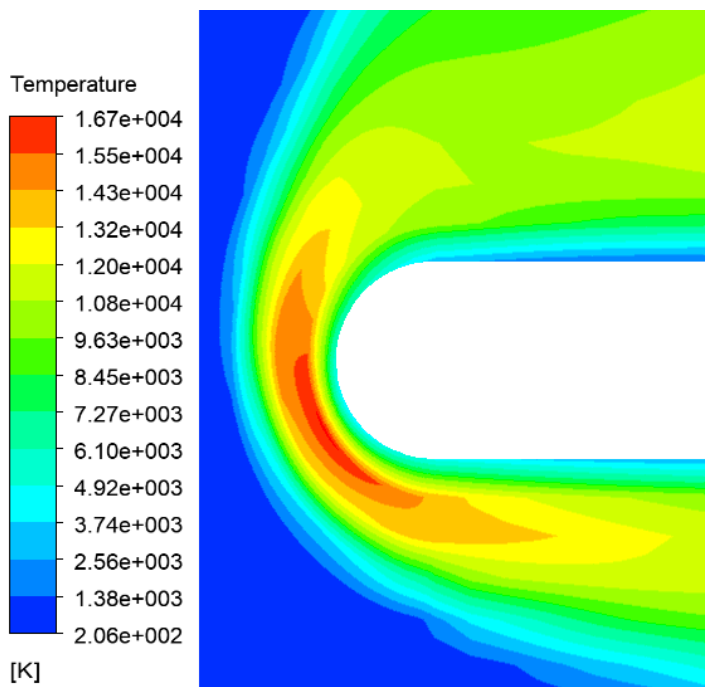


Fig (A) $H = 76.20\text{Km}$

$M = 25.42,$

$\rho = 3.3 \cdot 10^{-5} \text{ Kg/m}^3$

Fig(B) $H = 67.06\text{Km},$

$M = 20.15,$

$\rho = 1.23 \cdot 10^{-4} \text{ Kg/m}^3$

Fig(C) $H = 60.96\text{Km},$ 145

$M = 15.56,$

$\rho = 2.74 \cdot 10^{-4} \text{ Kg/m}^3$

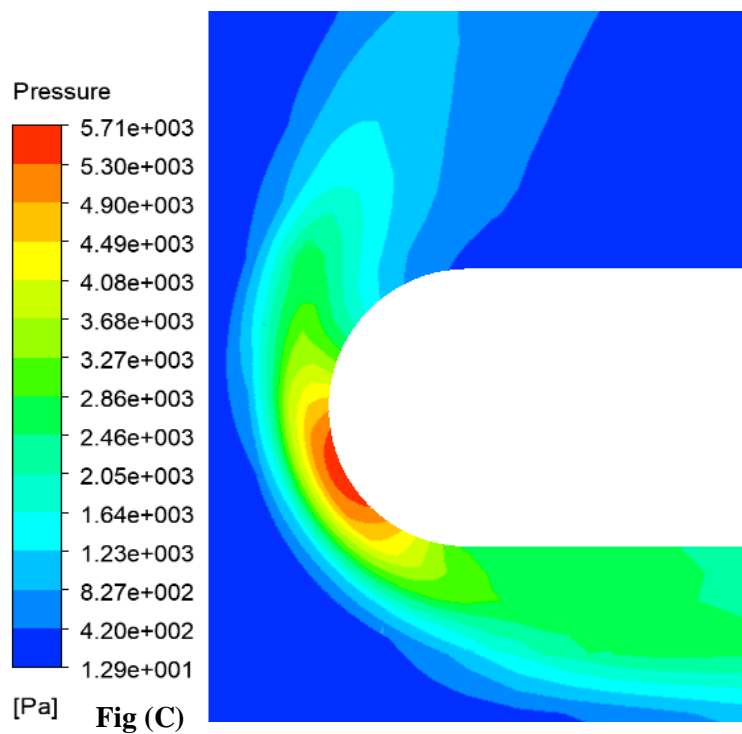
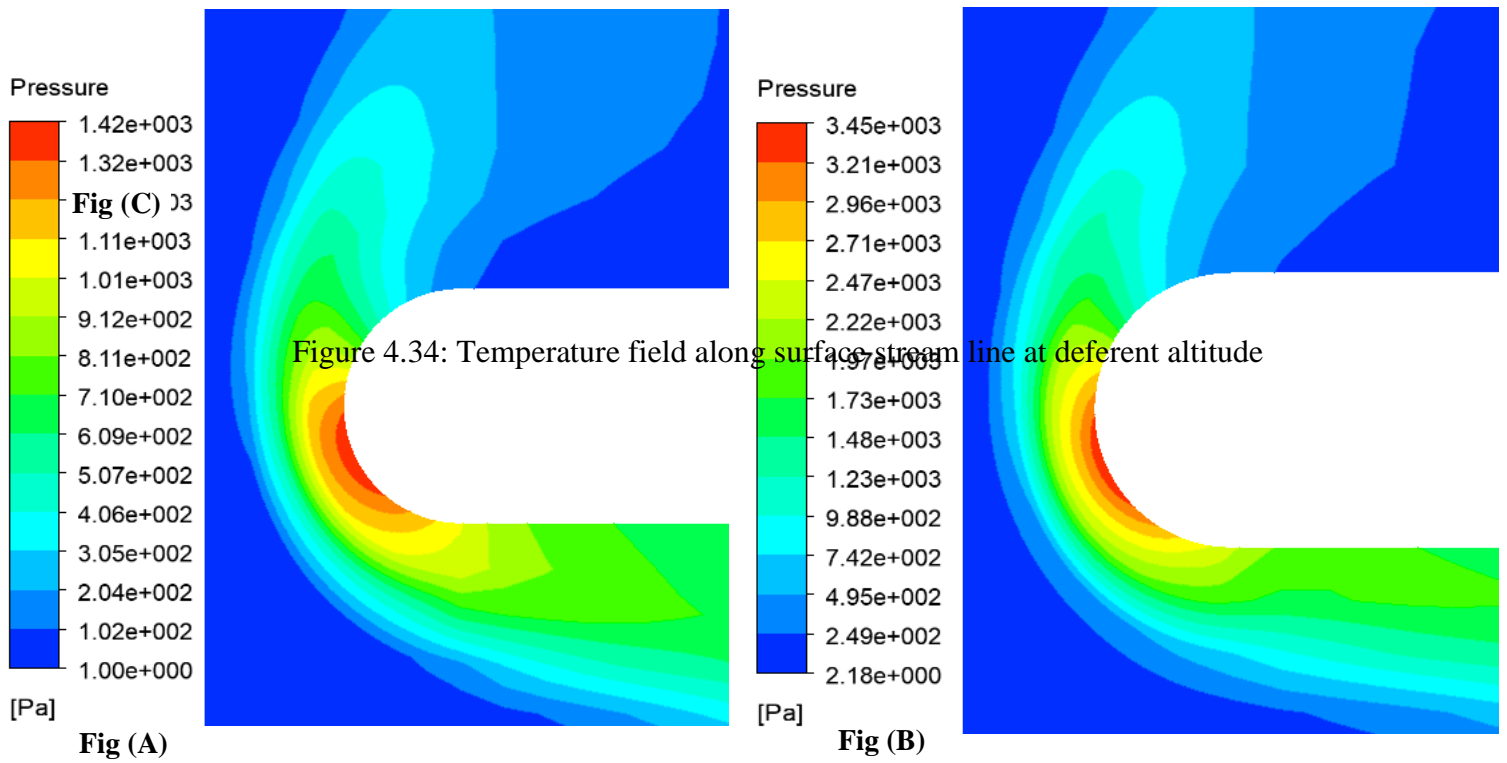


Figure 4.35: Pressure field along surface stream line at different altitudes

$$H = 76.20Km$$

$$M = 25.42,$$

$$\rho = 3.3 \cdot 10^{-5} Kg/m^3$$

$$H = 67.06Km,$$

146

$$M = 20.15,$$

$$\rho = 1.23 \cdot 10^{-4} Kg/m^3$$

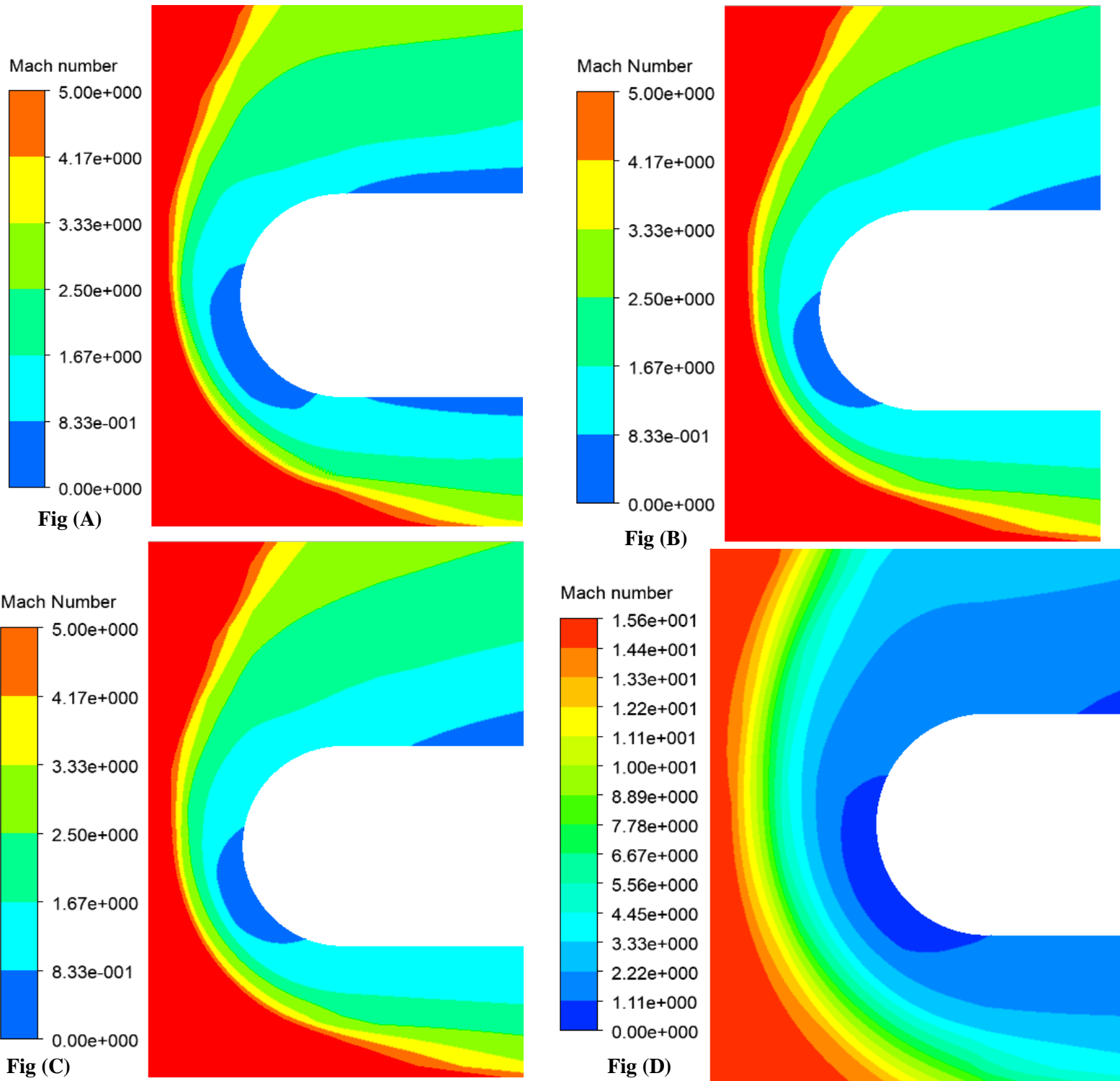


Figure 4.36: Mach Number field along surface stream line at deferent altitude

4.4 Results of Blunt spike

A CFD simulation was conducted to avoid stronger shocks and also for reducing the temperature, spikes are placed at frontal portion of the nose region, blunt spike design produces more drag. But they are closable as aero heating is concerned.

❖ Validation

Our numerical solution validation was carried out by comparing the numerical wave structure and experimental Schlieren flow field as shown in Figure 4.37. The conditions were set as $M_\infty = 6.0$ and $L/D = 1.0$. Numerical and experimental results are in agreement, indicating the main flow field structures, including conical shock, reattached shock, shear layer, and separation zone.

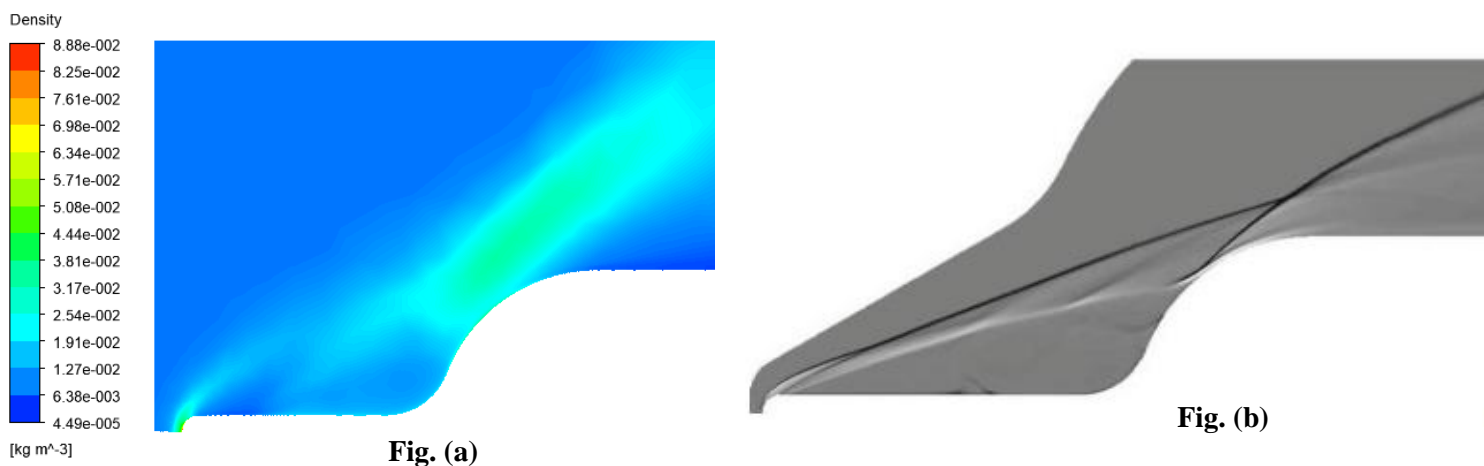


Figure 4.37: Flow field wave structure of spiked blunt body with spike length $L/D = 1.0$; (a) experimental Schlieren photograph (b) numerical Schlieren photograph [40].

The maximum temperature increases from 8600k to 9020k when we introduce the blunt spike in front of the nose due to the bluntness effect, but in the other hand, the frontal nose geometry of the spike helps to withstand, distribute, and dissipate these loads from the nose vehicle.

We observed that the temperature at the nose for the Blunt Spike Re-entry Hypersonic vehicle was 9020k. The shock wave scattered along the length and decreases the temperature in the vehicle nose surface to a value of 7140k as noticed in figure 4.38.

The presence of the spike, blunt transform the bow shock into a weaker conical shock. Consequently, the levels of flow pressure and temperature increased are significantly reduced by 12.5%.

The high-speed flow travelled to the blunt body shoulder in figure 4.39, result in a reattached shock formation with a high-pressure zone as shown in figure 4.41; the unfavourable pressure gradient inverses the gas flow to the spike nose. Thus, a circumfluence zone was generated around the spick and the blunt body nose which induce a lower velocity

than that after the conical shock, generating a shear layer, which reduce some of the fluid in the circumfluence area.

So, the combined effect of the reduced foreshock and the recirculation zone on the main body can result in significant reductions in aero heating.

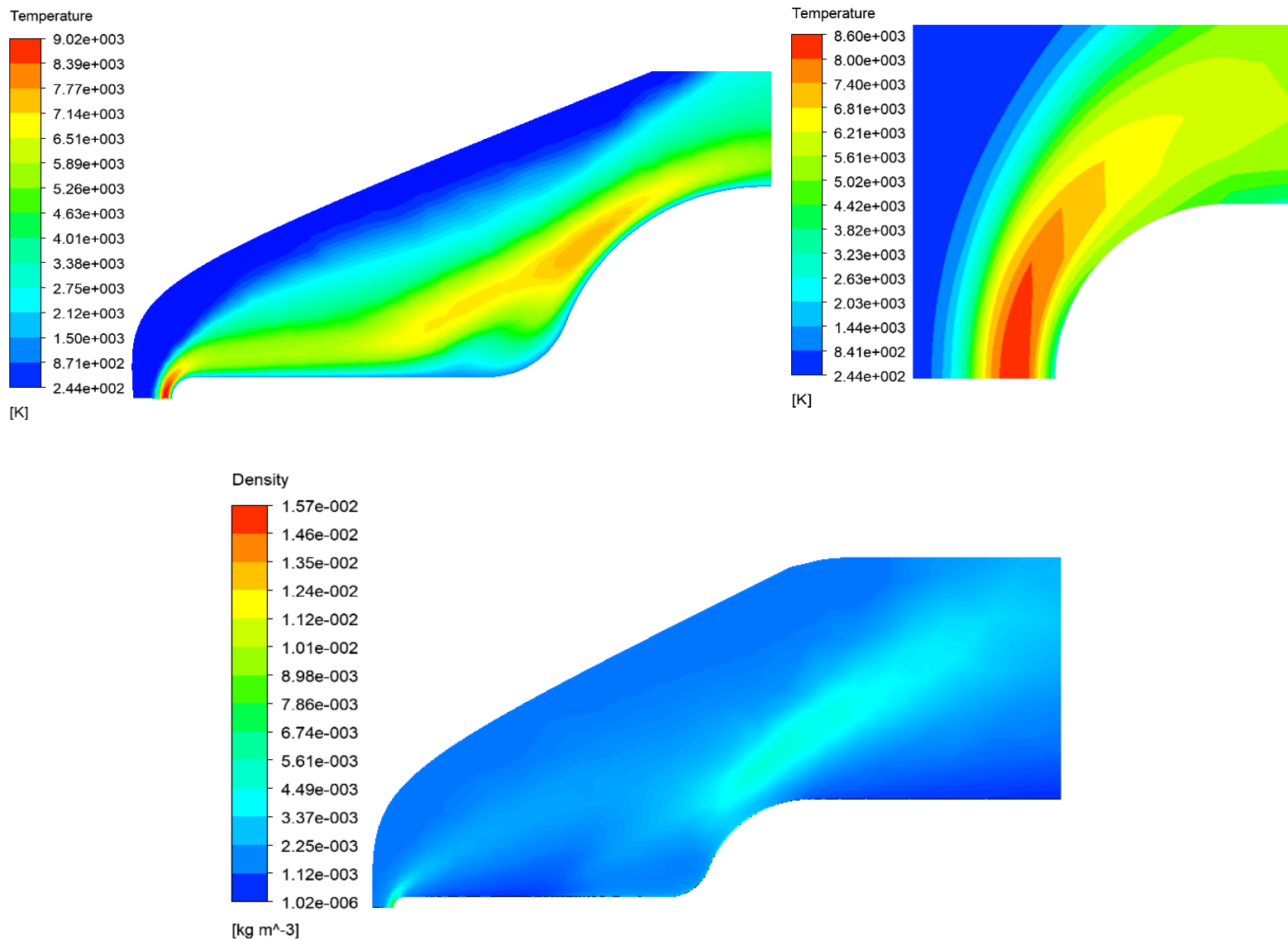


Figure 4.38: Blunt spike temperature contours

Figure 4.39: Blunt spike density contours

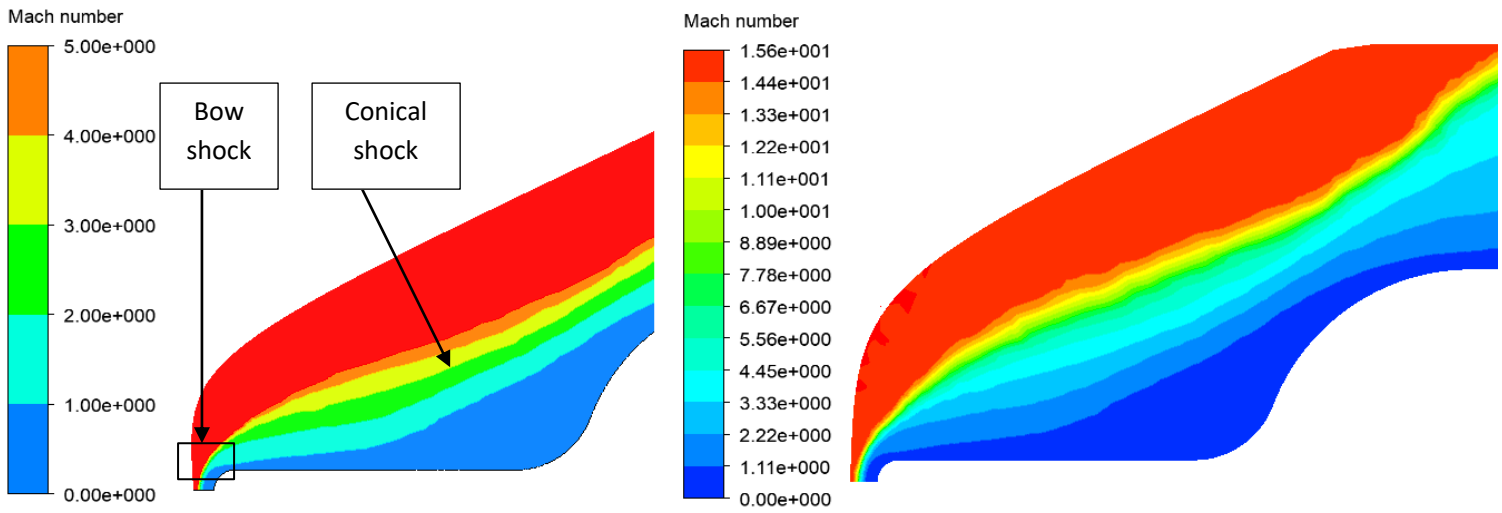


Figure 4.40: Blunt spike Mach number contours

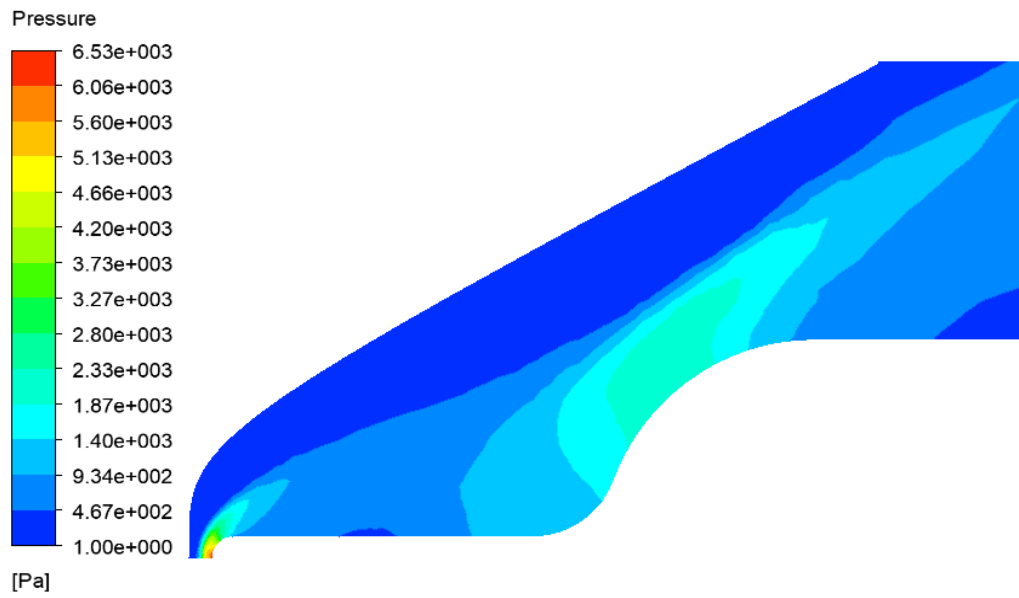


Figure 4.41: Blunt spike pressure contours

4.5 Result of Hypersonic Flow over a delta body

One of the most common shapes of a reusable launch vehicle is the delta body, which is capable of propelling a launch vehicle to space more than once. It differs from expendable launch systems, in which each launch vehicle is launched once and then discarded, opening the prospect of lowering the cost of each mission.

❖ Validation

By comparing our result of figure (4.42) with that of the article [41] which shows the variation of the temperature along outer stream line, one notices a good agreement between the two results. The difference is due to the fact that John.Lourdi considered the ionization process which absorbed more heat in the post shock region than the dissociation considered in our case. the results are presented by a full-scale body length of 2×10^2 .

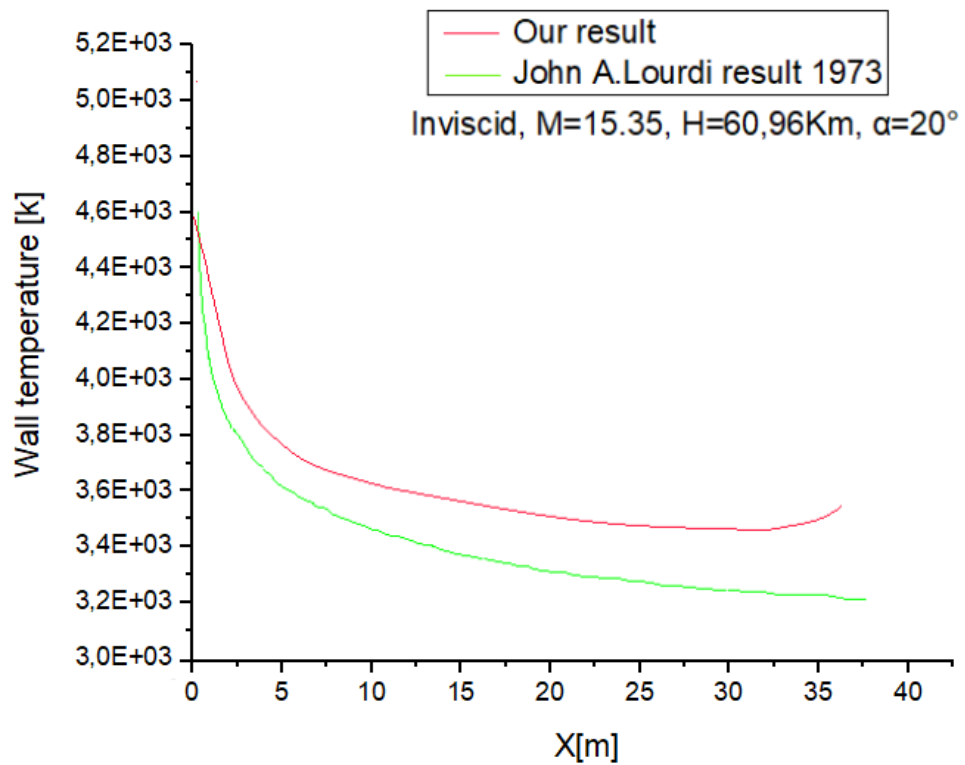


Figure 4.42.- wall temperature distribution along body outer streamline [41]

4.5.1 Oblique shock wave:

We always have a detached bow shock with a small subsonic ($M < 1$) pocket behind blunt-nosed body (Figure 4.43). The bow shock dissipates far downstream of the vehicle, and its inclination against the free-stream direction approaches the free-stream Mach angle approximately. Although the shock seems to be linear over the majority of the body, it curves at the leading edge due to hypersonic bluntness and viscous interaction effects creating oblique shock wave while the bluntness effects become less relevant further downstream of the leading edge, and viscous effects tend to dominate. We can capture the shock formation by an increase in entropy (figure 4.44), which is equivalent to a loss of total pressure (figure 4.45). [57]

Isotropic heating of the air molecules within the compression waves is what cause the shock layer heating due to the friction-based entropy, in which the entropy rise is greatest when the shock is normal to the free-stream flow (normal shock), and it decreases as the shock's inclination against the free-stream flow decreases (oblique shock) as we can notice in

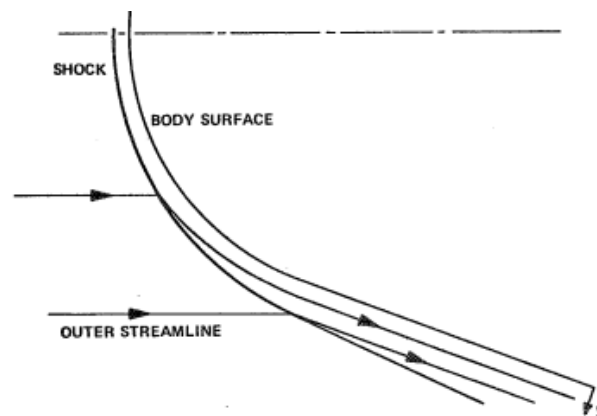


figure (4.46).

Normal shock

Oblique shock wave

Expansion waves

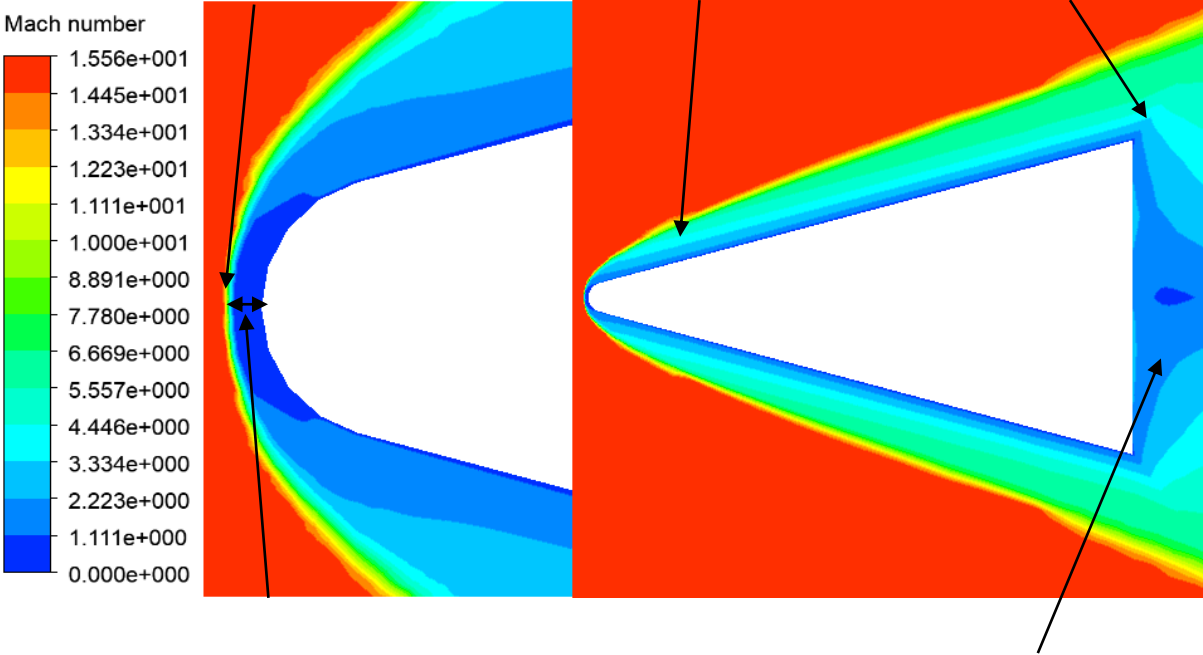


Figure 4.43: Iso-Mach distribution along delta wing-body

Relaxation zone

Recirculation zone

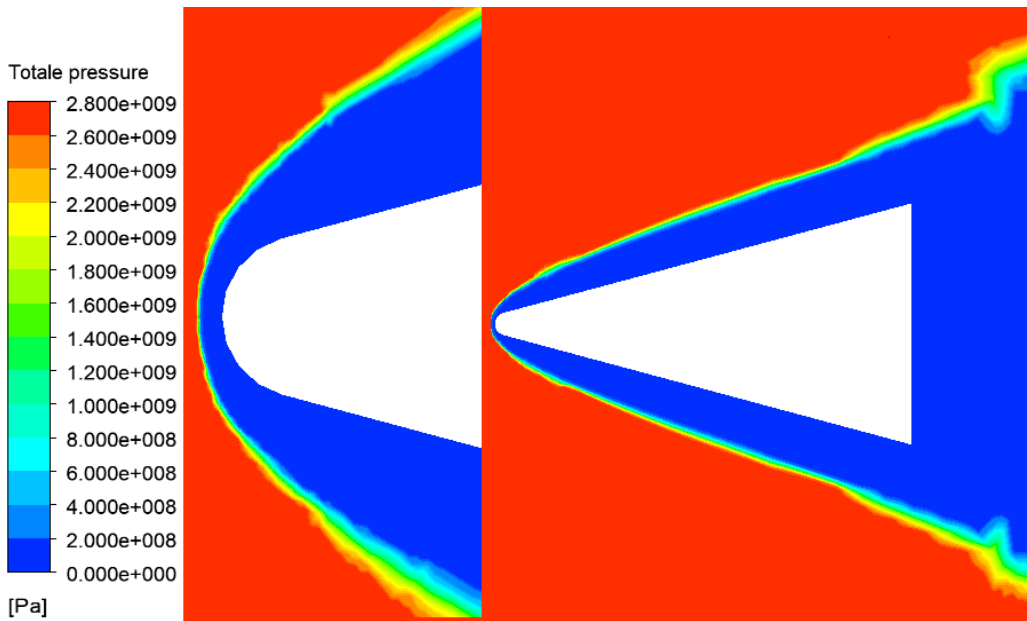
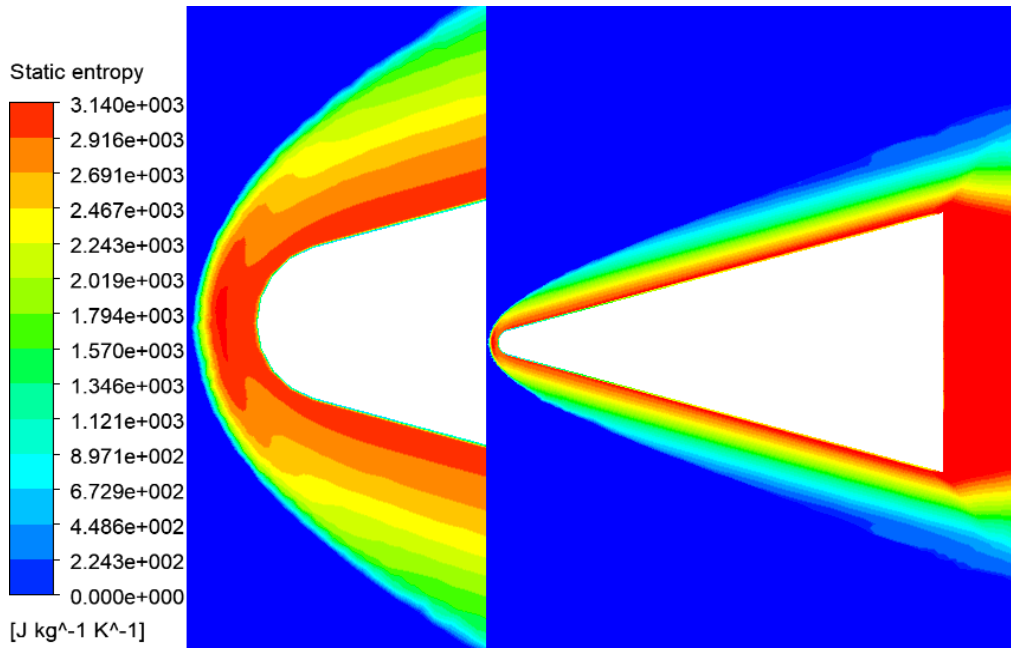


Figure 4.44: static entropy distribution along delta wing-body

Figure 4.45: Total pressure distribution along delta wing-body

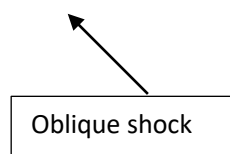
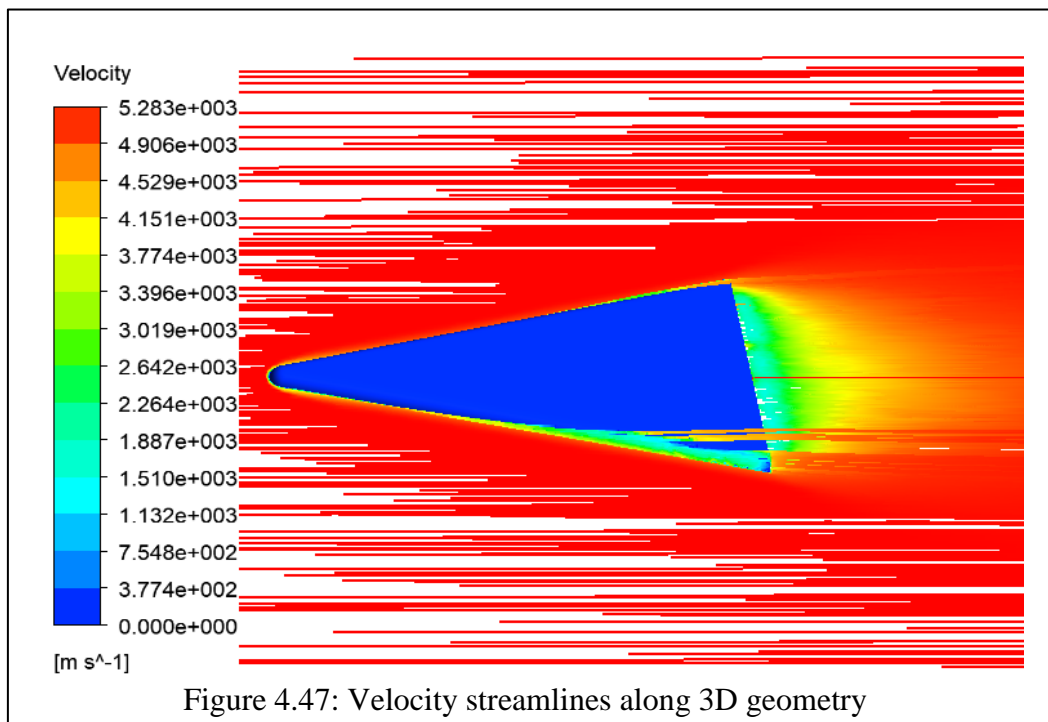


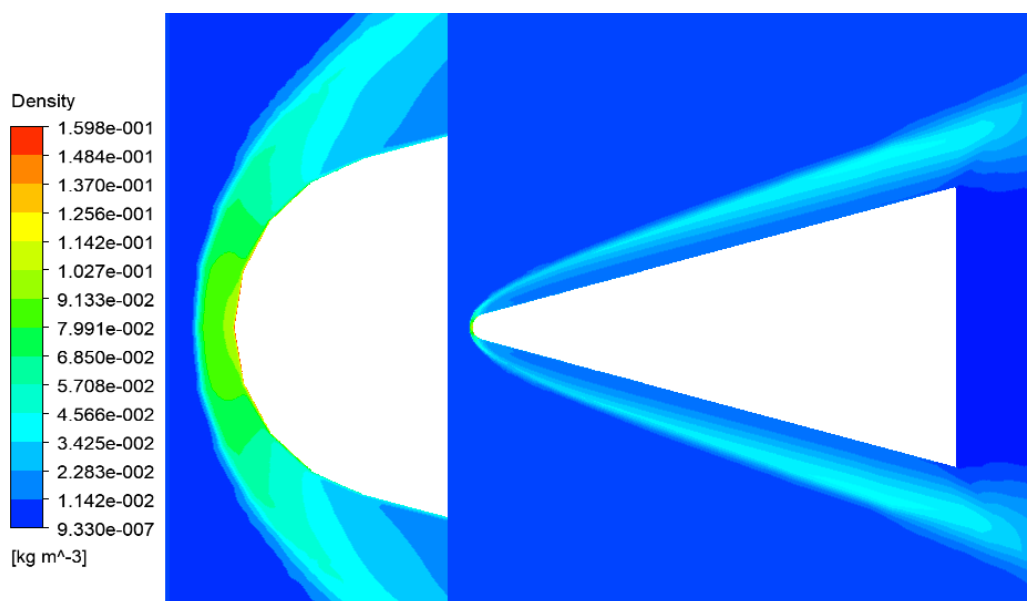
Figure 4.46: Temperature distribution along delta wing-body

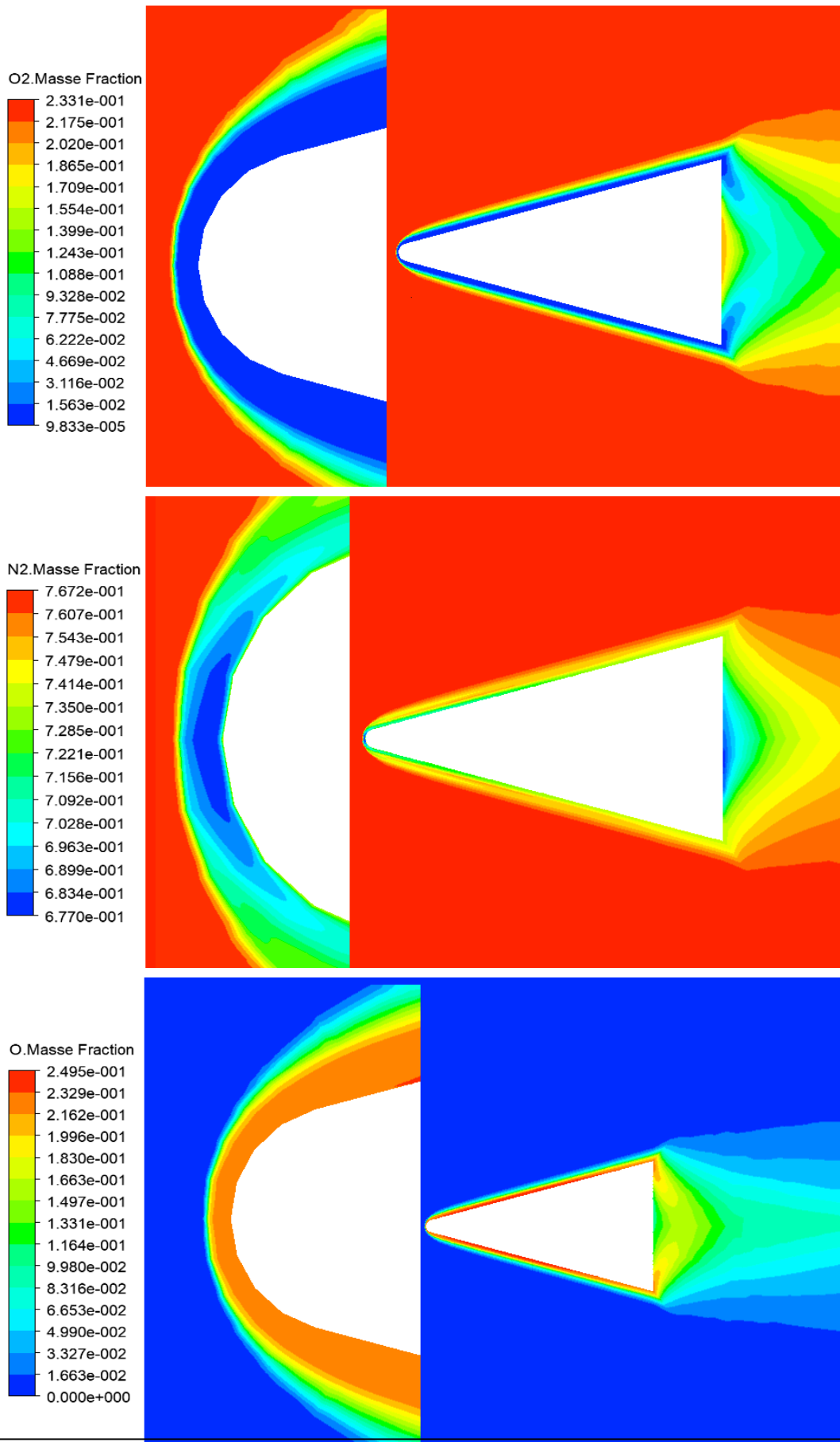


4.5.2 Reaction effect

The result shows in figures (4.49,50) shows that when the flow proceeds downstream, there might be sufficient time for chemical reactions to occur.[57]

As the expansion around the corner of the model nose proceeds, the rapidly falling temperature and density once again (figure 4.48) causes the recombination reactions to slow, leaving the gas passing onto the flat plate region of the body in a highly dissociated but nearly non-reacting state. What explain the disappearances of the NO molecules into the flat plate region, in the other hand the presences of the molecules O and N due to the short characteristic dissociation time compared to the chrematistic recombination time.





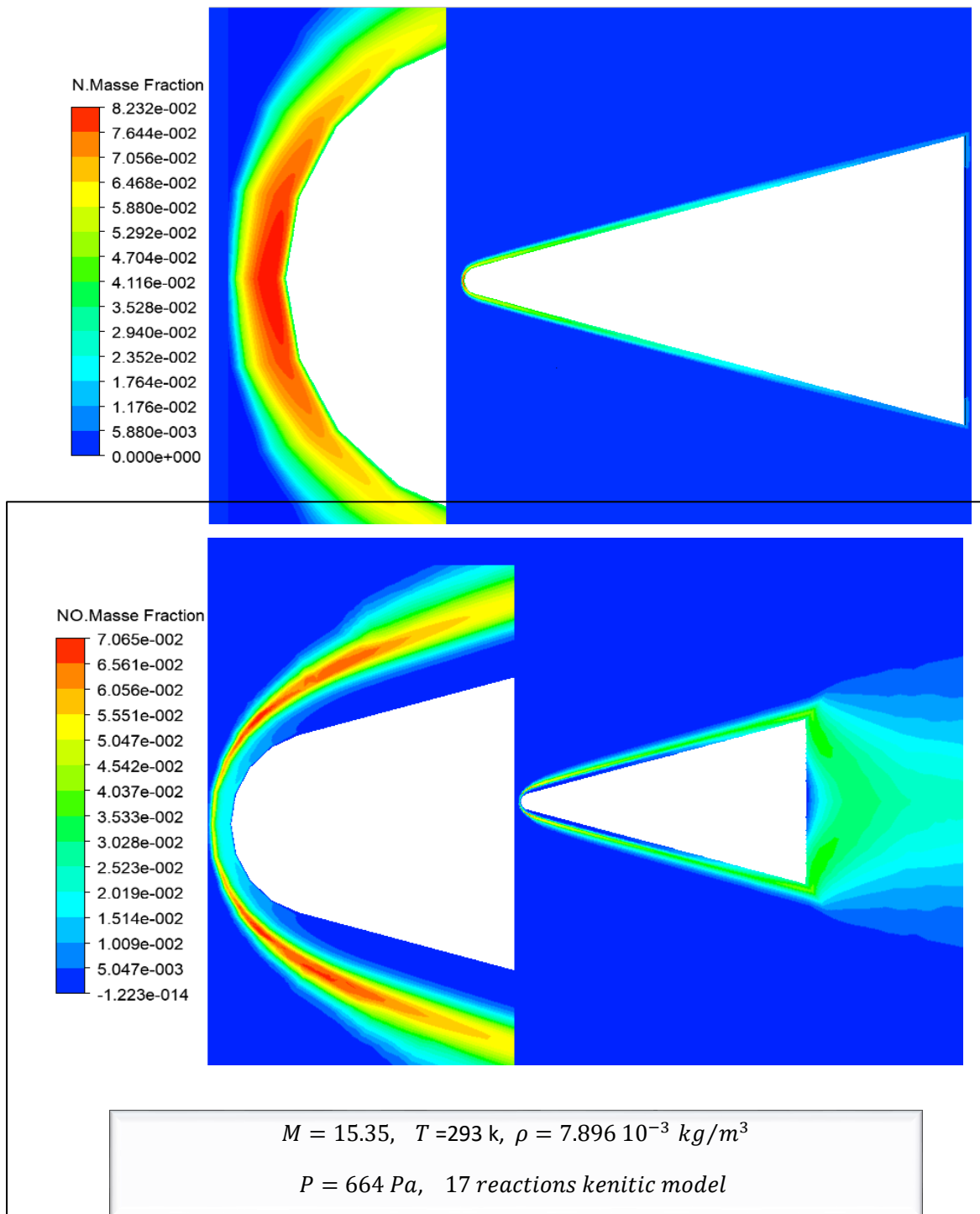
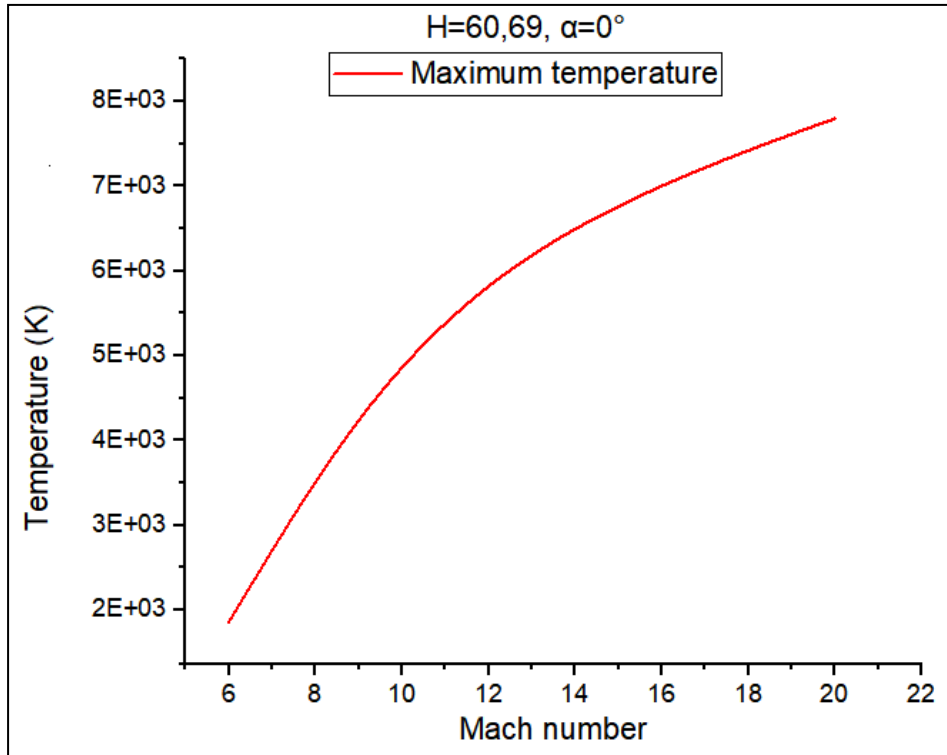


Figure 4.50: Mineur species distribution along delta wing-body

4.5.3 Velocity Effect

A higher re-entry velocity results in more maximum wall heating, as seen in the figure (4.51) the stagnation wall temperature increases from 2000k to 8000 for 6 to 20 Mach number respectively thus because of the compression waves which are more important at high Mach numbers due to the abrupt transition of flow regime from 20 to a subsonic Mach

number, leads to a significant temperatures rate just after the shock. Regardless of the presence of the physicochemical effect that absorb the energy in the post shock region, The temperature stayed significant on the wall. If we consider skipping rocks, as we already mentioned, this should make sense. The harder we through a rock into the water, the bigger



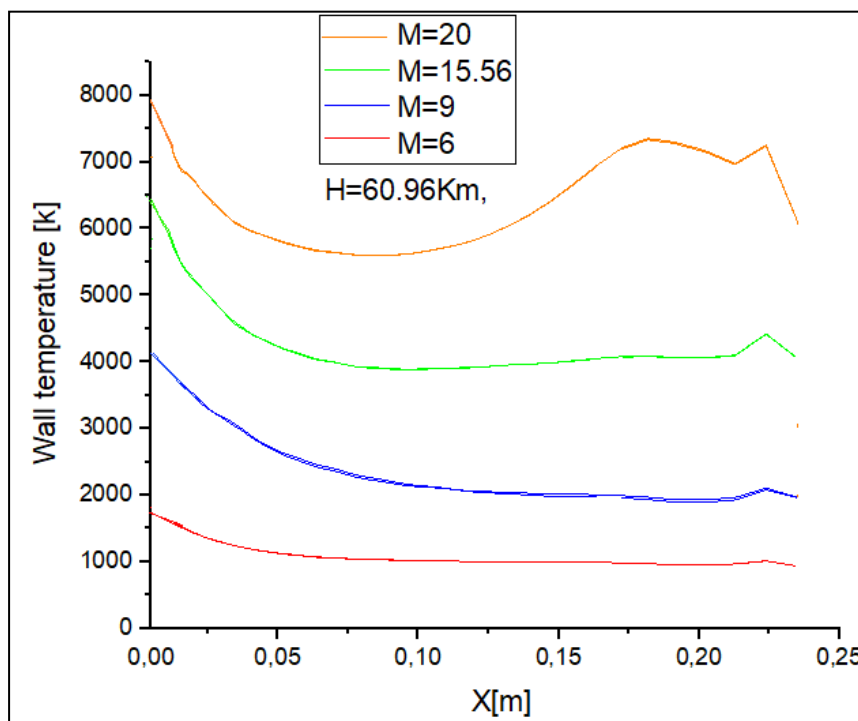
the splash a rock makes in the water.

Figure 4.51: Maximum wall temperature in function of Mach number

Figure 4.52: wall temperature stream lines for different Mach number

Recirculation region :

When the incident oblique shock wave hits the boundary layer, it propagates at a certain angle until it reaches the separation point. The unfavourable pressure gradient of the



impinging shock causes the boundary layer to detach from the wall and produce a recirculation bubble figure (4.53).[76] Flow is displaced by the recirculation bubble, which forces it to bend around it. The reflected compression waves on the flat plan of the body are created by the formation of the expansion waves in the separation points; which results in an increase in temperature; this phenomenon is obvious at high Mach numbers as noticed in graph (4.52).

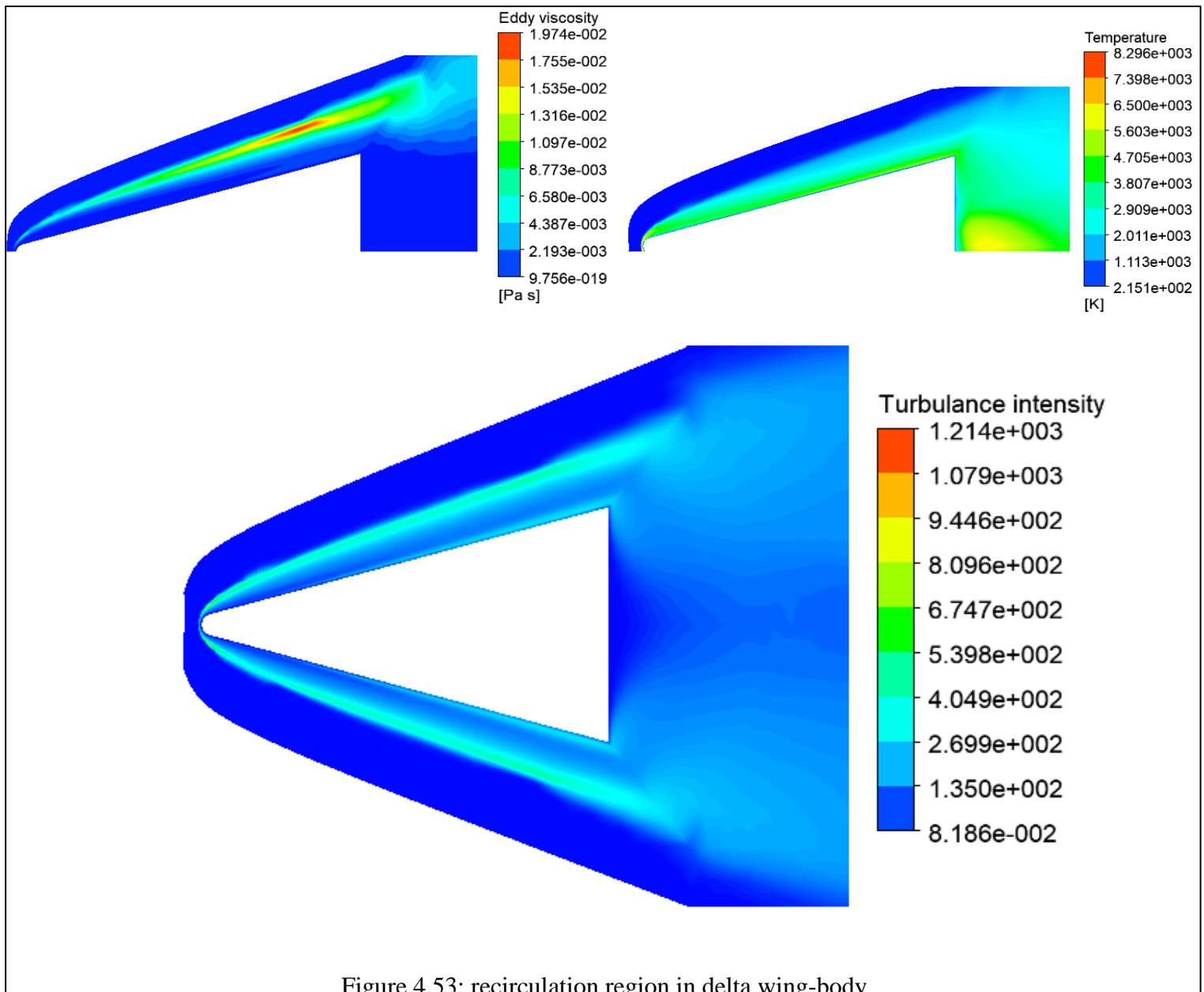
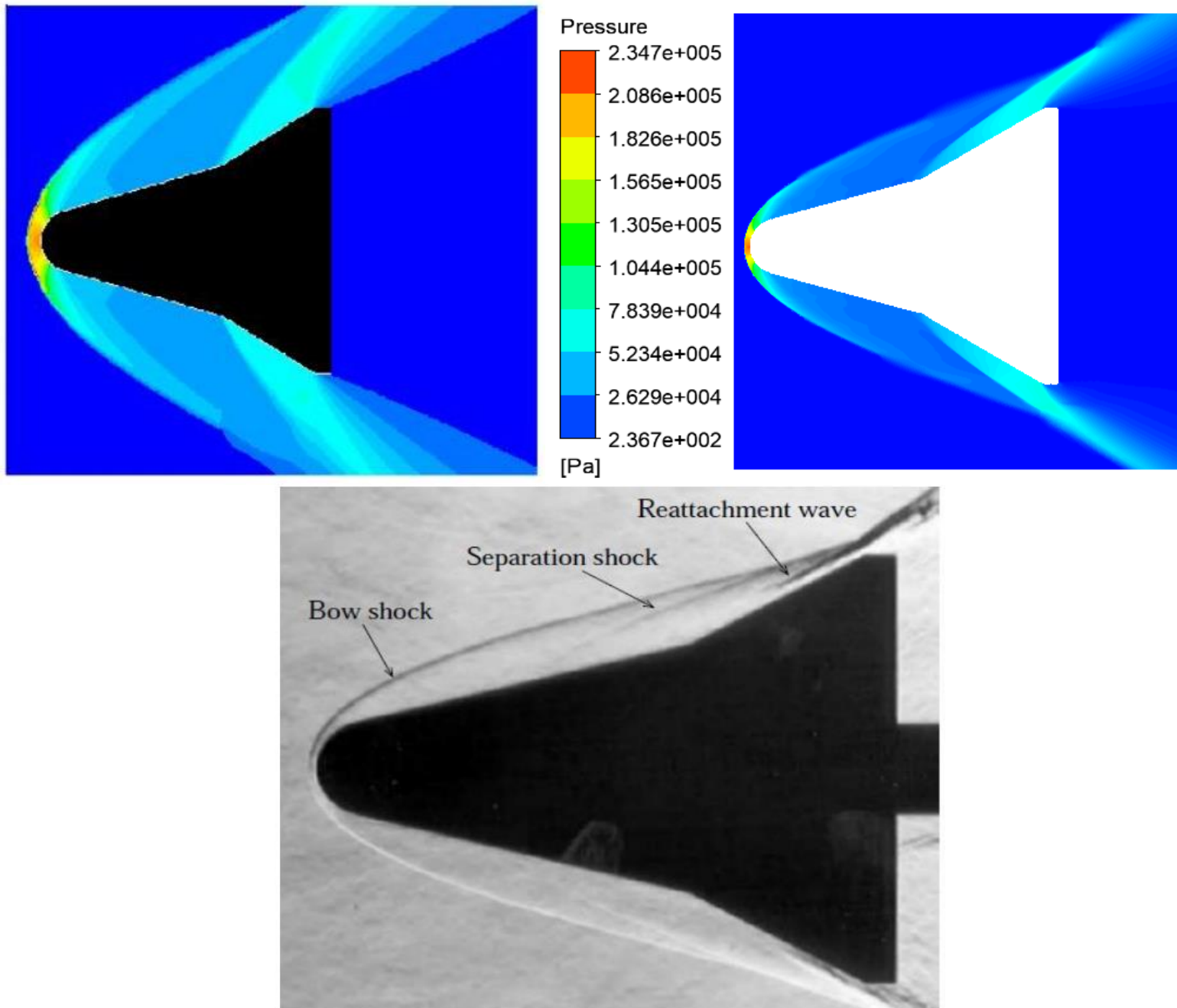


Figure 4.53: recirculation region in delta wing-body

4.6 Result of Hypersonic Flow over a Circular Cone

❖ Validation

The figure (4.54) shows the experimental schlieren graph. This graph shows the shock wave pattern and the fluent generated shock wave pattern for the same experimental input so we are comparing the both graphs for validation. One notices a good agreement between the



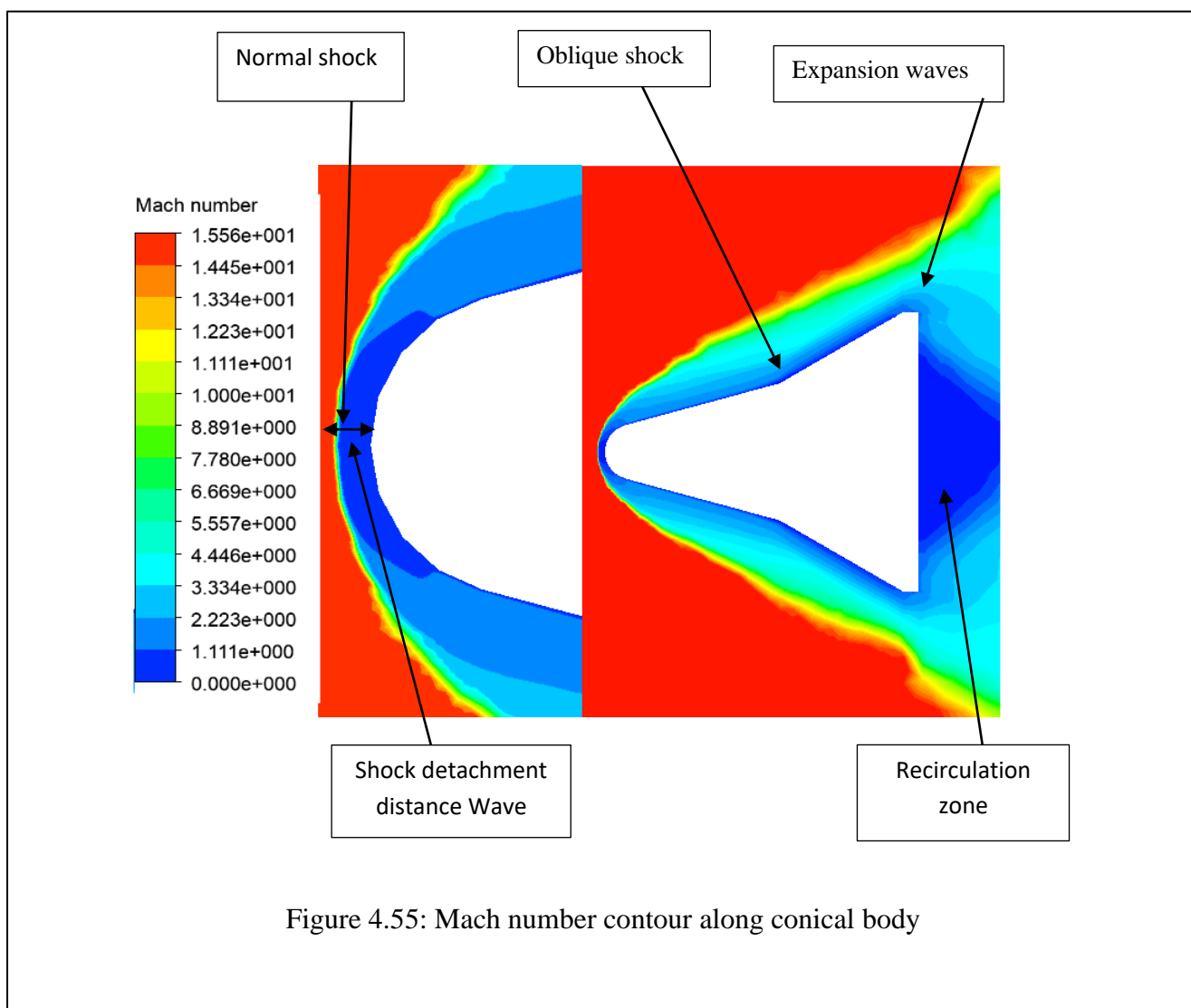
two results.[34]

Figure 4.54: Comparison of Experimental Result with analytical result

4.6.1 Shock wave

The flow turns almost perpendicularly away from the convex corner of the nose-body junction, forming an expansion fan. Through this expansion fan, the subsonic flow near the stagnation point accelerates. The expansion at the ramp surface causes additional acceleration at the body surface in the flapping form due to the convergence geometry of the flare. The flow is turned toward it by the flap, resulting in the production of an oblique shock (figure 4.55) which decelerate the flow. Finally, the expansion fan at the base edge accelerates the flow.

A circumferentially uniform expansion fan arises at the circular base edge, deflecting the flow along the longitudinal axis. The streamwise vortices are caused by the finite spanned flap, and a complex base flow field with the recirculation zone is generated as a result. [34]



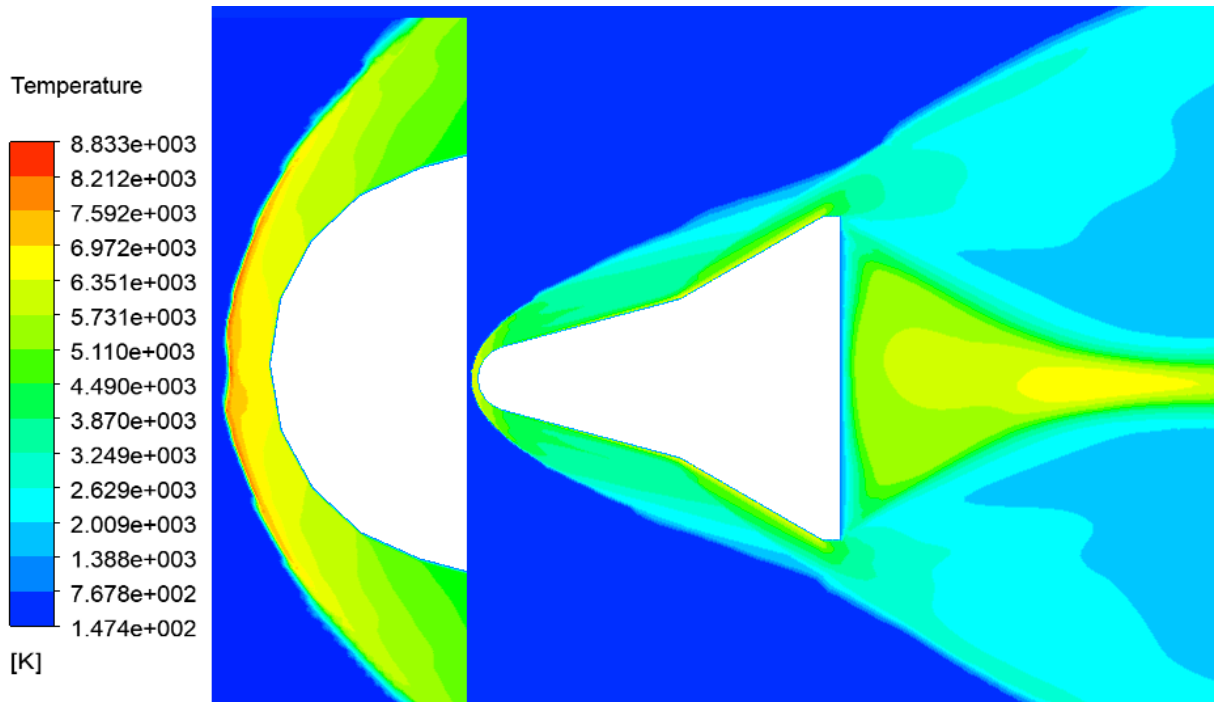


Figure 4.56: Temperature counter along conical body

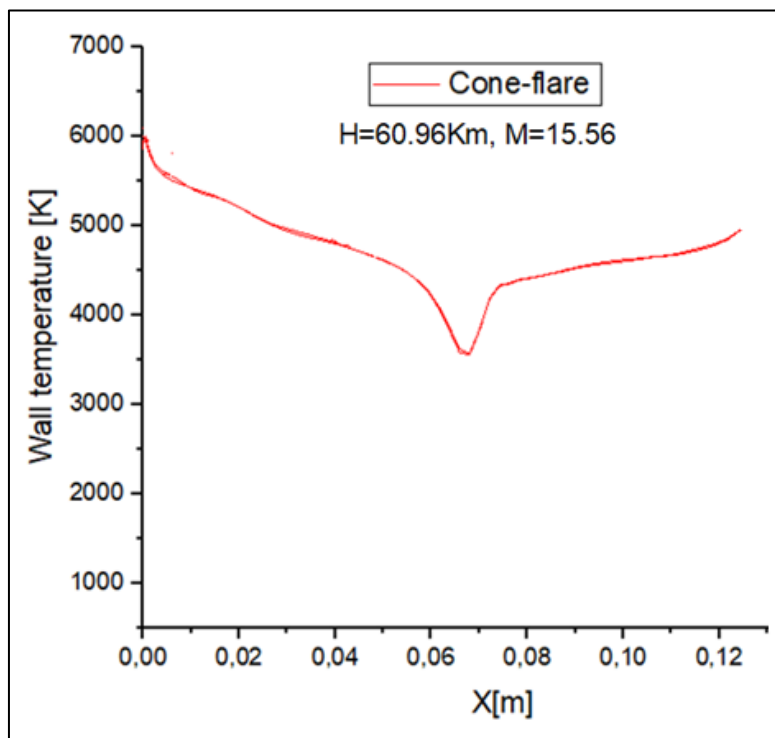
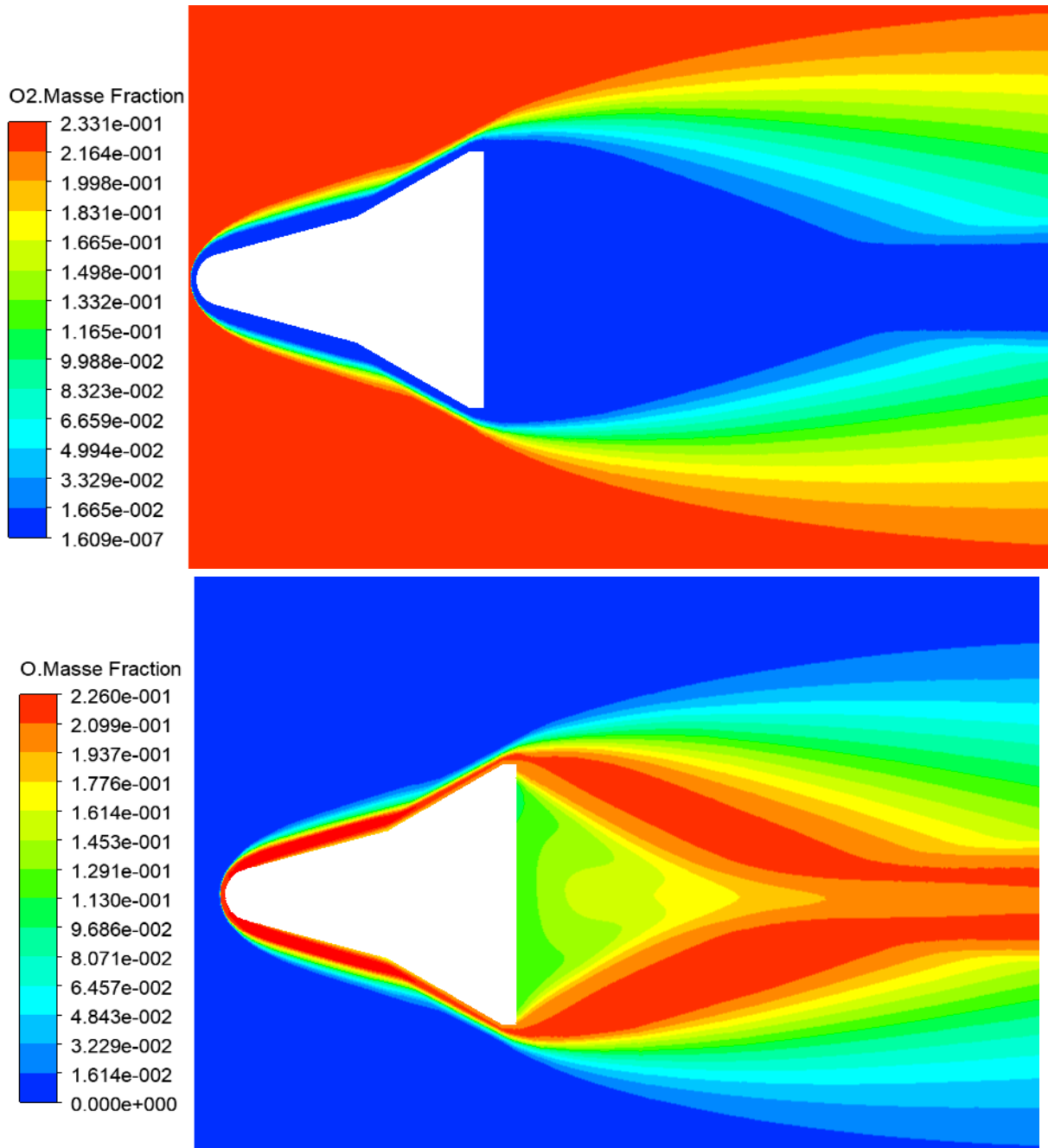


Figure 4.57: Cone-flare body outer streamlines distribution

5.6.2 Reaction effects

The real gas effect defers from the delta body shape only in the flaps part, we notice in figure (4.59) the formation of NO molecules where the flow is decelerated due to the compression waves that gives more time for the recombination process, in the other hand, figure (4.58) shows that the O₂ and N₂ dissociation layer contract in the flap region due to the formation of NO molecules.



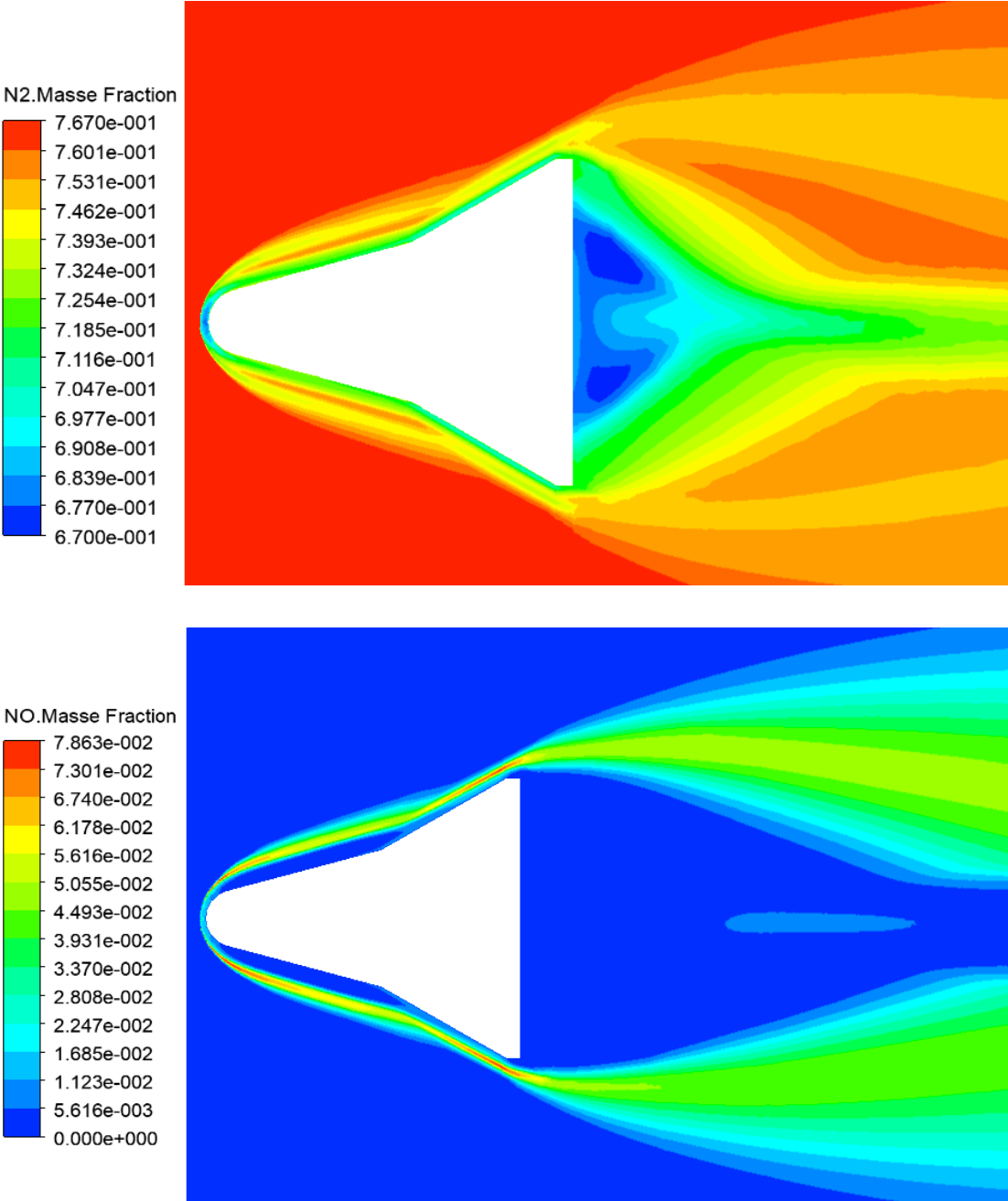


Figure 5.58: major species flied along conical body

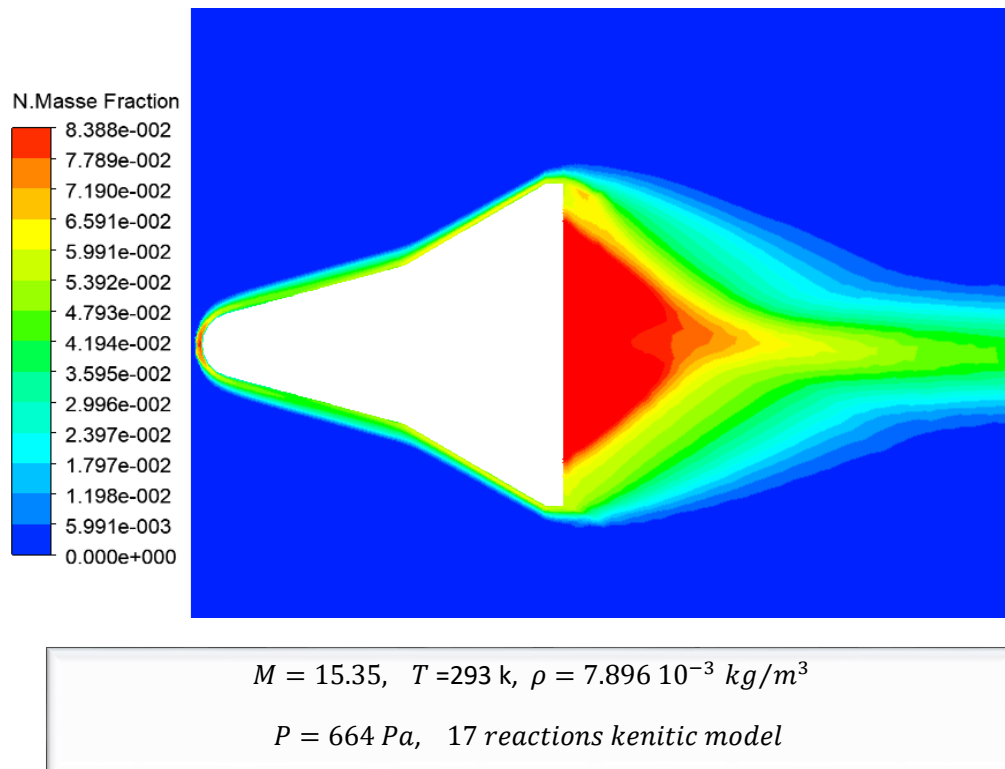


Figure 4.59: Mineur species filed along conical body

4.7 Vehicle shape

The drag coefficient, C_D , is the most difficult component of BC to calculate for re-entry vehicles because it is mostly determined by the vehicle's shape. We could simply put a model of the vehicle in a wind tunnel and take precise measurements to determine C_D at low speeds. Wind tunnel testing isn't possible at re-entry speeds nearing 25 times the speed of sound since no tunnels work at those speeds. To solve the problem with the highest accuracy, we need to use high-speed computers, this approach is now a specialized area of aerospace engineering known as computational fluid dynamics (CFD).

4.7.1 Effects of Vehicle Shape on Deceleration

Now that we have a way to find BC, we can use the numerical tools to see how the drag changes a re-entry vehicle's deceleration rate. Let's start by looking at two different vehicles entering Earth's atmosphere at deferent angles of attack and a velocity of 4877 m/s.

The results in figure (4.60) shows that the conical body (high BC) have more important air resistance at low angles of attack (0,10) than a delta wing body, because the

characteristic surface that faces the velocity stream lines at 0° is more important than a straight delta wing body (low BC). While we notice that there is an abrupt increase in the drag coefficient at high angles of attack, here where the effect of the planner geometry starts to appear, it has been observed that the moduli of wave drag and wall friction drag for the delta wing lifting body optimized at high angle of attacks which improves the lift-to-drag ratio by using the shock waves generated by its own flight as the lift surface, a phenomenon known as compression lift. [6]

We can notice in figure (4.60,61) that the delta wing body increase the lift and drag coefficient at high angle of attack, which enhance the drag to lift ratio by 63% compared to a ballistic cone-flare body.

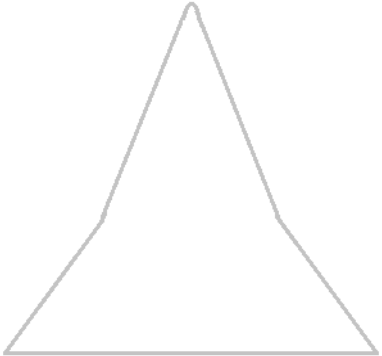
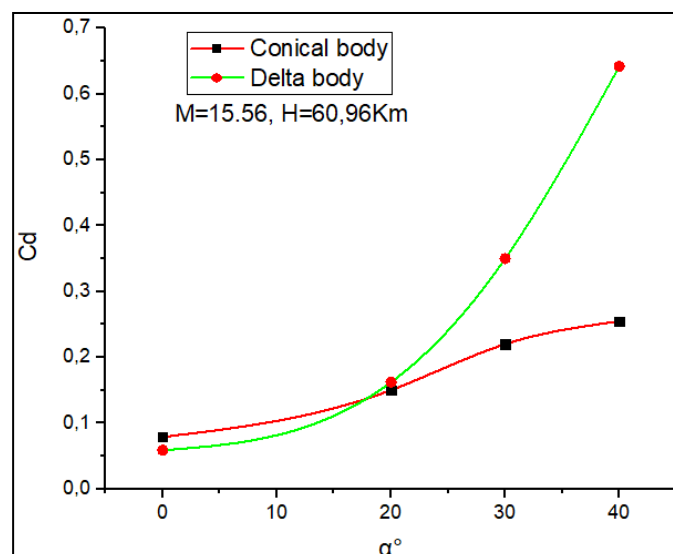
Vehicle Shape	Drag coeff	Lift coeff	Ballistic coeff	L/D
	0.36	0.462	$1.753 \cdot 10^{-5}$	1.28
	0.22	0.092887	$1.869 \cdot 10^{-4}$	0.422

Table 4.2: Effect of vehicle shape on deceleration



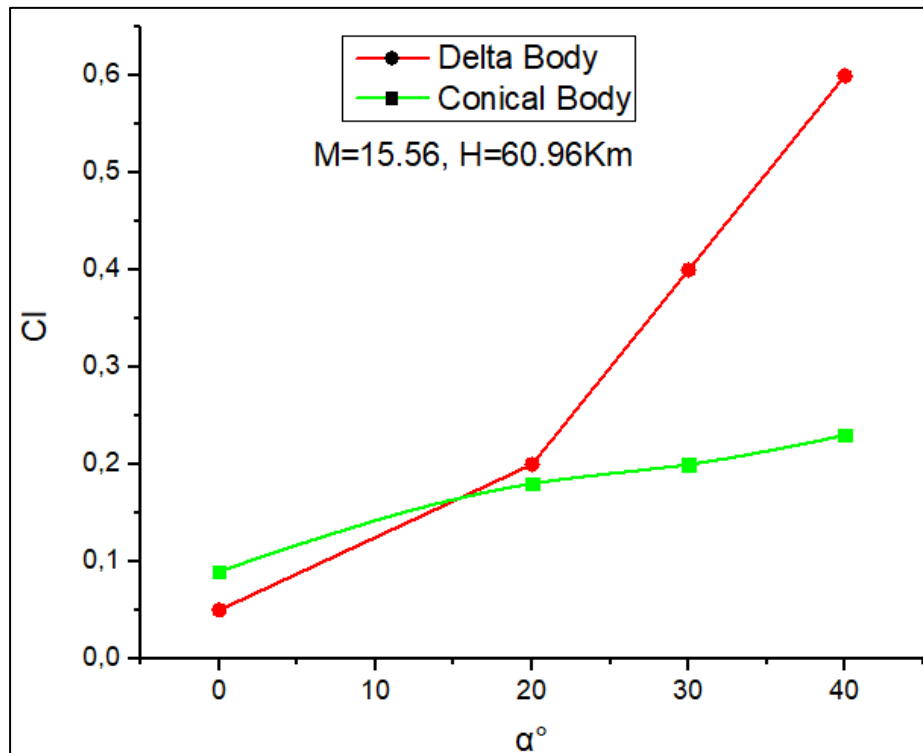


Figure 4.61: Lift coefficient in function of deferent angle of attack

Effects of Vehicle Shape on re-entry time

As we've seen before, a more streamlined conical (high-BC) vehicle reaches maximum deceleration much lower in the atmosphere than a delta (low-BC) vehicle; thus, it reaches the ground more quickly but generate severe heating rates.

One of the most important aspects that a delta wing serve is maintaining a safe and controlled descent, so here we are again in compromise between spending a little time in space even through accept more severe heating rates, in the other hand, with this lift- drag capability, the delta body has a side-to-side range capability of about 2000 km, that means spend more time in space but for a controlled and safe landing.

Effect of vehicle Shape on re-entry velocity

If we compare the re-entry velocity for deferent re-entry vehicle shape in figure 4.62, we notice that the conical body can handle a lower wall temperature for the range of 15 to 9 Mach number. While the cone re-entry shape has more available temperatures for less than 6 and more than 20 Mach number.

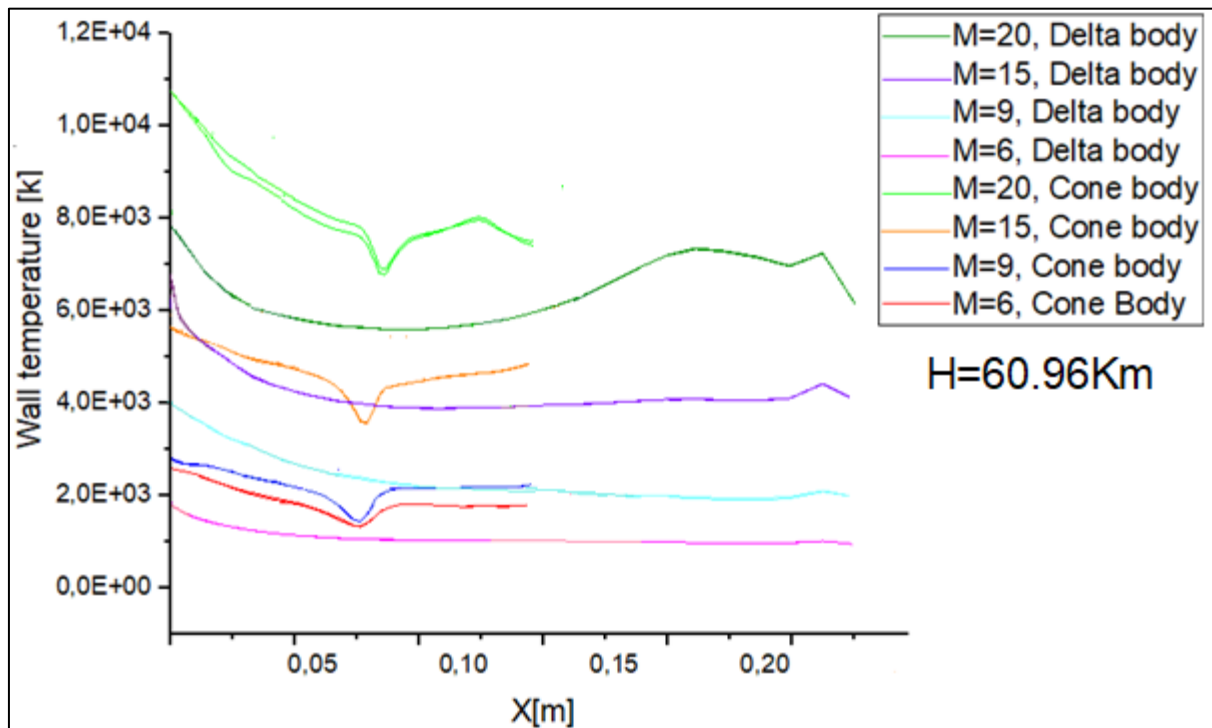


Figure 4.62: Wall temperature in function of Mach number

CONCLUSION

Conclusion

This modest work contributes to the study of reactive hypersonic flows in thermochemical non-equilibrium around nose-type geometries of the representative space shuttle orbiter configuration and Blunted Cone-Flare body, to ensure better thermal protection of spacecraft with good flight quality.

The physicochemical phenomena encountered during atmospheric re-entry, namely the vibration and dissociation of molecules as well as heat transfer, account for the behaviour of air at high temperature. The air is assumed in the shock layer of a reactive gas composed of five species (N_2, O_2, O, N, NO), two models of elementary reactions of 5 and 17 chemical reactions were chosen. The phenomena of ionization and radiation are neglected. The studied phenomena prevail during atmospheric re-entry for the deferent angle of attack 0° to 40° at an altitude range of from 60.96 to 76.20 km for 4.88 to 7.32 km/sec velocities.

This study is carried out using ANSYS V19 software reveals and highlights many very important physical aspects, that originate downstream from the intense shock wave that appears upstream of the obstacle, these can be summarized in what follows:

- ✓ The effects of reactive gases at high temperature are essential for the evaluation of hypersonic flows in the atmospheric re-entry phase, and the accuracy of the results depends on the reactions number to be considered, an advantageous effect on the wall cooling of the spacecraft is observed and became more important for 17 chemical reactions model compared to the 5 chemical reactions model, with a temperature gain of 1407K where molecules absorb energy to recombinate or to break the links between them which cause a decrease in temperature, the heat flux absorbed increase for more important dissociation reactions number which are endothermic processes.
- ✓ The endothermic phenomena are more important at high Mach numbers where the gas is very agitated and the number of collisions is very large which quickly promotes dissociation Fig (4.9). Our results corroborate with Tristan results with an error of 2.89% ref [49]. Fig. (4.3)
- ✓ A steep re-entry causes low surface heating rate. On the other hand, shallow re-entries lead to higher surface heating rates and causes an increase in the aerodynamic forces, drag and lift, so from our result Fig (4.28), it is noted that the drag coefficient increases by a rate of approximately 83% going from a zero AOA to an AOA of 40° , with an increase in wall temperature of 700k Fig (4.30), this allows our delta planner vehicle to manoeuvre the forces operating on it to the intended landing area. Therefore, in order to make a compromise between high aerodynamic forces and low heating rates, the results show that the 30° to 40° re-entry angle of attack is the appropriate range, where the vehicle produce an increase in lift force by 51% from 30° to 40° AOA for the same aero heating load rate.
- ✓ A decrease in the drag coefficient is recorded as a function of the Mach number, evaluated at 89% from Mach 6 to Mach 20 with a gain of 15% in wall temperature, and an estimated decrease of 82% passing from an altitude of 60Km to 76Km, which

confirms that introducing high angle of attack at the upper altitude risks the vehicle to bouncing off the atmosphere and back into space, even producing low aero heating rates, so we concluded that it's more appropriate to introduce high angle of attack at low altitude ,where the aerodynamic forces are significant to decelerate the vehicle and avoid the risk of the vehicle rebounding into deep space.

- ✓ The function of the blunt spike plays a significant role in reduction mechanism of wall heating, which produces a decrease in temperature from 8600k to 7770k without and with blunt spike function respectively Fig (4.38). Our results corroborate with Harish Panjagala results with an error of 3.84% ref [45].
- ✓ The delta wing body configuration generate higher lift force compared to the cone-flare body by evaluating the lift to drag ration by 63%, which enhance the control landing process of the lifting bodies. Our result corroborates with the work of Mr. Muhammad Imran Afzal ref [58].

At the end of this work, we can conclude that the complexity of correctly modelling the hypersonic flows applied to atmospheric re-entry lies in the multidisciplinary nature of the problem with which the spacecraft is confronted including at the same time aerodynamics, chemistry, thermodynamics and heat transfer problems, mastery of these disciplines is essential and a challenge to be met, in order to meet and obey the requirements of aerospace studies. This work is only an outline concerning the phenomena encountered in hypersonic regimes where research is very intense. This area remains a field of research, although no lifting vehicle is in operation, our goal is to approach more of the realization of such a design knowing very well its criteria.

Perspective

Finally, Other points which, without changing the configuration, could be the subject of further study through certain perspectives that can be envisaged from different aspects, are those concerning the following points:

- Taking into account the phenomenon of ionization: for which the various attempts to model it have failed during this work.
- Resume this study by a numerical calculation code
- The study of the influence of the spike length variation on the improvement of heat load reduction.
- The study of the interaction between the fluid and the structure, the description of the movements of the structures in contact with the fluid itself in motion and more precisely the determination of how the fluid modifies the behaviour of structures.
- Resume this study with the Open-source code
- Resume the 3D geometry which we have not can perform due to the time limit factor

APPENDIX A

Park's thermochemical model for a five species neutral air mixture the Park model considers a total of 17 reactions, i.e., 15 dissociation reactions (five for each molecule) and two Zeldovich (exchange)

TABLE A: Thermochemical model table

Reaction	M	Pre-exponential Factor	Activation energy (j/kgmol)	Tempretture exponent(k)
Dissociation Reaction				
$O_2 + M \leftrightarrow 2O + M$	O	1e+19	4.947e+08	-1.5
	N	1e+19	4.947e+08	-1.5
	NO	1e+19	4.947e+08	-1.5
	O_2	1e+19	4.947e+08	-1.5
	N_2	1e+19	4.947e+08	-1.5
$N_2 + M \leftrightarrow 2N + M$	O	3e+19	9.412e+08	-1.6
	N	3e+19	9.412e+08	-1.6
	NO	3e+19	9.412e+08	-1.6
	O_2	3e+19	9.412e+08	-1.6
	N_2	3e+19	9.412e+08	-1.6
$NO + M \leftrightarrow O + N + M$	O	1.1e+14	6.277e+08	0
	N	1.1e+14	6.277e+08	0
	NO	1.1e+14	6.277e+08	0
	O_2	1.1e+14	6.277e+08	0
	N_2	1.1e+14	6.277e+08	0
Recombination				
$N_2 + O \leftrightarrow NO + N$		1.8e+11	3.193e+08	0
$NO + O \leftrightarrow N + O_2$		2400000	1.598e+08	1

REFERENCES

- [1] Wallace, J. M., and P. V. Hobbs. Atmospheric Science: An Introductory Survey. 2nd Edition. New York, 2006.
- [2] I.J. Keshtiban, F. Belblidia and M.F. Webster, "compressible flow solvers for low mach number flows", Institute of Non-Newtonian Fluid Mechanics, University of Wales, Swansea SA2 8PP, UK, 2004
- [3] Sudharsan Thiruvankadam, "A Computational model to characterize different flow regimes microscale re-entry satellites", 1st edition, Master of science engineering, The University of Texas at Arlington in Partial Fulfilment, Arlington, December 2013
- [4] Dr Edmondo Minisci, "Space Debris and Asteroids (Re)Entry Analysis Methods and Tools", Vol. 156. p. 3993-4011 19 p. AAS 15-557. Centre for future Air-Space transportation technology (cFASTT), University of Strathclyde, Glasgow, UK, Dept of Mechanical & Aerospace Engineering, Glasgow, UK, 2013.
- [5] Benjamin M. Sandoval, "Oblique Shock Visualization and Analysis using a Supersonic Wind Tunnel", 85281, Arizona State University - A. Fulton School of Engineering, Tempe, AZ, Iran 2016.
- [6] John D. Anderson, J, "Oblique Shock Waves, MAE 5420 - Compressible Fluid Flow", Chapter 4 pp.127-145, National Air and Space Museum, Smithsonian Institution, Washington, 2019.
- [7] Marcel Zijlema, "The role of the Rankine-Hugoniot relations in staggered finite difference schemes for the shallow water equations", P.O Box 5048, 2600 GA Delft, Delft University of Technology, Department of Hydraulic Engineering, Netherlands, August 14, 2019.
- [8] Anderson, "Normal Shock waves, Compressible Fluid Flow", Second Edition Chapter 3 pp. 88-125, Blacksburg, Virginia, 2019.
- [9] Robert Gerald Dominy, "Rarefied hypersonic shock wave and blunt body flows", DSC:DX221474, A Thesis submitted for the Degree of Doctor of Philosophy, of the University of London, London, September 1987.
- [10] DINESH K PRABHU, "High-temperature effects in hypersonic flows", Vol. 20 pp. 781-814, Division, National Aerospace Labo, Bangalore, India, MS received 31 August 1994; revised 21 January 1995.
- [11] W. NIEHAUS, "Heat shield concept and materials for re-entry vehicles part reaction of air to hypersonic flow", Defence documentation centre, Virginia, July 15, 1963.
- [12] Eberhard Morgenroth, "Characteristic Time NonDimNumbers", ETH_SAMM L07.RTD, Institut für Umweltingenieurwiss. in Gujer10/29/2015.
- [13] Roger D. Launius and Dennis R. Jenkin, "Coming home," re-entry and recovery from space", LT1060.L38. Library of Congress Cataloguing NASA/SP, Washington; 2011
- [14] Monti, R. Janovsky, M. De Stefano Fumo, "Exploiting Lift Force in Reentries from Exploration Missions"; Thesis for: Doctora, Institute of Space Technology, DGLR International Symposium 'To Moon and Beyond', Bremen, 2007.
- [15] Rodney C. Wingrove; "A Study of Guidance to Reference Trajectories for Lifting Re-entry at Super-circular Velocity"; MIU01-011432524, National Aeronautics and Space Administration, University of Michigan Library Repository, Washington Dec-1963

- [16] Loïc van Ghèle. “Analyse aérothermodynamique de la rentrée atmosphérique d’un véhicule réutilisable depuis une orbite basse terrestre”. Sciences de l’ingénieur [physics]. Université de Toulouse, Français, 2020
- [17] R. Dale Reed, “the lifting Body story, with Darlene Lister”, Nasa sp-4220, the NASA history Series, Washington 1997.
- [18] L.H. Townend, “Research and Design for Lifting Re-entry”, edition 31 Progress in Aerospace Sciences, UK 1979.
- [19] Paolo Baiocco, “PRE-X experimental re-entry lifting body design of flight test experiments for critical aerothermal phenomena”, edition 18 Saint-Médard-en-Jalles Cedex, France, 2019.
- [20] G. N. Dudin, “Hypersonic viscous gas flow over delta wing in the intermediate interaction regime with allowance for wake flow”, 28 edition, Fluid Dynamics, Moscow, 21 February 1992
- [21] Izv. Akad. Nauk SSSR, Mekh. Zhidk. “Numerical analysis of heat transfer on the surface of delta wing in a hypersonic air flow at large angle of attack”, edition No. 3, 164. University of Technology Fluid Dynamic Moscow, (1982).
- [22] S. A. Gorokhov, V. V. Eremin, and A. M. Polyakov “Entropy effect in hypersonic flow over blunted wings”, 26, pages 304–307 edition, University of Technology Fluid Dynamic Moscow, MARCH 1991.
- [23] L. Gonor and N. A. Ostепенko, “Hypersonic flow past delta wing of finite thickness, Fluid Dynamics volume”, edition 5, 394–402, University of Technology Fluid Dynamic, Moscow, 1970.
- [24] G.Z. Genhuni, E. M. Zhukhovitskii and III. s. Iurkov, “Hypersonic flow past a delta wing”, PMM vol. 34, N3 edition University of Technology Fluid Dynamic Moscow, Received January 31, 1969.
- [25] M. Cevdet Celenligil and James N. Moss, “Hypersonic rarefied flow about a delta wing - direct simulation and comparison with experiment”, Vol 30 N8 edition, NASA Langley research center, Hampton Virginia, August 1992.
- [26] A. V. Vaganov, D. V. Grachikov, V. M. Kashin, V. D. Nemykin, A. Yu. Noev, V. N. Radchenko, A. S. Skuratov, and V. I. Shalaev, “Experimental study of hypersonic boundary layer transition on a flat plate delta wing”, 1st edition, Science and Technology on Space Physics Laboratory, China Academy of Launch Vehicle Technology, China 3 June 2019.
- [27] Sanjeev Kumar, M.Tech. “Numerical Simulation of Chemically Reactive Hypersonic Flows”, 1st edition A95-95357, European Computational Fluid Dynamics, Germany 22. Dezember 2005.
- [28] Ideen Sadreghighi, Ph.D. “Turbulence Modeling”, 1 edition PhD in Mechanical Engineering, CFD Open Series, Mason, Ohio, États-Unis 2006.
- [29] Ismail B. Celik, “Introductory Turbulence Modeling”, 1 edition, P.O. Box 6106, University Mechanical & Aerospace Engineering Dept. West Virginia December 1999.
- [30] Goodarz Ahmadi, “Introduction to turbulence modelling”, 13699-5725 Department of Mechanical and Aeronautical Engineering, Clarkson University Potsdam, 1994.
- [31] Gerald Recktenwald, “Introduction to Turbulence Modeling”, edition 4, for CFD, Mechanical and Materials Engineering Department Portland State University, Portland, Oregon, February 19, 2020.
- [32] L. Cutrone, F. Battista, “Assessment of Wall-functions $k-\epsilon$ Turbulence Models for the Prediction of the Wall Heat Flux in Rocket Combustion Chambers”, 80125 Dipartimento di Ingegneria Aerospaziale, DIAS Università degli Studi di Napoli “Federico II”, Piazzale Tecchio, Naples, Italy January- 2018.
- [33] Ahmed Al Makky, “Coding Tutorials for Computational Fluid Dynamics”, First edition, University of

- the West of Scotland ,United Kingdom 2014
- [34] Alexandra Elbakyan , Hirsch, C. Structured and Unstructured Grid Properties”. Edition 42(249-277 chapter 6 ,Numerical Computation of Internal and External Flows, Elbakyan, 2007.
- [35] Francois Duchaine, ”Génération du maillage structuré par Krigeage avec raffinement elliptique local ”,1^{er} édition Ecole de technologie supérieur université du Québec, Montréal, 3 septembre 2004.
- [36] Josep Sarrate, ”A brief introduction to mesh generation” , Laboratori de Càlcul Numèric (LaCàN), Department d’Enginyeria Civil Ambiental, Department d’Enginyeria Civil i Ambiental Universitat Politècnica de Catalunya (Spain)2015.
- [37] Patrick M.Knupp, ”Remarks on Mesh Quality” , NM87185 ,Aerospace Sciences Meeting and Exhibit,7- Sandia National Laboratories,Sandia 10January, 2007.
- [38] ANSYS, Inc. Chapter 15. ”Reporting Mesh Statistics” , Technology Drive, April 15 2008 .
- [39] A BOULAHIA, ”Couche Limite hypersonique dans des écoulements visqueux en déséquilibre chimique” 1^{er} édition,thèse de Doctorat, département physique, Université Mentouri, Constantine 2010.
- [40] OUCHENE samir, GHENDOUR Nabil, ALLOUCHE Rachid,RENANE Rachid, ” Simulation numérique d’écoulement hypersonique en hors équilibre thermochimique derriere l’onde de choc intense ” . 1st edition ,Université Saad Dahleb Blide institut d’Aéronautique et des études spatiales Blida, Septembre2015
- [41] John A. ordi, Robert J. idal, and Charles B. Johnson “ Chemical Nonequilibrium effects on the inviscid flow in the windward plane of symmetry of two simplified shuttle configurations”, first edition , *Cornell Aeronautical Lab., Inc. Hampton, VA, United States, NASA Langley Research Center* ,Washington 1973.
- [42] Franke ,J,Hellsten,A,Schlunzen ans Carissimo,B, ”best practice guide for the For the CFD simulation of fows in the urban environment” ,cost Action732:quality assurance and improvement of microscale meteorological models, Belgium 2007.
- [43] Tominaga ,Y,Mochida,A,Yoshie,R,Kataoke,H,Nozu,T,Yoshikawa,M,and Shirasawa ,T, ”ALJGUIDELINES for pratical application of CFD to pedestrian wind envirement around buildings” , 96, Tohoku University, Aoba 06, Aramaki, Aoba-ku, Sendai-City, Miyagi, Urban on Conference International seventh ,yokohama japan, 2009 July 3 - June .
- [44] Guilai Han and Zonglin Jiang, “Hypersonic Flow Field Reconfiguration and Drag Reduction of Blunt Body with Spikes and Sideward Jets”, 4 edition,State Key Laboratory of High Temperature Gas Dynamics, Institute of Mechanics, Chinese Academy of Sciences, Beijing, China ,13 April 2017.
- [45] Harish Panjagala, «Aerothermodynamics topology optimization of hypersonic re-entry vehicle with aerospike by using CFD”, pp. 1114 – 1123, Article ID: IJMET_09_01_119, International Journal of Mechanical Engineering and Technology, Andhra Pradesh, India, 2018.
- [46] "ANSYS Help14.5"ANSYS Computing Platform Support Summary , Irvine October 2012
- [47] ANSYS 13.0 Tutorial, "Customer Training Material".: ANSYS ,Irvine 12/2010
- [48] Jun Hyeok Chae, , Tapan K. Mankodi, , Seong Man Choi ,, Rho Shin Myong ,”Combined Effects of Thermal Non-equilibrium and Chemical Reactions on Hypersonic Air Flows Around An Orbital Re-entry Vehicle”, edition 4,International Journal of Aeronautical and Space Sciences, Korean S ,2020.
- [49] Tristan Soubrie "Prise en compte de l’ionisation et du rayonnement dans la modélisation des écoulements de rentrée terrestre et martienne",1^{er} édition L’école National Supérieure de L’Aéronautique et de l’espace, Paris 2006.
- [50] DR R.Kennethlobb, ” Experimental measurement of shock detachment distance on sphere fired in air at hypervelocity’s”.133 édition In W. C. Nelson, editor, Proc. of the AGARD-NATO in The High

- Temperature Aspect of Hypersonic Flow. Pergamum Press, Maryland ,1962.
- [51] V. Joly, F. Coquel, C. Marmignon, W. Aretz, S. Metz, and H. Wilhelmi. “Numerical modelling of heat transfer and relaxation in nonequilibrium air at hypersonic speeds”. La Recherche Aérospatiale, Aachen university ,1994
- [52] Séror, Stéphane. ”Extension de l’approche déficitaire pour le calcul des couches limites hypersoniques en déséquilibre chimique et vibrationnel. Modélisation du couplage Vibration/Réactions d’échange ”, Département d’Etudes et de Recherches en Aérothermodynamique -DERAT. PhD thesis, SupAero Toulouse, 1997
- [53] G. Tchuén,. ”Modélisation et simulation numérique des écoulements a haute enthalpie : influence du déséquilibre électronique”. See also AIAA paper 2004–2462, PhD thesis, Université d’Aix-Marseille I, 2003.
- [54] B. Sc. II-Sem, Catalysis,Lethbridge University , 2020
- [55] Zongshu Mei ,”Coupled simulation for reentry ablative behavior of hypersonic vehicles”, Mater. Sci. Eng.892 012028, IOP Materials Science and Engineering People’s Republic of China, china, 2020.
- [56] Wiley-VCH Verlag GmbH & Co. KgaA Editors: D. Jacob, G. Sachs, S. Wagner “Characterization of High-Enthalpy Flows”, 31, 70550 edition pp.199-220 Chapter: 4.7 , Universidad Stuttgart, Institut für Raumfahrt systeme, Pfaffenwaldring , Stuttgart ,November 2005.
- [57] S. G. Mallinson, S. L.Gai, and N. R. Mudford ,”High-Enthalpy, Hypersonic Compression Corner Flow” , Vol. 34. No. 6 ,Australian Defence Force Academy, Canberra ACT 2600, Australia,. June 199
- [58] Muhammad Imran Afzal,”Design and analysis of vehicle and guidance concept for interplanetary return mission”, Thesis for: Doctoral ,Institute of Space Systems, Stuttgart ,2010.
- [59] Cole, J. D. and Brainerd, J. J. “Slender wings at high angles of attack in hypersonic flows”. In Hypersonic Flow Research (Ed. F. R. Riddell) California Institute of Technology, Pasadena, , Academic Press, California ,1962.
- [60] Kennet, M. “The inviscid hypersonic flow on the windward side of a delta wing”. 1st edition ,Inst. Aerospace Sci. Preprint ,1963.
- [61] Antonov, A. M. and Hayes, W. D. “Calculation of the hypersonic flow about blunt bodies.” 30, 421-427 edition , J. Appl. Math. Cambridge ,Mech., 1966.
- [62] Messiter, A. F. “Lift of slender delta wings according to Newtonian theory”. VOL. 1, NO. 4,California Institute of Technology, Pasadena, Calif ,April 1963.
- [63] Squire, L. C. “Calculated pressure distributions and shock shapes on thick conical wings at high supersonic speeds” Q., XVIII, 185-206. University Engineering Department, Trumpington Street, Cambridge, England ,Aero., UK MinistryMay 1967.
- [64] Squire, L. C.” Calculation of pressure distributions on lifting conical wings with application to the off-design behaviour of wave riders”. AGARD CP 30. University Engineering Department, Trumpington Street, Cambridge, UK Ministry1968.
- [65] Hillier, R. “The effects of yaw on conical wings at high supersonic speeds”. 21, 3, 199-210. Aero. Q., Cambridge University,UK Ministry of Defence August ,UK,1970.
- [66] Hillier, R. “Some applications of thin shock layer theory to hypersonic wings”. 1st edition ,Ph.D. Doctoral Thesis, University of Cambridge, 1970.
- [67] Roe, P. L. Private comuncations to author, No. 70-18edition , Thame, 1970.
- [68] Hillier, R. “Three-dimensional wings in hypersonic flow”. Gaza, No.5, pp. 148–161edition , Translated

- from Izvestiya Rossiiskoi Akademii Nauk, Mekhanika Zhidkosti , Gaza, 1992.
- [69] Shanbhag, V. V. “Numerical studies on hypersonic delta wings with detached shock waves”. 7edition , Aeronautical Research Council Current Papers ,US , 1973
- [70] Roe, P. L. “Correlation between the heat transfer to a reentering space vehicle and the inviscid flow field”. RAE TR to be published , Université Lyon,lyon 2013
- [71] Richards, B. E. and Houwink, R. “An experimental study of space vehicle configurations with high lift during re-entry”. VKI TN 117 edition. Inst. for Fluid Dynamics, Rhode-Saint-Genese (Belgium), Cambridge, Engl., Apr. 1976 .
- [72] Squire, L. C.” The effects of recessed lower surface shape on the lift and drag of conical wings at high incidence and high Mach number”. Aero. Q., 26, I, I-10. Edition, University Engineering Department, Trumpington Street, Cambridge, England February ,1975.
- [73] Squire, L. C. “Private communications to author ,2nd edition UK Ministry of Defence, 1970
- [74] Fey, W. A. “Use of a lifting upper stage to achieve large offsets during ascent to orbit”. AIAA Paper 66-60 edition, , Structural Collapse Technician,UK,1966.
- [75] Irwin E. Alber,Estimating,” the Orbiter reentry trajectory and the associated peak heating rates”, Aerospace Engineering on the Back of an Envelope , Los Angeles, California 18 January 2012
- [76] Nathaniel Hildebrand,1 Anubhav Dwivedi,1 Joseph W. Nichols, Mihailo R. Jovanovi´and Graham V. Candler” Simulation and stability analysis of oblique shock-wave/boundary-layer interactions at Mach 5.92”, edition 25,Department of Aerospace Engineering and Mechanics, University of Minnesota, 110 Union Street SE, d 26 January 2018